

BULGARIAN CHEMICAL COMMUNICATIONS

2016 Volume 48 / Special Issue A

Proceedings of the Fourth Scientific Seminar of Physical Chemistry for
Young Scientists and PhD Students, Sofia, 2015

*Journal of the Chemical Institutes
of the Bulgarian Academy of Sciences
and of the Union of Chemists in Bulgaria*

Dear readers,

This special issue of Bulgarian Chemical Communications is dedicated to the *Fourth Seminar in Physical Chemistry for Young Scientists and PhD Students* that has been organized by the Institute of Physical Chemistry "Acad. Rostislaw Kaischew", Bulgarian Academy of Sciences. Initiated four years ago by a group of young scientists the seminar became an annual event, currently covering a wide range of research fields related to physical chemistry, and attended by participants from the whole country. The articles of this issue represent a diverse scientific matter that even extends beyond the *conventional frame* of physical chemistry in the large branch of natural science. It includes also papers from the researchers who won the seminar's competition for best oral and poster presentation - Mariya Kalapsazova and Silviya Pehlivanova, respectively.

We also devote this issue to our colleague Ivan Slivkov, who was exceptionally awarded for his impressive scientific debut. It is with deep regret that we have to announce his sudden death in the middle of 2015 summer.

Anna Gyurova & Ivaylo Dimitrov
Guest Editors

Kinetic and equilibrium properties of foam films stabilized by mixtures of *n*-dodecyl- β -D-maltoside with nonionic or ionic surfactants

D. S. Ivanova^{1*}, J. K. Angarska¹, E.D. Manev²

¹Faculty of Natural Sciences, Konstantin Preslavsky University of Shumen, Universitetska str. 115, 9712 Shumen, Bulgaria

²Faculty of Chemistry and Pharmacy, Sofia University, James Bourchier Blvd. 1, 1164 Sofia, Bulgaria

Submitted on July 9, 2015; Revised on October 5, 2015

Experimental data for kinetic and equilibrium parameters for foam films, stabilized by mixtures of *n*-dodecyl- β -D-maltoside ($C_{12}G_2$) with hexaethyleneglycol monododecyl ether ($C_{12}E_6$), dodecanol ($C_{12}E_0$), and dodecyl trimethylammonium bromide ($C_{12}TAB$) are obtained interferometrically. The influence of mixture composition and total surfactant concentration on the film thinning, film type and its stability is investigated at low (0.001M) and high (0.1 M) ionic strength. The results follows that: (i) the film stability strongly depends on the surfactant nature at low ionic strength; (ii) the thinning rate for films from mixtures of 50:1 correlates with that for films stabilized by pure $C_{12}G_2$; (iii) for films from mixtures of 1:1 thinning rate is controlled by the component dominating in the adsorption layer - for films from mixtures of $C_{12}G_2 + C_{12}E_6$ it is determined primarily by $C_{12}E_6$, while for the $C_{12}G_2 + C_{12}TAB$ mixtures – by both components.

Keywords: foam films; *n*-dodecyl- β -D-maltoside, hexaethylene glycol dodecyl ether, dodecyl trimethylammonium bromide, film thickness; velocity of film thinning.

1. INTRODUCTION

Since in the practice colloids are usually stabilized by mixtures of surfactants, investigations of films in the presence of such surfactant mixtures are of primary importance. The present study comprises the non-ionic surfactant *n*-dodecyl- β -D-maltoside ($C_{12}G_2$ or G_2) and its mixtures with the nonionic hexaethyleneglycol monododecyl ether ($C_{12}E_6$ or E_6), or dodecanol ($C_{12}E_0$ or E_0), and the ionic surfactant dodecyl trimethylammonium bromide ($C_{12}TAB$ or TAB). The choice of these surfactants, possessing the same hydrophobic tail, but with different head groups, is not accidental - they have the following special properties: (i) sugar-based surfactants are non-toxic, biodegradable, insensitive to temperature, pH, and are not affected by the concentration of Ca and/or Mg ions in the water. Information about the advantages of these surfactants as an alternative to some widely used nonionic surfactants is given in Refs. [1-3]; (ii) ethylene oxides (C_jE_j) surfactants are widely used in the practice as stabilizers of colloidal systems, because of their low surface tension, CMC and foamability, as well as in mixture with other surfactants [3]; (iii) small traces of dodecanol in many commercial surfactants as impurity, its strong adsorption on interface at low

adsorption of some ionic surfactants at interface [4] as well as to increase the surface elasticity [5] and viscosity [6] make it an interesting additive; (iv) $C_{12}TAB$ is often used as a stabilizer of foams and foam films [4, 7, 8] as well as an additive to nonionic surfactants [9-11]. Varying its concentration in the individual solution or its content in the mixture allows the surface charge on the film surfaces to be controlled. Furthermore, the investigation of mixtures with $C_{12}TAB$ is of importance because of their antibacterial, antifungal and antiseptic action.

From the literature review, it is clear that there is a significant interest to the use of $C_{12}G_2$ and its mixtures as stabilizers of thin films. Their equilibrium [1,2,8,9] and kinetic [11-14] properties are studied intensively. Moreover, in these papers there is no convincing conclusion which surfactant in the mixture has the dominant role in the film behavior. Such a conclusion could be reached if the properties of the films from mixtures are compared to those of films with individual surfactants.

The above considerations determine the aims of the presented study:

- to test and discuss the influence of the surfactant type and concentration, ionic strength and molar ratio of the components in the mixture on the equilibrium state and velocity of thinning for films from mixed surfactant solutions: of $C_{12}G_2$ with the nonionic $C_{12}E_6$, or $C_{12}E_0$ and the cationic $C_{12}TAB$;

*To whom all correspondence should be sent:
E-mail: D.Ivanova@shu-bg.net

volume concentration and ability to compete the

- to compare the drainage rate of films from the mixtures to that of films from solutions of the individual surfactants, in order to differentiate their characteristics.

2. EXPERIMENTAL PART

2.1. Materials

The nonionic surfactants: *n*-dodecyl- β -*D*-maltoside (C₁₂G₂, purity>99.5%), purchased from Glycon; dodecanol (C₁₂E₀), purchased from Merck; hexaethyleneglycol monododecyl ether (C₁₂E₆), purchased from Fluka, were used without further purification. The cationic dodecyl trimethylammonium bromide (C₁₂TAB, purity >98%) was purified by a procedure given in [10]. Sodium chloride (NaCl) and sodium bromide (NaBr) were obtained from Merck and Sigma, respectively. They were roasted for 4h at 400°C to remove the organic contaminants.

All glassware was cleaned with concentrated chromic sulphuric acid and then was rinsed thoroughly with double distilled water before use. All solutions were prepared with double distilled water immediately before each experiment at 25°C \pm 1°C.

2.2. Experimental conditions

In accord with the aim of the presented study, experiments were performed with foam films of different radii, obtained from mixed solutions of varied total surfactant concentration, molar ratios of the surfactants and ionic strength. In order to compare the results for different mixtures, all concentrations are given in terms of their CMC, chosen as a reference. The used CMC values are given in [15]. The equilibrium surface tension (see Figs. 1-2) of mixed solutions, from which the foam films were formed, was measured by the Wilhelmy plate method.

2.3. Interferometric method for foam films investigation

From each solution of defined composition at least 50 foam films of different radii (from 0.05 to 0.15 mm) were obtained in a glass cell (with radius of the holder 2.15 mm) designed by Scheludko and Exerowa [16]. Each film was visually observed in reflected monochromatic light (wavelength, $\lambda = 551$ nm, 6.3 \times objective lens and 5 \times eye-piece) immediately after filling the holder of cell with solution, but its evolution was recorded (by Sony-SSC-M388CE photo camera) when the equilibrium state in the system was reached (after 1 hour). The film thicknesses at every one moment as well as equilibrium thickness (h_{weq}) were determined by a procedure described in details in [12]. The real equilibrium thickness (h_{eq}) was obtained by

correcting of h_{weq} value based on five (for C₁₂G₂ + C₁₂E₆), or three (C₁₂G₂ + C₁₂TAB) layers model of film structure [13,11]. The values of equilibrium thicknesses are presented in Table.1. They were used for calculating of the surface potential by the equilibrium method [17].

2.4. Determination of the film thinning velocity

For velocity of thinning in [18] is used the empirical equation (Eq.1) and it is shown that its form (Eq.2) yields a linear dependence whose slope gives the value of the drainage coefficient α

$$-dh/dt = \alpha h \quad (1),$$

$$\ln h = \ln h_0 - \alpha t \quad (2),$$

where: h is the current thickness; h_0 is the initial thickness (after the maximum in the kinetic curve), from which the time of thinning t from h_0 to h is measured.

Base on the linear dependence $\ln h$ vs. t the drainage coefficients for all investigated films were received (for details see Refs.12,13,15). It is clear that the thinning velocity expressed through α is obtained from the experimental $h(t)$ data, it is not derived from any of the models. We have employed the empirical parameter α for several worthy reasons; namely, it: (i) gives the real experimental thinning rate; (ii) accounts for all known and unknown factors, which affect film thinning; (iii) yields reliable information about the film thinning rates in the relevant thickness range below 100 nm.

3. RESULTS AND DISCUSSION

In this study we present experimental data for the equilibrium parameters and kinetic behavior of films from mixed solutions of C₁₂G₂ with non ionic surfactants C₁₂E₆ and C₁₂E₀ or the ionic C₁₂TAB. The results are systematized in two groups depending on the ionic strength of the solutions.

3.1 Equilibrium properties of foam films

Films, obtained from solutions with low ionic strength (0.001M). The experiments under these conditions allow checking the role of surfactant adsorption on the surface charge density, as well as the influence of the electrostatic repulsion on the equilibrium state and velocity of film thinning. From data presented in Table 1 the following conclusions can be extracted:

✓ Below 0.5 CMC all films are stable except the films stabilized by mixtures C₁₂G₂: C₁₂E₀ = 50:1 and C₁₂G₂: C₁₂TAB = 50:1.

✓ At 1 CMC are obtained several types of films: (i) stable CF from C₁₂E₆, C₁₂G₂: C₁₂E₆ = 1:1 and C₁₂G₂: C₁₂TAB = 50:1 solutions; (ii)

metastable CF, or NBF from $C_{12}G_2$ and $C_{12}G_2:C_{12}E_6 = 50:1$ solutions; (iii) NBF from $C_{12}G_2:C_{12}E_0=50:1$ solution.

Decreasing of the equilibrium thickness with an increase of the surfactant concentration, is due to the increasing of surfactant adsorption, which leads to a decrease of the surface charge. It was found that some films obtained from solutions of $C_{12}G_2$ or $C_{12}G_2:C_{12}E_6 = 50:1$ at concentration 1CMC, spontaneously jump into NBF, while some films become equilibrium CF. It means that these films are in a metastable state. The stability of the obtained CF can be connected with an electrostatic force, while the stability of NBF - with steric repulsive force.

The films, obtained from the mixed $C_{12}G_2:C_{12}E_0= 50:1$ solution, with concentration up to 0.5 CMC are unstable, which can be explained with the influence of $C_{12}E_0$ as an antifoaming agent. According to [5] the foams produced from dodecanol solution are unstable. Because of the

dodecanol high surface activity, even at low concentration, it predomines in the adsorption layer, which probably leads to a decrease in the film stability. When the total surfactant concentration of the $C_{12}G_2:C_{12}E_0= 50:1$ solution is above 0.5 CMC, the obtained films are stable NBF. At this condition their surfaces are covered predominantly of $C_{12}G_2$ molecules.

The films formed from a mixed solution $C_{12}G_2 : C_{12}TAB = 50:1$ up to 1CMC are unstable, too. It follows that a small addition of cationic surfactant leads to a full reset of the surface charge. In the films, from solutions at 0.5 CMC, mobile black spots appear which very quickly merger and rupture the film. It means that the adsorption of $C_{12}G_2$ under these conditions is high enough, but it is not sufficient to stabilize the film. The films formed of this mixture but at 1 CMC are equilibrium CF and they jump into NBF but only after some contraction.

Table 1.Type, stability, equilibrium thickness (nm) and surface potential (φ_0 , mV) for films obtained from single or mixed surfactant solutions with low and high ionic strength.

Ionic strength 0.001M			
	below 0.5 CMC	0.5 CMC	1.0 CMC
$C_{12}G_2$	CF (59.7 nm) $\varphi_0 = 44.6$ mV	CF (51.8 nm) $\varphi_0 = 23.9$ mV	CF (42.5 nm), $\varphi_0 = 14.1$ mV NBF (6 nm)
$C_{12}E_6$	CF (50.1 nm) $\varphi_0 = 22.7$ mV	-	CF (44.0 nm) $\varphi_0 = 14.4$ mV
$C_{12}TAB$	-	-	CF (28 nm) at $I = 0.15M$
$C_{12}G_2:C_{12}E_6=50:1$	CF (56.25 nm) $\varphi_0 = 31.9$ mV	-	CF (31.5), $\varphi_0 = 9.0$ mV NBF (6 nm)
$C_{12}G_2:C_{12}E_6=1:1$	CF (57.1 nm) $\varphi_0 = 33.1$ mV	CF (59.0 nm) $\varphi_0 = 31.8$ mV	CF (45 nm) $\varphi_0 = 15.0$ mV
$C_{12}G_2:C_{12}TAB=50:1$	unstable	unstable	CF (50.0 nm), $\varphi_0 = 19.5$ mV NBF (6 nm)
$C_{12}G_2:C_{12}E_0 = 50:1$	unstable	unstable or NBF	NBF (6 nm)
Ionic strength 0.1M			
$C_{12}G_2$	unstable	NBF (6.5 nm)	NBF (6.5 nm)
$C_{12}E_6$	unstable	CBF (12.0 nm)	CBF (12.0 nm)
$C_{12}TAB$	unstable	-	CBF (15.0 nm)
$C_{12}G_2:C_{12}E_6=50:1$	unstable	NBF (6.5 nm)	NBF (6.5 nm)
$C_{12}G_2:C_{12}E_6=1:1$	unstable	NBF (6.5 nm) CBF (13.0 nm)	CBF (12.0 nm)
$C_{12}G_2:C_{12}TAB=50:1$	-	-	NBF (6.7 nm)
$C_{12}G_2:C_{12}TAB=1:1$	unstable	-	CBF (16.0 nm)
$C_{12}G_2:C_{12}TAB=1:50$	-	-	NBF (6.7 nm) CBF (16.0 nm)

Films, obtained from solutions with high ionic strength (0.1M). At high ionic strength the stabilizing role of electrostatical disjoining pressure can be excluded and the film behavior could be connected with some appropriate non-DLVO forces. From data presented in Table 1 it follows:

✓ up to 0.5 CMC all films are unstable;

✓ at 1 CMC the obtained films are CBF (from $C_{12}E_6$; $C_{12}G_2:C_{12}E_6 = 1:1$; $C_{12}TAB$; $C_{12}G_2 : C_{12}TAB = 1:1$ and $1:50$ solutions), or NBF (from $C_{12}G_2$; $C_{12}G_2:C_{12}E_6 = 50:1$; $C_{12}G_2 : C_{12}TAB = 50:1$ solutions). The latter ones form by spontaneous transition from CF.

These results show that the film type depends on the surfactant type and the composition of the mixture. The films from the mixed solutions of $C_{12}G_2$ with $C_{12}E_6$ and $C_{12}TAB$ (at molar ratio 50:1) jump spontaneously into NBF, which is an evidence of the significant role of $C_{12}G_2$ on the film equilibrium state. Data for films from $C_{12}G_2 : C_{12}E_6 = 1:1$ solution at 0.5 CMC, show that the film reaches to different equilibrium states: NBF and CBF, which could be associated with a small difference in the predominant adsorption of the surfactants from the mixture on the film interfaces. At total concentration 1 CMC the obtained films are only CBF, which is a proof for the dominating role of $C_{12}E_6$ in the film surfaces. The impact of the competitive adsorption in the films from mixed solution of $C_{12}G_2 : C_{12}TAB = 1:1$ is strongly expressed. In the films produced from it, before

reaching of the equilibrium state of adsorption (in the first few films), Newtonian spots, arise which is an evidence of the dominant adsorption of $C_{12}G_2$ molecules. When the equilibrium state in the system is reached, the films have a thickness similar to that of films stabilized by single $C_{12}TAB$. It is a proof that in the films from a mixed solution 1:1 the surfaces are firstly covered by $C_{12}G_2$ molecules, partially replaced afterwards by $C_{12}TAB$ species through a competitive adsorption.

3.2. Influence of the surfactant type and the molar ratio of the components in the mixture on the velocity of film thinning

Comparison of the velocity of thinning for films from solutions of low ionic strength. Fig.1ab presents the values of the drainage coefficient α

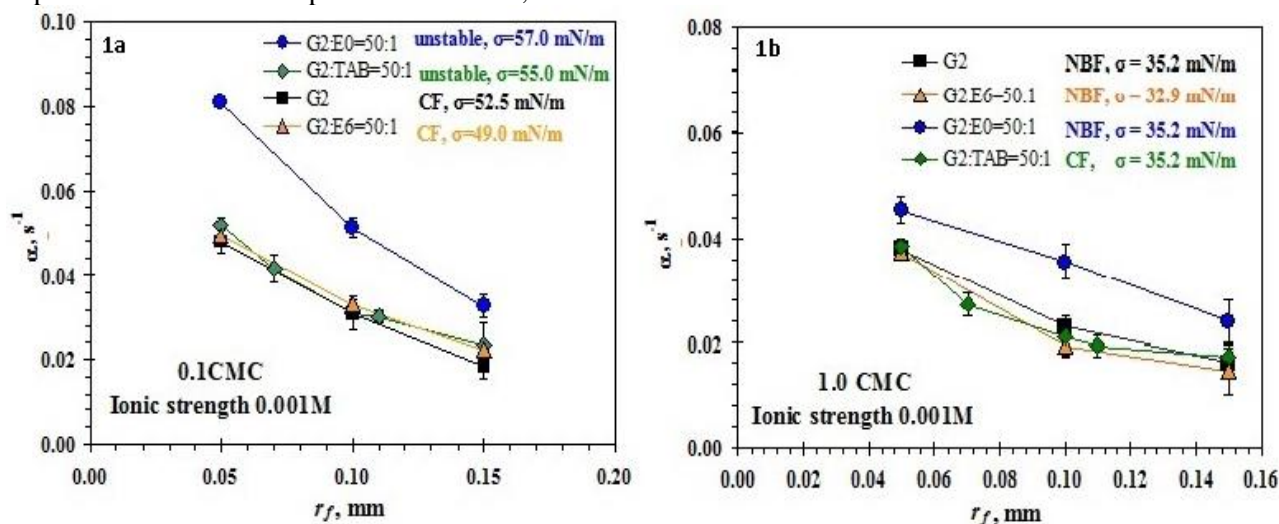


Fig.1. Drainage coefficient (α) of foam films stabilised by $C_{12}G_2$ or by its mixtures with three different additives - $C_{12}E_6$, $C_{12}E_0$ and $C_{12}TAB$ at ratio $C_{12}G_2$: additive = 50:1: (a) at 0.1 CMC; (b) at 1.0 CMC.

for films stabilized by $C_{12}G_2$ and its mixtures with $C_{12}E_6$, $C_{12}E_0$ and $C_{12}TAB$. The mixed solutions are at total surfactant concentration 0.1 CMC (a), or 1.0 CMC (b) and molar ratio $C_{12}G_2 : \text{additive} = 50:1$. From the dependences shown, it is clear that in both cases the rates of thinning of the films from the mixture with $C_{12}E_0$ are higher than those for $C_{12}G_2$ films. The dependences $\alpha(r_f)$ for films from the other mixtures have a similar trend. They are close to the values for individual $C_{12}G_2$ films. From data presented in Fig.1 it follows that:

✓ adding of $C_{12}E_0$ to the solution of $C_{12}G_2$ accelerates the film drainage which means that the films surfaces have greater capability of corrugation. We expected dodecanol to boost up the Gibbs elasticity and viscosity of the mixed surface layer with $C_{12}G_2$. Our measurements by the DSA method revealed that Gibbs elasticity increased

with the concentration, but only up to 0.5 CMC. Elasticity decreased above this level, to reach its minimum at CMC, which explains the accelerated thinning. Indeed, the measured Gibbs elasticity of mixed adsorption layers (at 0.1 or 1.0 CMC) is lower (46.6 and 26.3 mN/m) than that of $C_{12}G_2$ layers (50.1 and 67.0 mN/m);

✓ Adding $C_{12}E_6$ and $C_{12}TAB$ to the solution of $C_{12}G_2$ at molar ratio 50:1 does not substantially affect the film thinning, but it changes the film stability: the films from the mixture with $C_{12}TAB$ are unstable while those with $C_{12}E_6$ are stable.

Comparison of the velocity of thinning for films from solutions of high ionic strength. Fig. 2 presents juxtaposition of the coefficients of thinning for films from solutions of individual substances $C_{12}E_6$, $C_{12}E_0$ and $C_{12}TAB$ and their mixtures of different molar ratios. By comparing the data for individual surfactants with those for the

corresponding mixtures we aim to establish which of the substances in the mixture has the predominant effect on α . For mixtures with a molar ratio 50:1 the answer to this question is almost trivial, since $C_{12}G_2$ concentration is strongly prevailing. Of a particular interest is the mixture of molar ratio 1:1, for which the dominating component could not be predicted.

Fig. 2a presents data for α of films from mixed solutions from nonionic substances. It can be seen from that there are no large differences in the values of α , regardless of the composition. The

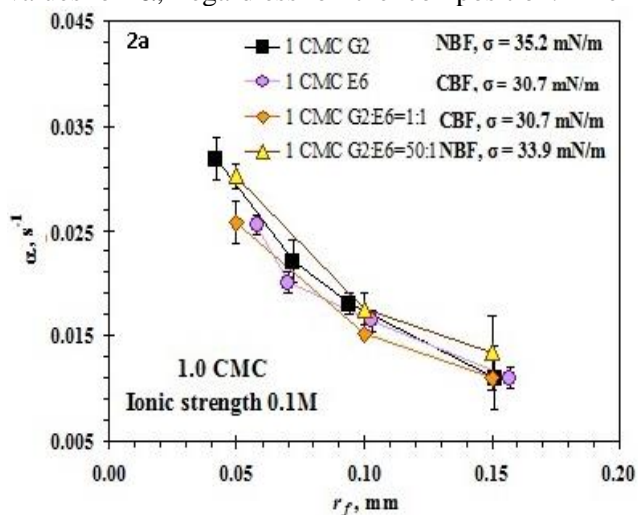
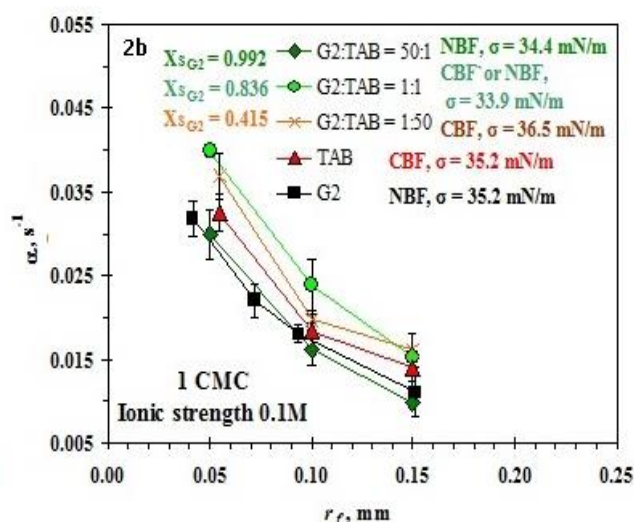


Fig.2 Comparison of the drainage coefficient (α) for foam films stabilized by individual surfactants and their mixtures of molar ratios 1:1 or 50:1: (a) for $C_{12}G_2 + C_{12}E_6$; (b) $C_{12}G_2 + C_{12}TAB$.

Fig. 2b presents data for α of films with close-packed surfaces (1.0 CMC) from a mixture of $C_{12}G_2$ and $C_{12}TAB$. The curves for films from mixtures of molar ratios 1:1 and 1:50 are situated higher than the curves for films from pure $C_{12}G_2$ and $C_{12}TAB$. The films formed from mixed solution 1:1 (after time, sufficient for attaining adsorption equilibrium) and 1:50 are CBF, as are the films from pure $C_{12}TAB$. According to Ref. [17] at these molar ratios the presence of $C_{12}TAB$ in the adsorption layer leads to positively (re)charged film surfaces. Indeed, the added electrolyte 0.1 M should have screened the positive charge, but the fact that such films are formed indicates the presence of some residual electric charge. This charge affects considerably the films equilibrium state, but to a lesser extent the velocity of thinning. That is why we connect the differences found for the thinning of films from these mixtures with the different composition of the adsorption layer, which determines its capability for corrugation. From the data for the molar part of $C_{12}G_2$ (see Fig. 2b) in the mixed adsorption layer (obtained by the procedure of Ingram [11]) is clear that in the film from a mixture with molar ratio 1:1

mixture with molar ratio 1:1 is with surface tension close to that of $C_{12}E_6$, but lower than that for $C_{12}G_2$. Consequently, $C_{12}E_6$ is the dominant component in this mixture. Accordingly, the α values of films from 1:1 mixtures should be similar to those of films from $C_{12}E_6$. Such a tendency emerges in Fig 2a, but only for films of small radii. Thus the films are divided into two groups, according to their drainage coefficients: from $C_{12}G_2$ solutions and a mixture of $C_{12}G_2:C_{12}E_6 = 50:1$; from $C_{12}E_6$ and a mixture of $C_{12}G_2:C_{12}E_6 = 1:1$.



$C_{12}G_2$ again has the dominant role in the interfaces. The molecular interaction parameter in the adsorption layer is evaluated equal to 2.29, which shows that the mixture does not behave as an ideal one. Although the content of $C_{12}TAB$ in the adsorption layer is (relatively) low, its presence there makes the layer non-homogeneous and reduces its coherence. The presence of domains of $C_{12}G_2$ and/or $C_{12}TAB$ modifies the adsorption layer corrugation capability, which we believe to be the reason for the higher values of drainage coefficient. Increase of the amount of $C_{12}TAB$ in the mixture 1:50 adds to the coherence in the layer and decelerates the film thinning.

5. CONCLUSIONS

In the presented study data of the kinetic and equilibrium properties for films from mixed solutions of $C_{12}G_2$ with the nonionic surfactants $C_{12}E_6$, or $C_{12}E_0$ and ionic $C_{12}TAB$ in the presence of electrolyte (0.001 and 0.1M) have been obtained and discussed. The experimental results follow that:

- at low ionic strength the film stability strongly depends on the surfactant nature;

➤ at high ionic strength, the influence of additive nature on the type of equilibrium films (CBF or NBF) manifest only when the films surfaces are covered;

➤ the velocity of thinning of films from mixtures at molar ratio 50:1 correlates with that of the films stabilized by single $C_{12}G_2$ solutions (see Fig.1-2); with the exception of films from mixture $C_{12}G_2:C_{12}E_0 = 50:1$, which was attributed to the low elasticity of the mixed adsorption layer;

➤ the rate of thinning of films from mixtures of molar ratio 1:1 depends on the impact of the species dominating in the adsorption layer; for a mixture of $C_{12}G_2 + C_{12}E_6$ it is determined by $C_{12}E_6$ (see Fig.2a), while for a mixture of $C_{12}G_2 + C_{12}TAB$ both components contribute substantially (see Fig.2b).

Acknowledgement: This paper is supported by two projects:

1. BG051PO001-3.3.06-0003 The Project is realized by the financial support of the Operative Program "Development of the human resources" of the European Social Fund;

2. RD - 08-255/09.03.2015 realized by the Scientific Fund of Konstantin Preslavsky University, Shumen, Bulgaria.

REFERENCES

1. C. Stubenrauch, J.Schlarmann, R.Strey, *Phys.Chem.Chem.Phys.*, **4**, 4504 (2002).
2. R. M. Muruganathan, R. Krustev, H. J. Muller, H. Mohwald, B. Kolaric, R. Klitzing, *Langmuir*, **20**, 6352 (2004).
3. C. Stubenrauch, P. Claesson, E. Rutland, E. Manev, I. Johansson, J. Pedersen, D. Langevin, *Adv. Colloid Interface Sci.*, **155**, 5 (2010).
4. V. Bergeron, *Langmuir*, **13**, 3474 (1997).
5. H. Fruhner, K.-D. Wantke, K. Lunkenheimer, *Colloids and Surfaces A*, **162**, 193 (1999).
6. St. Karakashev, Anh Nguyen, *Colloids and Surfaces A*, **293**, 229 (2007).
7. J. Schlarmann, N. Buchavzov, C. Stubenrauch, *Soft Matter*, **2**, 584 (2006).
8. N. Buchavzov, Thesis submitted in fulfillment of the requirements for the Ph.D., Koln, Germany, 2007.
9. N. Buchavzov, C. Stubenrauch, *Langmuir*, **23**, 5315 (2007).
10. S. Patil, N. Buchavzov, E. Carey, C. Stubenrauch, *Soft Matter*, **4**, 840 (2008).
11. D.S. Ivanova, Zh.K. Angarska, S.I. Karakashev, E.D. Manev, *Colloids and Surfaces A*, **382**, 93 (2011).
12. D. S. Ivanova, J.K. Angarska, *Colloids and Surfaces A*, **438**, 93 (2013).
13. J. Angarska, C. Stubenrauch, E. Manev, *Colloids and Surfaces A*, **309**, 189 (2007).
14. V. Simulescu, J. Angarska, E. Manev, *Colloids and Surfaces A*, **319**, 21 (2008).
15. J. K. Angarska, D. S. Ivanova, E. D. Manev, *Colloids and Surfaces A*, **481**, 87 (2015).
16. D. Exerowa, P.M. Kruglyakov (Eds.), *Foam, Foam Films: Theory, Experiment, Application*, Marcel Dekker, New York, NY, 1997.
17. E. Manev, R. Pugh, *J. of Colloid and Interface Sci.*, **151**, 505 (1992).
18. E. Manev, R. Tsekov, B. Radoev, *J. Disper. Sci. Technol.*, **18**, 769 (1997).

КИНЕТИЧНИ И РАВНОВЕСНИ СВОЙСТВА НА ПЕННИ ФИЛМИ ОТ СМЕСЕНИ РАЗТВОРИ НА n-ДОДЕЦИЛ-β-D-МАЛТОЗИД С НЕЙОННИ И ЙОННИ ПОВЪРХНОСТНОАКТИВНИ ВЕЩЕСТВА

Д. Ст. Иванова^{1*}, Ж. Кр. Ангарска¹ и Е. Д. Манев²

¹Шуменски университет „Епископ Константин Преславски”, Факултет по природни науки

²Софийски университет „Свети Климент Охридски”, Факултет по химия и фармация

Постъпила на 9 юли, 2015 г.; коригирана на 5 октомври, 2015 г.

(Резюме)

Чрез интерферометричния метод са получени експериментални данни за кинетичните и равновесни параметри на пенни филми от смесени разтвори на n-додецил-β-D-малтозид ($C_{12}G_2$) с хексаетиленгликол монододецил етер ($C_{12}E_6$); додеканол ($C_{12}E_0$) и с додецил триметиламониев бромид ($C_{12}TAB$). Анализирани са влиянието на типа на ПАВ, молното им съотношение и тотална концентрация в сместа върху вида, стабилността и скоростта на изтъняване на филмите при ниска (0.001M) и висока (0.1M) йонна сила. Резултатите показват, че: (i) влиянието на природата на ПАВ върху стабилността на филмите е силно изразено при ниската йонна сила; (ii) скоростта на изтъняване на филмите от смеси с молно съотношение 50:1 е много близка до тази на филмите, стабилизирани само с $C_{12}G_2$; (iii) за филмите, получени от разтвори на смеси с молно съотношение 1:1, скоростта на изтъняване зависи от доминиращия компонент в адсорбционния слой - за сместа $C_{12}G_2 + C_{12}E_6$ - се определя от $C_{12}E_6$, докато за $C_{12}G_2 + C_{12}TAB$ - от двата компонента.

Influence of corticosteroids on formation and stability of thin liquid films from pulmonary therapeutic preparations

I. K. Terziyski*, R. K. Todorov, D. R. Exerowa

Rostislav Kaischew Institute of Physical Chemistry, Bulgarian Academy of Sciences, 1113 Sofia, Bulgaria

Submitted on August 3, 2015; Revised on November 3, 2015

Drugs containing corticosteroids are used for treatment of lung inflammations. Due to corticosteroid's amphiphilic nature, they are surface active molecules which are able to modify surface properties of pulmonary surfactant. In the present study natural and synthetic pulmonary therapeutic preparations (PTP) are used as a model of the (lung) pulmonary surfactant. Effect of corticosteroids on surface activity of PTP is evaluated by the black foam film method and probability for formation of black foam films stabilized with PTP in the presence of corticosteroids is assessed. Stable black foam films are formed at higher concentrations. Disjoining pressure isotherms indicate an increase of film thickness in mixtures from PTP and corticosteroids. The results suggest that in the presence of corticosteroids, a mixed adsorption layer of the pulmonary surfactant is formed. Effect observed is stronger in synthetic PTP.

Key words: *thin liquid foam films, pulmonary surfactant, corticosteroids*

INTRODUCTION

Pulmonary surfactant (PS) is a complex lipid-protein mixture [1]. PS forms a variety of thin films at the alveolar surface and prevent alveoli collapse during the process of breathing. The PS consists of lipids and specific proteins (SP-A, SP-B, SP-C, and SP-D). Polar phospholipids (mainly dipalmitoylphosphatidylcholine (DPPC), phosphatidylglycerol, represent about 70% of the pulmonary surfactant. Respiratory distress syndrome (RDS) is a significant cause of morbidity and mortality in preterm infants. RDS is caused by a deficiency, dysfunction, or inactivation of pulmonary surfactant. Pulmonary therapeutic preparations (PTP) are drugs that are administered by instillation into the trachea and they are used to treat RDS in neonates and adults.

Corticosteroids are anti-inflammatory drugs that can be used in asthma to reduce airway hyper-responsiveness and to decrease bronchial edema and mucus secretion [2]. In clinical practice, PTP and corticosteroids are often used together. Their simultaneous use shows larger effect in comparison with their separate application. Administration of PTP and Budesonide enhance lung functions and alleviate inflammation more effectively than Budesonide-only and surfactant-only treatment, as reported in Mikolka et al. [3]. PTP are used as carriers of medical drugs to lung epithelium [4, 2]. So far little is known about the interaction between these medicines and complexes of pulmonary surfactant [4]. Therefore, the impact of

corticosteroids on pulmonary surfactant (PS) is of great interest.

Recently, the advantageous simultaneous application of corticosteroids and PTP has been reported [5]. PTPs are used as carriers of corticosteroids to deliver them to the lung epithelium [4, 5]. Identified advantages refer to avoiding first-pass metabolism and eliminating potential side effects caused by high systemic dosage. This makes pulmonary drug delivery an ideal method for treating respiratory diseases, such as asthma, chronic pulmonary infection, emphysema, cystic fibrosis, pulmonary hypertension, and lung cancer [5]

Wang et al. [5] have investigated biophysical interaction between natural PTP Infasurf and two corticosteroids: Budesonide and Beclomethasone dipropionate. Their interaction is assessed by the surface activity measurements by the Langmuir balance and lateral film structure studied by atomic force microscopy suggesting an optimal concentration range of corticosteroids for pulmonary delivery. Infasurf may carry less than 1% Budesonide and up to 10% Beclomethasone without significantly compromising its surface activity [5]. The use of corticosteroids is beneficial in the case of asthma and croup, but their effect could be controversial in other diseases [6]. Investigation of clinically used PTP as carriers of corticosteroids and their influence on PTP properties are important from a practical point of view. The standard protocols of corticosteroid applications should be followed, and physicians should be alerted to the potential hazards of their prolonged use, as reported in [6]. Curosurf, a natural porcine surfactant, combined with

*To whom all correspondence should be sent:
E-mail: iterziyski@ipc.bas.bg

Beclomethasone at 800 $\mu\text{g}/\text{kg}$, is effective in reducing the oxidative lung stress and improving the respiratory function in preterm lambs with RDS, as reported in Dani et al. [7].

In our study we investigate the effect of two corticosteroids, Budesonide and Beclomethasone, on Curosurf, a natural-origin PTP, and on a synthetic PTP containing two phospholipids and two peptides analogues of human surfactant proteins B and C, using the thin liquid foam film methods.

EXPERIMENTAL

Natural and synthetic PTP are used as a model of pulmonary surfactant. As a natural PTP we used Curosurf, provided by Chiesi Pharmaceuticals, Italy. Curosurf preparation is obtained from porcine lung mince and consists of approximately 98% phospholipids and 2% hydrophobic surfactant proteins (SP-C and SP-B). It is provided as an aqueous suspension with concentration of 80 mg/ml in physiological electrolyte concentration (0.15 M NaCl). For the purposes of the study, a stock solution with concentration 800 $\mu\text{g}/\text{ml}$ at the same electrolyte concentration was prepared from the ready-made suspension and further used to prepare the working solution with the respective concentration.

Synthetic PTP consists of 98.3% (1,2-dipalmitoyl-sn-glycero-3-phosphocholine) DPPC and (palmitoyl-oleoyl-sn-glycero-3-phosphoglycerol) POPG in a ratio (DPPC:POPG=1:1) and two synthetic peptide analogues of SP-C (1.5%) and SP-B (0.2%) [8].

Corticosteroid stock solutions of 1.5 mg/ml dimethyl sulfoxide (DMSO) were prepared.

Studies of microscopic foam films were carried out with modernized microinterferometric method of Scheludko and Exerowa. To study the probability of black foam film formation, we used a cell with a cylindrical holder. In this cell, the film was formed at constant capillary pressure, when two surfaces of a biconcave drop approach one another. The measurements of the disjoining pressure isotherms were carried out with Exerowa-Scheludko cell with porous plate [9-11], enabling application of variable pressure. The foam film was formed in the orifice of the porous plate when pressure was applied.

Using the thin liquid foam film method we carried out investigation of probability (W) of black foam film formation on surfactant concentration (C). In general, probability is determined experimentally as the ratio of the number of films in which black films are observed ΔN to the total

number of studied films N, and can be expressed as percentage or parts of a unit. The two most important characteristics obtained from a W(C)-curve are critical concentration (C_{cr}) and threshold concentration (C_t). C_{cr} is defined as the highest concentration at which all films are ruptured without black film formation ($W=0$). C_t is the lowest concentration above which all films become black ($W=1$).

Film stability was determined by observing films at two different waiting times (30 min and 60 min), the waiting time being defined as the time for which the solution is left as a drop in the cylinder holder of measuring cell before film formation.

RESULTS AND DISCUSSION

The films from natural and synthetic PTP and their mixtures with Beclomethasone were studied. Film destabilization was not observed for the synthetic and natural PTP at both corticosteroid concentrations studied. At lower corticosteroid concentration (3 $\mu\text{g}/\text{ml}$ Beclomethasone), there was no significant difference between C_{cr} for mixtures and for the pure natural preparation. C_t for mixture shifted to lower concentrations of PTP (Fig. 1)

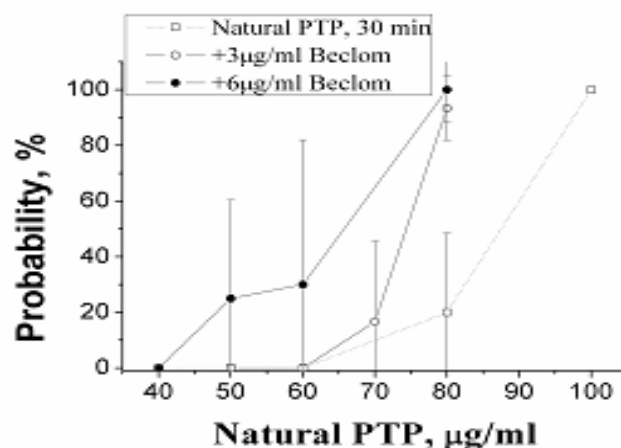


Fig. 1. Probability of formation of black foam films stabilized with natural PTP and mixture of natural PTP with added 3 $\mu\text{g}/\text{ml}$ Beclomethasone and 6 $\mu\text{g}/\text{ml}$ Beclomethasone at 30 min waiting time.

At higher concentrations of Beclomethasone (6 $\mu\text{g}/\text{ml}$), W(C_s) curves for natural PTP (Fig. 1) shifted towards lower concentrations (i.e. the films are stabilized). For synthetic PTP the same dependency was observed but the scattering of results was larger (data not shown). This scattering might be due to uneven saturation of film interfaces and disruption of aggregates coming from the solution bulk when they last approach the surfaces.

The probability of black foam films formation for pure natural and synthetic PTP and for their mixtures with 3 $\mu\text{g}/\text{ml}$ Budesonide and 6 $\mu\text{g}/\text{ml}$ Budesonide at 30 min and 60 min waiting time,

were also investigated. At 3 $\mu\text{g/ml}$ Budesonide at both 30 min and 60 min waiting times for synthetic PTP, the $W(C_s)$ -curves (data not shown) shifted to higher surfactant concentrations (i.e. destabilization of films was observed). At 6 $\mu\text{g/ml}$ Budesonide, $W(C_s)$ curves (data not shown) shifted to lower surfactant concentrations (i.e. stabilization of films was observed). For synthetic PTP, within this Budesonide concentration interval, alteration in Budesonide concentration effect on the stability of films was observed.

C_{cr} and C_t for natural PTP practically coincided with these for pure PTP and its mixtures with 3 $\mu\text{g/ml}$ Budesonide at both studied waiting times 30 min and 60 min (data not shown) (i.e. change in film stability after addition of corticosteroids was not observed).

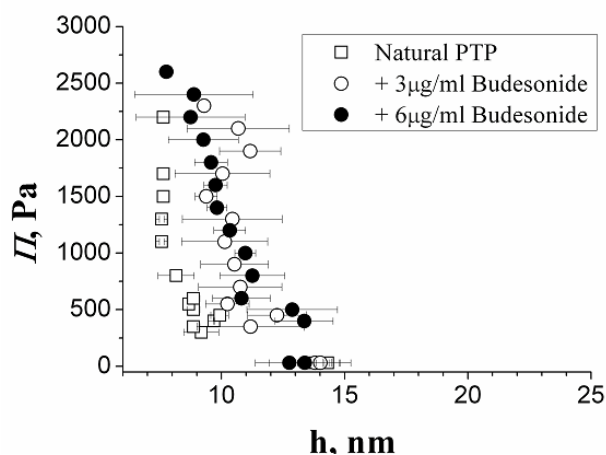


Fig. 2. Disjoining pressure isotherm of natural PTP and its mixture with 3 $\mu\text{g/ml}$ Budesonide (open symbols) and with 6 $\mu\text{g/ml}$ Budesonide (filled symbols).

$\Pi(h)$ -disjoining pressure isotherms of pure natural and synthetic PTP and of their mixtures with corticosteroids were measured. Fig. 2 depicts $\Pi(h)$ -isotherms for natural PTP in the presence of 3 $\mu\text{g/ml}$ and 6 $\mu\text{g/ml}$ Budesonide and Fig. 3 – at 3 $\mu\text{g/ml}$ and 6 $\mu\text{g/ml}$ Beclomethasone. As it can be seen in Fig. 2, the isotherms of natural PTP Curosurf with added 3 $\mu\text{g/ml}$ and with 6 $\mu\text{g/ml}$ Budesonide practically coincide. They shifted to higher film thicknesses compared to isotherm of pure natural PTP Curosurf.

For synthetic PTP we measured isotherms in the presence of 6 $\mu\text{g/ml}$ Budesonide (Fig. 4) and 6 $\mu\text{g/ml}$ Beclomethasone (Fig. 5). Corticosteroid concentrations were selected to be the same as concentrations at which $W(C_s)$ curves were obtained.

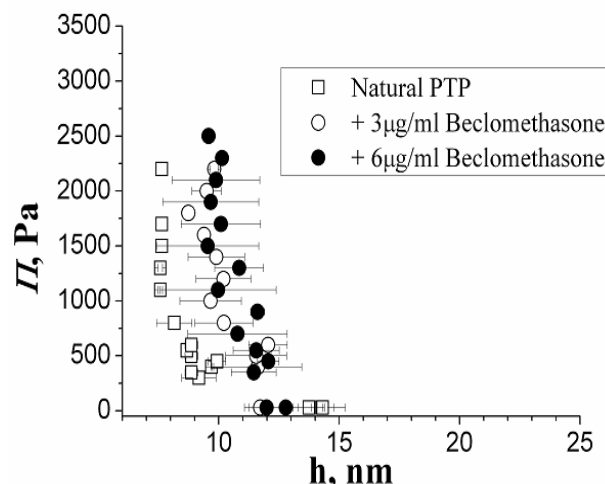


Fig. 3. Disjoining pressure isotherm of natural PTP and its mixture with 3 $\mu\text{g/ml}$ Beclomethasone (open symbols) and with 6 $\mu\text{g/ml}$ Beclomethasone (filled symbols).

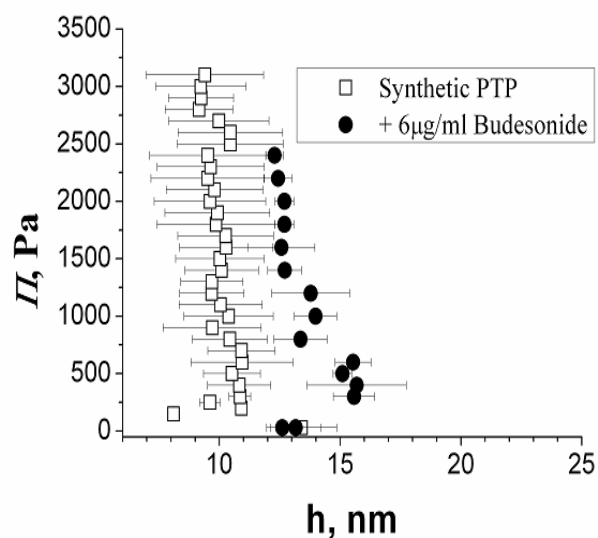


Fig. 4. Disjoining pressure isotherm of synthetic PTP (open symbols) and its mixture with 6 $\mu\text{g/ml}$ Budesonide (filled symbols).

In this case, the isotherms for pure preparation and for mixtures for both corticosteroids shifted to higher thicknesses compared to natural preparation. Film thickness for mixtures was higher than the thickness for pure synthetic PTP while scattering of the results for synthetic preparation was larger.

The shift of isotherms for mixtures of PTP with corticosteroids to higher film thicknesses suggests that a mixed surface layer from PTP and corticosteroids is formed. The isotherms from pure synthetic PTP and its mixtures with corticosteroids have different course in the region below 1500 Pa. The isotherms for mixtures show smooth transition from 15 nm to 12 nm in the region below 1500 Pa, while isotherms for pure synthetic PTP have almost the same thickness, approximately 11 nm.

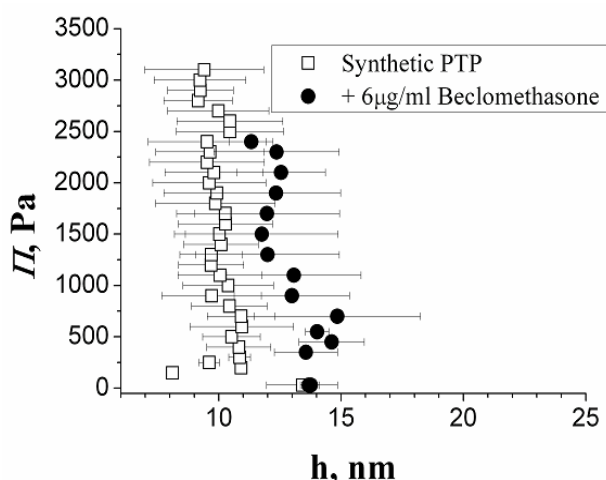


Fig. 5. Disjoining pressure isotherm of synthetic PTP (open symbols) and its mixture with 6 $\mu\text{g/ml}$ Beclomethasone (filled symbols).

Likewise, there is a difference in isotherm course for pure natural PTP and pure synthetic PTP in the region below 1000 Pa. For pure natural PTP the films show smooth thinning from 10 nm to 7 nm. In the same region, the isotherm for pure synthetic PTP shows almost no change in film thickness, approximately 11 nm. It is possible that the smooth thinning observed in the isotherms for pure natural PTP and in isotherms for mixtures and synthetic PTP with corticosteroids, is due to the long electrostatic forces acting in them. Above 1000 Pa, no changes in film thicknesses are observed in the isotherms for pure natural and pure synthetic PTP. As for the mixture of synthetic PTP with 6 $\mu\text{g/ml}$ Budesonide, no changes in film thickness appear above 1500 Pa. These observations may be attributed to the steric forces acting within this range.

In our study we established that at low concentrations Budesonide destabilized thin liquid foam films from Curosurf, while at higher concentrations it stabilized these films. Beclomethasone showed a stabilizing effect at all concentrations studied. This result is in compliance with the observation of Wang et al. [5], namely, that Infasurf may carry less than 1% Budesonide and up to 10% Beclomethasone without significantly compromising its surface activity. Our study was carried out with approximately 3% and 6% of corticosteroids from the weight of the mixture with natural or synthetic PTP. A

destabilization of foam films from synthetic PTP in the presence of 3% of Budesonide was observed.

CONCLUSION

The obtained results show that corticosteroids influence formation and stability of pulmonary surfactant foam films. They also suggest that a mixed adsorption layer from pulmonary surfactant studied components is formed in the presence of corticosteroids. This effect is more pronounced in synthetic PTP.

The study shows differences in surface properties of synthetic and natural PTP when Budesonide and Beclomethasone are present, which could be attributed to differences in the formation of the mixed adsorption layer.

The results obtained confirm that the black foam film method is applicable to the study of drug influence on pulmonary surfactant surface activity.

Acknowledgment: This work has been done under the umbrella of COST Action MP1106.

REFERENCES

1. Zuo Y., R. A. W. Veldhuizen, A. W. Neumann, N. O. Petersen, F. Possmayer, *Biochim. Biophys. Acta*, **1778**, 1947 (2008).
2. C. M. Thorp, Pharmacology for the Health Care Professions, John Wiley & Sons, Chichester, 2008.
3. P. Mikolka, D. Mokra, J. Kopincova, L. Tomcikova-Mikusiakova, A. Calkovska, *Physiol. Res.*, **62**, 191 (2013).
4. E. Lopez-Rodriguez, J. Perez-Gil, *Biochem. Biophys Acta*, **1838**, 1568 (2014).
5. Y. Wang, H. Zhang, Q. Fan, C. Neal and Y. Zuo, *Soft Matter*, **8**, 504, (2012).
6. F. M. de Benedictis, A. Bush, *Am. J. Respir. Crit. Care Med*, **185**, 12 (2012).
7. C. Dani, I. Corsini, S. Burchielli, V. Cangiamila, M. Longini, F. Paternostro, G. Buonocore, F. Rubaltelli, *Pediatr. Pulmonol.*, **44**, 1159 (2009).
8. A. Sato, M. Ikegami, *PLoS One*, **7**, e39392 (2012).
9. R. Cohen, D. Exerowa, *Adv. Colloid Interface Sci.* **134-135**, 24 (2007).
10. D. Exerowa, A. Kruglyakov, Foam and foam films, Elsevier, Amsterdam, 1998.
11. D. Platikanov, D. Exerowa, Thin liquid films. In: Lyklema J. (editor). Fundamentals of interface and colloid science. Soft colloids. Academic Press/Elsevier. Chapter 6, 2005.

ВЛИЯНИЕ НА КОРТИКОСТЕРОИДИ ВЪРХУ ФОРМИРАНЕТО И СТАБИЛНОСТТА НА ТЪНКИ ТЕЧНИ ФИЛМИ ОТ ПУЛМОНАРНИ ТЕРАПЕВТИЧНИ ПРЕПАРАТИ

И.К. Терзийски*, Р.К. Тодоров, Д.Р. Ексерова

Институт по физикохимия „Академик Ростислав Каишев”, Българска академия на науките, София 1113

Постъпила на 3 август, 2015 г. коригирана на 3 ноември, 2015 г.

(Резюме)

За лечение на възпаление на белите дробове се използват лекарства съдържащи кортикостероиди. Поради амфифилната природа на кортикостероидите, те са повърхностно активни молекули и могат да променят повърхностните свойства на пулмонарния сърфактант. В настоящото изследване, природни и синтетични пулмонарни терапевтични препарати (ПТП), се използват като модел на пулмонарния сърфактант. Влиянието на кортикостероидите върху повърхностната активност на ПТП е изследвано с метода на черния пенен филм. При определянето на вероятността за образуването на черни пенни филми, стабилизирани със синтетични ПТП в присъствието на ниски концентрации на кортикостероиди, се наблюдава дестабилизация на филмите. При високи концентрации филмите се стабилизират. Изотермите на разклинящото налягане показват повишаване на дебелината на филмите от ПТП и кортикостероиди. Резултатите предполагат формирането на смесен адсорбционен слой на пулмонарния сърфактант в присъствието на кортикостероиди. Регистрираният ефект е по-силен при синтетичните ПТП.

Foam films stabilized with lysophosphatidylglycerol in the presence of Na⁺ and Ca²⁺

S.A. Alexandrov*¹, R.K. Todorov², A.G. Jordanova³, Z.I. Lalchev³, D.R. Exerowa²

¹ Medical University of Sofia, Department of Medical Physics and Biophysics, "Zdrave" 2 St., 1431 Sofia, Bulgaria, E-mail: svobodan@abv.bg

² Institute of Physical Chemistry, Bulgarian Academy of Sciences

³ Sofia University "St. Kliment Ohridski"

Submitted on July 23, 2015; Revised on December 7, 2015

Abstract: This work presents investigation of foam films stabilized with soluble phospholipid palmitoyl lysophosphatidylglycerol (LPG). The films have been studied by measuring the thickness/electrolyte concentration and disjoining pressure/thickness isotherms in the presence of Na⁺ and Ca²⁺ in the solution. At low NaCl we have obtained formation of thick silver-colored films with equilibrium thickness. With the increase of the concentration of Na⁺ the films became thinner and at 0.5 mol dm⁻³ their equilibrium thickness was ~9 nm (common black films). Foam films in the presence of Ca²⁺ followed the same dependence, but at concentration of electrolyte 5×10⁻² mol dm⁻³ and higher, Newton black films were formed. The formation of equilibrium Newton black films happened with "jump" from silver films during the thinning process. The isotherms of disjoining pressure for both electrolytes had shown lightly decrease for the thickness of the films, without any transitions.

Key words: lysophospholipids, black foam films, disjoining pressure isotherms of LPG

INTRODUCTION

Many studies, using different techniques, have been carried out on model bilayer systems, as is well known the cell membrane is mainly constituted of zwitterionic phospholipids [1]. Lysophospholipids attract the interest of the investigators, because of the role they play in the functioning of biological membranes. Also their presence in alveoli in small amounts is important for the dysfunction of pulmonary surfactant [2].

Phosphatidylglycerol is a second major phospholipid in pulmonary surfactant which constitutes ~10% of the surfactant phospholipid pool. Phospholipase-mediated surfactant hydrolysis may disrupt surfactant function by generation of lysophospholipids and free fatty acids and/or depletion of native phospholipids. Small amounts of lysophosphatidylcholine, lysophosphatidylethanolamine, lysophosphatidylglycerol (LPG) are generated by this mechanism [2].

Although not nearly as well studied as protein inhibition of pulmonary surfactant, an inhibition mechanism involving unsaturated membrane phospholipids, lysophospholipids, and other amphipathic molecules has been identified [3]. Lysophospholipids are phospholipids containing a single fatty acid chain per molecule and are

generated by phospholipase A2 secreted by white blood cells and likely type II cells, particularly during respiratory distress syndrome (RDS), an important cause of neonatal mortality of premature newborns [4]. Such lipid substances can be considered diluents of the specific surfactant lipid assembly. Thus, insertion and mixing of these unsaturated amphipathic lipid and fatty acid molecules with the surfactant phospholipid molecules would significantly fluidize the phospholipid monolayers and could promote early collapse, thus preventing low surface tension from being reached. The inactivation due to lipid penetration cannot be effectively overcome by raising surfactant concentration [3].

A long time ago thin liquid films have been studied as a good model on stability of colloidal systems in liquid dispersion media. Thin liquid films form when two compartments of disperse phase (droplets, or bubbles, or particles) come close to each other. Foam films between two gas phases are an example of symmetrical thin liquid films. The most important factor which determines the properties of foam films is the interaction between the two adjacent phases across the liquid film. The thermodynamic quantity disjoining pressure Π is a result of these attractive or repulsive interactions due to different types of surface forces acting in the films [5]. The thicker common black film appears at lower electrolyte concentrations. The electrostatic double

*To whom all correspondence should be sent:

layer repulsion is suppressed at higher electrolyte concentrations, and the equilibrium state in this case is a very thin Newton black film. Once this state is reached, the film thickness is independent on the electrolyte concentration and is only determined by the direct interaction of the surfactant adsorption layers by short-range surface forces. Although the mechanism of Ca^{2+} binding by charged phospholipids is not completely clarified, it seems that it depends on the structure and properties of the polar head groups.

During the last three decades have been published several data about foam films stabilized by biosurfactants, such as pure phospholipids. After that, lipid and lipid–protein thin liquid films gained a significant interest and many papers and books proved the foam films as an adequate model system for studying of pulmonary surfactant [6].

The aim of this work was to study foam films stabilized with LPG with microscopic foam films in the presence of monovalent and divalent ions. For that purpose the equilibrium thicknesses of the obtained foam films have been measured at different conditions (electrolyte concentration, external pressure).

EXPERIMENTAL

Materials. Palmitoyl lysophosphatidylglycerol (LPG), purchased from Avanti Polar Lipids, was used in the experiments.

NaCl (Suprapur) and $\text{CaCl}_2 \cdot 2\text{H}_2\text{O}$ (p.a.) were obtained from Merck. NaCl was roasted at 500°C for 4 h to remove surface active contaminations. $\text{CaCl}_2 \cdot 2\text{H}_2\text{O}$ (p.a.) was used as obtained.

All solutions were prepared with triple distilled water. All experiments were carried out at a temperature of 22°C .

Methods. The measurements were performed using the well-known microinterferometric experimental technique [7]. All films in our experiments were formed with the same radius, 0.01 cm. The capillary pressure, $P\sigma$, in these films was determined as $P\sigma = 2\sigma/R$, where σ is the surface tension and R is the radius of the glass capillary, where the microscopic horizontal film forms in the center of a double-concave drop.

The measuring cell of Scheludko and Exerowa [7] has proven to be a suitable and reliable tool for formation of microscopic horizontal foam films. It is presented in Figure 1. The foam film **c** is formed in the middle of a biconcave drop **b**, situated in a glass

tube **a** of radius R , by withdrawing liquid from it (variant A) and in the hole of porous plate **g** (variant B). The periphery of the foam film is in contact with the bulk phase, i.e. with the solution from which it is obtained.

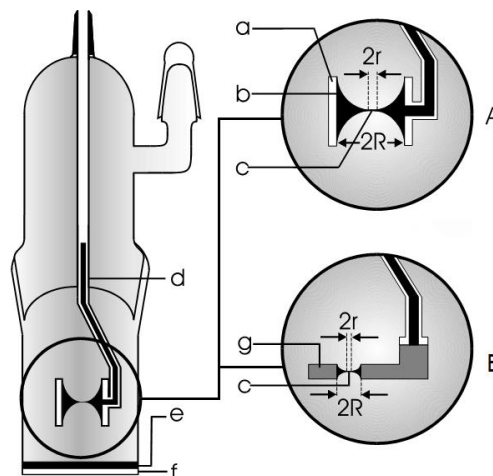


Fig. 1. Scheme of the measuring cell of Scheludko and Exerowa for the study of microscopic foam films; **A**: in a glass tube; **B**: in a porous plate; **a** - glass tube film holder; **b** - biconcave drop; **c** - microscopic foam film; **d** - glass capillary; **e** - surfactant solution; **f** - optically flat glass; **g** - porous plate. (taken from D. Exerowa, P. Kruglyakov, *Foam and foam films*, Elsevier, Amsterdam, 1998.)

Classical optics provides relations that can link the thickness of the film with its optical characteristics. If foam films are observed in white light, it can be seen that during thinning their coloration changes periodically. Initially the process runs rather rapidly and gradually slows down. Such a course of the interference can be registered as a curve photo-current/time in which the extrema correspond to the interference maxima and minima, i.e. film thicknesses are divisible to $\lambda/4n$ (where λ is the wavelength and n is the refractive index). Film thickness (between a maximum and a minimum) is calculated from the ratio between the intensities measured of the reflected monochromatic light I , corresponding to a certain thickness, and I_{\max} , corresponding to the interference maximum [7].

The direct measurements of the disjoining pressure isotherms were performed by means of the specially designed “porous-plate technique” which has repeatedly been used in microscopic foam film studies. The external pressure that balances the pressure in the film was applied utilizing the special membrane pump and measured with an accuracy of ± 5 Pa [8].

The processing of the interferometrically obtained photometric data yields the so-called equivalent film thickness, which is found considering the film as homogeneous with an index of refraction equal to the refraction coefficient of the solution from which the film is obtained, in our case 1.33. The accuracy of the so determined microscopic thin liquid film thicknesses is ± 0.2 nm.

According to the classical DLVO theory, $\Pi = \Pi_{el} + \Pi_{vw}$, where Π_{el} is the electrostatic and Π_{vw} is the van der Waals component of the disjoining pressure Π . The following expression for the van der Waals component of disjoining pressure in a symmetric film bordering gas or condensed phases is obtained $\Pi_{vw} = -K_{vw}/h^3$, where K_{vw} is the van der Waals-Hamaker constant [7]. Calculations for Π_{el} were based on asymptotic equations for 1:1 electrolyte [10] and 2:1 electrolyte [11]. For electrolyte solution the thickness of diffusive electric double layer (κ^{-1}) for aqueous solution can be calculated with the

following equation: $\kappa^{-1} = \left(\frac{\epsilon_0 \epsilon k T}{2 \rho_{oi} z_i^2 e^2} \right)^{1/2}$ [9].

RESULTS AND DISCUSSION

The results of measurements of equilibrium thickness of foam films from LPG as a function of NaCl concentration are shown in Figure 2. The investigations were carried out at two different phospholipid concentrations (C_s) - 2.4×10^{-6} mol dm⁻³ and 1.5×10^{-5} mol dm⁻³. For both surfactant concentrations at low electrolyte concentration (C_{el}) thick equilibrium films were formed and gradually decreased in thickness with the increase in C_{el} . At $C_{el} = 5 \times 10^{-2}$ mol dm⁻³ a transition to common black film formation occurred. Further increase of C_{el} did not affect the type of black films. The thickness is slightly decreased to ~ 9 nm at 0.5 mol dm⁻³ NaCl. The dependence of the foam film thickness by reducing the concentration of the electrolyte follows a similar tendency, but at the higher concentration of lipid lies entirely up of the curve for the lowest C_s . These findings are in accordance with previous studies with mixtures between uncharged and charged lipids in which have shown [13] that the thickness of the investigated films increases with the concentration of the charged surfactant.

An experimental scatter of about ± 3 nm was observed only in the region of formation of the thicker silver-colored films at the low C_s . In all other experiments the experimental film thickness values were obtained within the accuracy of the

microinterferometric technique. According to the frame of experimental error there is no significant difference in the thickness of the films.

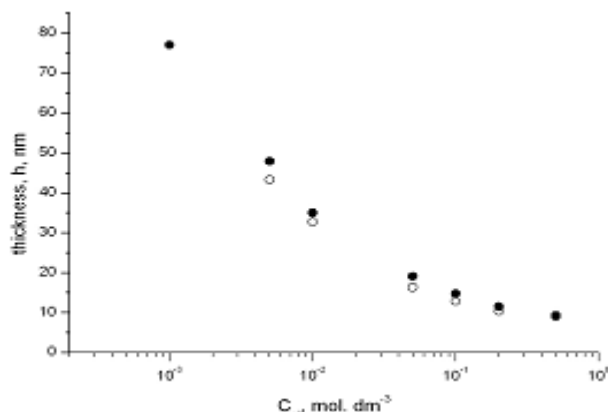


Fig. 2. Equilibrium thickness (h , nm) of microscopic foam films stabilized with LPG (C_s) as a function of NaCl concentration (C_{el}): ○ $C_s = 2.4 \times 10^{-6}$ mol dm⁻³; ● $C_s = 1.5 \times 10^{-5}$ mol dm⁻³.

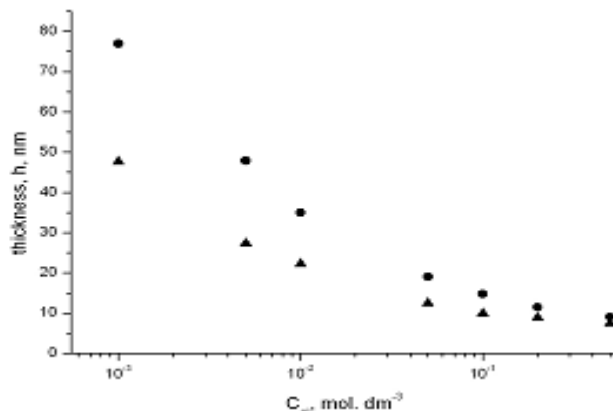


Fig. 3. Equilibrium thickness (h , nm) of microscopic foam films, stabilized with LPG ($C_s = 1.5 \times 10^{-5}$ mol dm⁻³) as a function of CaCl₂ concentration (▲). For comparison are given data at the same C_s from Figure 2 in the presence of NaCl concentration (●).

The effect of CaCl₂ on equilibrium thickness of the foam films studied is shown in Figure 3. The results are compared at the same figure with the results, obtained with NaCl at the same C_s for LPG. The experiments were carried out only with $C_s = 1.5 \times 10^{-5}$ mol dm⁻³.

At $C_{el} = 5 \times 10^{-3}$ mol dm⁻³ the thinning of foam films leads to formation of common black films without observation of black spots. Curiously, the process of thinning changed dramatically at $C_{el} = 5 \times 10^{-2}$ mol dm⁻³ where Newton black films were observed. The transition from thick silver films to Newton black films happens without observation of black spots. At $C_{el} = 0.5$ mol dm⁻³ CaCl₂ the

thickness ~ 7.5 nm. Probably, in the case when the positive Ca²⁺ bind to the phospholipids head group, they reduce the initially negative surface charge and lead to weaker repulsive electrostatic interactions than in the case with NaCl added. That's why the comparison of the results for Na⁺ and Ca²⁺ shows that the presence of divalent ions lead to significant decrease of the thickness of foam films.

Important information on foam film interactions have been obtained from directly measured disjoining pressure isotherm. All experiments were carried out at $C_s = 1.5 \times 10^{-5}$ mol dm⁻³ LPG. The results obtained with 1×10^{-4} mol dm⁻³ NaCl added and 2×10^{-4} mol dm⁻³ CaCl₂ added are shown in Figures 4 and 5, respectively.

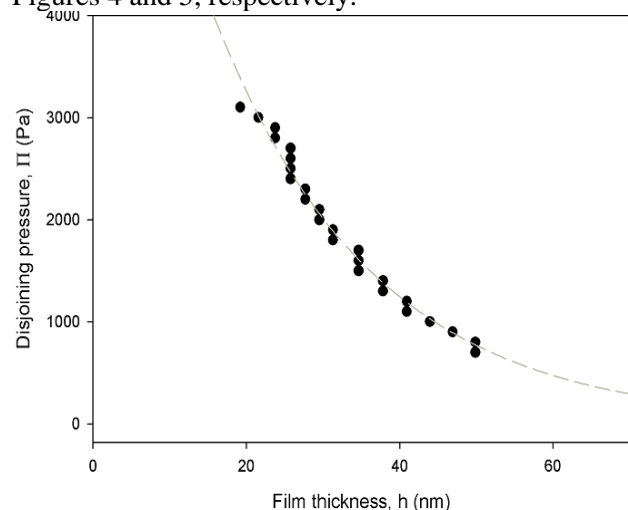


Fig. 4. $\Pi(h)$ isotherm (with guideline), measured at $C_s = 1.5 \times 10^{-5}$ mol dm⁻³ LPG with $C_{el} = 1 \times 10^{-4}$ mol dm⁻³ NaCl added.

As seen in Figure 4, the increase in the applied pressure leads to a gradual decrease of the equilibrium thicknesses. At pressure 3.1 kPa we have measured ~ 19 nm film thickness. No “jump” transitions have been detected. The course of the obtained isotherm with CaCl₂ added, shown in Figure 5, is similar to the obtained with NaCl although the C_{el} is different (in Figure 4). The film thickness at pressure 3.1 kPa we have measured is lower ~ 14.5 nm.

According to classical DLVO theory we are able to determine the diffuse electric layer ϕ_0 at the film interfaces. Obtained values for ϕ_0 in the measurements with NaCl is 2,45 mV and for solution with CaCl₂ is 1,7 mV. For low potentials, below 25 mV [9], the potential becomes proportional to the surface charge density. The magnitude of the Debye length depends solely on the properties of the

solution and not on any property of the surface such as its charge or potential. For solutions with Ca²⁺ the obtained value for κ according to estimated predictions is 0.08035 nm⁻¹ and as for the experimental data estimated value is twice lower - 0.04373 nm⁻¹. When recalculating the concentration of Ca²⁺, based on the theory for Debye length, we obtain estimated very low value $\sim 6 \cdot 10^{-5}$ mol dm⁻³. These data compared with low potential for solution with Ca²⁺ can be explained with further interaction between divalent ions and phosphate residues from the polar head of the lipid molecules [10].

As in previous reports for negative-charged lipids [12] our observations also indicate that Ca²⁺ has a marked effect on the nature of the bilayer surface.

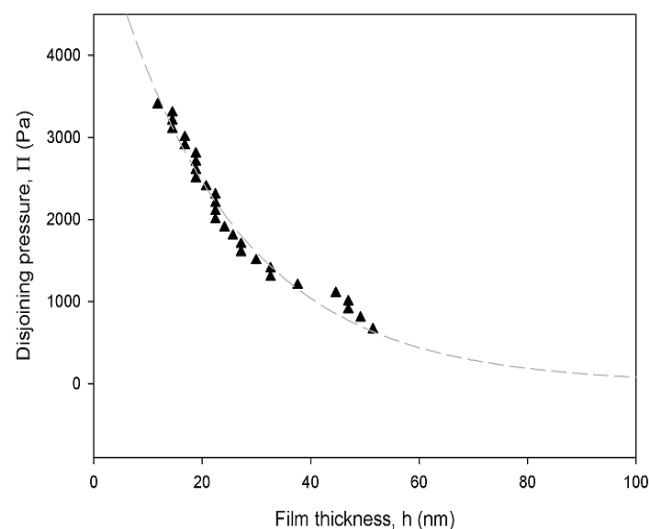


Fig. 5. $\Pi(h)$ isotherm (with guideline), measured at $C_s = 1.5 \times 10^{-5}$ mol dm⁻³ LPG with $C_{el} = 2 \times 10^{-4}$ mol dm⁻³ CaCl₂ added.

Probably, apart from double layer interactions, other more specific factors like bridging, conformational changes might play an important role.

CONCLUSION

This work shows properties of thin liquid films stabilized with charged phospholipids in the presence of monovalent and the influence of divalent ions on the properties of the foam films. The process of thinning of the equilibrium thickness of the films of LPG in the presence of Na⁺ with the increase of the electrolyte concentration results in the formation of the common black films. At higher concentration of the lipid, were measured thicker films and the effect is significant at middle electrolyte concentrations. The possible explanation may be

founded in the repulsion forces between the layers in the film structure.

The study of the foam films of LPG in the presence of Ca²⁺ shows a very strong interaction of these ions with the polar group of the lipid molecules resulted in formation of Newton black films at higher concentration of electrolyte. The equilibrium thickness in these very thin foam films probably depends on the short-range interactions between the monolayers of LPG. This statement is supported by recalculated and much lower concentration of electrolyte from obtained experimental results, obtained low value for ϕ_0 and low value for k . Probably, the reason is in decisive influence of phosphoric polar head group of lipid structure in connection with Ca²⁺. In the case when the positive Ca²⁺ bind to the phospholipid head group, they reduce the initially negative surface charge and lead to weaker repulsive electrostatic interactions than in the case with NaCl added.

Acknowledgment. This work has been done under the umbrella of COST Action MP1106.

REFERENCES

1. R. Cohen, D. Exerowa, T. Yamanaka, *Langmuir*, **12**, 5419 (1996).
2. R. Hite, M. Seeds, R. Jacinto, B. Grier, B. Waite, D. Bass, *Biochim. Biophys Acta*, **1720**, 14 (2005).
3. Y. Zuo, R. Veldhuizen, A. Neumann, N. Petersen, F. Possmayer, *Biochim. Biophys Acta*, **1778**, 1947 (2008).
4. B. Kramer, *Intensivmedizin*, **44**, 403 (2007).
5. R. Todorov, *Curr. Opin Colloid Interface Sci.*, **20**, 130 (2015).
6. Z. Lalchev, R. Todorov, D. Exerowa, *Curr. Opin. Colloid Interface Sci.*, **13**, 183 (2008).
7. D. Exerowa, P. Kruglyakov, *Foam and Foam Films*, Elsevier, Amsterdam, 1998.
8. D. Exerowa, D. Kashchiev, D. Platikanov, *Adv. Colloid Interface Sci.*, **40**, 201 (1992).
9. J. Israelachvili, *Intermolecular and Surface Forces*, Third edition, 2011.
10. E. Verwey, J. Overbeek, *The Theory of Stability of Lyophobic Colloids*, Elsevier, Amsterdam, The Netherlands, 1948.
11. V. Muller, *Zh. Kolloidn.*, **38**, 704 (1976).
12. J. Marra, *Biophys. J.*, **50**, 815 (1985).
13. J. Herrera, N. Krasteva, H.-J. Muller, R. Krastev, *Adv. Colloid Interface Sci.*, **207**, 93 (2014).

ПЕННИ ФИЛМИ ОТ ЛИЗОФОСФАТИДИЛГЛИЦЕРОЛ В ПРИСЪСТВИЕ НА Na⁺ И Ca²⁺

С. А. Александров*¹, Р. К. Тодоров², А. Г. Йорданова³, З. И. Лалчев³, Д. Р. Ексерова²

¹ Медицински университет - София, Катедра „Медицинска физика и биофизика“, 1431 София, България

² Институт по физикохимия, Българска академия на науките

³ Софийски университет “Св. Климент Охридски”

Постъпила на 27 юли, 2015 г.; коригирана на 7 декември, 2015 г.

(Резюме)

Лизолипидите привличат интереса на изследователите заради участието и значението им при функционирането на биологичните мембрани. Тази работа представя изследване на пенни филми, стабилизирани с разтворимия фосфолипид палмитинов лизофосфатидилглицерол. Проучени бяха зависимостта на дебелината на филма от концентрацията на електролита в присъствие на натриеви и калциеви йони в разтвора, както и изотерми на разклинящо налягане. При ниска концентрация на NaCl се образуват дебели сиви филми с равновесна дебелина. С увеличаване на концентрацията на Na⁺ филмите изтъняват и при 0.5 mol dm⁻³ достигат до равновесна дебелина около 9 nm (обикновени черни филми). Пенните филми в присъствие на Ca²⁺ следват същата зависимост, но при концентрация на електролита по-висока от 5×10⁻² mol dm⁻³ се образуват нютонови черни филми (НЧФ). Вероятно, равновесната дебелина на тънките НЧФ зависи от близкодействащи сили между взаимодействащите монослоеве от лизолипида във филма. В подкрепа на това твърдение е преизчислената много по-ниска стойност на концентрацията на електролита, стойността на потенциала, както и Дебаевата дебелина. Изотермите на разклинящо налягане и при двата електролита показват плавно изтъняване на филмите без преходи.

Hofmeister anions effect on the thickness and morphology of polyelectrolyte multilayers for biofunctionalization of cardiovascular stents

T. D. Andreeva^{1*}, A. K. Danailova¹, P. Terziyska², S. B. Krumova¹, S. G. Taneva¹, R. Krastev^{3,4}

¹ *Institute of Biophysics and Biomedical Engineering, Bulgarian Academy of Sciences, Acad. G. Bonchev Str., bl. 21, 1113 Sofia, Bulgaria*

² *Georgi Nadjakov Institute of Solid State Physics, Bulgarian Academy of Sciences, 72, Tzarigradsko Chaussee, Blvd., 1784 Sofia, Bulgaria*

³ *The Natural and Medical Sciences Institute at the University of Tübingen (NMI), department "Biomaterials", Markwiesenstraße 55, 72770 Reutlingen, Germany*

⁴ *Reutlingen University, Faculty of Applied Chemistry, Alteburgstraße 150, 72762 Reutlingen, Germany*

Submitted on July 9, 2015; Revised on October 8, 2015

The effect of Hofmeister anions on the surface properties of polyelectrolyte multilayers built from hyaluronan and chitosan by layer-by-layer deposition is studied by ellipsometry and atomic force microscopy. The thickness, roughness and morphology of the resulting coatings were found to depend on the type of the anion. Relationship between the surface properties and the biological response of the polyelectrolyte multilayers is established by assessing the degree of protein (albumin) adsorption.

Key words: polyelectrolyte multilayers, ellipsometry, AFM, Hofmeister anions

INTRODUCTION

Coronary artery disease (CAD) is globally one of the major causes of morbidity and mortality, affecting over 17 million people per year (4 million in Europe) (data from the World Health Organization). In addition to medical treatment, coronary stent implantation is for many patients the method of choice for the management of coronary atherosclerosis. However bare metal coronary stents can fail to maintain vessel patency due to either restenosis or stent thrombosis. Metal stents coated with an outer layer of polymer (bioabsorbable or non-bioabsorbable) can be drug-loaded, thus providing more controlled and sustained drug delivery, that might allow optimal drug-tissue interactions [1].

In the recent years the use of polyelectrolyte multilayers (PEMs) fabricated by layer-by-layer (LbL) self-assembly of polycations and polyanions has emerged as a powerful and versatile strategy to engineer surface films for biofunctionalization and drug delivery [2-4]. A wide variety of polyelectrolytes (PE) ranging from designed synthetic polymers to naturally derived biopolymers may be employed for film build-up. The resulting biomimetic PEM films are of special interest for coating dental and orthopedic implants, particularly when they contain components of the native extracellular matrix of bone.

The physicochemical characteristics of the PEM films, such as thickness, stiffness, chemistry, stability, permeability, composition, biofunctionality and dynamics, can be tunable to a large extent and they can act as a key to modulate the interaction with biomolecules and cells [5, 6]. Scanning- or atomic force microscopy have been widely used for studying the topography and the mechanical properties of PEMs [7-11].

This study addresses the optimization of biocompatibility of PEM films built from the biodegradable linear polysaccharides hyaluronan (HA) and chitosan (Chi), possessing an enhanced thrombo-resistance [12], by addition of various Hofmeister anions and monitoring of the thickness and morphology of the resulting coatings. The exchange of counterions between the dipping solutions and the multilayers represents a promising way to tune PEMs' hydrophobicity [13, 14]. We focus on the effect of monovalent chaotropic (ClO_4^-), kosmotropic (F^- and CH_3COO^-), and neutral (Cl^-) anions on the biological response of the PEMs, evaluating the albumin adsorption. Thereby we establish proper conditions for optimal biocompatibility of the studied matrices for blood-exposed cardiac stents.

*To whom all correspondence should be sent:
E-mail: t_andreeva@abv.bg

EXPERIMENTAL

Materials. Polyethylenimine (PEI) (MW \approx 750 kDa, 50 wt.% solution), chitosan (Chi) (MW \approx 50–190 kDa, 75–85% deacetylated), both from Sigma Aldrich (Steinheim, Germany), and hyaluronic acid (HA) (MW \approx 360 kDa) from Lifecore Biomedical, LLC (Chaska, USA) were used as received. HA and Chi were dissolved in 250 mM solutions of NaCl, NaF, NaClO₄ or CH₃COONa (all from Sigma-Aldrich) to a concentration of 1 mg/ml, pH 5.5. PEI was dissolved in ultrapure water to a concentration of 2 mg/ml and deposited as a first layer acting as a uniform anchoring network for the formation of consecutive layers.

Preparation of PEM films. PEM films PEI(HA/Chi)_{3.5-12.0} (sub indexes denote the number of the deposited bilayers) were prepared by layer-by-layer (LbL) technique using the hand dipping method [15] on silicon (100) wafers (10×10 mm, CrysTec GmbH, Germany) preliminary cleaned by consecutive ultrasonication in acetone and isopropanol (2 min each) and activated by oxygen plasma cleaning. The film build-up was pursued at 25°C by alternating dipping of the silicon wafers into HA and Chi solutions (for 10 min) and three washing steps (2 min each) in the corresponding 250 mM electrolyte solution. The number of deposited HA/Chi bilayers varied from 3.5 to 12. After the last deposition step the samples were washed in water and dried in a nitrogen stream.

Atomic force microscopy (AFM) imaging was performed with NanoScopeV system (Bruker Inc.) in tapping mode in air. Standard silicon nitride (Si₃N₄) probe tips (Budget Sensors, Innovative solutions Ltd., Bulgaria) were used (tip radius <10 nm). The PEM-covered silicon wafers were fixed to the metal pads and scanned with rate 0.5 Hz. Each sample was examined at 5 different locations all over the surface. The images (512×512 pixels) were captured in height and deflection modes and roughness analysis was performed using NanoScope 6.13R1 software. All images are presented with a simple first-order flattening.

The adsorption of bovine serum albumin (BSA) (from Serva Electrophoresis GmbH) on the PE-coated silicon substrates was also investigated by AFM. BSA, at a concentration 0.5 mg/mL, was adsorbed on the outer layer of the PE films. After 60 min the samples were rinsed with water to remove all free and loosely bound albumin molecules, dried with nitrogen and scanned.

Ellipsometry was used to monitor the film growth. Woollam M2000D rotating compensator spectroscopic ellipsometer with wavelength range from 193 to 1000 nm was used. Measurements were performed at an angle of incidence 69°. To obtain the film thickness the raw data were fitted by four-layer model, considering the contribution from the air, PEM, SiO₂, and Si.

RESULTS AND DISCUSSION

The typical ordering of the anions in the Hofmeister series is as follows: SO₄²⁻, HPO₄²⁻, OH⁻, F⁻, HCOO⁻, CH₃COO⁻, Cl⁻, Br⁻, NO₃⁻, I⁻, SCN⁻, ClO₄⁻, but this order can be slightly different, depending on the phenomenon under examination. The species to the left of Cl⁻ (neutral anion) are referred to as kosmotropes (water structure makers), while those to its right are chaotropes (water structure breakers). Sodium salts of F⁻, CH₃COO⁻, Cl⁻, and ClO₄⁻ were selected for HA/Chi multilayers deposition. The specific ion effects on the properties of PE multilayers become important above 100 mM for anions and 250 mM for cations [16]; therefore we used electrolyte concentration of 250 mM.

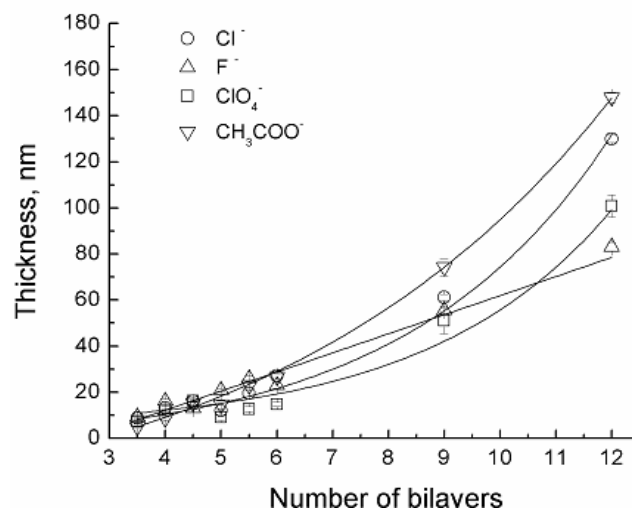


Fig. 1. Thickness of PEM films with different number of HA/Chi bilayers built in the presence of different Hofmeister anions.

(HA/Chi) multilayers growth. The change in films thickness during the deposition of up to 12 bilayers in the presence of different electrolytes is presented in Figure 1. For the thin multilayers composed of less than 6 bilayers the thickness is poorly dependent on the type of the Hofmeister anion involved in the build-up process, and the maximal difference between the thinnest and the thickest film is less than 10 nm, while after deposition of more than 6 bilayers the

thickness difference increases reaching 70 nm at 12 bilayers. The thickness of (HA/Chi)₁₂ films depends strongly on the type of the Hofmeister anion present in the dipping HA and Chi solutions and increases in the order $F^- < ClO_4^- < Cl^- < CH_3COO^-$. Except the films built in the presence of F^- , the thickness of the other HA/Chi films increase in accordance with the arrangement of the anions in the Hofmeister series and the growth of the ion hydration radius. The chaotropic anion ClO_4^- causes thinning of the HA/Chi multilayers, compared to these containing Cl^- . As opposite the kosmotropic anion CH_3COO^- increases the thickness.

The film thickness increases in a nonlinear (exponential) fashion in the presence of the neutral Cl^- , the large kosmotropic CH_3COO^- and chaotropic ClO_4^- anions, whereas the addition of the small kosmotropic F^- anion results in a linear thickness growth. These results corroborate the findings of Picart and co-workers [17], who attributed the exponential growth mechanism to Chi's ability to diffuse in and out of the entire HA/Chi film at each deposition step. These authors also reported that HA is non-diffusing specie in LbL assembly of PEMs. Detailed studies on the film build up of systems comparable to HA/Chi films have also been reported by Porcel et al. [18, 19]. The same linear thickness growth is reported by Salomäki et al. [20] for PSS/PDADMA films built in the presence of F^- , while addition of Cl^- and ClO_4^- leads to exponential growth.

In the case of interaction of ions with strong polyelectrolytes it is generally accepted that the increase in the hydration shell of the ions, which is related to weaker polarizability, leads to weaker interaction between the ions and the polyelectrolytes.

This is associated with weaker coiling of the polyelectrolyte chain, which in turn decreases the thickness and roughness of the multilayers [16, 20-22]. In the case of monatomic ions as in the halide series (F^- , Br^- , and Cl^-) the interaction between anion and synthetic PSS/PDADMAC polyelectrolytes increases with the increase of the ion size and ionic strength [16, 20, 21, 23]. However, we observe clearly expressed opposite effect. Since our experimental data included also polyatomic anions, the use of the anion radius in the characterization of polyelectrolyte binding is not relevant. More accurate interpretation would involve precise consideration of anion hydration shell and the factors affecting it. Several reasons can be suggested for this behavior. Due to its strong binding affinity and low extent of hydration the chaotropic anion ClO_4^- would dehydrate the film, while the kosmotropic anion CH_3COO^- brings along the largest amount of water into the film. It seems that for polymer couples consisting of two or at least one strong polyelectrolyte the interaction between that polyelectrolyte and the counter-ion plays a key role for the final thickness. However for the couple HA/Chi of weak natural polyelectrolytes that are highly hydrated (the water content of the (HA/Chi)₅ multilayer is around 400%, as obtained by thermogravimetry analysis [24]) the degree of hydration of the multilayers is of crucial role.

Films' Morphology. Each step of HA/Chi films build up was imaged by AFM. At the early stages of the deposition small islets are seen but they coalesce and become larger as the number of deposited bilayers increases. After the deposition of approximately 5 bilayers, the surface becomes fully

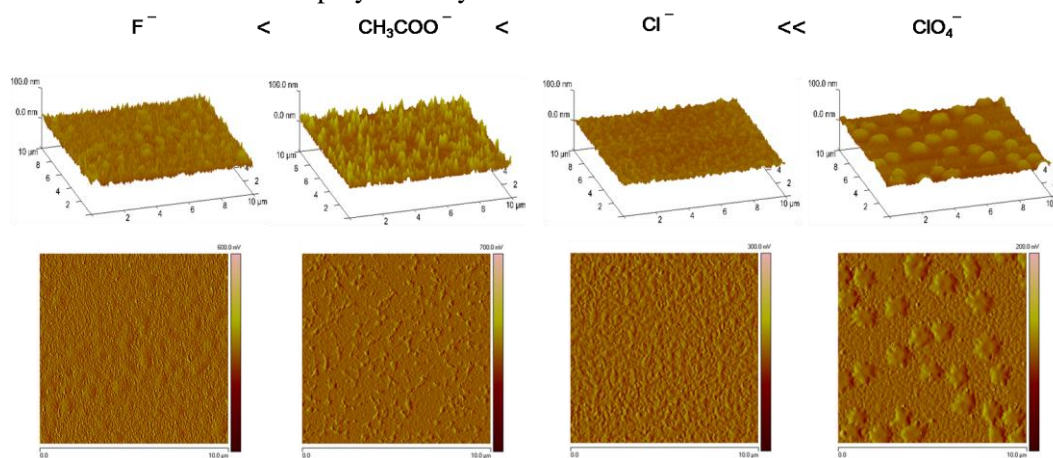


Fig. 2. Typical 3D- (top) and deflection- (bottom) images of (HA/Chi)₅ films on silicon taken by AFM in tapping mode.

coated and a homogeneous film is formed. Figure 2 shows clear difference in the surface morphology of the PEMs triggered by the introduction of different anions into the dipping HA and Chi solutions. Analogously to previous studies, in the presence of Cl^- wormlike or vermiculate pattern emerges [17]. The bumps are about 15 nm in depth and 350-400 nm wide, although these numbers may be an overestimate because of AFM tip convolution effects [25]. Addition of the kosmotropic CH_3COO^- anion results in formation of tread-like interlaces, much smaller but twice higher than the vermiculate pattern. The other kosmotropic anion, F^- , favors the formation of multiple and even smaller, needle-like structures, whereas the chaotropic anion, ClO_4^- , induces formation of star-like islands with uniform shape and diameter of 1 μm . The size of the surface structures formed during the deposition follows the Hofmeister series $\text{F}^- < \text{CH}_3\text{COO}^- < \text{Cl}^- < \text{ClO}_4^-$.

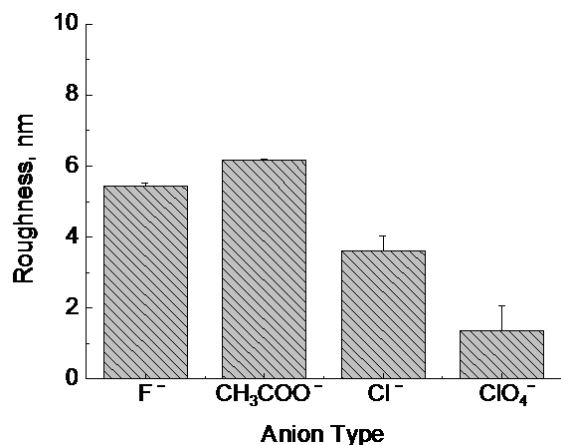


Fig. 3. Root-mean-square roughness of $(\text{HA}/\text{Chi})_5$ films built in the presence of Hofmeister anions.

As anticipated, the observed changes in the films' morphology are reflected in the root-mean-square roughness (Rrms) of the surface. Figure 3 illustrates

that the surface roughness of HA/Chi films (derived from five images with scanned area $10 \times 10 \mu\text{m}$, including the images in Fig. 2) grows in the order $\text{ClO}_4^- < \text{Cl}^- < \text{F}^- < \text{CH}_3\text{COO}^-$, thus following the Hofmeister series. It has been found that in the case of polyelectrolyte multilayers built of strong synthetic PE [16, 20-22, 26], chaotropic ions screen stronger the charge of the oppositely charged PE than the kosmotropic, which in turn leads to folding of the PE chain and to a greater thickness and higher roughness of the resultant multilayer. Our results show a pronounced opposite effect - the addition of the chaotropic ClO_4^- anion to the weak polysaccharide solutions results in the construction of very smooth films with surface roughness about 1.4, that is in the range of the substrate roughness, and about 2.6 times lower than the roughness of the films built with Cl^- -addition, which amounts to ca. 3.6 nm. At the same time the roughness of the coatings built in the presence of the kosmotropic anions F^- and CH_3COO^- is 1.5 and 1.7 times higher than that of the reference films, reaching 5.5 and 6.2 nm, respectively.

Biocompatibility. To test the biological response of the resulting PEM films we made a qualitative assessment of the degree of adsorption of the protein albumin. In our case the negatively charged BSA mainly adsorbs on the Chi-ending multilayers. The surface morphology of the multilayer films before and after albumin adsorption is presented in Figure 4. The albumin adsorption depends on the surface properties, the most pronounced one being observed on coatings prepared in the presence of chaotropic anion, which are smoother and albumin accumulation on them strongly increases the roughness thereof (the Rrms in Fig. 4 is derived from five images with scanned area $1.5 \times 1.5 \mu\text{m}$, including the images in Fig. 4).

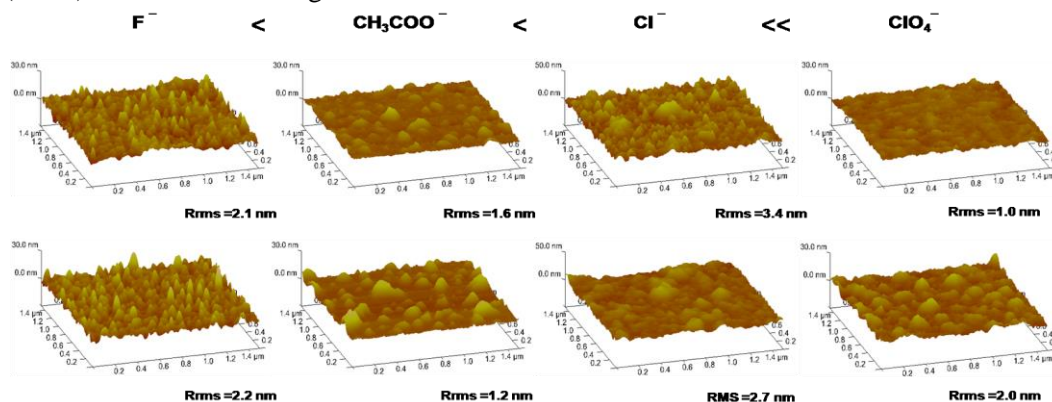


Fig. 4. 3D-topography images of $(\text{HA}/\text{Chi})_5$ films, before (top) and after (bottom) BSA adsorption, taken by AFM in tapping mode at magnification $1.5 \times 1.5 \mu\text{m}$.

In the case of HA/Chi films deposited in the presence of Cl^- , characterized with highly furrowed and rough surface, the albumin molecules accumulate in the indentations and fill them, and as a result the roughness is reduced. Very weak or completely absent adsorption of albumin is observed on the surface of HA/Chi multilayers prepared in the presence of kosmotropic anions, the surface roughness in the presence of CH_3COO^- is slightly decreased, while it remains the same in the presence of F^- .

CONCLUSIONS

We demonstrate that the physicochemical properties of polyelectrolyte multilayer films, built from the natural linear polysaccharides hyaluronan and chitosan, can be successfully modified by addition of chaotropic and kosmotropic anions belonging to the Hofmeister series. We also proved that the introduction of kosmotropic anions improves the PEMs' biocompatibility contributing to increase of the surface roughness and decrease of the albumin adsorption. Although the adsorption of proteins is very important for the accommodation of medical devices such as surgical tools and implants inserted in a human body, in some cases, like cardiovascular stents implantation, protein adsorption on biomaterials can be an extremely unfavorable event; and the adhesion of clotting factors may induce thrombosis, which may lead to stroke or other blockages [27].

Acknowledgements. This work is supported by the Bilateral academy exchange grant PPP Germany 01/9 2014, Bulgarian Science Fund/DAAD. The authors acknowledge the partial support of the EU FP7 funded Project INERA under the contract REGPOT 316309.

REFERENCES

1. C. D. Rogers, *Rev. Cardiovasc. Med.*, **5**, S9 (2004).
2. G. Decher, *Science*, **277**, 1232 (1997).
3. C. S. Peyratout, L. Dahne, *Angew. Chem. Int. Ed.*, **43**, 3762 (2004).
4. A. Volodkin, A. Skirtach, H. Möhwald, *Adv. Polym. Sci.*, **240**, 135 (2011).
5. C. Picart, *Curr. Med. Chem.*, **15**, 685 (2008).
6. K. Ariga, J. P. Hill, Q. Li, *Phys. Chem. Chem. Phys.*, **9**, 2319 (2007).
7. A. J. Engler, L. Richert, J. Y. Wong, C. Picart, D. E. Discher, *Surf. Sci.*, **570**, 142 (2004).
8. L. Richert, F. Boulmedais, P. Lavalle, J. Mutterer, E. Ferreux, G. Decher, P. Schaaf, J. C. Voegel, C. Picart, *Biomacromolecules*, **5**, 284 (2004).
9. L. Richert, A. J. Engler, D. E. Discher, C. Picart, *Biomacromolecules*, **5**, 1908 (2004).
10. A. Schneider, G. Francius, R. Obeid, P. Schwinté, J. Hemmerlé, B. Frisch, P. Schaaf, J. C. Voegel, B. Senger, C. Picart, *Langmuir*, **22**, 1193 (2006).
11. A. Schneider, L. Richert, G. Francius, J. C. Voegel, C. Picart, *Biomed. Mater.*, **2**, S45 (2007).
12. B. Thierry, F. M. Winnik, Y. Merhi, J. Silver, M. Tabrizian, *Biomacromolecules*, **4**, 1564 (2003).
13. J. B. Schlenoff, A. H. Rmaile, C. B. Bucur, *J. Am. Chem. Soc.*, **130**, 13589 (2008).
14. L. M. Wang, Y. Lin, Z. H. Su, *Soft Matter*, **5**, 2072 (2009).
15. G. Decher, J. D. Hong, J. Schmitt, *Thin Solid Films*, **210/211**, 831 (1992).
16. J. Wong, H. Zastrow, W. Jaeger, R. V. Klitzing, *Langmuir*, **25**, 14061 (2009).
17. L. Richert, P. Lavalle, E. Payan, X. Z. Shu, G. D. Prestwich, J. F. Stoltz, P. Schaaf, J. C. Voegel, C. Picart, *Langmuir*, **20**, 448 (2004).
18. C. Porcel, P. Lavalle, V. Ball, G. Decher, B. Senger, J. C. Voegel, P. Schaaf, *Langmuir*, **22**, 4376 (2006).
19. C. Porcel, P. Lavalle, G. Decher, B. Senger, J. C. Voegel, P. Schaaf, *Langmuir*, **23**, 1898 (2007).
20. M. Salomäki, P. Tervasmäki, S. Areva, J. Kankare, *Langmuir*, **20**, 3679 (2004).
21. R. V. Klitzing, J. Wong, W. Jaeger, R. Steitz, *Curr. Opin. Coll. Int. Sci.*, **9**, 158 (2004).
22. S. T. Dubas, J. B. Schlenoff, *Macromolecules*, **32**, 8153 (1999).
23. S. Dodoo, R. Steitz, A. Laschewsky, R. von Klitzing, *Phys Chem Chem Phys.*, **13**, 10318 (2011).
24. L. Quankui, X. Xu, W. Bailiang, S. Chenghui, T. Junmei, H. Yuemei, C. Hao, *J. Mater. Chem. B*, **3**, 3695 (2015).
25. P. Markiewicz, M. C. Goh, *Langmuir*, **10**, 5 (1994).
26. M. Salomäki, M. Laiho, J. Kankare, *Macromolecules*, **37**, 9585 (2004).
27. M. B. Gorbet, M. V. Sefton, *Biomaterials*, **25**, 5681 (2004).

ЕФЕКТ НА ХОФМАЙСТЕРОВИ АНИОНИ ВЪРХУ ДЕБЕЛИНАТА И МОРФОЛОГИЯТА НА ПОЛИЕЛЕКТРОЛИТНИ МУЛТИСЛОЕВЕ ЗА БИОФУНКЦИОНАЛИЗИРАНЕ НА КАРДИОВАСКУЛАРНИ СТЕНТОВЕ

Т. Д. Андреева^{1*}, А. К. Данаилова¹, П. Терзийска², С. Б. Крумова¹, С. Г. Танева¹, Р. Кръстев^{3,4}

¹ *Институт по биофизика и биомедицинско инженерство, Българска академия на науките, ул. „Акад. Г. Бончев”, бл. 21, 1113 София, България*

² *Институт по физика на твърдото тяло „Георги Наджаков” Българска академия на науките, бул. „Цариградско шосе” 72, 1784 София, България*

³ *Институт по естествени и медицински науки, Университет на Тюбинген, група “Биоматериали”, Марквайсенцрасе 55, 72770 Рьотлинген, Германия*

⁴ *Университет на Рьотлинген, Факултет по приложна химия, Алтебургщрасе 150, 72762 Рьотлинген, Германия*

Постъпила на 9 юли, 2015 г. коригирана на 8 октомври, 2015 г.

(Резюме)

Ефектът на хофмайстерови аниони върху повърхностните свойства на полиелектролитни мултислоеви изградени от хиалуронан и хитозан, е изследван посредством елипсометрия и атомно силова микроскопия. Установено е, че дебелината, грапавината и морфологията на получените покрития зависят от типа на аниона. Посредством оценка на степента на адсорбция на протеин (албумин) е дефинирана зависимостта между повърхностните свойства на полиелектролитните мултислоеви и биологичния им отговор.

Optimization of the classical method for nucleation and growth of rhombohedral insulin crystals by pH titration and screening

F.V. Hodzhaoglu¹, M. Conejero-Muriel², I.L. Dimitrov¹, J.A. Gavira^{2*}

¹*Institute of Physical Chemistry, Bulgarian Academy of Sciences, Department of Phase Formation, Crystal and Amorphous Materials, Acad. G. Bonchev Str., block 11, 1113 Sofia, Bulgaria*

²*Laboratorio de Estudios Cristalograficos, CSIC-UGR, Avenida de las Palmeras No 4, E-18100, Armilla, Granada, Spain*

Submitted on September 8, 2015; Revised on November 23, 2015

Crystallization of hexameric zinc-containing insulin in its rhombohedral space group is accomplished by step titration of an acidic insulin solution containing an excess amount of Zn²⁺ ions either in the presence of acetone or not. During the preparation of the mixture, precipitation was observed when crossing a critical pH value. This precipitate dissolves and produces a clear solution after the addition of acetone. We investigated the influence of the pH on the crystallization of both porcine and recombinant human insulin by means of a systematic study of the pH evolution. Taking into account the volume fractions and concentrations of all components, by varying the ratio between the initial acid solution (0.02M HCl pH 1.55) and the citrate buffer (0.1M pH 6.98) we modulated the rate at which the critical pH was reached. This characterization allows us to precisely tune the conditions for obtaining small crystals in batch crystallization droplets in the presence or absence of acetone.

Keywords: Insulin hexamers, rhombohedral crystals, crystallization screening

INTRODUCTION

Insulin is a hormone present in the blood stream and involved in glucose homeostasis. In a healthy body, insulin is stored as rhombohedral single crystals in the granules of the pancreas beta-cells. This specific crystal form is well known and the building blocks of the crystals are insulin-zinc hexamers [1, 2]. The nanocrystals formed in the granules are released into the blood stream where they dissolve very fast [3] delivering a sufficient amount of insulin monomers, the active form that binds to cell insulin-receptors to control glucose assimilation in the intracellular space [1, 2]. In the case of disorders like *diabetes mellitus* type I, this vital hormone is administered externally, most often subcutaneously, by using medical solutions or suspensions based on recombinant human insulin or different insulin analogues of controlled formulations [4-6]. The type of insulin formulation and the dosage strongly depends on the prescribed medical treatment. Comprehensible, the numerical studies on insulin crystallization have focused in two main directions: 1) investigations of the formation and dissolution of natural (rhombohedral) zinc-containing insulin crystals [3, 7]; 2) the formulation of fast, intermediate and long-period acting insulin drugs [4-6]. The first trend is related to the better understanding of the factors governing the *in-vivo* crystallization and dissolution of insulin, whereas the second one

covers the needs of patients with insulin disorders.

The studies on the crystallization of insulin and insulin-complexes have greatly contributed to the optimization of the growth of single protein crystals for crystallographic structure determinations by X-ray and neutron diffraction methods but open questions remains on the nucleation and growth to control both processes that are of fundamental relevance for the pharmaceutical industry. X-ray crystallography has also been used to characterize the insulin-protamine complex, typically used in pharmaceutical formulation [8] although a clear picture of this interaction is still to come. Several of these studies [7-18] have extensively screened different crystallization conditions in order to get crystals of sufficient size for X-ray characterization. Nevertheless, the rhombohedral crystal form has been investigated at the nucleation and growth stage in an effort to understand which parameters affect the formation of insulin crystals *in vivo* [9-13]. Atomic Force Microscopy (AFM) of well faceted crystal faces has enabled the observation of insulin hexamers as building blocks of rhombohedral crystals, the natural storage form in the pancreas gland [9]. Moreover, the role of acetone on the growth of insulin crystals has also been investigated as well as the increased step kinetic coefficient linked to an entropic effect of acetone [14] that is due to the hydrophobic driven assembly of insulin hexamer proposed by Yip et al. in 1998 [10].

*To whom all correspondence should be sent:

E-mail: jgavira@iact.ugr-csic.es

In most studies, insulin from different sources has been crystallized following a well-established strategy used in the pioneering works of Schlichtkrull [15-17] in which an insulin stock solution is prepared by the dissolution of the lyophilized insulin in low concentration hydrochloric acid. This procedure allows for the preparation of stock solutions with high insulin concentration that remains stable for several days at temperatures below 20°C [18]. The formation of the insulin-zinc hexamer building block is guaranteed by the strong coordination of insulin dimers with Zn²⁺ ions provided in the solution as ZnCl₂, while supersaturation is reached by decreasing the solubility of insulin-zinc hexamers driven by increasing the pH, typically above pH 6.00, with citrate buffer. Other additives such as sodium chloride or sodium hydroxide are typically used to stabilize and keep clear the stock solutions while acetone or phenol are essential additives to either control the nucleation and growth or to obtain the desired insulin polymorph, respectively.

In this work we present a systematic study for the preparation of supersaturated insulin solutions based on the most common method that contains ZnCl₂ and sodium citrate buffer as the main components, and either with or without acetone. Based on these results, a comprehensive protocol for the preparation of crystallizing solutions of hexameric insulin to produce a controllable nucleation density is presented.

EXPERIMENTAL

For the preparation of the protein stock solutions, lyophilized porcine (Sigma Aldrich, Ref. I5523) and human recombinant insulin (Roche Diagnostics GmbH, Ref. 11376497001) were used without further purification. Insulin stock solutions (20 mg/ml) were prepared by dissolving the insulin in 0.02 M HCl (J. T. Baker, analytical grade). The citrate buffers at 0.065, 0.1, 0.15 and 0.2 M were prepared at pH 6.98 by titration of the buffer salt with a citric acid solution. Zinc chloride stock solution was prepared at 0.05 M concentration. The buffer components and zinc chloride were of analytical grade from Sigma. Acetone (Chromasolv plus for HPLC > 99.9%) was used as provided by the supplier (Sigma Aldrich, Ref. 650501). All solutions were prepared with MilliQ water.

The titration experiments were monitored with a GRISON pH-meter equipped with a standard pH microelectrode under continuous stirring in 1.5 mL eppendorf tubes with insulin and 10 mL glass vessel without insulin.

The insulin stock solutions were prepared in small eppendorf tubes by precise gravimetric measurements of small amounts of lyophilized protein and the addition of diluted hydrochloric acid solution (0.02 M) to obtain a final concentration of 20 mg/ml. The final concentration of insulin stock solution was determined using a CARY 1E UV-Visible Spectrophotometer and an extinction coefficient of 1.04 ml mg⁻¹ cm⁻¹ [19] with 0.02M HCl as reference sample.

The crystallization screening was performed in micro-batch crystallization plates with 12x8 cylindrical reservoirs (Hampton Research). The crystallization droplets (20µL) were prepared in a single PCR eppendorf tube for appropriate mixing of the solution components before transferring each sample to the plate under a layer of several millimetres of paraffin oil (Hampton Research). Two stock solutions of human and porcine insulin were prepared and the concentration was determined spectrophotometrically at 19.0 and 17.0 mg/ml respectively. In the crystallization experiments, the final protein concentrations were varied from 0.95 to 7.6 mg/ml and from 0.85 to 6.8 mg/ml for human and porcine insulin respectively (Table 1). The volume portion of HCl (40% v/v) and the concentration of ZnCl₂ (5.0 mM) were kept constant while the amount of citrate buffer was varied to study the pH effect in the presence of acetone (15% v/v, samples 1 to 6) or without acetone (samples 7 to 12). Table 1 summarizes the final composition of the mixtures represented both in concentrations and in percentage of volume. Figure 1 also shows schematically the recipe volume ratio used in this study.

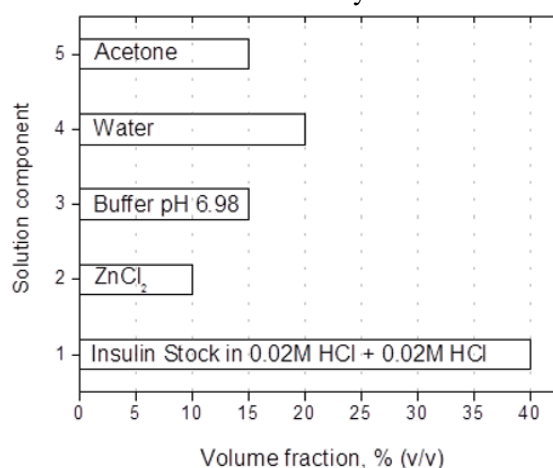


Fig. 1. Volume fractions of each component of the standard mixture for the crystallization of insulin

All experiments were performed at constant room temperature (24°C) and the evolution of the crystallization experiments over time were followed by optical microscopy (Nikon AZ100).

Table 1. Final concentrations of the components-mix in each batch experiment.

Insulin	Porcine			Human			Porcine			Human			Recipe components
	1	2	3	4	5	6	7	8	9	10	11	12	
A to H	8	8	8	8	8	8	8	8	8	8	8	8	mM HCl mM ZnCl ₂ mM Buffer Water (%) Acetone (%)
	5	5	5	5	5	5	5	5	5	5	5	5	
	15	25	35	15	25	35	15	35	50	15	35	50	
	20	10	0	20	10	0	35	15	0	35	15	0	
	15	15	15	15	15	15	0	0	0	0	0	0	
A	0.85	0.85	0.85	0.95	0.95	0.95	0.85	0.85	0.85	0.95	0.95	0.95	Insulin (mg/ml)
B	1.70	1.70	1.70	1.90	1.90	1.90	1.70	1.70	1.70	1.90	1.90	1.90	
C	2.55	2.55	2.55	2.85	2.85	2.85	2.55	2.55	2.55	2.85	2.85	2.85	
D	3.40	3.40	3.40	3.80	3.80	3.80	3.40	3.40	3.40	3.80	3.80	3.80	
E	4.25	4.25	4.25	4.75	4.75	4.75	4.25	4.25	4.25	4.75	4.75	4.75	
F	5.10	5.10	5.10	5.70	5.70	5.70	5.10	5.10	5.10	5.70	5.70	5.70	
G	5.95	5.95	5.95	6.65	6.65	6.65	5.95	5.95	5.95	6.65	6.65	6.65	
H	6.8	6.8	6.8	7.60	7.60	7.60	6.8	6.8	6.8	7.60	7.60	7.60	
Volumetric composition (% v/v)													
Sample	1	2	3	4	5	6	7	8	9	10	11	12	
A to H	40	40	40	40	40	40	40	40	40	40	40	40	0.02M HCl 0.05M ZnCl ₂ 0.1M Buffer Water Acetone
	10	10	10	10	10	10	10	10	10	10	10	10	
	15	25	35	15	25	35	15	35	50	15	35	50	
	20	10	0	20	10	0	35	15	0	35	15	0	
	15	15	15	15	15	15	0	0	0	0	0	0	

RESULTS AND DISCUSSION

1. Dissecting the insulin-hexamer crystallization procedure

There are a number of publications in which the titration of an acidic (HCl) insulin solution containing an excess of Zn²⁺ is titrated with citrate buffer in the presence or absence of acetone to crystallize insulin in its rhombohedral form. Table 2 summarizes the final composition and relevant notes of a representative group of publications using this procedure and modifications thereof [7, 9, 12-16, 20-23]. It is very impressive that even though all the consulted works seem to follow a similar protocol, none of them achieve an identical final composition or follows an exact preparation protocol. Without taking into account the sample heating prior to crystallization, as used in several published protocols, we can find different approaches to clear the crystallizing solution. For example, increasing the pH by adding NaOH, lowering the pH with HCl or using the combination of NaOH and NaCl to stabilize the solution. This variability may hinder the proper interpretation of the observed output.

Therefore, following the previously published composition of the crystallization cocktail, in this study we decide to fix the final volume and to study the influence of the most relevant variables, protein concentration, pH and acetone, while keeping the rest of the components at a fixed concentration to

provide a reproducible protocol for future investigations.

In order to characterize the described system we started our study by titrating the HCl solution containing the zinc chloride with citrate buffer in the absence of insulin. The buffer solution was added stepwise in aliquots of 250 µL while following the pH evolution of the system. At the final step acetone was added (Figure 2). Four trisodium citrate buffer concentrations, 65, 100, 150 and 200 mM, at a fixed pH of 6.98, were tested in order to evaluate the influence of the initial buffer concentration on the pH evolution of the titration system. The components' volume ratios were kept constant as depicted in the experimental section and corresponded to 8:2:7:3 for HCl, ZnCl₂, trisodium citrate and acetone, respectively, and therefore the final buffer concentrations were 22.75, 35, 52.5 and 70 mM.

In all cases the minimum reported pH for crystallization (pH 5.65) [7] was achieved. As expected, the lower citrate buffer concentration only overcomes this value in the final steps and the maximum attainable pH was 6.5 with the highest buffer concentration. Note that the titration behaviour with the 150 mM citrate buffer was similar to that of the 200 mM buffer and the titration slopes are steeper even with the minimal volume of the drop. However, our preliminary screenings have showed that the final sodium

Table 2. Representative compositions of crystallization solutions published to date.

Insulin (mg/ml)	HCl (mM)	ZnCl ₂ (mM)	Citrate (mM)	Acetone (% v/v)	Notes	Ref.
4.8	NG	7 [‡]	NG	-	pH _{Final} 5.65; pH _{Buffer} 6.98, 0.624% (w/v) Cl ⁻	[7]
NG	20 [§]	150 [§]	200 [§]	-	pH _{Final} 8.5; 750 mM NaOH for complete dissolution plus 5% phenol and 1.0 M NaCl	[9] [§]
0.75-5.0	10 or 13	6	50	0 or 15	pH _{Final} NG; Acetone was replaced with HCl (20 mM)	[12] [14] ^{&}
NG	NG	5	50	-	pH _{Final} 7 (citric buffer)	[13]
0.5% [#]	NG	0.04%	50	15	pH _{Final} 6.0-6.3 (sodium citrate)	[15]
0.5% [#]	NG	2-5%	50	15	pH _{Final} 6.0	[16]
2.0	1	5	50	15	pH _{Final} NG; pH _{buffer} 6.98	[20]
4-8	1	5	50	15	pH _{Final} NG; pH _{buffer} 6.98	[21]
5	10	7.5 [§]	50	16.6	pH _{Final} 6.39; adjusted from pH 10.6 to pH _{Final} with 1.0 M NaOH and HCl	[22]
1.25	10	1.8	50	-	pH _{Final} 6.1	[23] [*]

NG: Not given. ^{*}The volume of insulin is stated as 100 ml but it should be a mistake. We have used 10 mL in our calculations. [#]As appears in the original article. [§]Zinc acetate was used instead of zinc chloride. Given concentrations correspond to stock solution. [‡]From zinc sulfate. [&]Acetone 0 or 20% (v/v).

citrate concentrations in the crystallizations samples should be approximately 50 mM to avoid the growth of imperfect insulin crystals. This observation validates the final concentration of 50 mM of citrate buffer used in most of the reported experiments. Finally, acetone was added following the classical protocol provoking a rise of the pH of approximately 0.2 units. Since zinc ions are needed to stabilize the formation of the insulin-hexamer, we also investigated the possible role of zinc chloride, used in most procedures, on the pH.

In Figure 2b the influence of adding the zinc chloride after titration of the samples is shown to emulate the protocol used by Nanev and co-workers [21]. In this case the pH briefly dropped, which could cause aggregation of the protein if the citrate buffer concentration is not high enough e.g. 65 mM. We have also studied the titration behaviour of HCl solutions, containing zinc chloride or just water, as a function of the citrate buffer concentration. The results clearly show that the pH evolution is retarded in the presence of zinc chloride. This effect was stronger at the lowest buffer concentration and therefore the inclusion of zinc chloride impedes the ability of the buffer to increase the pH. As we will explain in the next section, this may play a relevant role on the formation of insulin-hexamer aggregates during the titration of the crystallizing solution.

2. Stepwise titration of the insulin crystallizing solution

In order to correlate the behaviour of the crystallizing solutions with the evolution of the pH, we monitored the pH during the titration of insulin dissolved in 0.02 M hydrochloric acid, with trisodium citrate buffer (100 mM). Figure 3 shows the evolution of the pH of human and porcine insulin solutions (20 mg/ml stock solution) in the presence of zinc chloride, titrated with 100 mM trisodium citrate following the volume ratios described above (Figure 1). The initial pH of the 20 mM hydrochloric stock solution was 1.55-1.58, and it increases to approximately pH 2.0 after adding 20 μ L of the insulin stock solution (in 20 mM HCl) and 10 μ L zinc chloride stock solution. At this point a clear difference was observed between human and porcine insulin. While for human insulin the pH rises to 1.90, in the case of porcine insulin it increases to pH 2.25, 0.35 units of difference that was maintained during the whole experiment. This increment cannot be attributed to a different pI since porcine insulin differs from human insulin only in having alanine instead of threonine at the carboxyl terminal of the B-chain (B30). As deduced from Figure 2 the pH increments cannot be insulin source. The titration was started by stepwise addition of 1 μ L of citrate buffer (100 mM, pH 6.98). The pH of both types of insulin solutions changed at the same rate until the pH reached 3.8, which coincided with the observation of a cloudy

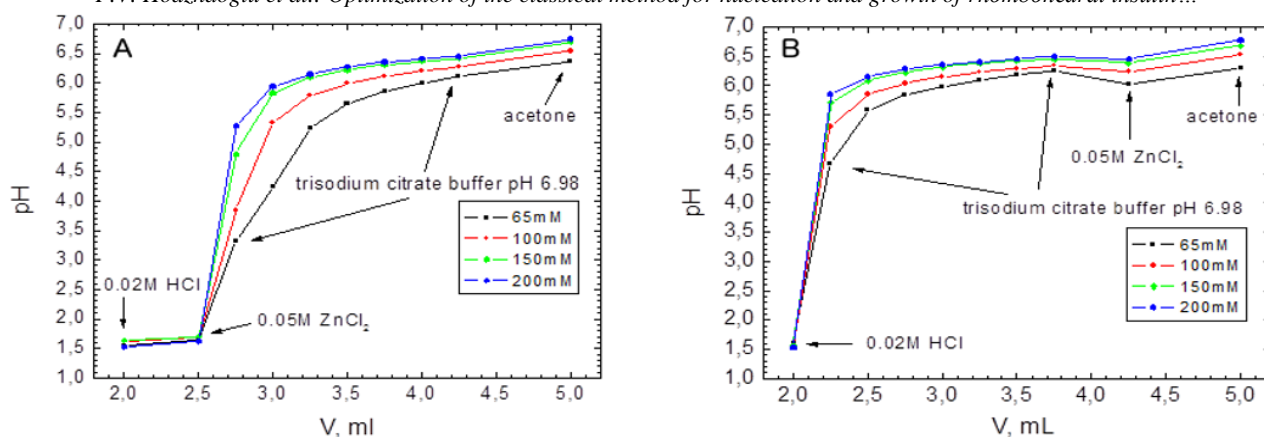


Fig. 2. Titration curves of hydrochloric acid solution with citrate buffer in presence of zinc chloride (A) or adding the zinc chloride before the acetone (B). The incorporation points of zinc chloride and acetone are indicated with arrows. The titration interval with citrate buffer is flanked with two arrows.

precipitation in both types of insulin. At this point the rate of variation of the pH was slower in the case of human insulin. In both cases an inflexion point was detected at a pH near 4.5 that is softer in the case of porcine insulin. Beyond pH 5.0 the change of pH was identical for both preparations. At pH 5.72 the insulin solution becomes visibly clear and the precipitate completely dissolves at pH 5.84. When the total volume reached 80 μ L the change in pH was small and the titration was finished by adding 5 μ L of citrate buffer. As the last step of the procedure, acetone was added to the insulin crystallization mixture which increased the pH 0.25-0.27 units while in the absence of insulin it was 0.2 pH units.

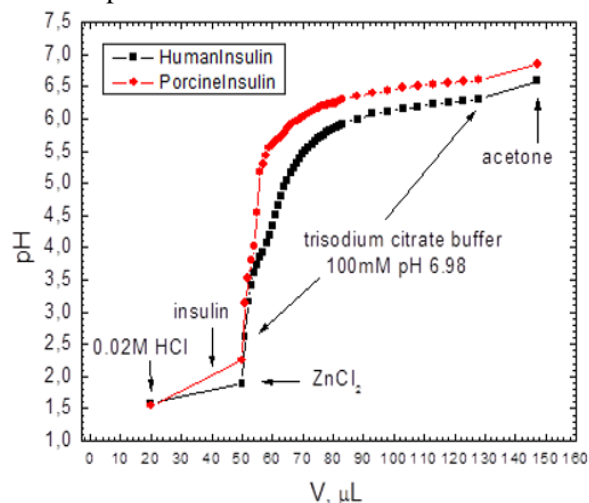


Fig. 3. Titration curves of insulin (porcine and human) dissolved in HCl solution with citric buffer.

The behaviour of the insulin crystallizing solution in the pH range 3.4 to 5.8 has already been described in the literature pointing out that approximately 99% of the total insulin forms aggregates in this range of pH [8] and also fits with the early studies of Wintersteiner and Abramson who demonstrated that the solubility of insulin in

acetate buffer was very low in the pH range 4.8 to 6.2 (approximately $4 \cdot 10^{-3}$ mg/ml) [24]. This aggregation driven by the change in pH suggests the possibility of exerting a precise control over the nucleation rate of insulin crystals by a precise control of the pH.

3. Micro-batch under oil crystallization of porcine and human insulin

We have carried out a study on the influence of acetone, buffer and protein concentrations on the crystallization of insulin (human and porcine). This investigation was carried out using the batch under-oil method. The set up was designed to cover, as much as possible, all the variations found for that particular procedure for the preparation of supersaturated insulin solutions. Besides the comparison between porcine and human insulin and the influence of acetone (0% or 15% v/v), the ratio between the final concentrations of HCl and citrate buffer, i.e. final pH, were also addressed in this multi-parameter aggregation screening.

The summary of results is shown in Table 3 in which “O” represent clear drops; “FC” well-faceted crystals; “RC” rough crystals, ranging from 1 (low) to 3 (high) the number of observed crystals; “CP” crystalline precipitate, ranging from 1 (light) to 3 (heavy) depending on the size and the number of micro-particles; “AP” amorphous precipitates, ranging from 1 (light) to 3 (heavy) depending on the visible density of aggregates and “CG” for crystalline granule-like tiny aggregates. An example of each type of precipitate is shown in Figure 4. The approximate pH values of each drop (last row of Table 3) were determined from similar experiments without insulin.

When comparing the results from porcine and human insulin it can be seen that, regardless of the final crystallization conditions, the level of

Table 3. Crystallization results of human and porcine insulin as a function of the final pH (see last row), protein concentration (increasing from A to H) and used or not of acetone at 15% v/v, samples 1-6 and 7-12, respectively.

Insulin	Porcine			Human			Porcine			Human		
Sample	1	2	3	4	5	6	7	8	9	10	11	12
A	O	O	O	CG1	FC2	O	O	O	O	AP1	O	O
B	FC2	FC1	O	CG1	FC2	FC2	O	O	O	AP2	O	O
C	FC3	FC1	O	CP3	CP1	CP1	RC1	O	FC1	AP3	O	O
D	CP1	FC1	FC2	CP3	CP1	FC3	RC1	O	O	AP3	O	FC1
E	CP2	FC3	FC1	CP3	CP2	FC2	RC1	O	RC1	AP3	FC1	RC1
F	FC3	FC2	FC2	CP3	CP3	CG	RC3	FC1	FC1	AP3	RC1	RC1
G	CP2	FC2	FC2	CP3	CP3	CP3	RC1	FC2	FC2	AP3	RC1	FC2
H	CP3	FC3	FC2	CP3	CP3	CP3	RC1	FC2	RC1	AP3	RC1	FC2
acetone	+			+			-			-		
pH*	6,07	6,45	6,59	6,07	6,45	6,59	5,87	6,34	6,48	5,87	6,34	6,48

O: clear droplet or light precipitate; well faceted (FC) or rough (RC) insulin crystals XC1: 1-10; XC2: 10-100; XC3: 100-1000 insulin crystals; crystalline insulin precipitates CP1: transition of the insulin crystals to small crystalline particles; CP2: fine crystalline insulin particles; CP3: heavy crystalline insulin precipitation; CG: precipitate in the form of crystalline granules; amorphous insulin precipitation AP1: initial stage of aggregation; AP2: slightly aggregation; AP3: full aggregation.

* Measured from separate experiments without insulin.

supersaturation reached with human insulin was always higher than that for porcine insulin.

The direct consequence, as observed in comparative single drops, is that the nucleation density was always higher in experiments with human insulin. The lower solubility of human insulin is also reflected by the prevalence of aggregation in samples 4 (with acetone, pH 6.07) and 10 (without acetone, pH 5.87). In these two rows the final concentration of citrate buffer is the lowest among all the experiments indicating the relevant role of the pH on the crystallization of insulin. In the case of porcine insulin under identical conditions (samples 1 and 7, pH 6.07 and 5.87, respectively) most of the drops produced crystals. This can be understood considering that the final pH of porcine insulin is slightly higher, as already shown during the titration experiments (Figure 3). The solubility differences of porcine and human insulin are clearly illustrated in Figure 5 in which the output of low (A), medium (D) and high (H) protein concentration experiments are compared.

The role of acetone was also considered in this study due to its prevalence in many crystallization studies (see Table 2), at a concentration of 15% (v/v). At this concentration two different effects have been described by Vekilov and co-workers: the increase of insulin solubility as acetone concentration rises [14] and the increase of the step kinetic coefficient [12], i.e. higher growth rate as a direct consequence of higher acetone concentration. In our study, the use of acetone reduced the solubility of insulin regardless of the hormone source. At all tested protein concentrations, the

number of crystals was higher in the presence of acetone.

This effect is more pronounced in the case of human insulin. In Figure 6 we compared both proteins crystallized in the presence (3 and 6) and in the absence of acetone (8 and 11) while keeping constant the citrate buffer concentration at 35 mM. The observed increase of nucleation density cannot be directly related to the change of pH, 6.59 and 6.34 for samples 3-6 and 8-11, respectively, high enough to be out of the aggregation point detected during the titration experiments. It is also worth mentioning that crystals grown in the absence of acetone have higher propensity to show a higher amount of visible defects including rough faces (See picture H11 of Figure 6 as an example) which will need further investigation.

Finally, we compared the effect of the final pH of the solution, shown in Table 3, on the nucleation of porcine and human insulin. As we mentioned earlier, there was a critical point during the titration of insulin that lies beyond the isoelectric point of the protein (pI 5.30-5.35 as referenced by the suppliers), identified above pH 5.40 as the maximum flocculation point [24]. Accordingly, the closer to this pH value the lower the solubility of insulin in solution and the higher the nucleation density. Our observations are therefore in good agreement with the study of Wintersteiner and Abramson [24] that successfully explained the crystallization behaviour of insulin in the pH range 5.60-5.65 previously reported by Abel and co-workers [25].

However, as deduced from our results, this pH range, 5.60-5.65, is too close to the isoelectric point

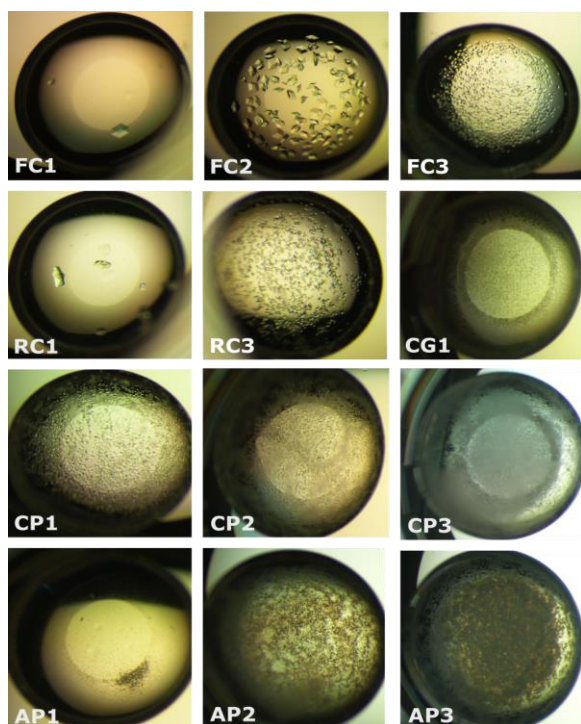


Fig. 4. Selected pictures of the crystallization events corresponding to the notation used in the text and Table 3, i.e. FC1 to FC3, and RC1 to RC3, corresponding to low and high number of crystal and rough crystals, respectively; CP1 to CP3 and AP1 to AP3 corresponding to light and heavy micro-particles and amorphous precipitated, respectively.

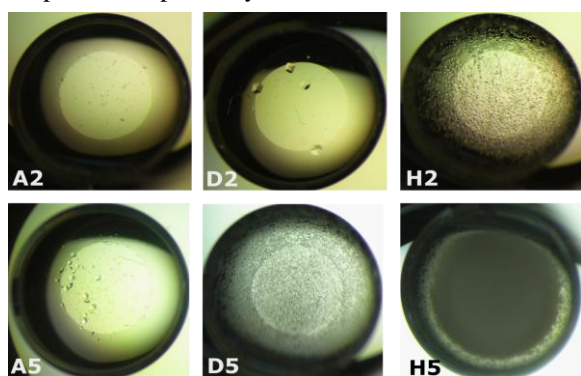


Fig. 5. Comparison between samples from the crystallization plate with porcine (A2 to H2) and human (A5 to H5) insulin concentration 1,0 (A), 4,0 (D) and 8,0 (H) mg/ml respectively.

to exert a reasonable control on the nucleation of insulin. In this line, human insulin seems to be more sensitive to pH changes than porcine insulin that, at this point, can only be attributed to a possible different composition of the lyophilized powder. This is clearly observed at the lowest pH used in this study, 5.87 (Table 3), for which human insulin is fully precipitated (samples 10) while porcine insulin still produces crystals (samples 7). This observation is confirmed in the presence of 15% (v/v) acetone, samples 1 and 4, for porcine and

human insulin, respectively, but enhanced due to the reduction of the solubility of insulin.

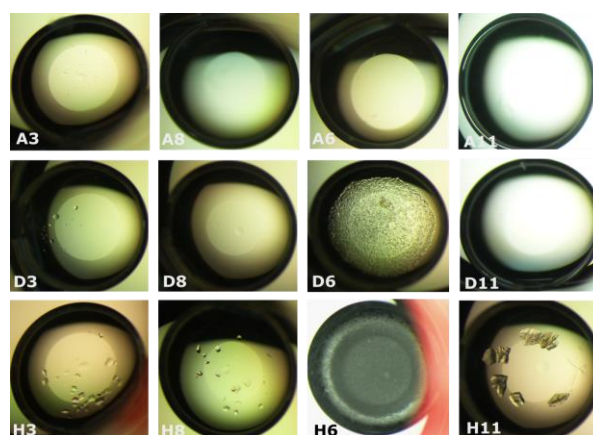


Fig. 6. Comparison of porcine (A3-H3 and A8-H8) and human (A6-H6 and A11-H11) insulin crystallized in the presence (numbers 3 and 6) and in the absence of acetone (numbers 8 and 11).

CONCLUSIONS

Crystallization of proteins is a multiparameter and multicomponent process in which the role of each precipitant-component is unknown. Applying a fixed volume-ratio procedure we have been able to study the main variables of the precipitant cocktail influencing the nucleation behavior of human and porcine insulin. We have identified the pH as the variable that exerts a fine control on the nucleation of insulin crystals. It has been demonstrated that acetone is not an essential additive for the crystallization of insulin although its presence reduced the solubility and facilitated the formation of well-faceted crystals. Porcine and human insulin showed, in general, similar crystallization behavior but with remarkable differences explained from their dissimilar titration behavior.

The formulation of the crystallizing insulin solution that has been used provides a complete picture of the nucleation behavior, it is useful for further fundamental studies and should be taken into consideration for the mass production of insulin crystals.

Acknowledgements. This research was funded by the projects "Science-Business" BG051PO001-3.3.05-0001 (FVH) and Short Term Scientific Mission (STSM) program of the COST initiative project CM1306-26833 (FVH), by the MICINN (Spain) projects BIO2010-16800 (JAG) and "Factoría Española de Cristalización" Consolider-Ingenio 2010 (JAG & MCM). FVH is thankful to the Laboratorio de Estudios Cristalográficos, IACT (CSIC-UGR) as receiving institution of the COST project.

REFERENCES

1. A. Chausmer, *J. Am. College Nutrition*, **17**, 109 (1998).
2. G. Dodson, D. Steiner, *Curr. Opinion Struct. Bio.*, **8**, 189 (1998).
3. I. Dimitrov, F. Hodzhaoglu, I. Ivanov, *Dissolution Technologies*, **11**, 11 (2011).
4. J. Brange, L. Langkjær, *Pharm. Biotechnol.*, **10**, 343 (1997).
5. D. Owens, B. Zinman, G. Bolli, *The Lancet*, **358**, 739 (2001).
6. R. Hilgenfeld, G. Seipke, H. Berchtold, D. R. Owens, *Drugs*, **74**, 911 (2014).
7. C. Nanev, I. Dimitrov, F. Hodzhaoglu, *Cryst. Res. Technol.*, **46**, 119 (2011).
8. M. Norrman, F. Hubalek, G. Schluckebier, *European Journal of Pharmaceutical Sciences*, **30**, 413 (2007).
9. C. Yip, M. Ward, *Biophysical Journal*, **71**, 1071 (1996).
10. C. Yip, M. Brader, M. DeFelippis, M. Ward, *Biophysical Journal*, **74**, 2199 (1998).
11. C. Yip, M. DeFelippis, B. Frank, M. Brader, M. Ward, *Biophysical Journal*, **75**, 1172 (1998).
12. I. Reviakine, D. Georgiou, P. Vekilov, *J. Am. Chem. Soc.*, **125**, 11684 (2003).
13. D. Georgiou, P. Vekilov, *PNAS*, **103**, 1681 (2006).
14. L. Bergeron, L. Filobelo, O. Galkin, P. Vekilov, *Biophysical Journal*, **85**, 3935 (2003).
15. J. Schlichtkrull, *Acta Chemica Scandinavica*, **10**, 1459 (1956).
16. J. Schlichtkrull, *Acta Chemica Scandinavica*, **10**, 1455 (1956).
17. J. Schlichtkrull, *Acta Chemica Scandinavica*, **11**, 439 (1957).
18. D. Waugh, D. Wilhelmson, S. Commerford, M. Sackler, *J. Am. Chem. Soc.*, **75**, 2592 (1953).
19. N. Pace, F. Vajdos, L. Fee, G. Grimsley, T. Gray, *Prot. Sci.*, **4**, 2411, (1995).
20. A. Penkova, I. Dimitrov, C. Nanev, *Ann. N. Y. Acad. Sci.*, 1027, 56 (2004).
21. C. Nanev, F. Hodzhaoglu, I. Dimitrov, *Crystal Growth & Design*, **11**, 196 (2011).
22. G. Christopher, A. Phipps, R. Gray, *Journal of Crystal Growth*, **191**, 820 (1998).
23. K. Waizumi, M. Plomp, W. van Enkevort, *Colloids and Surfaces B: Biointerfaces*, **30**, 73 (2003).
24. O. Wintersteiner, H. Abramson, *J. Biol. Chem.*, **99**, 741 (1933).
25. J. Abel, E. Geiling, C. Rouiller, F. Bell, O. Wintersteiner, *J. Pharmacol. and Exp. Therap.*, **31**, 65 (1927).

ОПТИМИЗАЦИЯ НА КЛАСИЧЕСКИЯ ПОДХОД ЗА ЗАРАЖДАНЕ И РАСТЕЖ НА РОМБОЕДРИЧНИ КРИСТАЛИ ОТ ИНСУЛИН ЧРЕЗ ПРОВЕЖДАНЕ НА рН ТИТРУВАНЕ И КРИСТАЛИЗАЦИОНЕН СКРИНИНГ

Ф. В. Ходжаоглу¹, М. Конехеро-Муриел², И. Л. Димитров¹, Х. А. Гавира²

¹Институт по физикохимия, Българска академия на науките, Секция: “Фазообразуване, кристални и аморфни материали”, ул. “Акад. Г. Бончев”, блок 11, 1113 София, Р. България

²Лаборатория за кристалографски изследвания, ул. “Авенида де лас Палмерас”, No 4, E-18100, Армила, Гранада, Испания

Постъпила на 8 септември, 2015 г. коригирана на 23 ноември, 2015 г.

(Резюме)

Осъществена е кристализация на инсулин в присъствие на цинкови йони под формата на хексамерни единици, които образуват ромбоедрични кристали, чрез постъпково титруване на разтворения инсулин в разрежена солна киселина с натриево цитратен буфер и ацетон. При смесване на разтворите се наблюдава характерна преципитация на инсулиновите молекули, поради преодоляване на критични стойности на рН в близост до изоелектричната точка на този белтъчен хормон. При последващо повишаване на рН на разтвора получените белтъчни агрегати се разтварят обратимо, като процеса е подпомогнат и от благоприятното въздействие на добавка от ацетон. В настоящата работа е изследвано влиянието на рН върху кристализацията на две търговски субстанции лиофилизиран инсулин: свински, изолиран от панкреас, и човешки рекомбинантен. Изследвана е агрегационната способност на тези субстанции чрез провеждане на паралелно рН титруване в рамките на използваната рецепта за кристализация. Осъществен е стриктен контрол на всички кристализационни компоненти по отношение на техните концентрации чрез използване на едни и същи обемни части на изходните разтвори. рН на кристализационните смеси е моделирано чрез фиксиране на количеството на солната киселина (0.02M HCl рН 1.55) и единствено вариране на количеството на използвания буфер (0.1M рН 6.98). Този подход допринася за финно оптимизиране и подбор на условията за получаване на инсулинови кристали в малки “batch”- кристализационни системи (20 μ L), както в присъствие, така и в отсъствие на ацетон. Скринингът е проведен в комерсиално 12x8 кристализационно плате. На базата на всички (96 бр.) наблюдавани проби са определени оптималните условия за получаване на добре остенени инсулинови кристали. Освен тях, под внимание са взети и всички останали комбинации за формиране на аморфни и кристални преципитати, кристални суспензии и финни инсулинови гранули, които в частност представляват интерес за фармацевтичната индустрия. Отчетени са и условията, при които добре остенените кристали се израждат в други форми или нарастват с груби дефекти.

Influence of the gold sub-layer on the catalytic properties of magnetron sputtered Pt and Ir thin films

E. Petkucheva^{1,*}, E. Lefterova¹, J. Heiss², U. Schnakenberg², E. Slavcheva¹

¹"Acad. Evgeni Budevski" Institute of Electrochemistry and Energy Systems, Bulgarian Academy of Sciences, Acad. G. Bonchev str., bl. 10, Sofia-1113, Bulgaria

²Institute of Materials in Electrical Engineering 1(IWE1), RWTH Aachen University, Sommerfeld str. 24, Aachen-52074, Germany

Submitted on July 13, 2015; Revised on October 29, 2015

Abstract: The paper presents a research on the influence of the gold sub-layer in composite magnetron sputtered Au-M (M = Pt, Ir) films on their catalytic activity toward the hydrogen evolution (HER), oxygen evolution (OER) and oxygen reduction (ORR) reactions in sulphuric acid solution. The test samples are deposited on glass substrates upon 25 nm thick adhesive titanium layer. The thickness of the underlying Au is 240 nm and that of the top functional metal (Pt or Ir) is 10 nm. The properties of the sputtered films are studied using X-ray diffraction (XRD), X-ray photoelectron spectroscopy (XPS), and electrochemical methods of cyclic voltammetry and quasi steady state polarization curves. The performed morphological and electrochemical investigations reveal that the specific catalytic efficiency of the composite Au-Pt and Au-Ir films is superior compared to that of the pure metals which allows for essential reduction of the catalytic loading at preserved performance.

Keywords: platinum; gold; iridium; iridium oxide; magnetron sputtering; bi-functional catalysts

1. INTRODUCTION

One of the key goals of catalyst manufacturing for hydrogen energy systems (fuel cells, water electrolyzers, and bi-functional reversible cells) is the development of new materials with improved cost efficiency. It is possible to design catalysts with enhanced activity and selectivity by alloying two or more metals [1, 2]. The bimetallic catalysts have demonstrated enhanced activity compared to the corresponding monometallic ones. They are extensively used in many catalytic and electrocatalytic applications [3].

One of the approaches to produce bimetallic surfaces is to replace either the sub-monolayer or the over-layer coverage of the single crystal with an ad-metal. The electronic and chemical properties of a metal in a bi-metallic surface may change due to two important factors - formation of hetero-atom bonds changing the electronic environment (ligand effect) and change in the orbitals overlap affecting the geometry of the bimetallic surface (strain effect). Both factors lead to shift in the surface d-band, resulting in decrease or increase of the adsorbate binding energy [4, 5, 6, 7, 8, 9]. Sinfelt and Rodriguez [4, 7] have shown how two metals interacting on a surface can form compounds with structures not seen in the bulk alloys. By

experimental and density functional theory (DFT) modeling it has been found that the monolayer ad-metal can interact with the host metal substrate by: i) occupying the top-most surface sites to produce a surface monolayer; ii) diffusing into the subsurface region to form the subsurface monolayer; and iii) alloying with surface to produce inter-mixed bimetallic surfaces. DFT modeling results have indicated that the modification on the surface d-band center is significantly different for the three types of bimetallic structures [1, 2, 3, 10].

Since the surface catalyzed reactions are extremely sensitive to the atomic-level details, the choice of the method for preparation of smooth thin layers with good mechanical strength is essential for tuning of the catalytic activity and utilization. Usually the catalysts are powders consisting of metal nanoparticles deposited on catalytic support with high surface area. There are various catalyst preparation techniques such as wet chemical reduction, sol-gel, thermal decomposition of metal salts, electrochemical deposition, underpotential deposition etc. [11-22]. The choice of the method depends also on several strict criteria such as efficiency, reproducibility, time consumption, cost as well as the technological availability in regard to the application. In the last decade the method of plasma enhanced physical vapour deposition (PVD), also called direct current magnetron sputtering (DCMS), has been introduced as an

*To whom all correspondence should be sent:
E-mail: elitsapetkucheva@gmail.com

alternative of the classical methods for catalysts preparation [23, 24]. The magnetron sputtered catalysts are deposited as thin compact (mono, bi- or poly-metallic and/or oxide) films upon selected substrate materials and could have extremely low precisely controlled metal loading [25-27].

Platinum is the best known pure metal catalyst for hydrogen evolution (HER), hydrogen oxidation (HOR), and oxygen reduction (ORR) reactions, while it is not so efficient with respect to the oxygen evolution (OER). In order to increase the catalytic activity and reduce the cost of catalysis Pt is often alloyed with cheaper metals from the transition series such as Ni, Co, Fe and etc. or with other noble metals (Ru, Ir, Os) which improve not only the efficiency but also the stability of the composite catalysts [16, 19, 20, 21, 27, 28]. The most commonly studied catalysts for OER are Ir, IrO_x, RuO_x [29-31].

This work concerns the preparation of thin composite catalytic films in which an essential part of the efficient but expensive Pt and Ir is substituted by dense Au sub-layer using the method of magnetron sputtering and investigates the influence of the Au sub-layer on the catalytic activity toward the partial electrode reactions proceeding in sulphuric acid solution.

2. EXPERIMENTAL

2.1 Formation of the catalytic layers

Five different test samples are sputtered using a magnetron sputtering machine Nordiko 2550, equipped with 3 targets of high purity (99.999%) metals. The functional catalytic films are deposited on glass substrate upon 25 nm thick Ti sub-layer serving as an adhesion promoter. Three of the test samples are pure metals - Pt, Au, and Ir. Pt and Ir are deposited at previously optimized sputtering conditions ensuring high porosity (resp. high active surface per unit geometric area) combined with good mechanical stability of the films [27, 32]. The Au deposition at this stage is not optimized and the film is much denser. The composite Au-M catalysts consisting of two consecutive functional layers sputtered at conditions identical to those used for the single films. The total thickness of all samples is fixed to 250 nm as the top M-layer is 10 nm thick.

2.2 Test procedure

Physical characterization. The surface structure and morphology of the sputtered catalysts are studied by X-ray diffraction (XRD) and X-ray photoelectron spectroscopy (XPS). The diffraction data are collected using X-ray diffractometer Philips ADP15 with Cu-K α ($\lambda=1.54178$ Å)

radiation at a constant rate of 0.2⁰.s⁻¹ over an angle range 2 Θ =10-90⁰. The XPS spectra are recorded with ESCALAB MK II (VG Scientific, England) electron spectrometer. The photoelectrons are excited with twin anode X-ray source using Al K α ($h\nu = 1253.6$ eV) radiations.

Electrochemical tests. The electrochemical characterization of the sputtered Au-M films is performed in Ar-saturated 0.5M H₂SO₄ at room temperature by conventional electrochemical techniques of cycling voltammetry and quasi-steady state polarization curves. The cyclic voltammograms (CV) are recorded in the potential range between hydrogen and oxygen evolution at temperature of 20 °C and scan rate of 100 mV s⁻¹. The quasi steady state polarization tests are carried out in a potentiodynamic mode with scan rate of 1 mV s⁻¹. The experiments are performed with Galvanostat/Potentiostat POS 2 (Bank Elektronik, Germany) in a standard three electrode electrochemical cell using Ag/AgCl reference electrode and Pt-wire as counter electrode. The working area of the test electrodes is 0.5 cm².

3. RESULTS AND DISCUSSION

3.1 Surface analysis

The XRD spectra of the films are presented in Figure 1. The patterns of Au, Au-Pt and Au-Ir films show poly-crystalline structure of all metals with preferential [111] orientation which is more characteristic for Au. On the spectrum of the multi-layered catalysts, alloying is not registered.

The chemical state of the sputtered films is examined by XPS analysis. The high resolution Au4f-Pt4f and Au4f-Ir4f photoelectron spectra are presented in Figure 2 (a,b). The peak analysis and the performed fitting procedure indicate that Au, Pt and Ir present as pure metals (the registered amount of oxides on the Pt and Ir surface is negligible). The Pt4f peak is clearly seen in the spectrum of the Au-Pt (Figure 2a). It is situated at binding energy 71.5 eV. The Au4f peak is also well recognized. For the pure Au it is situated at 83.3 eV, while for the Au-Pt sample its position is at 84.3 eV. Berg at al. [33] have performed high-resolution photoelectron spectroscopy measurements of Au over-layers on Pt (100) surfaces and have found contributions to the Au 4f7/2core level spectrum from Au atoms in four different local environments in the surface: Au atoms at the Pt interface (83.32 \pm 0.02eV), surface Au atoms with (1 \times 1) symmetry (83.50 \pm 0.02eV), surface Au atoms with a (1 \times 7) symmetry (83.63 \pm 0.02eV), and bulk-like Au atoms at (83.87 \pm 0.02) eV. In our case the observed essential shift in the Au 4f7/2core level spectrum of the Au-

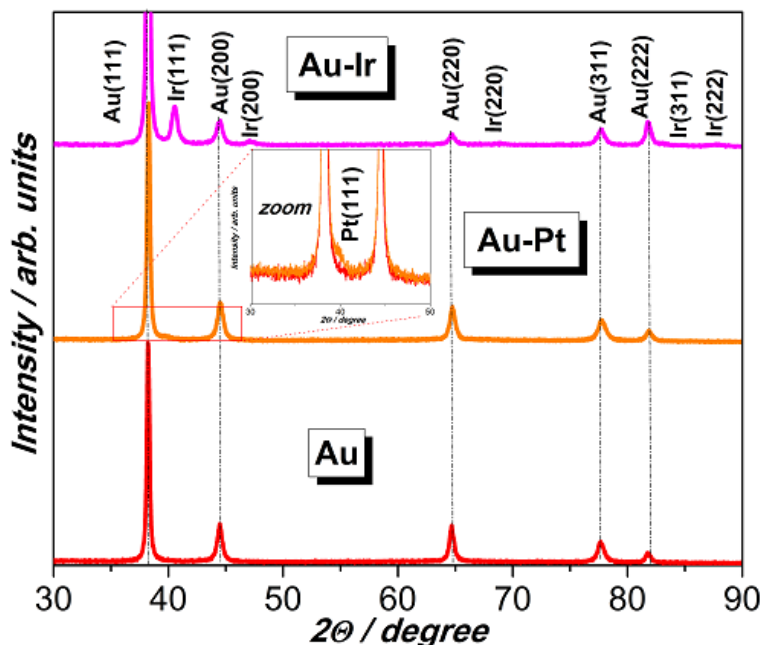


Figure 1. XRD spectra of the Au, Au-Pt and Au-Ir catalytic films.

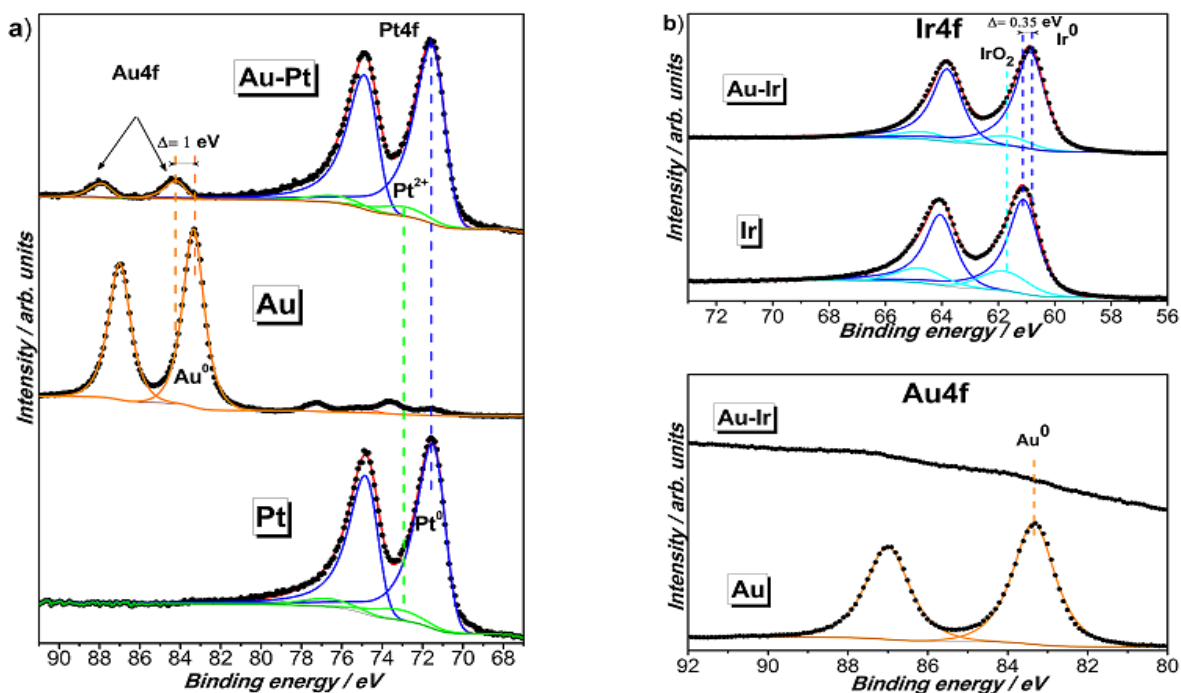


Figure 2. High resolution Au4f-Pt4f (a) and Au4f- Ir4f (b) photoelectron spectra of the sputtered catalytic films

Pt film to higher binding energy implies formation of Au-Pt interlayer on the Au-Pt boundary.

In the XPS spectra of Ir and Au-Ir (Figure 2b) the Ir4f peak is well recognized. At the same time the Au4f peak is only slightly hinted which most probably is due to the morphology of the functional top layer.

The Ir4f peak for the pure Ir is situated at 61.19 eV, while for the Au-Ir sample it is shifted in negative direction (60.75 eV). The reasons for the registered differences in the binding energy changes of both systems (Au-Pt and Au-Ir) are not

very clear and should be further investigated. For instance the morphology and/or density of the top functional layer could have an influence.

3.2 Electrochemical measurements

The obtained cyclic voltammograms of the catalysts under study are presented in Figures 3 (a,b) for the systems containing Pt and Ir, respectively. Figure 3a shows the effect of the partial substitution of Pt by Au. On the Pt and Au CV curves the characteristic curve peaks typical for the pure metals are clearly depicted – hydrogen

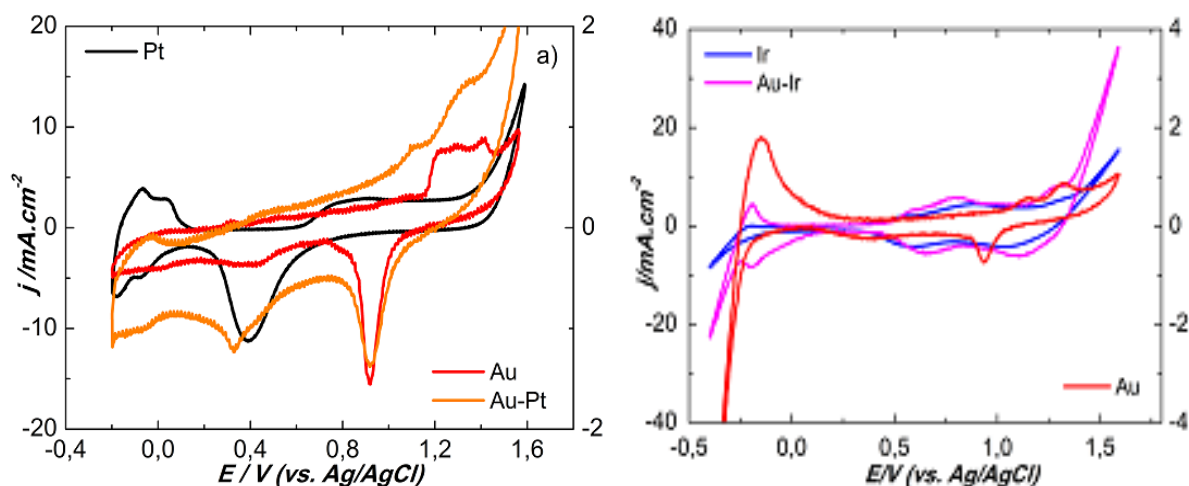


Figure 3 Cyclic voltammograms of Au-Pt (a) and Au-Ir (b) in 0.5M H₂SO₄; potential ranges (a) -0.2 to 1.6 V and (b) -0.4 to 1.6 V; scan rate 100 mV.s⁻¹.

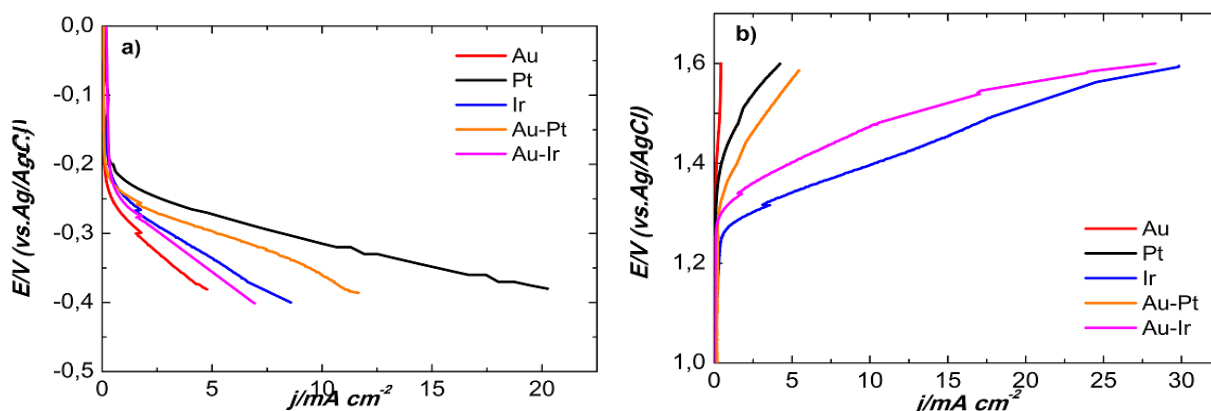


Figure 4. Quasi-steady state polarization curves - HER (a) and OER (b) of the sputtered catalytic films in 0.5M H₂SO₄; scan rate 1 mV.s⁻¹.

adsorption/desorption on Pt (0.0 to - 0.4V), formation/desorption of oxygen coverage on both metals (> 0.65V), and oxygen reduction (around 0.4V and 0.9V, respectively). The Au-Pt CVs show that the deposition of 10 nm Pt on the top of 240 nm Au layer results in a rather complex cyclic voltammogram. All current peaks characteristic both for Au and Pt are well recognized. Particularly clear are the oxygen reduction peaks situated at 0.9 V and 0.4 V. Figure 3b illustrates the effect of partial substitution of Ir layer by Au. The CV curve of the pure iridium shows all characteristic current peaks resulting from reversible changes in Ir valent state: from metallic iridium to iridium in second, third and fourth oxidation state Ir/Ir²⁺ (0.50 to 0.63 V), Ir²⁺/Ir³⁺(0.63 to 0.92 V), Ir³⁺/ Ir⁴⁺(1.16 to 1.34 V). The CV curve of the composite Au-Ir sample is identical in shape. The reversible current peaks are slightly smaller, while the oxygen evolution starts a bit earlier and is more intensive.

To evaluate the catalytic efficiency of the sputtered composite films toward the proceeding

partial electrode reactions, quasi steady state polarization curves are recorded.

Figure 4 (a,b) shows the hydrogen evolution (HER) and oxygen evolution (OER) reactions. As expected, the HER is most intensive on the pure Pt film. The next best catalyst is the composite Au-Pt. It should be stressed out that the Pt content in both samples is very different (the platinum content in the “pure” platinum film is 25 times less than that in the gold-platinum film). Since Pt is much more expensive than Au, the cost efficiency of the catalysis in the case of Au-Pt is strongly improved. Ir and Au-Ir catalysts are less active to HER compared to both Pt-containing samples as the reaction rate is not proportional to the thickness of the top iridium film.

The OER reaction is most intensive on the pure Ir film which facilitates the oxygen evolution stronger than Au-Ir. However, the difference in the reaction rate on both samples is much lower than the difference in the thickness of the functional iridium layer (250 to 10 nm). On the other hand, the

composite Au-Pt sample demonstrates higher catalytic efficiency toward the oxygen evolution compare to pure Pt, despite the difference in the Pt loading, implying strong synergetic effects between both metals. This assumption is supported by the XPS analysis (Figure 2a).

It is well known that Pt is a very active catalyst toward the ORR. The quasi steady state cathodic polarization curves of the pure Pt and Au-Pt recorded in the potential range where ORR takes place are presented in Figure 5. The achieved current densities and the values of the Tafel slopes are summarized in Table 1. They show some catalytic activity of Au-Pt and indicate different mechanism of the reaction compared to that on the pure Pt, which is in accordance with the results from the CV curves. In order to investigate the mechanism of ORR and to find out if Au-Pt could be used as a bi-functional reversible oxygen electrode catalyst, further experiments on RDE are currently in progress.

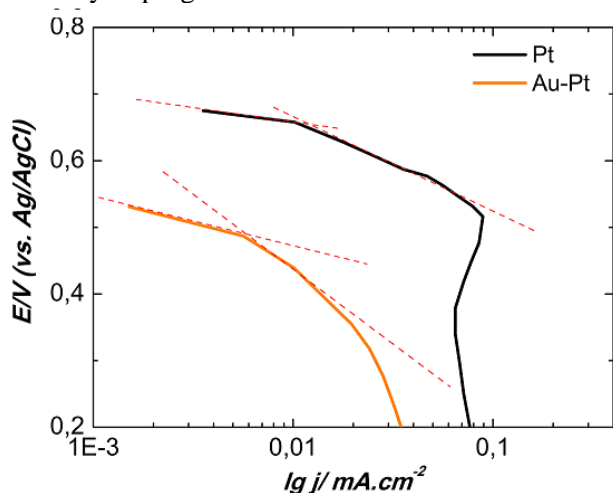


Figure 5 Quasi steady state polarization curves of ORR of the sputtered catalytic films in 0.5M H₂SO₄; scan rate 1 mV.s⁻¹.

To distinguish better the effect of the Au sub-layer on both systems performance, in Table 1 are given also the values of the reaction rates for HER and OER at constant potentials, presented in current

density and in specific activity (normalized to the thickness of the top functional layer). It is seen that there is no linearity between the thickness and the specific activity, which confirms the assumption for existence of synergism in the composite catalytic films. This is more clearly demonstrated in the case of Au-Pt.

4. CONCLUSIONS

The research performed proved that the method of DCMS can be used as precise technique for deposition of multi-layered catalysts with controlled thickness and tailored synergetic effects between the components. It was shown that the partial substitution of platinum and iridium by gold improves the specific activity and reveals possibilities for better utilization of the Pt and Ir catalysts and thus, for reduction of catalytic loading.

The polarization measurements showed an improved HER and OER activity of the Au-Pt films compared to pure Pt as well as an indication that it could behave as a bi-functional oxygen electrode for both ORR and OER.

The observed changes in the electrochemical performance of the composite films allow to assume a synergy between both metals, which is stronger in the case of Au-Pt. The synergetic effect is explained with formation of interfacial bimetallic layers and electronic interactions, confirmed by the registered shift in the binding of the metallic components. How exactly the BE shift affects the mechanism of the proceeding electrode reactions needs to be cleared in the ongoing research. The possibilities to enhance the observed synergetic effects by optimization of the layers order, number, and thickness will be also explored.

Acknowledgments. The research has been supported by NSF, Bulgarian Ministry of Education and Science, project DNTS 01/005.

Table 1. Catalytic activity of the sputtered films.

Catalytic Films	Hydrogen Evolution Reaction (HER) E= -0.35 V		Oxygen Evolution Reaction (OER) E= 1.6 V		Oxygen Reduction Reaction (ORR)	
	j/mA.cm ⁻²	js/mA.cm ⁻² .nm ⁻¹ Pt or Ir	j/mA.cm ⁻²	js/mA.cm ⁻² .nm ⁻¹ Pt or Ir	Tafel Slopes/ mV.dec ⁻¹	
					b1	b2
Pt	15.16	0.060	4.27	0.017	42	145
Au-Pt	9.30	0.930	5.82	0.582	77	223
Ir	5.65	0.023	29.9	0.120	-	-
Au-Ir	4.67	0.467	28.6	2.86	-	-

REFERENCES

1. S. R. Calvo, P. B. Balbuena, *Surf Sci*, **601**, 165 (2007)
2. D. H. Mei, E. W. Hansen, M. Neurock, *J Phys Chem B*, **107**, 798 (2003)
3. S. Linic, J. Jankowiak, M.A. Barteau *J. Catal.*, **224**, 489 (2004)
4. J. H. Sinfelt, *John Wiley and Sons*, New York, (1983)
5. J. G. Chen, C. A. Menning, M. B. Zellner, *Surf Sci Reports*, **63**, 201 (2008)
6. C. T. Campbell, *Annual Review of Physical Chemistry*, **4**, 775 (1990)
7. J. A. Rodriguez, D. W. Goodman, *J. Phys. Chem.*, **95**, 4196 (1991)
8. B. Hammer, J.K. Nørskov, *Advances in Catalysis*, **45**, 71 (2000)
9. J. R. Kitchin, J.K Nørskov, J.G. Chen, M.A Barteau *J Chem Phys*, **120**, 10240 (2004)
10. Mavrikakis M, Hammer B, Nørskov JK, *Phys Rev Lett*, **81**, 2819 (1998)
11. E. Antolini, J. R. C. Salgado, M. J. Giz, E.R. Gonzalez, *Int. J. Hydrogen Energy*, **30**, 1213 (2005)
12. S. Dsoke, A. Moretti, G. Giuli, R. Marassi, *Int. J. Hydrogen Energy*, **36**, 8098 (2011)
13. T. Nishimura, T. Morikawa, M. Yokoi, C. Iwakura, H. Inoue, *Electrochim. Acta*, **54**, 499 (2008)
14. H.R. Colon-Mercado, B.N. Popov, *J Power Sources*, **155**, 253 (2006)
15. R.R. Adzic, J. Zhang, K. Sasaki, M.B. Vukmirovic, M. Shao, J.X. Wang, et al., *Top Catal.*, **46**, 249 (2007)
16. F. Kadirgan, A.M. Kannan, T. Atilan, S. Beyhan, S.S. Ozenler, S. Suzer, et al., *Int J Hydrogen Energy*, **34**, 9450 (2009)
17. M. B. Vukmirovic, J. Zhang, K. Sasaki, A. U. Nilekar, F. Uribe, M. Mavrikakis, et al., *Electrochim Acta*, **52**, 2257 (2007)
18. E. B. Fox, H. Colon-Mercado, *Int J Hydrogen Energy*, **35**, 3280 (2010)
19. S. Dsoke, A. Moretti, G. Giuli, R. Marassi, *Int J Hydrogen Energy*, **36**, 8098 (2011)
20. M. Khosravi, M. K. Amini, *Int J Hydrogen Energy*, **35**, 10527 (2010)
21. Z.-M. Zhou, Z.-G. Shao, X.-P. Qin, X.-G. Chen, Z.-D. Wei, B.-L. Yi, *Int J Hydrogen Energy*, **35**, 1719 (2010)
22. S. M. S. Kumar, N. Hidyatai, J. S. Herrero, S. Irusta, K. Scott, *Int J Hydrogen Energy*, **36**, 5453 (2011)
23. M.D. Maciá, J.M. Campiña, E. Herrero, J.M. Feliu, *J. Electroanal. Chem.*, **564**, 141 (2004)
24. H.A. Gasteiger, S.S. Kocha, B. Sompalli, F.T. Wagner, *Appl. Catal. B-environ*, **56**, 9 (2005)
25. K.-L.Huang, Y.-C. Lai, C.-H. Tsai, *J Power Sources*, **15**, 224 (2006)
26. E.Slavcheva, I. Radev, G. Topalov, E. Budevski, *Electrochim Acta*, **53**, 362 (2007)
27. G. Topalov, G. Ganske, E. Lefterova, U. Schnakenberg, E. Slavcheva, *Int J Hydrogen Energy*, **36**, 15437 (2011)
28. J. Zhang, K. Sasaki, E. Sutter, R. R. Adzic, *Science*, **315**, 220 (2007)
29. R. S. Yeo, J. Orehotsky, W. Visscher and S. Srinivasan, *Electrochem. Soc.*, **128**,1900 (1981)
30. M. E. G. Lyons, S. Floqueta, *Phys. Chem. Chem. Phys.*, **13**, 5314 (2011)
31. L. Maa, S. Suib, Y. Zhaia, *J Power Sources*, **177** (2), 470 (2008)
32. E. Slavcheva, G. Ganske, G. Topalov, W. Mokwa, U. Schnakenberg, *Appl Surf Sci.*, **255**, 6479 (2009)
33. C. Berg, H. J. Venvik, F. Strisland, A. Ramstad, A. Borg, *Surface Science*, **409**, 1 (1988)

ВЛИЯНИЕ НА ПОДСЛОЙ ОТ ЗЛАТО ВЪРХУ КАТАЛИТИЧНИТЕ СВОЙСТВА НА ТЪНКИ МАГНЕТРОННО РАЗПРАШЕНИ ФИЛМИ ОТ Pt И Ir

Е.Петкучева^{1,*}, Е. Лефтерова¹, Й. Хайс², У. Шнакенберг², Е. Славчева¹

¹Институт по електрохимия и енергийни системи „Акад. Евгени Бudevски“, Българска академия на науките, ул.Акад. Г. Бончев бл. 10, София 1113, България

²Институт по материали за електротехниката 1(ИМЕ1), Технически университет Аахен, ул. Зомерфелд 24, Аахен-52074, Германия

Постъпила на 13 юли, 2015 г. коригирана на 29 октомври, 2015 г.

(Резюме)

Статията представя изследване на влиянието на златен подслой върху каталитичната активност на магнетронно разпрасени филми Au-M (M = Pt и Ir) спрямо парциалните електродни реакции на отделяне на водород (HER), отделяне (OER) и редукция (ORR) на кислород, протичащи в кисели водни електролити на сярна киселина. Филмите от Au-Pt и Au-Ir са отложени върху стъклена подложка, покрита със адхезивен слой от 25 nm Ti. Дебелината на всички проби е 250 nm – слой от 240 nm Au, върху който е отложен 10 nm функционален слой Pt или Ir. Свойствата на получените филми са изследвани чрез рентгеноструктурен анализ (XRD), рентгенова фотоелектронна спектроскопия (XPS), и електрохимичните методи – циклична волтаметрия и поляризационни криви. От проведените морфологични и електрохимични изследвания е установено значително увеличение на специфичната каталитичната активност на биметалните филми Au-Pt и Au-Ir, което позволява да се намали каталитичното натоварване като се запази ефективността на процеса.

A new method for synthesis of a new class reducing agent with expected application in nanotechnology

Ivan V. Slivkov^{1†}, Dimitar L. Lyutov^{2, *}, Zornitsa Pl. Pancheva¹, Lyudmil G. Lyutov¹

¹Faculty of Chemistry and Pharmacy, Sofia University, Blvd James Bouchier, 1, 1164 Sofia, Bulgaria

²Faculty of Physics, Sofia University, Blvd James Bouchier, 5, 1164 Sofia, Bulgaria

Submitted on July 31, 2015; Revised on December 2, 2015

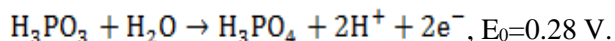
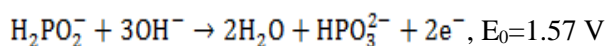
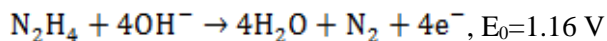
Abstract: It is of great importance for the monodispersion of nanomaterials to limit the nucleation in the initial stages of the synthesis, which is then followed by growth without new nucleation. A reducing agent, corresponding to these conditions, is the hydrazine bisphosphite $N_2H_6(H_2PO_2)_2$. There is no data about this compound, but related substances have long since been studied.

In this article a new synthesizing method of $N_2H_6(H_2PO_2)_2$ using $N_2H_4 \cdot 2HCl$ and $Na_2H_2PO_2 \cdot H_2O$ is proposed. The lateral sodium chloride $NaCl$ serves to later determine the degree of conversion and the yield of the target product.

Keywords: synthesis; new reducing agent; monodispersed particles; hydrazine (bis) hypophosphite

1. INTRODUCTION

It is of great importance to obtain monodispersed nanomaterials in nanotechnology. One way to achieve this goal is to limit the nucleation in the initial stages of the synthesis, which is followed by growth without new nucleation. A reducing agent, which is expected to fulfill these requirements, is the hydrazine (bis) hypophosphite $N_2H_6(H_2PO_2)_2$. Hydrazine (bis) hypophosphite is assumed to be able to act as reducer by both of its parts – anion and cation:



This means that a higher reduction potential in the beginning and an average reduction potential in the end of a process, based on the degree of reduction, can be achieved. That is a good prerequisite for controlling the supersaturation and the speed of separate stages during the process. Moreover, consumption of reducing agent in the course of time of nucleation, significantly decreases its concentration, reduction potential and supersaturation - Figure 1[1].

As the reducing agent is being consumed during the process of nucleation the supersaturation also decreases in areas I and II. Therefore, time of nucleation process is very short, and practically finishes. Afterwards a process of growth prevails

and nucleation is suppressed. As a result, monodispersed material can be obtained. This could happen if two-stage reducer is used which has significant difference of reduction potentials in both stages.

However, to the best of our knowledge there is not a study dealing with synthesis and properties of such a compound, even though the existence of this composite is predictable. We are aware of the existence of common compounds with similar anion parts, such as $NH_4H_2PO_2$, $(NH_3OH^+)(H_2PO_2^-)_2$, and a similar cation part – $N_2H_5H_2PO_4$ and $N_2H_6(H_2PO_4)_2$ [2, 3], but information on the synthesis and properties of $N_2H_6(H_2PO_2)_2$ is not available.

Currently known method of synthesis, developed by us [4] in the past and we have encountered some difficulties. The precursor compounds are difficult to access and are dangerous. The interaction between them releases a lot of heat and toxic fumes. In this work we propose a new method for synthesis of $N_2H_6(H_2PO_2)_2$ by using $N_2H_4 \cdot 2HCl$ and $Na_2H_2PO_2 \cdot H_2O$. The quantity of the co-product sodium chloride $NaCl$ serves to determine the degree of conversion and the yield of the target product. Potential applications of hydrazine (bis) hypophosphite for preparation of silver micro- and nano-particles will be examined according to aforementioned premises.

*To whom all correspondence should be sent:

E-mail: d_lyutov@phys.uni-sofia.bg

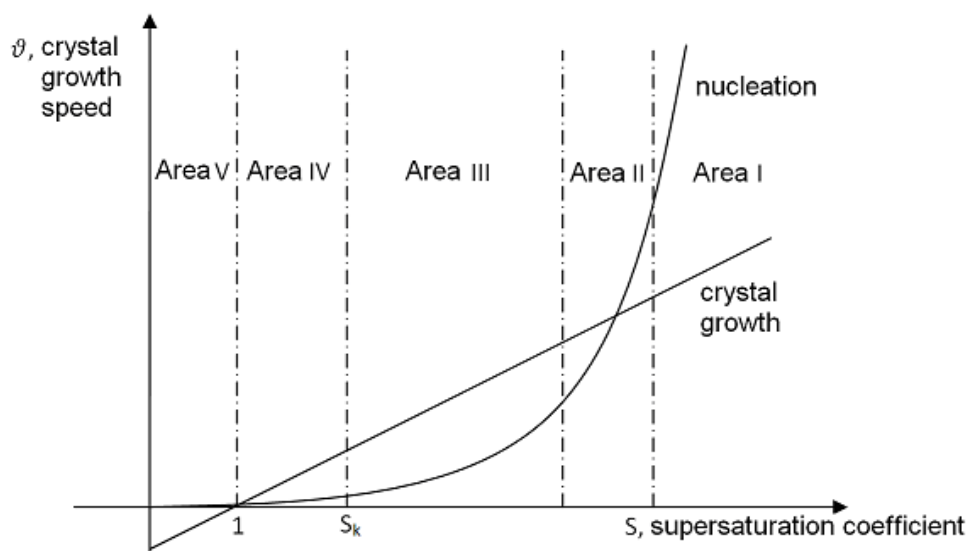


Figure 1. Speed of nucleation and crystal growth depending on supersaturation.

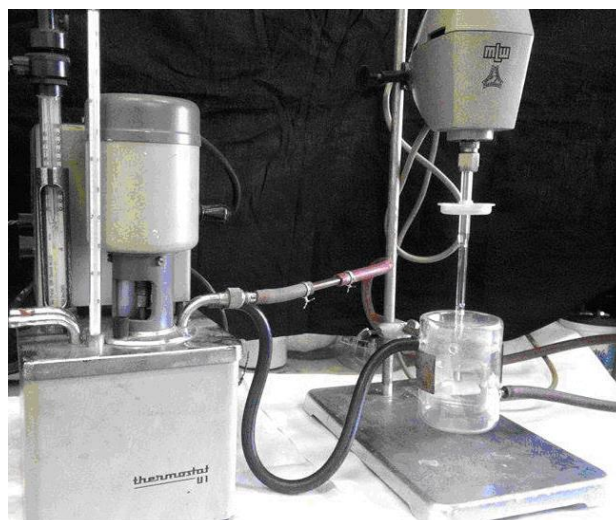


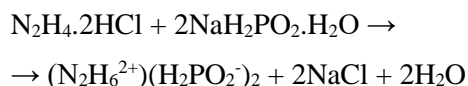
Figure 2. Cooling apparatus during synthesis.

2. EXPERIMENTAL

2.1. Materials, reagents and technical equipment

Hydrazine dihydrochloride $\text{N}_2\text{H}_4 \cdot 2\text{HCl}$ (CAS Number: 5341-61-7) and sodium hypophosphite monohydrate $\text{NaH}_2\text{PO}_2 \cdot \text{H}_2\text{O}$ (CAS Number: 10039-56-2) are the compounds used for synthesis of the new reducing agent.

2.2. Synthesis procedure



Hydrazine dihydrochloride $\text{N}_2\text{H}_4 \cdot 2\text{HCl}$ and sodium hypophosphite monohydrate $\text{NaH}_2\text{PO}_2 \cdot \text{H}_2\text{O}$ are weighed in a stoichiometric proportion and crushed to a very fine grade in a mortar. The received mixture is poured in a beaker and hypophosphorous acid (50% water solution) is

added, in order to acidify the solution. Meanwhile the water, contained in the acid, the solution becomes undersaturated for $(\text{N}_2\text{H}_6)(\text{H}_2\text{PO}_2)_2$ and oversaturated for NaCl, so the latter can crystallize from the solution. The mixture is stirred and heated until the complete dissolution of the solid phase. The crystallization of white NaCl can be observed immediately, whose crystals are difficult to be distinguished from the starting material. The suspension is dried in a vacuum desiccator dish, so highest possible quantity of NaCl could crystallize. After that the suspension is filtrated in a fritted filter and the sediment is washed in distilled water and ethyl alcohol, as NaCl's solubility in a water-alcohol solution sharply decreases. The filtrate is continuously stirred for about 12 hours under cooling (Figure 2), in order to get small and similarly-sized crystals of $(\text{N}_2\text{H}_6)(\text{H}_2\text{PO}_2)_2$, and not large crystals of it. The solution along with the crystals is filtered with a fritted filter and the

experimental yield is determined. The lateral NaCl is checked for chloride ions with AgNO₃. White photosensitive sediment of AgCl is observed, which proves that the separated crystals are NaCl. This, on its own, proves that in the solution remains the target product.

Based on the described method we calculated the necessary quantities of starting materials for the synthesis of 100 g product as follows: 64.00 g N₂H₄·2HCl and 124.29 g NaH₂PO₂·H₂O. For the acidification of the solution and the supersaturation by the target product were needed 157.2 ml H₃PO₂, which is calculated based on the solubility of N₂H₆(H₂PO₂)₂. As a result of the synthesis we gained 58.13 g NaCl and 56.7 g N₂H₆(H₂PO₂)₂. That shows that this method of synthesis leads to approximate yield of about 56.7%.

The previously known method of synthesis does not show exact quantitative data for the degree of conversion of the starting materials. They are difficult to determine, as hydrazine hydrate is a volatile liquid, and the vacuum-vaporization is not always complete. During vacuum-vaporization the temperature must not exceed 40-50 °C, because this may destroy the product and the initial compounds as well. On the other hand, the lack of byproducts is a prerequisite for higher purity of the target product.

By using the new method, dry starting materials, following vacuum-vaporization is not necessary and the reaction takes place without a noticeable enthalpy of formation. The extraction of lateral NaCl allows the potential determination of the yield of the products. Also, this synthesis method is safer. The difficult separation of the byproduct may cause impurity in the target product.

The choice of one of these methods may be determined by the pursued purity of the target product and the availability of initial compounds. This way it will be possible to make an easier assessment which of the two methods would be

preferred for a primary method of synthesis based on the concrete abilities of the laboratory and the team.

2.3. Methods used to identify new compound

The elemental analysis was carried out by using an elemental analyzer VARIO EL III “Elementer” Germany; pH measurements were done by using a precise digital pH-meter OP208-1 “Radelkis”-Budapest, Hungary with combined electrode HA 405-60/S7 WTW GmbH -Weilheim, Germany. The elemental analysis of crystals, give composition values very close to expected for (N₂H₆)²⁺(H₂PO₂)₂. Opposite to our expectations, we could not obtain specimen which shows elemental composition values comparable with (N₂H₅)⁺H₂PO₂⁻ at any change in acidity.

3. RESULTS AND DISCUSSION

The advantages and disadvantages of both methods developed by us could be compared as follows (Table 1).

3.1. Efficiency of the new reducing agent

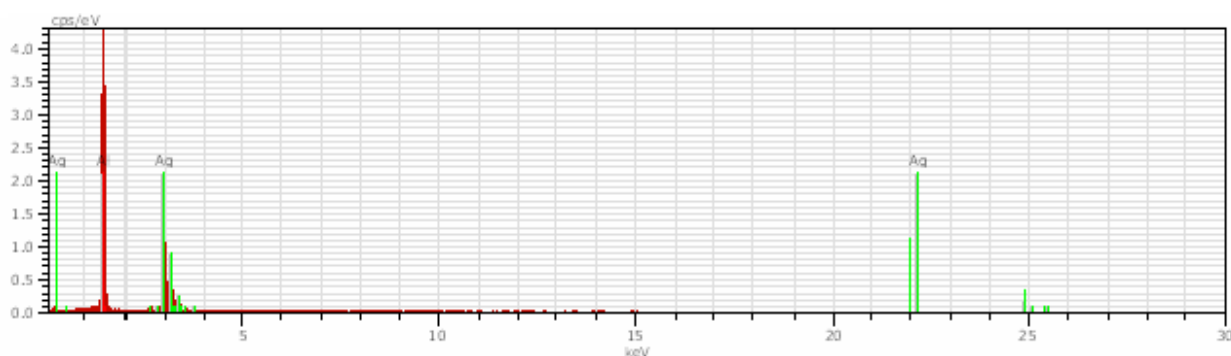
Reducing efficiency of hydrazine (bis) hypophosphite is extremely high: Reducing power of one mole of substance is 12 equivalents. (One mole of compound gives 12 N_A electrons!)

3.2. Application of the new reducing agent for synthesis of Ag nanoparticles

3.2.1. Methods used to characterize Ag nanoparticles. The received reducing agent was used for the synthesis of silver particles from AgNO₃ solution by the following procedure: polycrystalline material of the product was dissolved in distilled water and was mixed with a solution of silver nitrate under constant stirring. The obtained silver particles were washed thoroughly three times with bi-distilled water and centrifuged in-between. Dual beam scanning electron/focused ion beam system (SEM/FIB LYRA I XMU, TESCAN), equipped

Table 1. Comparison between the two methods.

	Earlier method [4]	Method in the present study
Safety measures	It is required to outlet the toxic vapors of hydrazine and to monitor temperature	Safe; the enthalpy of formation is insignificant
Determination of yield	Difficult	Relatively easy
Accessibility of compounds	Limited	High
Purity	High	Average



Acquisition 4652

Date:7/24/2015 3:48:54 PM

HV:30.0kV

Puls th.:0.95kcps

E1	AN	Series	unn. C [wt.%]	norm. C [wt.%]	Atom. C [at.%]	Error [%]
Al	13	K-series	42.32	47.47	78.32	2.2
Ag	47	L-series	46.83	52.53	21.68	1.7
Total:			89.15	100.00	100.00	

Figure 4. Elemental analysis data.

with EDX detector (Quantax 200, Bruker) is used to determine the size, shape and composition of the obtained Ag nano-particles.

SEM analysis was done in order to determine the qualitative composition and the approximate size of the particles. The EDX analysis (Figures 3 and 4) shows that the material which they were made of is silver.

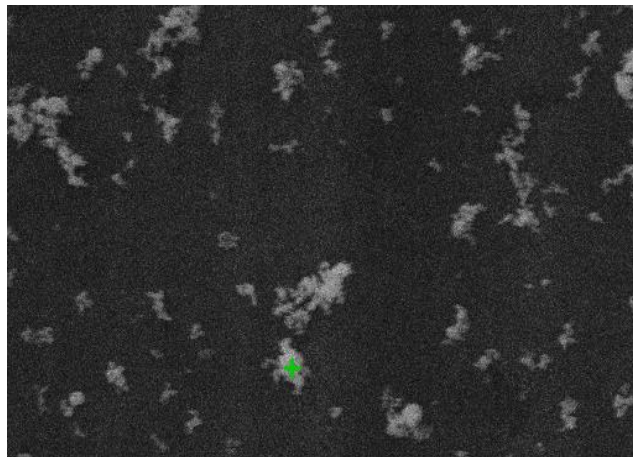


Figure 3. SEM map; the green point relates to the area of the EDX analysis.

The presence of Al is due to the fact that the signal of EDX cannot be received from a very small area. The resolution of the EDX analysis is approximately 1 μm . Since the pad is aluminum foil, we observe Al presence in the result.

Figure 5 shows approximately the monodispersed size of the particles. This trend

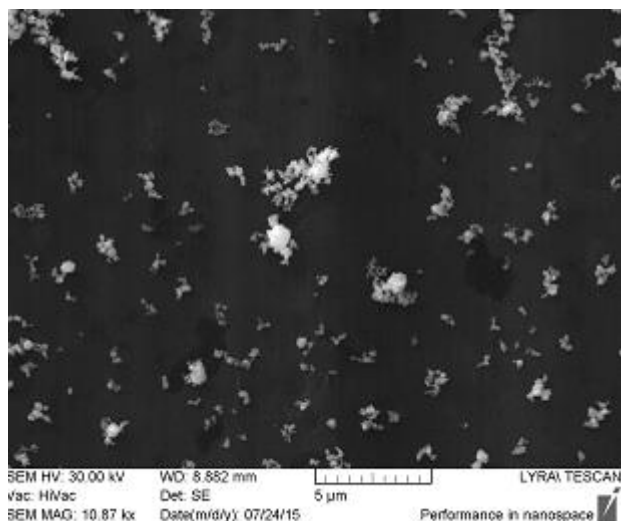
remains, even with a different particle concentration. A large portion of particle conglomerates have probably formed during the evaporation of the suspension, which is part of preparing the sample for analysis.

The monodisperse characteristics of the particles confirm the proposed theoretical formulation. The goal of the current study was precisely that – to support the given propositions and conclude upon the application of the new material based on the results. This opens up a new opportunity for conducting additional research on the synthesis of particles with a target size, by optimizing the process and the conditions of the experiment. With a series of further experiments it would be possible to find suitable concentrations of the reducing agent in solution and appropriate pH for obtaining monodispersed particles with the target size.

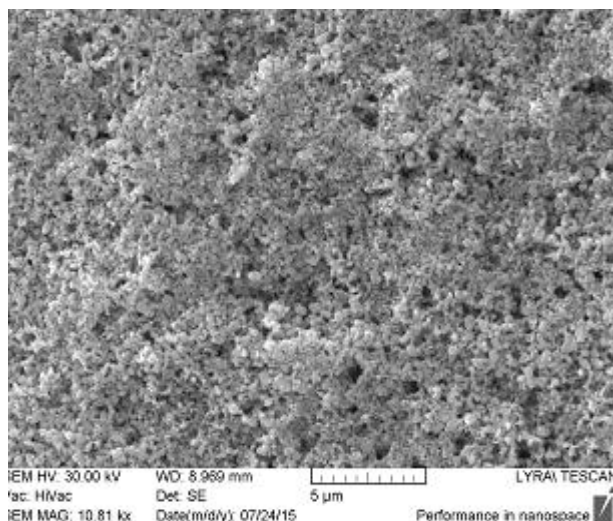
4. CONCLUSIONS

In the present study was submitted a new method of synthesis of a new reducing agent with specific hypothetical properties and a method for its application was proposed.

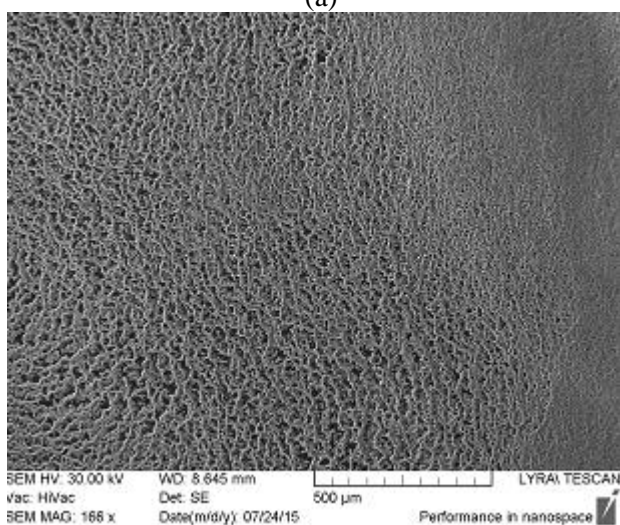
SEM analysis confirmed the correctness of the theoretical prerequisites for obtaining relatively monodispersed metal particles.



(a)



(b)



(c)

Figure 5. a) SEM image on a small particle population; b) SEM image on a large particle population; c) SEM image on lower magnification and ultra large particle population.

Acknowledgments: We give our special thanks to Materials technology laboratory, Department of Solid State Physics and Microelectronics, Faculty of Physics, Sofia University for providing thorough help with the preparing of the sample for SEM analysis and achieving the results.

REFERENCES

1. R. Boistelle, J. P. Astier, *J. Cryst. Growth*, **90**, 14 (1988).
2. P. L. Dulong, *Phil. Magazine*, **48**, 271 (1816).
3. A. P. J. Sabaneev, *Russian Phys. Chem Soc.*, **30**, 402 (1897).
4. L. Lyutov, D. Lyutov, G. Lyutov, *C R Acad Bulg Sci.*, **61**, 1407 (2008).

НОВ МЕТОД ЗА СИНТЕЗА НА НОВ КЛАС РЕДУКТОРИ С ОЧАКВАНИ ПРИЛОЖЕНИЯ В НАНОТЕХНОЛОГИИТЕ

Ив.В. Сливков^{1†}, Д.Л. Лютов^{2,*}, З.Пл. Панчева¹, Л.Г. Лютов¹

¹Факултет по химия и фармация, Софийски университет, бул. Дж. Баучер, 1, София 1164

²Физически факултет, Софийски университет, бул. Дж. Баучер, 5, София 1164

Постъпила на 31.07.2015 г.; коригирана на 2 декември, 2015 г.

(Резюме)

Идеята на настоящото изследване е да се получи монодисперсен Ag-зол като силно се ограничи времето през което е възможно зародишообразуване, а след това да се извършва само кристален растеж. Това се постига чрез 2 предпоставки: двустъпален редуктор със значителна разлика в редукионните потенциали на стъпалата и бързото изразходване на редуктора по стъпалото с по-висок редукионен потенциал по време на зародишообразуването.

Целта на изследването е да се провери експериментално тази идея и дали е възможно да се синтезира редукторът по процедура, не свързана с бурна реакция, а също така с по-малко опасни и лесно достъпни реактиви.

Предложената методика на синтез чрез двойно заместване между $N_2H_4 \cdot 2HCl$ и $Na_2H_2PO_2 \cdot H_2O$ дава по-ниски добиви (56.7%) и по-ниска чистота на продукта (% съдържание на Cl^-), но протича плавно без бурни реакции и без отделяне на токсични емисии.

Чрез провеждане на пилотен експеримент е показана приложимостта на $N_2H_6(H_2PO_2)_2$ като редуктор за получаване на Ag-зол. SEM-микрофотографии при различни популации показват, че разпределението по размери е в тесни граници, независимо от популацията. EDX- анализът показва, че материалът на частиците е Ag.

Obtaining and protective properties of passive films on Zn and Zn-Fe-P ternary alloys

M.T. Peshova, V.D. Bachvarov, S.D. Vitkova, N.S. Boshkov*

Institute of Physical Chemistry, Bulgarian Academy of Sciences, sofia 1113, Bulgaria

Submitted on July 15, 2015; Revised on November 3, 2015

Abstract: Protective Zn and ternary alloy Zn-Fe-P coatings are electrochemically obtained and additionally treated in special elaborated solution for chemical passivating based on tri-valent chromium compound. The elemental composition and surface morphology of the newly obtained Zn-Fe-P coatings without or with additional passive (conversion) film is determined by using of EDS and SEM. The corrosion behavior and protective ability of the system coating / passive (chromite) film are investigated by means of potentiodynamic polarization curves and electrochemical impedance spectroscopy (EIS) in model medium containing chloride ions as corrosion activators. As a result of the corrosion tests the influence of the passive film on the corrosion properties of the electrodeposited Zn and Zn-Fe-P alloy coating in that medium is analyzed and commented.

Key words: corrosion, passive films, zinc, Zn-Fe-P alloy

1. INTRODUCTION

Zinc coatings are widely used for metal prevention and protection against corrosion damages. The very strongly negative potential of the Zn (-0.76 V) defines its role of anodic (sacrificial) layer concerning the iron and steel substrate. The co-deposition of the zinc with other metals like Mn, Co, Ni, Fe leads to obtaining of coatings with improved physical and mechanical properties and increased corrosion resistance [1-11]. Contrary to the pure zinc most of these alloys have good adhesion concerning the finishing paints.

According to some investigations [12] the co-deposition of some of these alloys with P has a positive influence on their corrosion resistance. In addition, the incorporation of this element in the alloy in amounts less than 1 wt% usually decreases the residual stresses in the galvanic coatings.

Several patents for obtaining of thin alloy Zn-Fe-P coatings based on acidic or alkaline electrolytes are available in the literature [13-16]. The phosphorus content varies in the range 0 – 5 wt% while that of the iron is between 7 and 35 wt%. The authors report for good weldability, solderability and adhesion to finishing paints and coatings and increased corrosion resistance against local corrosion. The alloys with great zinc content have crystalline structure which changes to amorphous at higher P and Fe amounts.

Since the zinc coatings are not enough resistant in very aggressive environments additional surface treatment is applied in order to improve the

stability. The result is the appearing of a conversion (passive) film [17-22]. The so treated electrodeposits show lower susceptibility in aggressive corrosive solutions and can be an excellent basis for further treatment with organic paints or lacquers.

The tri-valent chromium-based (chromite) films have been developed due to the novel ecological requirements and are environmentally friendly compared to the Cr⁶⁺-based ones. Chromite layers on the metal surface play a very important role decreasing the zinc dissolution rate and lowering the rate of the oxygen reduction [23-26].

The present work is aimed to describe the experimental conditions for obtaining of passive films (PF) on zinc and Zn-Fe-P alloy coatings from environmentally friendly Cr³⁺-containing solution as well as to characterize their corrosion behavior in a model medium with chloride ions as corrosion activators.

2. EXPERIMENTAL

2.1. Sample preparation

All coatings are electrodeposited on a low carbon steel substrate with sizes 20x10x1 mm, whole surface area of 4 cm² and thickness of approximately 10 μm.

2.2. Electrochemical deposition

2.2.1. Zinc coatings are electrodeposited from electrolyte containing (in g/l): ZnSO₄·7H₂O - 150, NH₄Cl - 30, H₃BO₃ - 30, additives AZ-1 - 50 ml/l and AZ-2 - 10 ml/l at pH value between 4,5–5,0, ambient temperature of about 22 °C, zinc anodes and cathodic current density of 2 A/dm². No stirring or agitation is applied.

*To whom all correspondence should be sent:
E-mail: NBoshkov@ipc.bas.bg

2.2.2. Zn-Fe-P alloys are electrodeposited from electrolyte with a composition (in g/l): $\text{FeSO}_4 \cdot 7\text{H}_2\text{O}$ - 200, $\text{ZnSO}_4 \cdot 7\text{H}_2\text{O}$ - 70, $\text{Na}_3\text{C}_6\text{H}_5\text{O}_7 \cdot 5,5\text{H}_2\text{O}$ -50, $\text{NaH}_2\text{PO}_2 \cdot \text{H}_2\text{O}$ and H_3PO_2 - 11.4, NH_4Cl - 15 and additive ZC1 (20 ml/l) at pH 2.5, temperature of 40 °C, Ti-Pt anodes and cathodic current density in the range 5 - 20 A/dm², circulation of the electrolyte. In that case alloys with different Fe and P content are electrodeposited.

2.3. Corrosion medium and reproducibility

A model corrosion medium of 5% NaCl solution with pH~6.7 at room temperature of 22 °C is used. The results from the investigations are an average of 3 samples per type i.e. for each measurement 3 replicates of a Zn or ternary alloy Zn-Fe-P. Prior to the beginning of the test all samples are temporized for a definite period in the model medium at conditions of open circuit potential (OCP).

2.4. Passive films

The additional surface treatment of the zinc and of the ternary alloys is carried out in a solution consisting of CrNO_3 , HNO_3 and NaH_2PO_2 with pH value of 1.2. The immersion time was 40 s for all investigated samples.

2.5. Sample characterization

The sample characterization is realized by using of electrochemical workstation PAR “VersaStat 4” and application of the following methods:

- Potentiodynamic (PD) polarization – the measurements are performed at a scan rate of 1 mV/s in the potential range between -1200 and – 200 mV.

- Electrochemical impedance spectroscopy – the measurements are carried out in the frequency range of 100 kHz to 10 mHz by superimposing an AC voltage of 10 mV.

Additionally, for observation of the sample surface morphology and its peculiarities Scanning electron microscopy (SEM) with coupled EDS device is applied by using of INCA Energy 350 unit.

The electrochemical measurements are performed in a common three-electrode experimental cell (volume of 250 ml) with a Luggin-capillary for minimizing the ohmic resistance of the medium. Platinum plate serves as a counter electrode while the potentials are measured with respect to the saturated calomel electrode (SCE).

2.RESULTS AND DISCUSSION

3.1. Potentiodynamic polarization (PDP)

The cathodic and anodic potentiodynamic polarization (PD) curves of pure Zn and Zn-Fe-P alloy coatings with different Fe and P content without and with additional passive film (PF) on the surface are demonstrated in Figure1(A,B). In addition, the PD curve of the low carbon steel at the same conditions is also demonstrated.

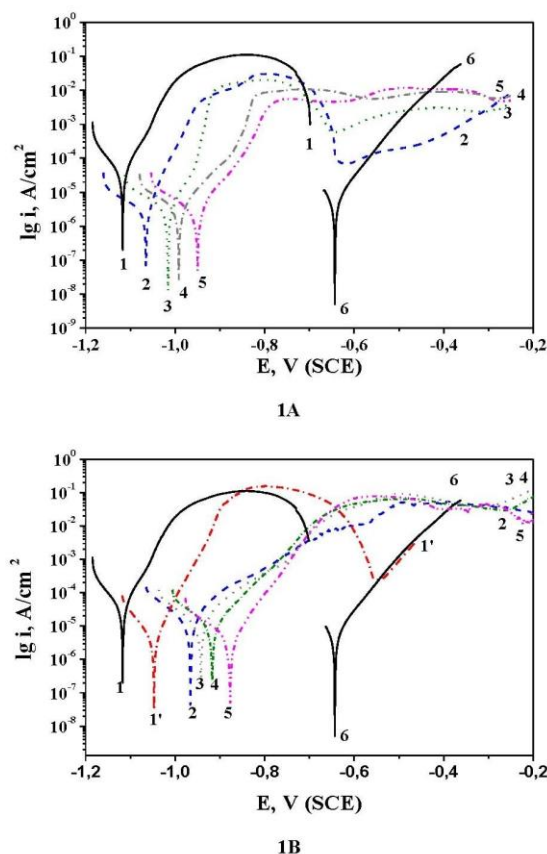


Figure 1. Potentiodynamic curves of Zn and Zn-Fe-P alloys: A – without passive film; B – with passive film. 1 – Zn(without PF); 1' – Zn(with PF); 2 - $\text{Zn}_{96}\text{Fe}_4\text{P}_0$; 3 - $\text{Zn}_{91.2}\text{Fe}_{8.5}\text{P}_{0.3}$; 4 - $\text{Zn}_{85.4}\text{Fe}_{14}\text{P}_{0.6}$; 5 - $\text{Zn}_{70.3}\text{Fe}_{28.5}\text{P}_{1.2}$; 6 – low carbon steel.

The obtained results clearly show that all coatings have corrosion potentials strongly negative compared to the steel which means that they will play a role of sacrificial coating i.e. they will be firstly dissolved in the case of corrosion attack protecting in such a way the underlying steel substrate – Fig. 1A.

The obtained results clearly show that all coatings have corrosion potentials strongly negative compared to the steel which means that they will play a role of sacrificial coating i.e. they will be firstly dissolved in the case of corrosion attack protecting in such a way the underlying steel substrate – Fig. 1A.

It can be also concluded that at external anodic polarization the pure Zn coating lasts up to about -720 mV while all ternary alloy sample curves are much longer. The corrosion current density values of the alloys (in the order of magnitude 10^{-6} A/cm²) are much lower compared to that of the zinc. The anodic parts of the PD curves of the alloys are generally with lower slope indicating slowing in the anodic rate and in addition a passive zone (although at relatively high current density value) seems to appear for the sample Zn₉₆Fe₄P₀. The latter has no P content registered by EDS analysis but is obtained from electrolyte containing this element. Generally, these PD curves could be divided in two groups according to their position and electrochemical parameters. Curves 4 and 5 which are the samples with greater P content have close anodic behavior and steep slopes indicating inhibiting of the anodic dissolution. Both other samples with lower P content (curves 2 and 3) show steeper anodic slopes and are placed at more negative potential values—Fig. 1A. The PD curves of the same sample types but with PF are shown in Figure 1B. Also here, the curve of the pure zinc is added for more clarity. The presence of PF on Zn changes its corrosion behavior leading to shifting of the corrosion potential in positive direction and to lower corrosion current density value. The passivated alloy samples show closer corrosion potentials compared to the non-passivated ones most probably due to the better surface homogeneity as a result of the treatment in the Cr³⁺-containing solution. The anodic slopes of the curves are much lower compared to these from Fig. 1A which means that the anodic process is to a certain degree inhibited.

3.2. Electrochemical impedance spectroscopy (EIS)

The results from the EIS measurements for the zinc and ternary alloys without PF are demonstrated in Figure 2(A,B). It can be concluded that most of the obtained EIS spectra responses are more or less depressed capacitive loops and in general two groups of samples could be divided – Zn₉₆Fe₄P₀ and Zn_{91.2}Fe_{8.5}P_{0.3} (and also pure Zn) from one side and Zn_{85.4}Fe₁₄P_{0.6} and Zn_{70.3}Fe_{28.5}P_{1.2} - from another. Both latter show polarization resistance values between 350 and 470 ohms, while the other three coatings have lower Rp - in the range between 150-200 ohms – Fig. 2A.

The results from the EIS investigations of Zn and ternary Zn-Fe-P alloys with PF are presented in Figure 2B. It can be registered that the sample with the highest Fe and P contents (No. 5) has the greatest Rp value – about 2200 ohms - followed by

sample No. 4 – 900 ohms. The other investigated samples have Rp values about 400-500 ohms.

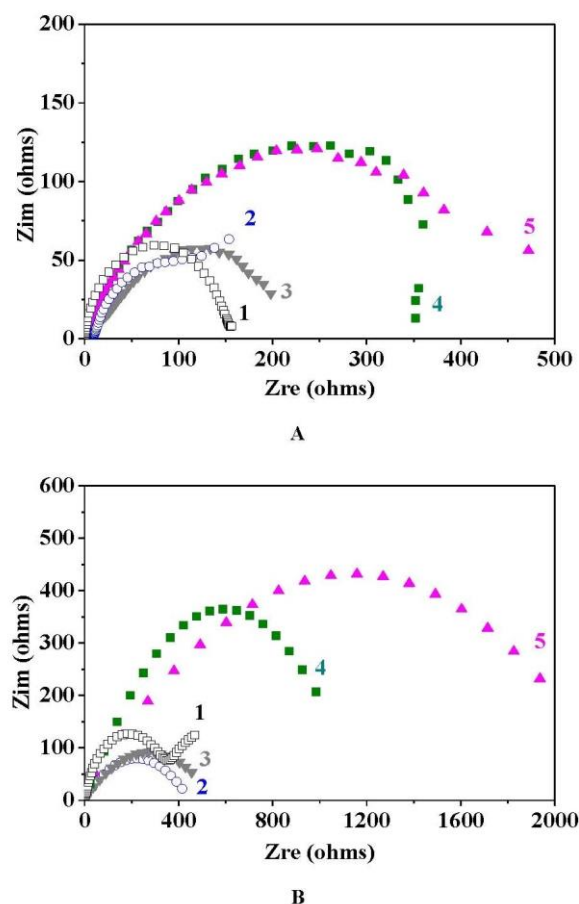


Figure 2. Overlay EIS spectra response of Zn and Zn-Fe-P alloys: A – without passive film; B – with passive film; 1 – Zn; 2 - Zn₉₆Fe₄P₀; 3 - Zn_{91.2}Fe_{8.5}P_{0.3}; 4 - Zn_{85.4}Fe₁₄P_{0.6}; 5 - Zn_{70.3}Fe_{28.5}P_{1.2}.

Compared to the non-passivated samples the passivated ones have greater Rp values – between two and four and a half times - which clearly demonstrate the positive influence of the additional treatment in Cr³⁺-containing solutions on the protective characteristics of the Zn and the ternary alloys. For most of the hereby discussed cases, the initial EIS response is modeled by an equivalent circuit presented in Figure 3A. The time constant Rp.CPE1 is attributed to the electrochemical reaction while Rs.CPE2 – to the surface properties. In one case (pure zinc with passive film shown in Fig. 2B) also Warburg impedance W is added – Fig. 3B. The replacement of pure capacitance with constant phase element (CPE) in the equivalent circuits is generally accepted, being denoted to inhomogeneities at different levels i.e. steel surface roughness, product layer heterogeneity [27], etc.

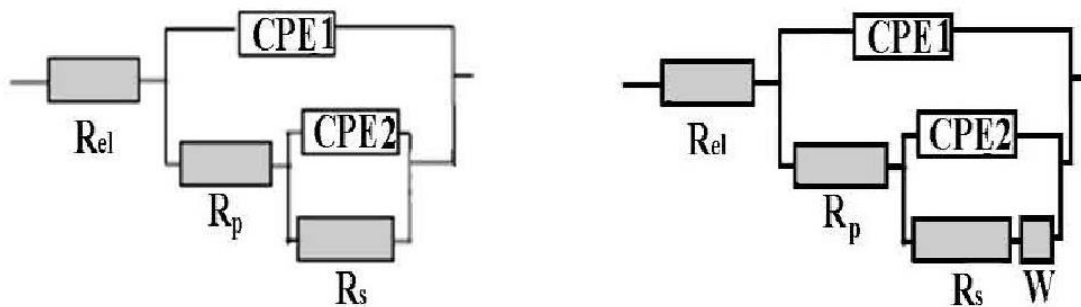


Figure 3. Equivalent circuits used in the EIS investigations.

At first look some of the obtained results seem to be to a certain degree controversial compared to the data registered from the PD curves. This phenomenon could be explained to some extent with the nature of the applied methods – the anodic polarization is a destructive method and during the dissolution of the coating the appearance of newly formed corrosion products is expected. The latter (depending on the value of their solubility) could inhibit for a definite period the dissolution process due to the so called “barrier effect”.

The type of the newly formed corrosion products strongly depend on the composition of the alloys so it can be expected that alloys with different composition will lead to different amounts or ratios of corrosion products. In the case of EIS the appearance of these products is less likely due to the non-destructive principle of this method.

3.3. EDS analysis and SEM

The results from the EDS analysis concerning the composition of the investigated ternary alloys before and after treatment in the solution for chemical passivating are demonstrated in Table 1.

It can be registered that as a result of the chemical passivating the zinc content in all alloy coatings become lower while the amounts of all other elements increase. These changes in the chemical composition of the passivated coatings can to a certain degree explain the differences registered by using of PD polarization and EIS methods.

As well known, during the chemical passivating the coating surface is partially dissolved as a result of the low pH - value predominantly the Zn which is the more negative metal. Also other elements like Fe and P will be included in the structure of the passive film together with Cr forming oxides and phosphates and leading in such a way to change in its potential. This newly formed film has a “barrier effect” and ensures the protection of the passivated zinc toward the steel substrate. In addition, it can be expected that if the surface is enriched with elements with more positive potential the sample will be more resistant against the corrosion attack.

The EDS analysis show that the greatest Fe and P amounts can be observed in alloys No. 3 and 4 from Table 1. The EIS data demonstrate that these coatings have the greatest R_p values to the dissolution reaction. EIS is an express and non-destructive investigating method and its conditions are close to the open-circuit conditions (OCP). Comparing the EIS data with the PD curves from Figure 1B it can be also registered that the same alloys with the highest Fe and P amounts distinguish with the most positive corrosion potentials. The surface morphology of the pure zinc and of the ternary Zn-Fe-P alloys is demonstrated in Figure 4. Marked differences can be observed between the presented samples. The zinc coating shows smooth and even surface with several “nodular” zones the latter most probably being a result from included contaminations during the electrodeposition.

Table 1. Chemical composition of ternary Zn-Fe-P alloys before and after passivating.

No	ELEMENTS						
	Alloy before passivating			Alloy after passivating			
	Zn	Fe	P	Zn	Fe	P	Cr
1	96.0	4.0	0.0	93.7	4.0	0.6	1.7
2	91.2	8.5	0.3	88.3	9.3	0.8	1.6
3	85.4	14.0	0.6	74.3	22.4	1.7	1.6
4	70.3	28.5	1.2	45.7	49.3	3.3	1.7

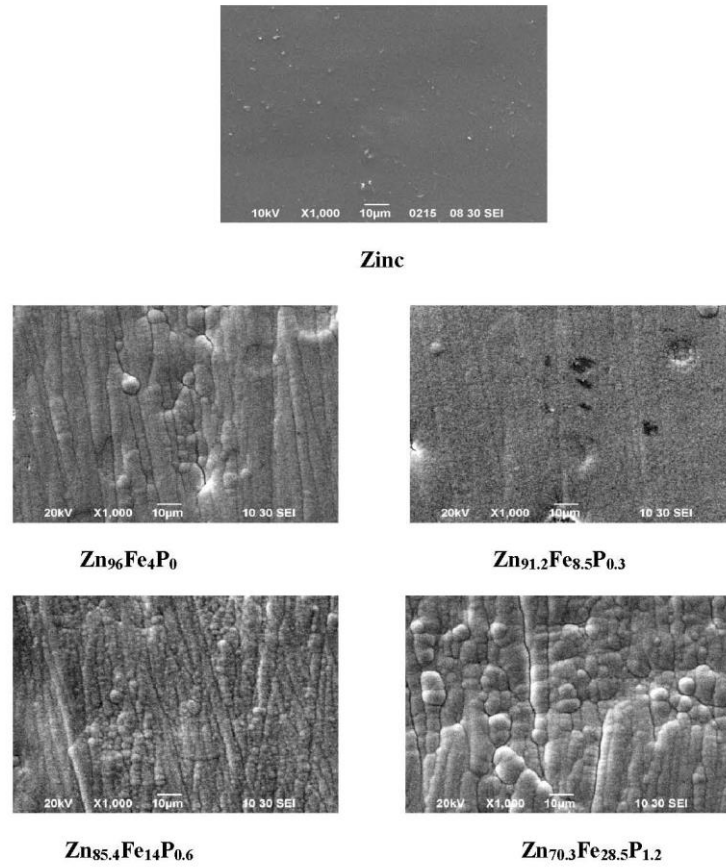


Figure 4. Surface morphology (SEI) of non-passivated Zn and ternary Zn-Fe-P alloys.

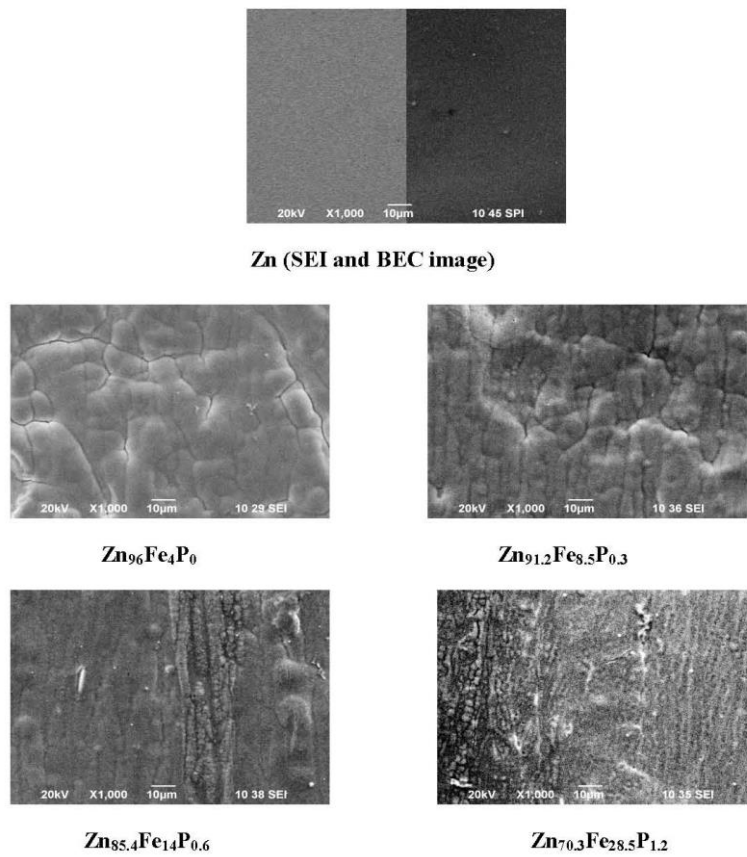


Figure 5. Surface morphology of Zn (SEI and BEC) and ternary Zn-Fe-P alloys (SEI) with passive films.

Contrary to this, the ternary alloys demonstrate practically uneven surface with some hackly areas as well as protruded and concaved zones depending on the electrodeposition conditions but mainly from the applied current density value.

The Zn and ternary alloys change their surface morphology after the chemical treatment in passivation solution – the surface looks more smooth and even which seems to be one of the reasons for their improved protective action compared to the samples without conversion passivation film (Figure 5).

4.CONCLUSIONS

The present work shows the possibility for obtaining of a solution for chemical passivating of Zn and ternary Zn-Fe-P alloys. This solution is based on Cr^{3+} - compounds and lead to appearance of additional protective layer on the coating surface aimed to improve the corrosion resistance.

The obtained passive films are investigated concerning their chemical composition and surface morphology as well as their corrosion behavior in model medium containing Cl^- ions as corrosion activators.

The PD curves demonstrate that the pure zinc has greater corrosion current density and dissolves with higher anodic current densities compared to the non-passivated Zn-Fe-P alloys. The treatment with the chemical conversion solution leads to delay of the anodic dissolution both for the Zn and for the ternary alloys.

The obtained results from the EIS measurements qualitatively confirm the improved protective characteristics of the passivated zinc and passivated ternary alloys compared to these without additional surface layer.

REFERENCES

1. N.R. Short, A. Abibsi, J.K. Dennis, *Trans. Inst. Met. Finish.*, **67**, 73 (1991).
2. P.C. Tulio, S.E.B. Rodrigues, I.A. Carlos, *Surf. Coat. Technol.*, **202**, 91 (2007).
3. T. Ohgai, K. Ogushi, K. Takao, *J. of Physics: Conference Series*, **417**, 012006 (2013).
4. L. Shi, C.F. Sun, F. Zhou, W.M. Liu, *Mater. Sci. Eng.A*, **397**, 190 (2005).
5. P.A. Gay, P. Bercot, J. Pagetti, *Surf. Coat. Technol.*, **140** 147 (2001).
6. G. Achary, H.P. Sachin, Y. Arthoba Naik, T.V. Venkatesha, *Bull. Mat. Sci.*, **30**, 219 (2007).
7. C. Muller, M. Sarret, M. Benballa, *Surf. Coat. Technol.*, **162**, 49 (2003).
8. B.M. Praveen, T.V. Venkatesha, Y. Arthoba Naik, K. Prashantaha, *Surf. Coat. Technol.*, **201**, 5836 (2007).
9. A. Shamsolhodaei, H. Rahmani, S. Rastegari, *Surf. Eng.*, **29**, 9, 695 (2013).
10. S. Pouladi, M.H. Shariat, M.E. Bahrololoom, *Surf. Coat. Technol.*, **213**, 33 (2012).
11. O. Hammami, L. Dhouibi, P. Bertzot, E. M. Rezrazi, *J. of Appl Electrochem*, **44**, 1, 115 (2014).
12. D.S. Slavkov, B.N. Popov, *Bulletin of the Chemist and Technologists of Macedonia* 20 (1) (2001) 3-17.
13. T. Irie, K. Kyono, S. Kurokawa, H. Kimura, US Patent № 4,541,903 (1985).
14. Kawaski Steel Corporation, Jpn. Kokai Tokkyo Koho, JP6089593, (1985).
15. K. Kyono, H. Kimura, S. Kurokawa, US Patent № 4,640,872 (1987).
16. K. Oshima, S. Yuasa, J. Ozawa, US Patent № 5,630,929 (1997)..
17. J. Hadley, W. Verberne, L. Wing, J. O'Grady, *Metal Finishing*, **100** 33 (2002).
18. R. L. Twite, G. P. Bierwagen, *Prog. Org. Coat.*, **33** 91 (1998).
19. S.A.M. Rafaey, S.S. Abd El-Rehim, F. Taha, M.B. Saleh, R.A. Ahmed, *Appl. Surf.Sci.*, **158** 190 (2000).
20. C. Muller, M. Sarret, E. Garcia, J. A. Ortega, *J. Electrochem. Soc.*, **149** 151 (2004).
21. D. Weng, P. Jokiel, A. Uebleis, H. Boehni, *Surf. Coat. Technol.*, **88** 147 (1996).
22. T.S.N. Sankaranarayanan, M. Subbaiyan, *Surf. Coat. Technol.*, **43/44** 543 (1990).
23. X. Zhang, C. van den Bos, W.G. Sloof, A. Hovestad, H. Terryn, J.H.W. de Wit, *Surf. Coat. Technol.*, **199** 92 (2005).
24. Y.T. Chang, N.-T. Wen, W.K. Chen, M.D. Ger, G.T. Pan, T.C.K. Yang, *Corr. Sci.*, **50** 3494 (2008).
25. N.T. Wen, C.S. Lin, C.Y. Bai, M.D. Ger, *Surf. Coat. Technol.*, **203** 317 (2008).
26. T. Bellezze, G. Roventi, R. Fratesi, *Surf. Coat. Technol.*, **155** 221 (2002).
27. V. Feliú, J.A. González, S.Feliú, *J. Electrochem. Soc.*, **151** B134 (2004).

ПОЛУЧАВАНЕ И ЗАЩИТНИ СВОЙСТВА НА ПАСИВНИ ФИЛМИ ВЪРХУ ЦИНК И ТРОЙНИ ЦИНКОВИ СПЛАВИ Zn-Fe-P

М.Т. Пешова, В.Д. Бъчваров, С.Д. Виткова, Н.С. Божков*

Институт по физикохимия, Българска академия на науките

Постъпила на 15 юли, 2015 г. коригирана на 3 ноември, 2015 г.

(Резюме)

Представени и дискутирани са резултати, свързани с електрохимичното получаване на композитни електрохимично са получени защитни покрития от цинк и тройни сплави Zn-Fe-P с различен състав. Всички те допълнително са третирани в специално разработен състав за химично пасивиране на базата на тривалентни хромни съединения. С помощта на сканираща електронна микроскопия е изследвана повърхностната морфология на цинка и тройните сплави. С EDS анализ е определен елементния състав на сплавите с и без наличие на пасивен филм. Изследвани са корозионното поведение и защитната способност на системата покритие / пасивен (хромитен) филм в моделна среда, съдържаща хлорни йони като корозионни активатори, с помощта на потенциодинамични поляризационни криви и електро-химична импедансна спектроскопия. Анализирани и коментирани са получените от корозионните тестове резултати относно влиянието на пасивния филм върху защитните свойства на електроотложените покрития от цинк и сплавта Zn-Fe-P.

Obtaining and comparative corrosion characterization of composite zinc and zinc alloy coatings with embedded stabilized polymeric micelles

N.D. Boshkova¹, P.D. Petrov², N.S. Boshkov^{1*}

¹ Institute of Physical Chemistry, Bulgarian Academy of Sciences

² Institute of Polymers, Bulgarian Academy of Sciences

Submitted on July 15, 2015; Revised on October 14, 2015

Abstract: The results concerning the electrochemical obtaining of composite zinc and some composite zinc alloy coatings (Zn-Co and Zn-Mn) with embedded core-shell type stabilized polymeric micelles (SPMs, based on polypropylene oxide and poly-ethylene oxide) are presented and discussed. The deposition and dissolution processes of the zinc and both zinc based alloys in the presence or absence of SPMs are investigated by using of cyclic polarization (cyclic voltammetric curves). The influence of the incorporated in the metal or alloy matrix SPMs on the surface morphology of the obtained coatings is shown and commented. The corrosion behavior and protective ability of the composite coatings are evaluated in a model medium containing chloride ions as corrosion activators and are compared to the same characteristics of the non-composite coatings. The influence of the SPMs on the corrosion resistance and protective properties of the zinc and zinc alloy coatings in that medium is analyzed and discussed.

Key words: corrosion, composite coatings, zinc, zinc alloys, stabilized polymeric micelles

1. INTRODUCTION

The electrodeposition of Zn and zinc alloy coatings on steel substrates has been for a long time applied to achieve high corrosion resistance [1-3]. Zinc is generally used as a sacrificial coating with an aim to protect the steel from corrosion damages. However, the safe exploitation of these coatings is to a certain degree limited due to the aggressive nature of environment containing industrial pollutants. As a result, additional efforts must be done in order to improve their corrosion resistance [4,5].

Electrodeposition of different composite coatings is a highly advanced method in material science leading to obtaining of materials with desired properties at easy conditions. Another important application is the possibility to co-deposit metal with metallic, non-metallic, polymeric particles etc. The demand for newly developed materials based on metal matrix composites shows an increasing tendency due to their potential applications in many industrial and other sectors [6-10].

Composite zinc and zinc alloy coatings can be also applied for corrosion prevention since it is well known that most of them exhibit very high corrosion resistance [11-16]. Aiming at increasing the protective ability of the zinc and its alloys different attempts have been realized in order to incorporate non-organic or organic micro- or nano-sized particles in them [17-29].

The aim of the present work is to obtain via electrochemical method composite Zn and zinc alloy

coatings, to characterize and evaluate their protective parameters and to compare the obtained results with these of the galvanic ones.

2. EXPERIMENTAL

2.1. Sample preparation

The selected zinc based alloy coatings have been previously investigated by us and have been classified as protective coatings with high corrosion resistance in 5% NaCl solution. The aim of the investigation is to clarify if the presence of SPMs in the alloy matrix will improve their protective ability toward the substrate.

All samples (composite and non-composite) are electrodeposited on low carbon steel substrates with sizes 20 x 10 x 1 mm, whole surface area of 4 cm² and coating thickness of approximately 12 μm. Deposition conditions are: current density 2 A/dm²; room temperature – 22 °C; metallurgical zinc anodes. In the case of Zn-Mn electrodeposition process the electrolyte is circulated.

2.2. Galvanic coatings

2.2.1. Zinc coatings are electrodeposited from electrolyte with a composition 150 g/l ZnSO₄·7H₂O, 30 g/l NH₄Cl, 30 g/l H₃BO₃, additives AZ-1 (wetting agent) - 50 ml/l and AZ-2 (brightener) - 10 ml/l, pH value 4,5–5,0.

2.2.2. Zn-Co (1 wt.%) alloy coatings are obtained from electrolyte containing 100 g/l ZnSO₄·7H₂O; 120 g/l CoSO₄·7H₂O; 30 g/l NH₄Cl; 25 g/l H₃BO₃; additives ZC-1 (wetting agent) - 20 ml/l and ZC-2 (brightener) - 2 ml/l; pH 3,0–4,0.

2.2.3. Zn-Mn (11 wt.%) alloy coatings are electrochemically received from the following

*To whom all correspondence should be sent:

E-mail: NBoshkov@ipc.bas.bg

electrolyte: $\text{ZnSO}_4 \cdot 7\text{H}_2\text{O}$ - 10 g/l; $\text{MnSO}_4 \cdot 7\text{H}_2\text{O}$ - 100 g/l; $(\text{NH}_4)_2\text{SO}_4$ - 60 g/l, additive AZ-1 – 40 ml/l.

2.3. Composite coatings

The composite coatings are electrochemically deposited from the same electrolytes and at the same electrodeposition conditions described above but with an addition of powdered stabilized nano-sized polymeric micelles (SPMs) in selected concentrations. The applied SPMs are based on $\text{PEO}_{75}\text{PPO}_{30}\text{PEO}_{75}$ (poly-ethylene oxide – poly-propylene oxide – poly-ethylene oxide) tri-block copolymer where PPO is the hydrophobic core and PEO – the hydrophilic shell.

2.4. Stabilized polymeric micelles (SPMs)

The main procedure for preparation of these SPMs is described elsewhere [30] and includes the formation of core-shell type micelles in aqueous media at 60 °C and immobilization of tetra-functional hydrophobic monomer - pentaerythritol tetra-acrylate (PETA) – followed by UV-induced polymerization and formation of a semi-interpenetrating polymer network. The stabilized micelles are dialyzed against distilled water and then added to the electrolytes described above. The sizes and shape of the applied SPMs are presented elsewhere [27].

2.5. Corrosion medium and reproducibility

A model corrosion medium of 5% NaCl solution with pH 6.7 at ambient temperature of about 30 °C is used for the investigations. The results from the electrochemical investigations are an average of 5 samples per type i.e. for each measurement 5 replicates of a Zn, zinc based alloys or their composites. Aiming at receiving of better reproducibility prior to the test all samples are temporized for a definite period in the model medium at conditions of open circuit potential (OCP).

2.6. Sample characterization

The sample characterization is realized by using of electrochemical workstation PAR “VersaStat 4” and application of the following methods:

- Cyclic voltammetry curves – to investigate the influence of the SPMs added to the electrolytes on the cathodic and anodic processes. The measurements are performed at scan rate of 10 mV/s.
- Potentiodynamic (PD) anodic polarization – the aim is to compare and evaluate the peculiarities of the anodic behavior of galvanic and composite coatings. The measurements are performed at a scan rate of 1 mV/s.

In addition, polarization resistance (R_p) measurements are carried out for a test period of 312

hours by using of “Corrovit” equipment in the range of ± 25 mV relative the corrosion potential. From the Stern–Geary equation [31] it is known that higher R_p value (in $\Omega \cdot \text{cm}^2$) corresponds to higher corrosion resistance and to lower corrosion rate.

The surface morphology of the samples is investigated with Scanning (SEM) electron microscopy by using of INCA Energy 350 unit.

All electrochemical measurements are carried out in a common three-electrode experimental cell (volume of 250 ml) with a Luggin-capillary for minimizing the ohmic resistance of the corrosion medium. Platinum plate is taken as a counter electrode and the potentials are measured with respect to the saturated calomel electrode (SCE).

3. RESULTS AND DISCUSSION

3.1. Cyclic voltammetry

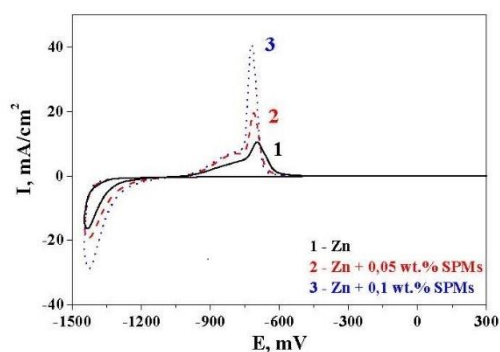
The results obtained by this method are presented in Figure 1(A-C). It is well visible that the presence of the SPMs in the zinc electrolyte facilitate the cathodic deposition process – the difference between the cathodic current density value of the electrolyte without SPMs (curve 1) and electrolyte with 0,1 wt.% SPMs (curve 3) is about 12-14 mA/cm² – (Figure 1A).

The presence of SPMs in the solution does not affect the polarization of the cathodic process at the initial stage but it is more intensive which means that the SPMs do not burden the electrodeposition. The weight of the obtained galvanic and composite coatings and their thicknesses are very close. Visually, no changes are observed concerning the hydrogen evolution rate.

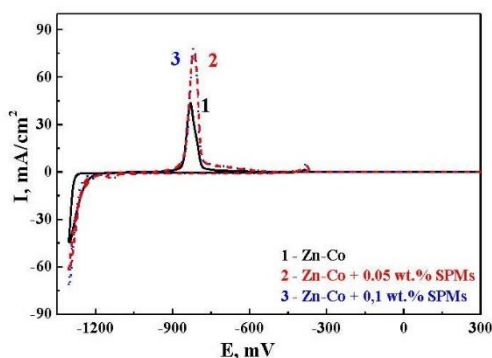
In general, the SPMs are regarded as electro neutral but the zinc ions can realize a coordination bond with the oxygen from the hydrophilic PEO chains. In addition, due to their very small sizes zinc ions can find place in the internal volume of the hydrophilic shell. As a result the SPMs transform in micelle-metallic (SPM-Zn) aggregates with partial positive charge due to the available Zn^{2+} . When the electrodeposition begins these aggregates will move electro-phoretically to the cathode and deposit there together with the individual zinc ions i.e. competitive electrodeposition of the zinc ions and of the zinc-SPMs aggregates occurs. The latter are much greater compared to the sizes of the zinc ions and thus discharge on (cover) greater surface of the cathode. In addition, a possible interaction of PEO-chains with the additive AZ1 (based on PEO-derivative) could be proposed which will mitigate the wetting of the cathode.

The anodic peaks of the composite zinc coating are much greater (up to 4 times) compared to the

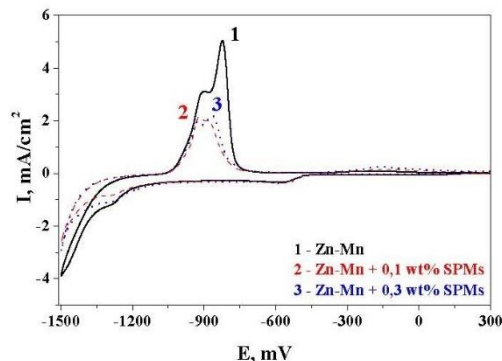
peak of the pure zinc – curves 1 and 3 – which qualitative corresponds to the cathodic part of the



A



B



C

Figure 1. Cyclic voltammetry (CVA) curves of: A - Zn coating and its composites; B - Zn-Co(1 wt.%) coating and its composites; C - Zn-Mn(11 wt.%) coating and its composites.

curves. In addition, an area with gradual increase of the anodic current appears in the potential zone between -990 and -740 mV which is most strongly expressed for the coating from the electrolyte with 0,1 wt.% SPMs. Possible reason for this phenomenon might be the accelerated dissolution of the zinc around the embedded SPMs and the following increase of the anodic current.

Figure 1B demonstrates the influence of the SPMs on the cathodic and anodic processes (deposition and dissolution) of Zn-Co (1 wt.%)

alloy. A depolarization can be registered in the cathodic part in the case of both alloy composites compared to the galvanic Zn-Co with about 80 mV (from -1270 mV up to -1190 mV). Also here, greater current density values are observed for the composites – about 60-70 mA/cm² compared to 40 mA/cm² for the galvanic alloy. According to this, greater anodic current density values for the composites and lower for the

galvanic alloy can be registered.

The reasons for these results can be also attributed to the comments presented above for the electrodeposition of the composite and non-composite zinc.

The CVA curves for both galvanic and composite Zn-Mn (11 wt.%) alloy are shown in Figure 1C. In the cathodic area the addition of SPMs leads to an overvoltage with about 80 mV for the composites compared to the non-composite Zn-Mn and in addition, the current density value of the latter is greater. In the anodic part the current density of the galvanic coating is also greater than that of both composites. Characteristic for all samples is the presence of two anodic dissolution peaks which most probably follow from the fact that Mn can appear in different valences.

It can be summarized that the presence of SPMs does not facilitate the electrodeposition of the Zn-Mn composite coatings comparing to the case of the Zn and Zn-Co. One reason for this observation could be the different valent values of Mn as well as the inhibited interaction of the manganese ions with the SPMs i.e. with their hydrophilic part.

3.2. Potentiodynamic anodic polarization

The anodic curves of the investigated Zn and its composite obtained from electrolyte with 0,1 wt.% SPMs in the model corrosion medium of 5% NaCl are presented in Figure 2 (A-C) The difference between them is the curve's length the latter being longer for the composite coating which means that it lasts more under external anodic polarization. In order to reduce possible errors from the substrate dissolution and appearance of a mixed current the sample was checked during the experiment to register if the coating still exist or is already dissolved.

As seen from Figure 2A the galvanic zinc coating is totally dissolved at potential values of about -500 mV while the composite Zn lasts up to about -300 mV. The composite Zn characterizes also with a pseudo-passive zone (since the anodic current is relative high – $2 \cdot 10^{-3}$ A/cm²) in the potential area between -380 mV and -460 mV which means that in this zone the anodic dissolution process is hampered.

Since the Zn does not characterize with a passive zone in such medium the obtained results can be regarded as a sign for the positive influence of the SPMs on the protective properties.

Figure 2B represents the anodic PD curves of the Zn-Co alloy and its composite obtained from electrolyte containing 0,1 wt.% SPMs in the model medium used. Contrary to the previous case no significant positive influence of the SPMs on the

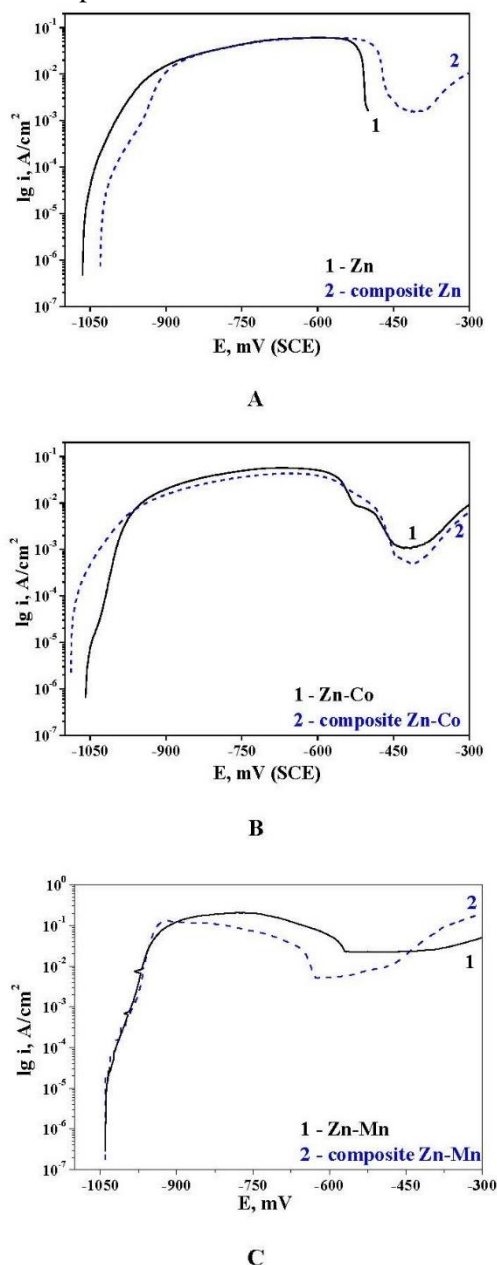


Figure 2. Potentiodynamic polarization curves of: A – Non-composite and composite Zn obtained from electrolyte with 0,1wt% SPMs; B - Non-composite and composite Zn-Co(1 wt.%) obtained from electrolyte with 0,1wt% SPMs; C - Non-composite and composite Zn-Mn(11 wt.%) obtained from electrolyte with 0,1wt% SPMs

disposal and on the length of the anodic curve of the composite coating can be registered. Both curves are

of the same length, have very close anodic current density values and show almost equal passive zones, i.e. pseudo-passive zones since the current density registered is very high – in the range of about $10^{-3} A/dm^2$.

The results obtained for the galvanic and composite coatings of Zn-Mn alloy the latter obtained from electrolyte with 0,1 wt.% SPMs are demonstrated in Figure 2C. The positive influence of the embedded SPMs on the electrochemical behavior of the composite is to a certain degree controversial. The length of both curves is almost

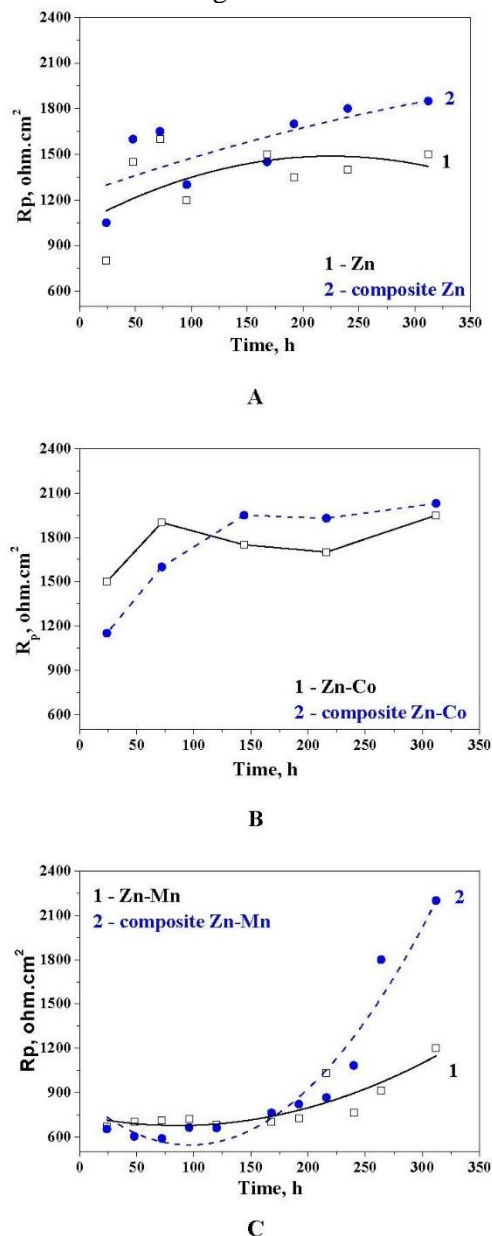


Figure 3. Polarization resistance (R_p) measurements of: A – Non-composite and composite Zn obtained from electrolyte with 0,1wt% SPMs; B - Non-composite and composite Zn-Co(1 wt.%) obtained from electrolyte with 0,1wt% SPMs; C - Non-composite and composite Zn-Mn(11 wt.%) obtained from electrolyte with 0,1wt% SPMs.

equal and the current density values in the area after the corrosion potential have close slopes and beta constants. A difference can be registered in the zone of the maximal anodic dissolution where the rate of the anodic process of the composite gradually decreases forming a pseudo-passive zone at relative high anodic current densities.

3.3. Polarization resistance (R_p) measurements

The results obtained by this method for galvanic and composite zinc coating (from bath with 0,1 wt.% SPMs) are shown in Figure 3A. After 312h it can be observed that the R_p of the Zn composite shows an increasing tendency and at the end is with about 350 ohms higher than that of the galvanic zinc. At the end of the test both coatings do not have remarkable damages on the surface but the composite one shows better decorative appearance. The reason for this can be explained with the formation of a mixed surface layer which consists of newly formed corrosion product – zinc hydroxide chloride (ZHC, registered also previously by us with XRD method) and SPMs. As well known ZHC characterizes with a low product of solubility ($\sim 10^{-14}$) which has a barrier effect toward the penetration of the corrosion medium into the depth of the coating. In the case of a mixed layer the hydrophobic part of the SPMs additionally increases this inhibiting effect.

The polarization resistance results concerning the Zn-Co galvanic alloy and its composite (from bath with 0,1 wt.% SPMs) is presented in Figure 3B. Both coating types show an increasing tendency of R_p during the first 72 hours but thereafter the composite one characterizes with higher R_p values. However, the difference between both coatings at the end of the period is very close - in the frames of about 70-80 ohms. This result partially corresponds to the PD investigations which do not show any significant difference between the potentiodynamic polarization curves of the galvanic and composite coating. The reason for this could be explained with the fact that the structure and surface morphology of the composite differ compared to the non-composite Zn and Zn-Co [27]. The surface morphology of the composite Zn-Co can be regarded as a net of SPMs-“chains” (“worm-like” shape), separating the alloy matrix in some kind of individual areas (see Fig. 4). At lower ambient temperature the alloy transforms readily to ZHC forming a protective surface layer. This process is accompanied by an increase of the

volume fraction of the product. Since at higher temperatures the rate is higher mechanical stresses appear and they cannot (there is not enough time to) relax. The resulting stresses lead to more ruptures so the final effect cannot be classified unambiguously as positive for the increasing of the protective ability of the coating.

The results obtained by this method for the galvanic and composite coatings of Zn-Mn (from bath with 0,1 wt.% SPMs) are shown in Figure 3C. It can be registered that the R_p values of the galvanic alloy coating gradually increase up to about 1100 ohm.cm² while the same parameter for the composite one initially decreases and after 150 h sharply increases up to about 2200 ohm.cm². Also here, the reason could be found in the surface morphology – see Figure 4. The galvanic alloy consists of greater aggregates with sizes of about 5-10 μm while the incorporation of SPMs lead to fine and more arranged structure especially in the case when more SPMs are embedded in the Zn-Mn matrix. In the latter case the newly formed ZHC creates something like a net which connect to the individual grains making them in such a case more sustainable and increasing the barrier effect by covering the separate opening on the surface.

4. SCANNING ELECTRON SPECTROSCOPY

Typical surface morphology of non-composite and composite zinc and zinc alloy coatings are presented in Fig. 4.

It is seen that the sample surfaces of the presented coatings exhibit marked differences. The surface of the pure zinc and Zn-Co are relatively smooth and even and the boundaries between the individual grains are not well defined. Contrary to this the surface morphology of the composite zinc is more uneven and the embedded SPMs are easy to be registered. The surface of composite Zn-Co distinguishes with “worm-like” shape which could be explained with additional aggregation of SPMs at these experimental conditions.

The surface of the composite Zn-Mn is in general close to this of the galvanic alloy but seems to be more compact. The embedded SPMs are not well visible and seem to be incorporated in the individual grains. However, their presence is confirmed by the electrochemical test since the composite coatings show better protective properties.

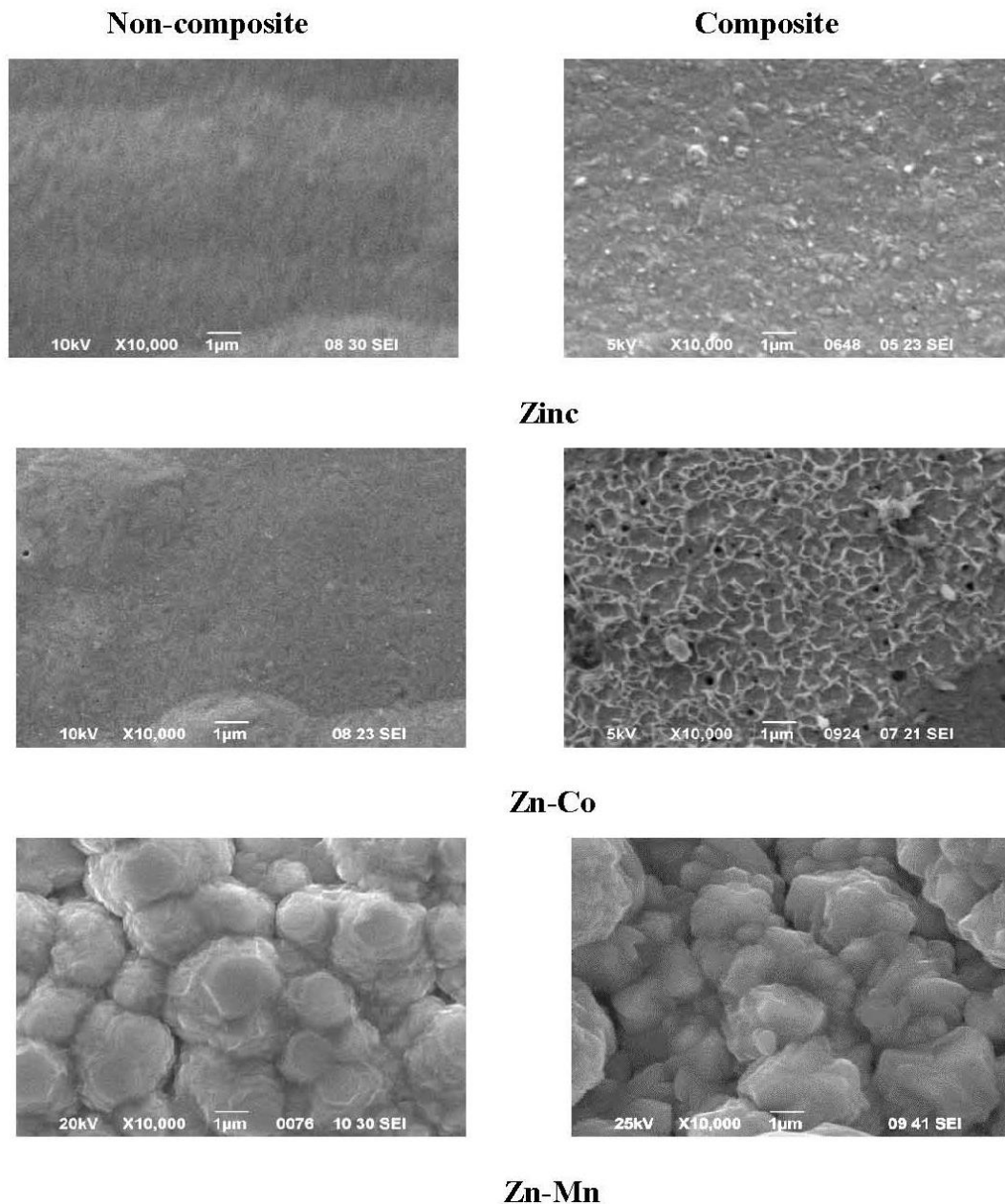


Figure 4. SEM images of non-composite (left) and composite (right) coatings of Zn and zinc based alloys.

5. CONCLUSIONS

The investigated galvanic and composite zinc and zinc based alloy coatings show different corrosion behavior and protective ability in a model medium of 5% NaCl and at ambient temperature of about 30 °C.

In the case of the zinc the incorporation of the SPMs leads to increase of the R_p and to appearance of a pseudo-passive zone at external anodic polarization which means that the composite Zn has better protective properties and susceptibility for passivating in that medium.

Contrary to this, the Zn-Co alloy and its nanocomposites demonstrate in general very close corrosion behavior at external anodic polarization and prolonged R_p measurements. In that case due to

the specific incorporation and distribution of the SPMs into the alloy matrix their influence on the protective ability is controversial.

In the case of Zn-Mn the embedded SPMs show a positive influence leading to greater R_p and to appearance of a pseudo-passive zone at external anodic polarization.

The reasons for this behavior can be summarized mainly in two points:

- the influence of the surface morphology which differs for the individual composites;
- the formation of a mixed barrier layer consisting of corrosion products with a low product of solubility and SPMs, which seems to reinforce in some way the ZHC layer and slows down the progress of the destructive processes into the depth of the coating.

REFERENCES

1. S. Hashimoto, M. Abe, *Corr. Sci.*, **36**, 2125 (1994).
2. P.C. Tulio, S.E.B. Rodrigues, I.A. Carlos, *Surf. Coat. Technol.*, **202**, 91 (2007).
3. T. Ohgai, K. Ogushi, K. Takao, *J. of Physics: Conference Series*, **417**, 012006 (2013).
4. N.R. Short, A. Abibsi, J.K. Dennis, *Trans. Inst. Met. Finish.*, **67**, 73 (1991).
5. T.J. Tuaweri, G.D. Wilcox, *Surf. Coat. Technol.*, **200**, 5921 (2006).
6. A. Grosjean, M. Rezaei, J. Takadoun, P. Bercot, *Surf. Coat. Technol.*, **137**, 92 (2001).
7. P.A. Gay, P. Bercot, J. Pagetti, *Surf. Coat. Technol.*, **140**, 147 (2001).
8. L. Shi, C.F. Sun, F. Zhou, W.M. Liu, *Mater. Sci. Eng. A*, **397**, 190 (2005).
9. Y. Arthoba Naik, T.V. Venkatesha, P. Vasudeva Naik, *Turk. J. Chem.* **26**, 725 (2002).
10. G. Achary, H.P. Sachin, Y. Arthoba Naik, T.V. Venkatesha, *Bull. Mat. Sci.* **30**, 219 (2007).
11. H.B. Muralidhara, Y. Arthoba Naik, T. V. Venkatesha, *Bull. Mat. Sci.* **29**, 497 (2006).
12. H.P. Sachin, G. Achary, Y. Arthoba Naik, T.V. Venkatesha, *Bull. Mat. Sci.* **30**, 57 (2007).
13. K.G. Kariyanna, T.V. Venkatesha, *Bull. Electrochem.* **21**, 547 (2005).
14. C. Muller, M. Sarret, M. Benballa, *Surf. Coat. Technol.*, **162**, 49 (2003).
15. B.M. Praveen, T.V. Venkatesha, Y. Arthoba Naik, K. Prashantaha, *Surf. Coat. Technol.*, **201**, 5836 (2007).
16. X.H. Chen, C.S. Chen, H.N. Xiao, F.Q. Cheng, G. Zhang and G.J. Yi, *Surf. Coat. Technol.* **191**, 351 (2005).
17. A. Vlasa, S. Varvara, A. Pop, C. Bulea, L.M. Mureshan, *J. of Appl. Electrochem.* **40**, 8, 1519 (2010).
18. A. Shamsolhodaei, H. Rahmani, S. Rastegari, *Surf. Eng.*, **29**, 9, 695 (2013).
19. O.S.I. Fayomi, A.P.I. Popoola, C.A. Loto, *Int. J. of Electrochem. Sci.*, **9**, 7, 3885 (2014).
20. O. Hammami, L. Dhouibi, P. Bertzot, E. M. Rezaei, *J. of Appl. Electrochem.*, **44**, 1, 115 (2014).
21. K. Wykpis, J. Niedba, M. Popczyk, A. Budniok, E. Bagiewka, *Russ. J. Electrochem.*, **48**, 11, 1123 (2012).
22. S. Pouladi, M.H. Shariat, M.E. Bahrololoom, *Surf. Coat. Technol.*, **213**, 33 (2012).
23. M. Sajjadnejad, H. Omidvar, M. Javanbakht, R. Pooladi, A.Mozafari, *Trans. Inst. Met. Finish.*, **92**, 4, 227 (2014).
24. K. Vathsala, T. V.Venkatesha, *Appl. Surf. Sci.* **257**, 21, 8929 (2011).
25. P.I. Nemets, M. Zaharescu, L.M. Muresan, *J. Solid State Electrochem.*, **17**, 2, 511 (2013).
26. P.I. Nemets, M. Lekka, L. Fedrizzi, L.M. Muresan, *Surf. Coat. Technol.* **252**, 102 (2014).
27. N. Boshkov, N. Tsvetkova, P. Petrov, D. Koleva, K. Petrov, G. Avdeev, Ch. Tsvetanov, G. Raichevsky, R. Raicheff, *Appl. Surf. Sci.*, **254**, 17, 5618 (2008).
28. D. Koleva, N. Boshkov, V. Bachvarov, H. Zhan, J.H.W. de Wit, K. van Breugel, *Surf. Coat. Technol.*, **204**, 3760 (2010).
29. D.A. Koleva, P. Taheri, N. Tsvetkova, N. Boshkov, K. van Breugel, J. H. W. de Wit, J.M.C. Mol, *ECS Transactions*, **33**, 35, 85 (2011).
30. P. Petrov, M. Bozukov, Ch.B. Tsvetanov, *J. Mater. Chem.*, **15**, 1481 (2005).
31. M. Stern, A.L. Geary, *J. Electrochem. Soc.*, **104**, 56 (1957).

ПОЛУЧАВАНЕ И СРАВНИТЕЛНО КОРОЗИОННО ХАРАКТЕРИЗИРАНЕ НА КОМПОЗИТНИ ЦИНКОВИ И СПЛАВНИ ЦИНКОВИ ПОКРИТИЯ С ВГРАДЕНИ СТАБИЛИЗИРАНИ ПОЛИМЕРНИ МИЦЕЛИ

Н.Д. Божкова¹, П.Д. Петров², Н.С. Божков^{1*}

¹ – Институт по физикохимия, Българска академия на науките

² – Институт по полимери, Българска академия на науките

Постъпила на 15 юли, 2015 г. коригирана на 14 октомври, 2015 г.

(Резюме)

Представени и дискутирани са резултати, свързани с електрохимичното получаване на композитни цинкови и цинкови сплавни покрития (Zn-Co и Zn-Mn) с вградени стабилизирани полимерни мицели (СПМ) на база полипропилен оксид и полиетилен оксид. Процесите на отлагане и разтваряне на цинка и двата вида цинкови сплави в присъствие и отсъствие на СПМ са изследвани с помощта на циклични волтаперометрични криви. Показано и коментирано е влиянието на включените в металната/сплавната матрица СПМ върху повърхностната морфология на получените. Изследвани са корозионното поведение и защитната способност на композитните и некомпозитните покрития в моделна среда, съдържаща хлорни йони като активатори на корозията. Анализирано е влиянието на СПМ върху корозионната устойчивост и защитните свойства на цинка и неговите сплави в тази среда.

Comparative study via nanoindentation of the mechanical properties of conversion corrosion protective layers on aluminum formed in Cr⁶⁺-containing and Cr⁶⁺-free solutions

G.S. Chalakova¹, M.D. Datcheva^{1,*}, R.Z. Iankov¹, A.I. Baltov¹, D.S. Stoychev²

¹*Institute of Mechanics, Bulgarian Academy of Sciences, Acad. G. Bonchev St., Block 4, 1113 Sofia, Bulgaria*

²*Institute of Physical Chemistry "Acad. Rostislav Kaishev", Bulgarian Academy of Sciences, Acad. G. Bonchev St., Block 11, 1113 Sofia, Bulgaria*

Submitted on July 17, 2015; Revised on November 5, 2015

Abstract: The application of chemical conversion coatings (such as chromate, oxide, phosphate, etc.) on various metals and alloys is widely used technology that provides adequate corrosion protection and improves paint adhesion. Most common conversion protective layers are produced by chromating processes using hexavalent chromium containing electrolytes. Although the chromating process has many technological and economic benefits, due to the high toxicity and carcinogenic nature of the used hexavalent chromium the use of chromate conversion coatings is now restricted and it is necessary to find alternative coating materials with relevant properties.

The main purpose of this study is to compare the mechanical properties of traditional chromate conversion coatings with a suggested as their alternative chromate-free cerium-containing conversion coating. For this purpose two chromate-containing and one chromate-free coatings with different thicknesses were deposited on the same Al substrate. As a result of the nanoindentation tests the indentation hardness and modulus of the studied "film-substrate" systems were determined and their relevance to the mechanical properties of the coatings is discussed.

Keywords: conversion protective layers; nanoindentation; indentation hardness; indentation modulus

1. INTRODUCTION

It is known that the native oxide layer (with a thickness of only a few nanometers), formed on aluminum and its alloys provides a certain level of corrosion protection in neutral pH environment. Under aggressive conditions, such as acidic and alkaline environment however, this protection is insufficient which requires the formation of a much thicker surface oxide layer on the order of a few microns (in case of heavy exploitation conditions, including sea conditions – up to ~200 μm). Such layers could be obtained by anodic electrochemical treatment ("anodizing"), using relatively complex, expensive and energy consuming technologies. An alternative of this process are the chemical methods of applying protective and protective-decorative layers on aluminum and its alloys. The main advantages of such chemically "conversion" coatings are the fairly simple equipment design, practically negligible energy costs and significantly reduced complexity and labor intensity of the entire process. This type of coatings, obtained on aluminum and its alloys, are preferably used as an intermediate layer before applying the paint and other functional organic coatings, as their porous

structure determines the required adhesion. The application of such protective system (Al/oxide layer/functional organic layer) fulfills one of the main requirements for protecting aluminum and its alloys – to suppress, as much as possible, the electrochemical activity of the highly electronegative basic metal.

The chemically deposited layer serves as an intermediate buffer layer which determines the bond strength between the organic coating and the aluminum substrate. Therefore, when thermal and mechanical stresses are applied to the system Al/functional layers, the mechanical properties of the chemically deposited intermediate oxide layer determines the bond strength between the top organic coating and the aluminum substrate.

Among the most commonly used conversion layers with proven properties are those obtained from hexavalent chromium-based electrolytes [1]. Due to their carcinogenic and toxic nature however [2], their usage has been forbidden by the European regulations [3]. During the past few years, extensive research to develop new, environmentally- and health-friendly compounds and technologies for deposition of functional oxide layers on Al and its alloys has been conducted.

The purpose of this study is to determine and compare mechanical properties of chemically deposited oxide layers on aluminum, considering

*To whom all correspondence should be sent:
E-mail: datcheva@imbm.bas.bg

the layer composition and processes technology. Three different coatings and technologies were used:

- “Alodine 1200” electrolyte and technology by the German brand Henkel (widely used current trade product);
- classical chromate electrolyte and technology (adopted as reference case) and
- thin cerium oxide layer free of toxic Cr^{6+} ions and simple electrochemical technology allowing cathodic deposition of these coatings that we developed (environment-friendly composition and technology).

2. THEORY OF NANOINDENTATION - BRIEF INTRODUCTION

Nanoindentation, also known as “depth sensing indentation” and “instrumented indentation” is a kind of mechanical test, which allows simultaneous registration of the applied load and indenter penetration depth. This method allows testing of small volumes, surface layers and very thin coatings against their mechanical response to the indenter penetration. As a result, an indentation curve that represents the relation between the applied load and the indenter penetration depth is obtained. Using analytical relationships and approximations, it is possible to derive mechanical characteristics such as indentation hardness (H_{IT}) and indentation modulus (E_{IT}) of the tested material from this curve.

The modern nanoindentation instruments allow registering of very small loads and displacements with very high accuracy and precision. Figure 1 schematically presents the nanoindentation experiment as well as depicts the main parameters, derived from the “load-displacement” curve.

There are three main parameters that can be derived from the curve shown in Figure 1: 1) maximal load P_{\max} ; 2) maximal displacement (penetration depth) h_{\max} and 3) the elastic stiffness at unloading [5]. The elastic stiffness, or contact stiffness is determined as the slope of the tangent at the upper part of the unload curve during the initial stage of unloading and is equal to $S = dP/dh$. The first portion of the unloading curve can be described by a simple power law relationship $P=K(h-h_f)^m$, with K and m being fitting parameters [6]. The deformation during unloading is assumed to be linear elastic and the indentation modulus of the tested material can be described by the contact theory of elasticity [6]. Following the Oliver and Pharr’s theory [6], the contact compliance in case of axisymmetric indenter penetrating elastic isotropic half-space is described via the equations:

$$C_s = \frac{1}{S} = \frac{dh}{dP} = \frac{\sqrt{\pi}}{2} \cdot \frac{1}{\sqrt{A}} \cdot \frac{1}{E_r}, \quad (1)$$

$$\frac{1}{E_r} = \frac{(1-\nu_s^2)}{E_{IT}} + \frac{(1-\nu_i^2)}{E_i}, \quad (2)$$

where A is the projected contact surface area, C_s is the ductility of the specimen and P – the applied force. In these formulas E_r is the elastic reduced modulus explaining the elastic deformation of both the indenter and the specimen. E_{IT} , E_i ; ν_s and ν_i are the modules of elasticity and the Poisson ratios of the specimen and the indenter, respectively. The following relation is used to determine the reduced modulus employing the information provided by the measured load-displacement curve $P(h)$:

$$E_r = \frac{dP}{dh} \Big|_{h=h_{\max}} \frac{\sqrt{\pi}}{2\beta\sqrt{A(h_c)}}, \quad (3)$$

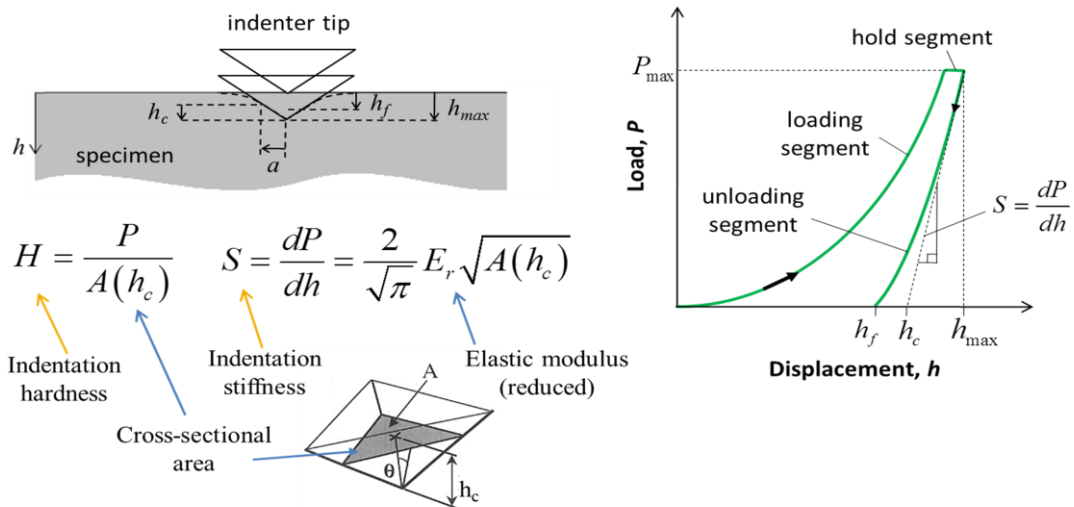


Figure 1. Scheme of the nanoindentation experiment, “load-displacement” curve and main analytical relationships [4].

For Berkovich indenter tips the coefficient $\beta = 1.034$. The projected area of the contact between the indenter and the specimen as a function of the contact depth h_c is introduced by the following approximation [6]:

$$A(h_c) \approx C_0 h_c^2 + C_1 h_c + C_2 h_c^{1/2} + C_3 h_c^{1/4} + C_4 h_c^{1/8} + C_5 h_c^{1/16} \quad (4)$$

The coefficients in equation (4) are determined by a calibration procedure that consists of a nanoindentation experiment on standardized quartz sample (fused silica) with known elastic modulus and hardness, independent of the indentation depth. Finally, the indentation modulus and hardness are calculated using the following equations [6]:

$$H_{IT} = \frac{P_{\max}}{A(h_c)}, S = Km(h_{\max} - h_f)^{m-1} \quad (5)$$

$$E_{IT} = (1 - \nu_s^2) \left[\frac{2\beta}{S} \sqrt{\frac{A(h_c)}{\pi}} - \frac{1 - \nu_i^2}{E_i} \right]^{-1} \quad (6)$$

3. EXPERIMENTAL

A series of nanoindentation tests on samples coated by three different conversion protective layers were performed. The purpose was to determine the basic mechanical characteristics of the thin layers – indentation hardness and indentation modulus – in order to compare chemical compounds and used technologies. The device used for the purpose is Nano Indenter Agilent G200 (Keysight Technologies) with a standard XP indenter head, which provide depth accuracy of $<0.01\text{nm}$ and applied load accuracy of 50 nN . The tip of the head is sharp tree-sided Berkovich pyramid. The performed calibration of the indenter tip according to equation (4) gave $C_0=24.5$, $C_1=191.949$, $C_2=9.1145$, $C_3=2.9682$, $C_4=1.9721$, $C_5=1.6836$.

The three thin coatings that are studied obey different thickness and chemical composition – the details are given in Table 1. The samples were prepared in the following way. First, specimens

with dimensions $2 \times 1 \times 0.1\text{cm}$, were cut from sheets of the conventional structure material – “technically pure aluminum AD-3”. The specimens were decreased in advance in organic solvent, etched after that for 1 minute in aqueous solution of NaOH (60g/L), then heated to 60°C and “enlightened” and finally put in aqueous solution of HNO_3 (50%). After they were washed with distilled water they were processed in the solutions and under the conditions given in Table 1. On the surface of the sample piece with Cr^{6+} -free coating it was observed a spot and in order to have representative data we performed indentation test in the spot area (Spot) and outside it (No Spot). It is expected to have difference in the quality and properties of the film in the colored (Spot) area. More detailed information about preparation conditions, structure and anti-corrosion behavior of these systems is given in [8].

We used two methods for indentation testing and these methods were applied to each of the three coating-substrate systems.

XP\G-Series Basic Hardness, Modulus at a Depth: allows indentation test program consisting in one single load – unloading cycle under displacement control. The indenter tip approaches the sample surface starting from prescribed *Surface Approach Distance* with a velocity defined as *Surface Approach Velocity*. After the indenter tip touches the sample surface, according to the criterion given by the *Surface Approach Sensitivity*, it starts to penetrate the material following a loading program with a *Strain Rate Target* until *Depth Limit* is reached. The *Depth Limit* defines the maximum applied load for the particular test and this load is kept constant for defined by the user *Peak Hold Time*. When the *Peak Hold Time* is exceeded the unloading starts up to a prescribed percentage (*Percent to Unload*) from the maximum achieved load followed by *Drift Test Segment* before the indenter to be completely withdrawn.

Table 1. Characteristics of the coatings and their processing parameters.

No.	Electrolytes	Concentration	Time of formation, min	T, °C	Colour	Thickness, μm
1	Al in air media	-	> 1	Room temperature	Colourless	3×10^{-3} [7]
2	Alodine 1200	9 ml/l A 8 g/l B	1	25	Light yellow	1.1
3	CrO_3 $(\text{NH}_4)\text{HF}_2$ $\text{K}_3[\text{Fe}(\text{CN})_6]$	8 g/l 2 g/l 1.5 g/l	1,5	25	Golden brown	1
4	$\text{CeCl}_3 \cdot 7\text{H}_2\text{O}$ CuCl_2 $\text{C}_2\text{H}_5\text{OH}$	66 g/l 1×10^{-3} g/l dissolving agent	60 ($\text{CD}=1\text{mA}/\text{cm}^2$)	12	Pale yellow	0.78

XP\G-Series Basic Hardness, Modulus, Tip Cal, Load Control. This method allows within one indentation test to perform loading-unloading cycles up to prescribed maximum load and number of cycles. The indenter approaches the sample surface with *Surface Approach Velocity* starting from the predefined *Surface Approach Distance*. The cyclic load algorithm starts when the criterion *Surface Approach Sensitivity* is satisfied. The maximum load for the *i*-th cycle of the loading program is defined as:

$$(Maximum\ Load/Time\ to\ Load) * (2^i / 2^{Number\ of\ Times\ to\ Load})$$

The loading stage of each cycle ends when *Load on Sample* reaches the values *Maximum Load * (2ⁱ / 2^{Number of Times to Load})*. At the maximum load for each of the cycles the *Load on Sample* is kept constant for time equal to the *Peak Hold Time*. After that the indenter is withdrawn with a rate defined as *Load Rate Multiple for Unload * Loading Rate*, until *Load on Sample* reaches *Percent to Unload * Load Limit*. This process of loading and unloading is repeated until reaching the specified number of cycles (*Number of Times to Load*).

Besides the mechanical characteristics of the coatings, the characteristics of the substrate are determined too. A single method was used for conducting the experiment following the program with 10 cycles to maximum indenter load (method - XP\G-Series Basic Hardness, Modulus, Tip Cal, Load Control).

3.1. Indentation testing program A

The method applied in testing program A is XP\G-Series Basic Hardness, Modulus at a Depth. Each testing procedure consists of 25 indentation tests per sample with 70 μm distance between the

centres of the imprints and prescribed maximum penetration depth approximately quarter of the film thickness – 250 nm for Alodine 1200 and Cr⁶⁺-containing film and for 200 nm for the Ce-containing film (the chosen indentation depths are ~25% of films thicknesses). The peak hold time at maximum reached load is 20 s.

3.2. Indentation testing program B

The testing program B employs the method XP\G-Series Basic Hardness, Modulus, Tip Cal, Load Control with 4 loading cycles with maximal loading of 0.95 mN providing this way experimental data at indentation depth close to that prescribed in testing program A. The distance between imprints is 50 μm and the total number of indentations is 25. The aim of this type of nanoindentation testing program is to investigate the influence of the cyclic loading on the results when penetrating the coatings under low force.

3.3. Indentation testing program C

The testing program C employs the same method as B testing program with prescribed parameters for the method given in Table 3. The distance between the centers of the imprints is again 150 μm and the number of the indentation tests per sample is kept 25 for checking the repeatability.

Figure 2 presents the comparison between the results obtained within A and B testing programs. We compare the results when cyclic and no-cyclic load is applied to the specimens. The maximum indentation depth - *h_{max}* for each specimen in both cases (A and B programs) is ~25% of film thickness. Figure 3 presents the results from Indentation testing program C.

Table 2. Input parameters for indentation testing program B

Input parameters for indentation testing program B	Units	Value
<i>Percent to Unload</i>	%	90
<i>Surface Approach Velocity</i>	nm/s	10
<i>Maximum Load</i>	gf	0.095
<i>Number of Times to Load</i>	integer	4
<i>Peak Hold Time</i>	s	20
<i>Surface Approach Distance</i>	nm	5000
<i>Poisson's Ratio</i>	[-]	0.3

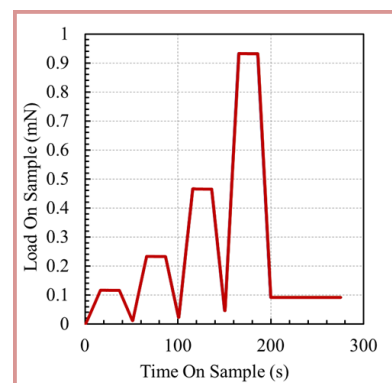
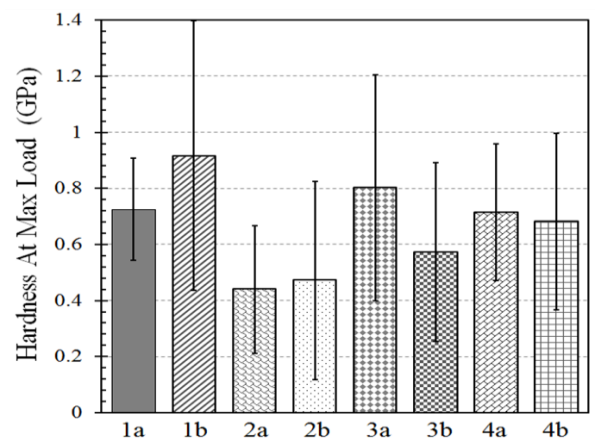
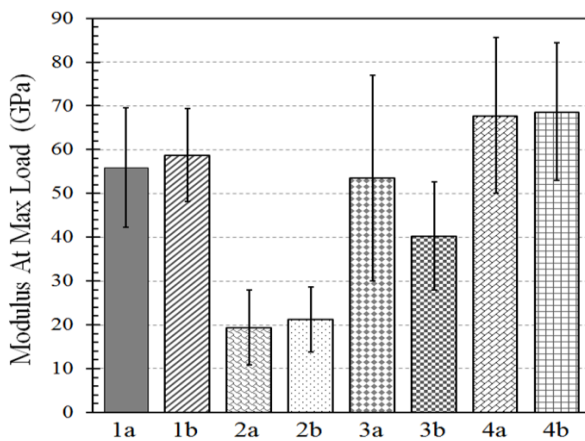
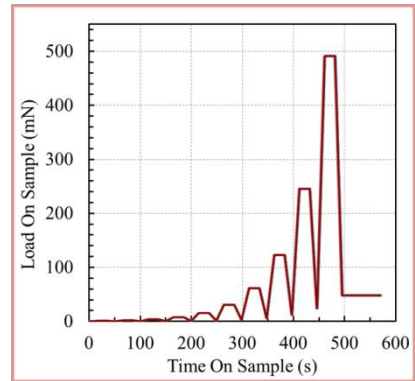


Table 3. Input parameters for indentation testing program C.

Input parameters for indentation testing program C	units	values
Percent to Unload	%	90
Surface Approach Velocity	nm/s	10
Maximum Load	gf	50
Number of Times to Load	integer	10
Peak Hold Time	s	20
Surface Approach Distance	nm	5000
Poisson's Ratio	[-]	0.3



Sample	Modulus at Max Load GPa	Hardness at Max Load GPa	Disp at Max Load nm	Max Load mN
1a Alodine1200 (Cr ⁶⁺ -containing) / AD-3 h _{max} 250 nm	55.888	0.725	259.7	1.136
1b Alodine1200 (Cr ⁶⁺ -containing) / AD-3 4 cycles up to 0.095gf (0.95 mN)	58.717	0.917	220.6	0.918
2a Cr ⁶⁺ -containing film / AD-3 h _{max} 250 nm	19.419	0.44	267.4	0.687
2b Cr ⁶⁺ -containing film / AD-3 4 cycles up to 0.095gf (0.95 mN)	21.228	0.472	347.4	0.913
3a (Cr ⁶⁺ -free) Ce-film NoSpot / AD-3 h _{max} 200 nm	53.542	0.802	214.1	0.826
3b (Cr ⁶⁺ -free) Ce-film NoSpot / AD-3 4 cycles up to 0.095gf (0.95 mN)	40.261	0.573	288.8	0.915
4a (Cr ⁶⁺ -free) Ce-film Spot / AD-3 h _{max} 200 nm	67.815	0.714	211.1	0.755
4b (Cr ⁶⁺ -free) Ce-film Spot / AD-3 4 cycles up to 0.095gf (0.95 mN)	68.643	0.682	256.9	0.915

Figure 2. Indentation modulus and hardness at max load for all samples – test programs A and B

Table 4 presents the comparison between the determined indentation hardness and modulus for all samples and for the substrate at maximum load 500 mN (results obtained from experimental program C).

4. DISCUSSION

The main feature of the obtained data is that at small displacements of the indenter (up to about 25% of the thickness of the tested coatings), there is relatively large scatter of the experimental data. This can be seen in Figure 2 where the error bars

are given. The main reasons for this scatter in the mechanical characteristics are most probably related to:

- non-uniform or non-homogeneous coating;
- severe roughness of the substrate surface, which determines severe roughness of the coatings as well;
- difference in the particular thickness of the tested coatings or/and varied coating thickness along the particular sample piece.

Increasing the depth of the penetration, when the indenter reaches the substrate and penetrates it,

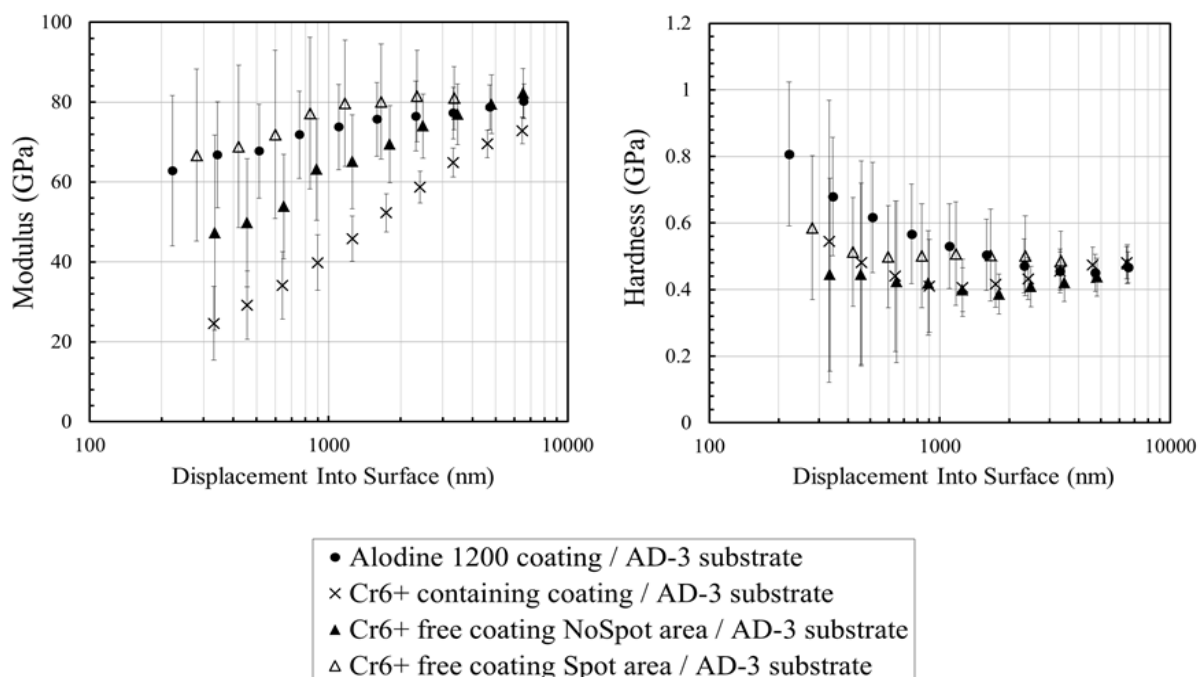


Figure 3. Indentation modulus and hardness for all samples – test program C.

Table 4. Indentation hardness and modulus for all samples and the substrate at maximum indentation load 500 mN (data obtained from indentation testing program C).

Sample	Modulus at Max Load, GPa	Hardness at Max Load, GPa	Displacement at Max Load, nm	Max Load, mN
Alodine 1200 (Cr⁶⁺-containing) /AD-3 10 cycles up to 50 gf (500 mN)	80.211	0.467	6642.3	483.578
Cr⁶⁺-containing film / AD-3 10 cycles up to 50 gf (500 mN)	72.901	0.481	6557.2	483.266
(Cr⁶⁺-free) Ce-film NoSpot / AD-3 10 cycles up to 50 gf (500 mN)	82.288	0.477	6589.2	484.937
(Cr⁶⁺-free) Ce-film Spot / AD-3 10 cycles up to 50 gf (500 mN)	80.940	0.488	6512.5	484.045
Al: AD-3 10 cycles up to 50 gf (500 mN)	85.722	0.481	6543.3	483.384

the scatter in the data gradually decreases. In this case, the obtained mechanical characteristics of the system are determined by the characteristics of the aluminum substrate, Figure 3.

5. CONCLUSIONS

In this study the mechanical properties of environment-friendly thin oxide layers of CeO₂ on aluminum substrate are determined via nanoindentation testing. The importance of the obtained results is related to the fact that the CeO₂ coatings may be considered as a long-term alternative to toxic and carcinogenic chromate conversion films, currently used to protect Al and its alloys. The comparison of the mechanical properties of the chromate and the newly proposed chromate free coatings determined by nanoindentation shows that the properties of the cerium oxide layer are not

inferior to those of Alodine 1200 and, moreover, are better than the mechanical characteristics of chemically applied classic chromate layers. The next outcome is that the results show that instrumented indentation is a promising experimental technique giving the opportunity to determine mechanical properties of these coatings, which is an important addition to the complete characterization of the chemical and mechanical behavior of metal-functional layer systems.

Acknowledgements. The financial support of the Bulgarian National Science Fund under grant T02/22 is gratefully acknowledged. The authors also wish to thank Dr. E. Stoyanova and MSc. Eng. R. Andreeva for their assistance in sample preparation and to Mr. S. Dobrev for helping with processing the experimental data.

REFERENCES

1. A.Ginberg, A.Ivanova, I.Kravchenko, Galvanotechnika (Handbook), Metallurgia, Moscow, p. 449, 1987 (in Russian).
2. H. Shafer, H.R. Stock, *Corrosion Sci.*, **47**, 963 (2004)
3. P.L. Hagans, C.M. Hass, ASM Handbook Volume: Surface Engineering, **5**, 405-41, (1994).
4. E. McCumiskey, Master's Thesis Presentation, 23 January 2008, Virginia Commonwealth University.
5. M. Datcheva, S. Cherneva, M. Stoycheva, R. Iankov, D. Stoychev, *Materials Sci. Appl.*, **2**, 1452 (2011).
6. W. Oliver, G. Pharr, *J. Materials Res.*, **7**, 1564 (1992).
7. S.Wernik, R.Piner, The Surface Treatment and Finishing of Aluminium and Its Alloys, Teddington, Robert Draper Ltd. 1972.
8. E. Lukanova, E. Stoyanova, M. Damyanov, D. Stoychev, *Bulg. Chem. Commun.*, **40**, 340 (2008).

СРАВНИТЕЛНО ИЗСЛЕДВАНЕ ЧРЕЗ НАНОИНДЕНТАЦИЯ НА МЕХАНИЧНИТЕ СВОЙСТВА НА КОНВЕРСИОННИ ЗАЩИТНИ СЛОЕВЕ ВЪРХУ АЛУМИНИЙ, ОТЛОЖЕНИ ОТ СЪДЪРЖАЩИ И НЕСЪДЪРЖАЩИ Cr^{6+} РАЗТВОРИ

Г. С. Чалъкова¹, М. Д. Дачева¹*, Р. З. Янков¹, А. И. Балтов¹, Д. С. Стойчев²

¹Институт по механика, Българска академия на науките

²Институт по физикохимия "Акад. Р. Каишев", Българска академия на науките

Постъпила на 17 юли 2015 г., коригирана на 5 ноември 2015 г.

(Резюме)

Нанасянето на химични конверсионни покрития (хроматни, оксидни, фосфатни и др.) върху различни метали и сплави е широко използвана технология, осигуряваща корозионна защита и подобряване на адхезията при нанасянето върху тях на лаково-бояджийски и други покрития. Най-често използвани в практиката са Cr^{6+} -съдържащите (т.нар. хроматни) конверсионни покрития, които се характеризират с много добри корозионно-защитни свойства. Въпреки известните технологични и икономически предимства обаче, използването им, към настоящия момент, е прекратено поради тяхната висока токсичност и канцерогенност. Необходимо е да се намерят достатъчно добри алтернативи на тези покрития, чиито свойства в максимална степен да се доближават до тези на хроматните. В настоящото изследване, чрез експеримент на nanoindentation, са определени механичните характеристики на три системи от типа „покритие - подложка”. В две от тези системи, върху отделни подложки от технически чист алуминий АД 3 с дебелина 1мм, са нанесени две конверсионни покрития с различни дебелини. В третата система, върху подложка със същите характеристики, е нанесено несъдържащо Cr^{6+} цериевооксидно покритие, което е пример за ново екологично конверсионно покритие. Целта на изследването е да бъдат сравнени механичните характеристики на две различни по състав хроматни покрития с предложеното ново, несъдържащо хром цериевооксидно покритие. В резултат от проведените експерименти са определени и сравнени две от основните механични характеристики на разглежданите системи – твърдост при индентация (H_{IT}) и индентационният модул (E_{IT}).

Silver electrocrystallization at PEDOT-coated electrodes – interpretation of current transients

Vassilena I. Karabozhikova, Vessela Ts. Tsakova*

Institute of Physical Chemistry, Bulgarian Academy of Sciences, 1113 Sofia, Bulgaria

Submitted on July 14, 2015; Revised on October 13, 2015

Abstract. Silver electrodeposition is studied at poly(3,4-ethylenedioxythiophene) (PEDOT)-coated electrodes under potentiostatic conditions. The PEDOT layers are obtained in the presence of polystyrene sulfonate (PSS) or dodecyl sulfate (DDS) ions in the polymerization solution. Sets of silver electrocrystallization current transients are registered at different constant potentials for both types of PEDOT layers. It is found that silver electrocrystallization is markedly more intensive on PEDOT/DDS-modified electrodes with larger number of crystals observed on the electrode surface. The current transients are interpreted by a theoretical model accounting for progressive nucleation and diffusion controlled growth of the metal phase. Discrepancies between the long-time behavior of experimental and theoretical current transients are discussed in terms of deviation from some of the prerequisites of the theory.

Keywords: electrocrystallization; silver; PEDOT; polystyrene sulfonate; dodecyl sulfate

1. INTRODUCTION

Numerous studies on the electrodeposition of metal particles on conducting polymer coated electrodes are conducted with the aim to obtain electrocatalytic materials with well dispersed metallic particles (see [1-4] and literature cited therein). There are several attempts to reveal the kinetics of nucleation and growth in various metal/polymer systems by studying the process under potentiostatic conditions. When considering the metal electrocrystallization process in these cases it is generally assumed that provided the polymer material is in its high conducting state the modified electrodes behave as conventional conducting substrates. Therefore, the usual theoretical models for electrochemical nucleation and growth are used to interpret experimentally obtained potentiostatic current transients. Especially when studying the process under diffusion controlled growth the well-known theoretical equation of Scharifker et al [5] is applied. It is known that this approach provides the opportunity to obtain data for the number of active sites for nucleation and the nucleation rate at a single nucleation site and thus gives insight into the role of the substrate for the metal nucleation process.

The present investigation aims at a detailed analysis of the feasibility of the Scharifker theoretical equation for describing silver electrocrystallization on poly(3,4-ethylenedioxythiophene) (PEDOT). This conducting polymer was

chosen not only because of its involvement in various applications and known stability [6,7], but also because its redox transition (i.e. the transition from high- to low-conducting state) occurs in a potential region which is far from the overpotential interval where silver is expected to deposit. Silver, on the other hand, was chosen both as a catalytic metal that may be involved in different electrocatalytic reactions, but also as a model metal that is known to have a high exchange current density. The latter is a prerequisite for fast establishment of diffusion controlled growth of the silver crystals, which is a necessary condition for the use of the theoretical expression for the current of nucleation and growth derived in [5].

Silver electrocrystallization was already studied on polyaniline (PANI)-coated electrodes with different thickness [8, 9]. In an early work [8] very thin PANI coatings (with average thickness not exceeding 50 nm) were used and the results related basically to silver deposition on a partially blocked platinum surface. Later, compact PANI layers were explored as substrates for the electrocrystallization of silver [9]. It was found that the metal phase formation occurs with large overpotentials so that in some experiments the silver deposition overpotential overlapped with the potential interval where the reductive transition of PANI takes place. Besides, even in the case where lower overpotentials were used large pseudocapacitive currents interfered with the silver electrocrystallization currents which complicated the interpretation of the experimental transients. Metal electrocrystallization under diffusion control on conducting polymer substrates was studied also

*To whom all correspondence should be sent:

E-mail: tsakova@ipc.bas.bg

in the case of Pd deposition on polypyrrole [10], polyaniline [10], and PEDOT [11], and silver deposition on poly(*o*-aminophenol) [12]. In all these cases, however, there were additional effects, e.g. large additional currents due to parallel reactions [10], significant delays in the onset of the nucleation process [11] or deposition on low-conducting substrate [12] which complicated the application of the theoretical model [5] for interpretation of the experimentally obtained current transients.

In the present study we use PEDOT layers with fixed polymerization charge corresponding to thick compact layers. Silver electrocrystallization is studied at low overpotentials so that there is no considerable contribution of the polymer intrinsic pseudocapacitive currents to the reductive currents measured in the course of electrocrystallization. Potentiostatic current transients are obtained at two types of PEDOT layers differing by the types of anions used in the course of their synthesis. It is known that anions present in the polymerization solution are involved in the charge compensation of the polymer chains and affect markedly the electrochemical polymerization process, the structure and surface morphology of the resulting layers as well as their electrocatalytic properties. This was demonstrated recently specifically for PEDOT polymerized in the presence of low amounts of organic anions and a large excess of perchlorate anions in the polymerization solution [13, 14]. Therefore, it could be expected that the nucleation process and most probably the number of active sites for nucleation will be also affected.

2. EXPERIMENTAL

The electrochemical measurements were carried out by means of a computer driven potentiostat/galvanostat (Autolab PGSTAT 12, Ecochemie, The Netherlands) in a three-electrode set-up. The working electrode was glassy carbon with surface area $S = 0.08 \text{ cm}^2$, a platinum plate was used as counter electrode and the reference electrode was a mercury/mercury sulfate electrode (Hg/Hg₂SO₄/0.5 M K₂SO₄). All potentials in the text are referred to the saturated mercury sulfate electrode (MSE) ($E_{\text{MSE}} = 0.66 \text{ V}$ vs. standard hydrogen electrode). The electrolyte solutions were de-aerated with argon before the onset of electrochemical measurements.

Polymerization of EDOT was carried out at constant potential $E_a = 0.38 \text{ V}$ in aqueous solutions of 10 mM PEDOT, 0.5 M LiClO₄ and 34 mM organic anionic dopant, either sodium polystyrene sulfonate (PSS) or sodium dodecyl sulfate (SDS).

The polymerization charge in the present series of experiments was fixed to 2 mC. This charge was reached for different times depending on the doping organic anions present in the solution [13, 14]. After synthesis the polymer-coated electrodes were transferred in supporting electrolyte (0.4 M HClO₄) to measure their voltammetric behaviour.

The solution used for electrocrystallization of silver consisted of 10 mM AgNO₃ and 0.4 M HClO₄. The equilibrium potential of silver in this solution is 0.0 V vs MSE. The electrodeposition of silver was carried out at different constant potentials and series of current transients were registered for each type of PEDOT layer. One and the same PEDOT layer was used for each series. In all cases several measurements were carried out until stable and repeatable current transients could be obtained. Under such conditions three current transients were registered for each potential. After each silver deposition experiment silver was dissolved in the silver plating solution by applying a voltammetric scan at potentials more positive than the equilibrium potential of Ag.

SEM was performed by using a Jeol 6390 device equipped with Inca Oxford EDX analyzer.

3. RESULTS AND DISCUSSION

Figure 1 shows sets of potentiostatic current transients of silver electrocrystallization registered at different potentials for the PEDOT/PSS- and PEDOT/DDS-coated electrodes. The comparison of the transients obtained at equal potentials for both types of layers shows that the current measured at PEDOT/DDS is markedly higher, thus, indicating to a more intensive metal nucleation and growth process. The dashed grey lines in the figure denote the limiting diffusion current of silver ions calculated by means of Cottrell equation:

$$I = \frac{SFzD^{1/2}c}{(\pi)^{1/2}} \quad (1)$$

with $D = 1.65 \times 10^{-5} \text{ cm}^2 \text{ s}^{-1}$ [15] and $S = 0.08 \text{ cm}^2$, i.e. the geometrical surface area of the electrode.

As should be expected the Cottrell current exceeds all measured current transients in the case of PEDOT/PSS (Fig. 1 a). However, the current transients measured at the PEDOT/DDS-coated electrode overshoot the Cottrell limit (Fig. 1 b), which contradicts one of the prerequisite of the model developed in [5].

The experimental current transients were further fitted by the well-known expression for nucleation and diffusion controlled growth derived by Scharifker et al. [5]:

$$I = \frac{P_3}{t^{1/2}} \left(1 - \exp \left(-P_2 \left(t - \frac{1 - \exp(-P_1 t)}{P_1} \right) \right) \right) \quad (2)$$

where

$$P_1 = A \quad (3)$$

$$P_2 = N_0 \pi D (8 \pi c \nu_\mu)^{1/2} \quad (4)$$

$$P_3 = S z F D^{1/2} c / \pi^{1/2} \quad (5)$$

In Eqns. (3-5) $A [s^{-1}]$ is the nucleation rate at a single nucleation site, $N_0 [cm^{-2}]$ is the number of active sites on the electrode surface, $c [mol cm^{-3}]$ is the concentration of the silver ions in solution, and ν_μ is the molar volume of silver. All remaining quantities have their usual meaning.

The fitting procedure was carried out by a best fit computational code using three free parameters (P_1 , P_2 and P_3). In fact, P_3 should be a constant for all experimental current transients once it is presumed that the same surface area is operative for the diffusion-controlled growth process. The use of three free parameters for fitting the experimental

transients resulted for both sets of measurements in a very good correspondence between experimental data and calculated ones. An illustration is shown in Fig. 2 for two potentials (-0.06 V and -0.03 V) with grey full lines denoting the best fit transients. However, it was found that the values of P_3 vary markedly with applied potential (Fig. 3) and this trend is more apparent in the PEDOT/DDS experimental series. With increasing overpotential in the case of PEDOT/PSS the value of P_3 gradually reaches the theoretical one, which should mean that for low overpotentials the complete geometrical surface area of the electrode is not operative for diffusion. On the other hand, the values of P_3 obtained from the PEDOT/DDS series exceed the theoretical one (grey line in Fig.3). If the final value of P_3 (at $E = -0.06 V$) is used to recalculate the involved surface it turns out that the surface area should have increased by 35%.

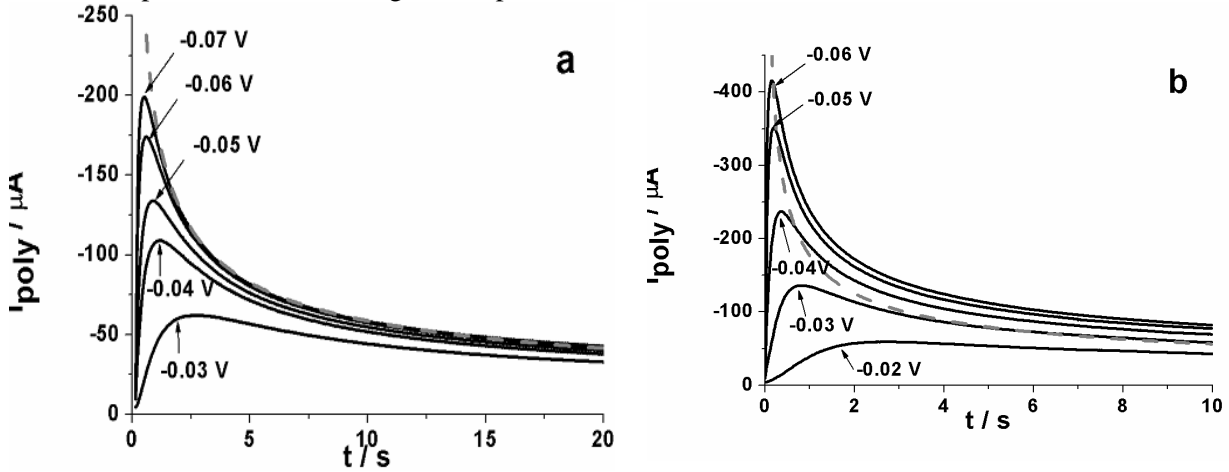


Figure 1. Potentiostatic current transients measured at different constant potentials at (a) PEDOT/PSS- and (b) PEDOT/DDS-modified electrodes. Dashed lines denote the Cottrell limiting current calculated according to eqn. (1)

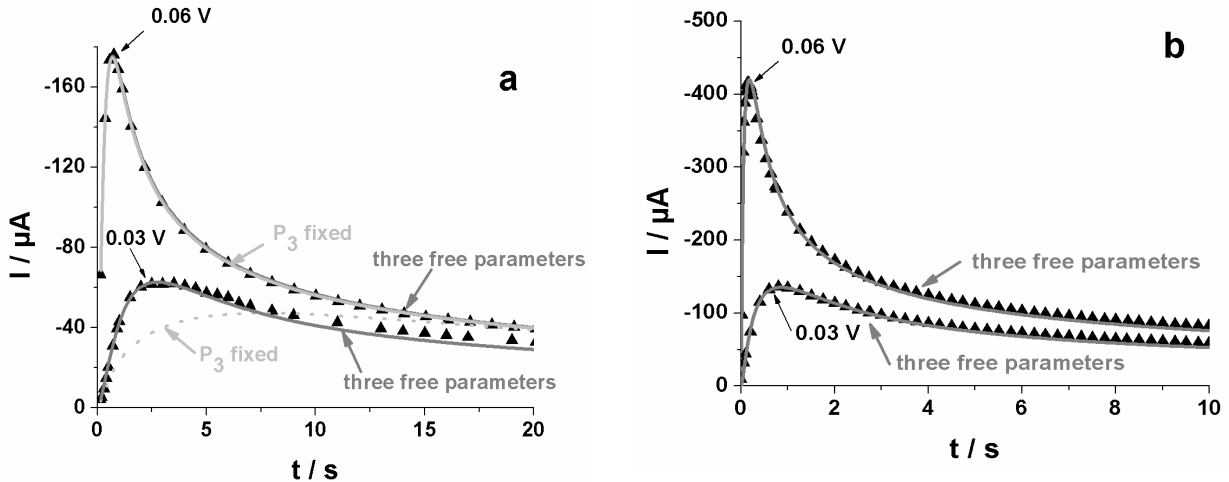


Figure 2. Best fit according to eqn. (2) (grey lines) of experimental current transients (black triangles) with three free parameters for experiments at PEDOT/PSS (a) and PEDOT/DDS (b) coated electrodes. The grey dotted line in (a) denotes the result from a best fit with fixed value of $P_3 = 1.77 \times 10^{-4} [C s^{-1/2}]$.

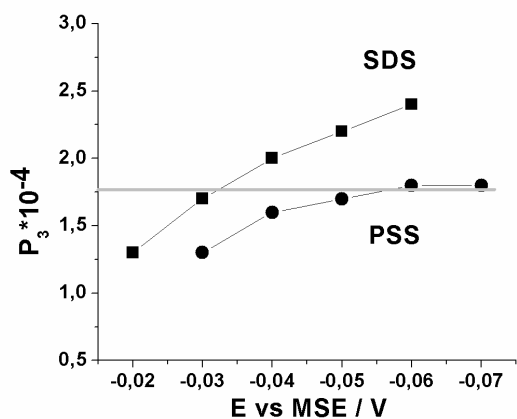


Figure 3. Data for P_3 obtained from best fit of the current transients in Fig. 1 from the PEDOT/PSS (●) and PEDOT/DDS (■) series. The grey line denotes the theoretical value of P_3 .

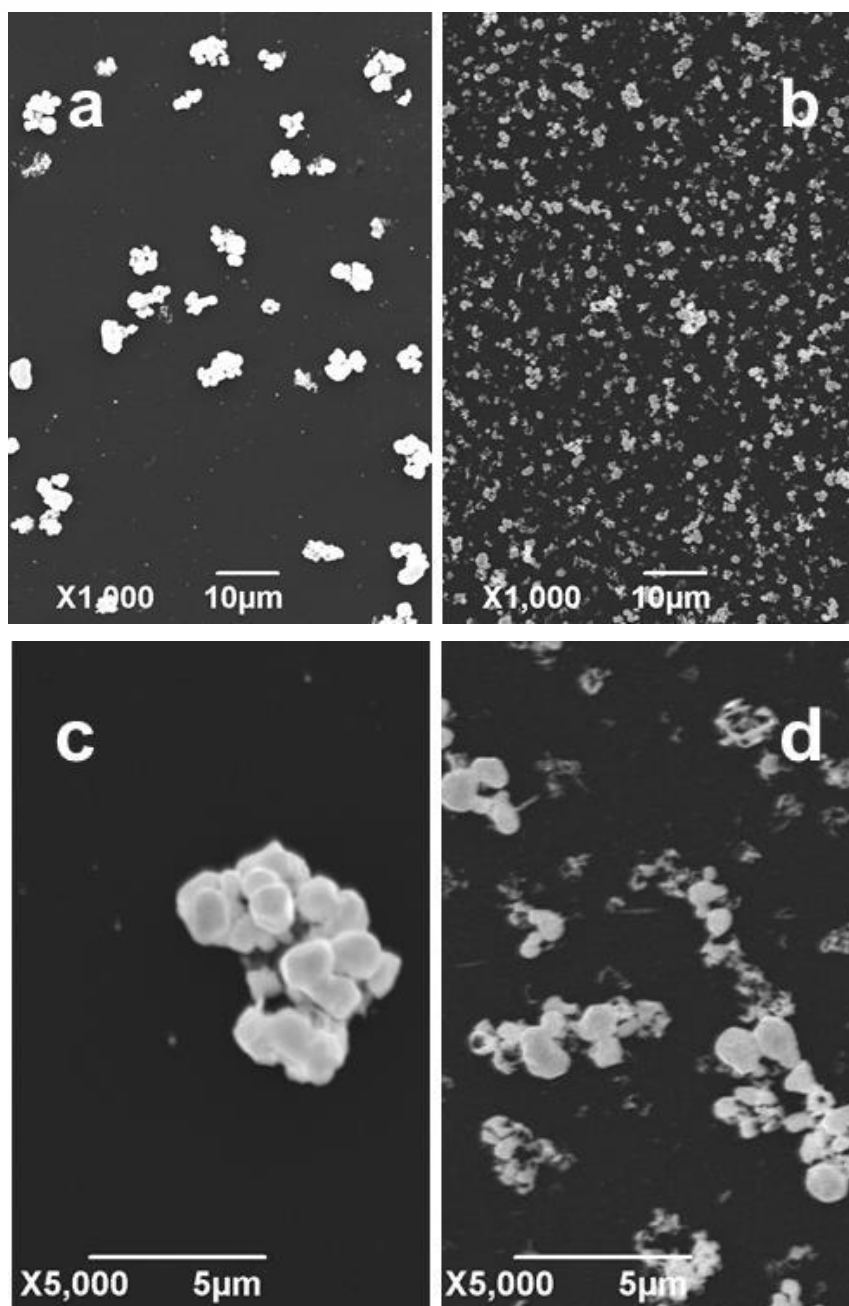


Figure 4. SEM micrographs of silver crystalline species obtained at (a, c) PEDOT/PSS- and (b, d) PEDOT/DDS-coated electrodes. The electrodeposition was carried out at $E = -0.05$ V.

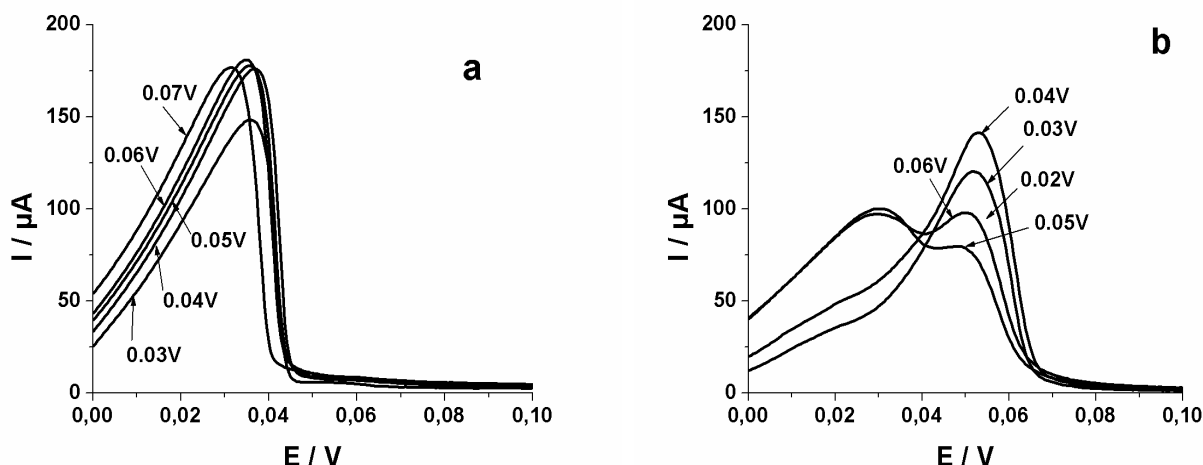


Figure 5. Voltammetric curves of silver dissolution obtained after deposition at different constant potentials at (a) PEDOT/PSS- and (b) PEDOT/DDS-coated electrodes.

Although the PEDOT-modified electrodes are expected to have surface roughness that may theoretically result in a surface area that is higher than the geometrical one, it remains still unclear why there is such a strong dependence of P_3 on applied potential.

To clarify this issue PEDOT/PSS- and PEDOT/DDS-coated electrodes with electro-deposited silver crystals were observed by SEM (Fig. 4). A definite difference in the type of the obtained silver deposit was found for both specimens. A small number (about $5.1 \times 10^5 \text{ cm}^{-2}$) of bulky crystals (or rather clustered crystals) was observed on PEDOT/PSS, whereas a much larger number (roughly about 10^7 cm^{-2}) of various types of crystalline species including bulky clustered crystals, dendrites and lace-like structures were found on the PEDOT/DDS surface. The latter seem to coat some loosely bound polymer structures. The current transients of silver deposition corresponding to the SEM specimens were fitted by Eqn.(1) and the data for the number of crystals observed microscopically were compared with the calculations for N_0 based on Eqn. (4) and the values of P_2 from the best fit procedure. In the case of PEDOT/PSS it was found that $N_0 = 5.6 \times 10^5 \text{ cm}^{-2}$ which is close to the microscopic value and shows that an instantaneous nucleation process has occurred. In the case of PEDOT/DDS, however, there is a discrepancy between calculated ($N_0 = 2.4 \times 10^6 \text{ cm}^{-2}$) and microscopic values (at least $N = 10^7 \text{ cm}^{-2}$) with number of observed crystals exceeding four times the number of active sites for nucleation. Together with the observed formal increase in the electroactive surface area with potential observed in the PEDOT/DDS case this is an indication for some inconsistency between the

studied electrocrystallization process and the theoretical equation used for current transient interpretation.

Finally, voltammetric curves of silver dissolution obtained after each experiment of silver electro-crystallization were also examined (Fig. 5). Depending on the type of the PEDOT substrate a marked difference was found – a single dissolution peak appears in the PEDOT/PSS series, whereas double dissolution peaks are found for PEDOT/DDS. In the latter case the position of the first peak corresponds to the one measured for PEDOT/PSS. The second dissolution peak (Fig. 5 b) is shifted by about 25 mV in more positive direction and gives evidence for more strongly bound silver crystalline species. Thus, the existence of at least two types of crystalline species should be presumed which is in accordance with the SEM observations.

The theoretical model developed in [5] is based on several assumptions: nucleation occurs at active sites having the same activity for nucleus formation; the clusters of the new phase are hemispherical and grow initially under hemispherical diffusion; the electrode surface is flat and nonporous. Furthermore, one of the main issues in the theoretical assessment of the process of electrochemical nucleation and growth on a flat substrate is to account for the overlap of diffusion zones arising around the growing crystals. The hemispherical flux to the individual crystals is recalculated in linear diffusive flux to the flat electrode surface by assuming that the linear diffusion becomes operative from the very beginning of applying the overpotential. Due to this reason the theoretical current transients (Eqn. 2) are not allowed to exceed the Cottrell limiting diffusion

current. The results in the present study show that a very good fitting of experimental current transients with Eqn. (2) may be obtained when using three free parameters. However, this occurs at the expense of a strongly varying P_3 parameter that is expected to be constant within the model. A smaller value of P_3 than the theoretical one can indicate that the entire electrode surface is not electroactive for the nucleation and growth process. In fact, such microscopic observations were made for some of the PEDOT/PSS specimens where part of the surface was found to be not populated by silver crystals. This means that the current transients obtained in the PEDOT/PSS case are compatible with the theoretical treatment of Scharifker and values of A and N_0 obtained by best fit procedure may be considered as reliable.

In contrast to the experimental findings for PEDOT/PSS the transients obtained in the PEDOT/DDS case overshoot the Cottrell limiting current. The question which arises is whether some of the Scharifker model's assumptions become violated in this experiment. Scharifker's model was discussed and modified by a number of authors [16-22] mainly by drawing attention to the way of recalculating the diffusive flux. It was shown that at low nucleation rates the maxima of the current transients appear at longer times and become delayed with respect to the limiting diffusion current with onset at the beginning of applying overpotential. Thus, it becomes possible that the electrodeposition transients exceed the Cottrell current in a given time interval, but in almost all models at sufficiently long times the nucleation and growth transient should still overlap with the limiting current. If such an effect was in the origin of the observations made in the PEDOT/DDS case, low nucleation rates should be expected. However, comparing the transients in the PEDOT/PSS and PEDOT/DDS series it is obvious that in the latter case the electrocrystallization process is much more intensive and no delay due to low nucleation rate can be anticipated. Moreover, the experimental transients overshoot the Cottrell limit in very long time limits (up to 20 times the time of the current maximum, t_{max}).

Therefore, some of the remaining assumptions of the theoretical model [5] should be put into question. The microscopic observations as well as the silver dissolution curves indicate the existence of at least two different types of silver crystalline species. Some of the species are bulk clustered crystals in direct contact with the polymer layer surface. However, there are also silver crystalline lace-like species that seem to cover loosely bound

polymer structures located above the polymer film. It could be expected that nucleation and growth on these two types of polymer sites may differ a lot. Besides, in such a specific situation the conditions for linear diffusion toward a flat surface are presumably not fulfilled.

4. CONCLUSIONS

The present investigation is focused on the feasibility of the theoretical model for electrochemical nucleation and diffusion controlled growth derived in [5] for the interpretation of current transients of silver electrocrystallization on PEDOT-coated electrodes. It is shown that the position of the long time parts of the current transients with respect to Cottrell limiting current can be considered as a diagnostic criterion for the suitability of the model. This long term behavior is reflected in the value of the P_3 parameter employed usually in best fit procedures. Lower values of P_3 than the theoretically expected ones can indicate to a nonhomogeneous surface with respect to the nucleation process at the macroscopic scale. In such a case an adequate application of the theoretical model is possible by accounting for the real active surface area of the electrode. Higher values of P_3 or current transients above the Cottrell limiting current registered at sufficiently long times mean that some of the main assumptions of the models for nucleation and diffusion controlled growth are violated. In our study it is shown that, besides the known effect of low nucleation rate, such a behavior may arise due to the presence of various types of active sites and therefore various types of growing crystalline species. The latter are expected to affect the linear diffusion limiting conditions.

Finally, the present investigation shows that by including small amounts of organic ions in the polymerization solutions the surface characteristics of PEDOT may be significantly influenced with respect to the number and type of active sites for metal nucleation and growth. This is an aspect that has so far remained out of the considerations in the field of metal electrodeposition on conducting polymer-coated electrodes and will be explored further in more details [23].

Acknowledgements. The support of the Laboratory of Electron Microscopy at Institute of Physical Chemistry, Sofia, is gratefully acknowledged.

REFERENCES

1. V. Tsakova, *J. Solid State Electrochem.*, **12**, 1421 (2008).

2. V. Tsakova, in: Nanostructured Conductive Polymers, A. Eftekhari (ed), John Wiley&Sons, Chichester, 2010, p. 289.
3. C. Janaky, C. Visy, *Analyt. Bioanalyt. Chem.*, **405**, 3489 (2013).
4. G. Ciric-Marjanovic, *Synth. Met.*, **170**, 31 (2013).
5. B. Scharifker, J. Mostany, *J. Electroanal. Chem.*, **177**, 13 (1984).
6. A. Elschner, S. Kirchmeyer, W. Lovenich, U. Merker, K. Reuter, PEDOT: Principles and Applications of an Intrinsically Conductive Polymer, CRC Press, Boca Raton, 2010.
7. W. Wei, H. Wang, Y. H. Hu, *Int. J. Energy Res.*, **38**, 1099 (2014).
8. V. Tsakova and A. Milchev, *Electrochim. Acta*, **36**, 1151 (1991).
9. S. Ivanov, V. Tsakova, *Electrochim. Acta*, **49**, 913 (2004).
10. A. Leone, W. Marino, B.R. Scharifker, *J. Electrochem. Soc.*, **139**, 438 (1992).
11. V. Tsakova, S. Winkels, J.W. Schultze, *J. Electroanal. Chem.*, **500**, 574 (2001).
12. H. Hernandez, J.M. Ortega, M. Choy, R. Ortiz, *J. Electroanal. Chem.*, **515**, 123 (2001).
13. D.G. Filjova, G. P. Ilieva, V. Ts. Tsakova, *Bulg. Chem. Commun.*, **45** (Special issue A), 196 (2013).
14. V. Tsakova, G. Ilieva, D. Filjova, *Electrochim. Acta*, in press.
15. M. Flury, T. Gimmi, in: Solute Diffusion, Methods of Soil Analysis, Part 4, Physical Methods, J.H. Dane, G.C. Topp (eds), Soil Science Society of America, Madison, WI, 2002, p. 1323.
16. M. Sluyters-Rehbach, J.H.O.J. Wijenberg, E. Bosco, J.H. Sluyters, *J. Electroanal. Chem.*, **236**, 1 (1987).
17. M. V. Mirkin, A.P. Nilov, *J. Electroanal. Chem.*, **283**, 35 (1990).
18. L. Heerman, A. Tarallo, *J. Electroanal. Chem.*, **470**, 70 (1999).
19. M. E. Hyde, R.G. Compton, *J. Electroanal. Chem.*, **549**, 1 (2003).
20. A. Milchev, L. Heerman, *Electrochim. Acta*, **48**, 2903 (2003).
21. E. Matthijs, S. Langerock, E. Michailova, L. Heerman, *J. Electroanal. Chem.*, **570**, 123 (2004).
22. D. Mazaira, C. Borrás, J. Mostany, B.R. Scharifker, *J. Electroanal. Chem.*, **631**, 22 (2009).
23. V. Karabozhikova, V. Tsakova, *in preparation*.

ЕЛЕКТРОКРИСТАЛИЗАЦИЯ НА СРЕБРО ВЪРХУ ЕЛЕКТРОДИ, ПОКРИТИ С ПЕДОТ – ИНТЕРПРЕТАЦИЯ НА ТОКОВИ ТРАНЗИЕНТИ

Василена И. Карабожикова, Весела Ц. Цакова*

Институт по физикохимия, Българска академия на науките, 1113 София, България

Постъпила на 14 юли, 2015 г.; коригирана на 13 октомври, 2015 г.

(Резюме)

Електроотлагането на сребро е изследвано върху електроди, покрити с поли(3,4-етилендиокситиофен) (ПЕДОТ) при потенциостатични условия. Слоевете от ПЕДОТ са получени в присъствие на полистиренсулфонатни (ПСС) или додецилсулфатни (ДДС) йони в полимеризационния разтвор. За двата типа слоеве от ПЕДОТ са получени серии от токови транзиенти, регистрирани при различни постоянни потенциали. Установено е, че електрокристализационният процес е значително по-интензивен върху слоевете от ПЕДОТ/ДДС, при които се наблюдава по-голям брой кристали върху електродната повърхност. Токовите транзиенти са интерпретирани с теоретичен модел за прогресивно зародишообразуване и дифузионно контролиран растеж на металната фаза. Несъответствието в дълговременното поведение на експерименталните и теоретични токови транзиенти е разгледано във връзка с отклонения от предпоставките на теорията.

Diamond electrodes for wastewater treatment

S. Pehlivanova^{1,2,*}, Ch. Petkov³, A. Surleva¹, P. Petkov¹, C. Popov³, T. Petkova²

¹University of Chemical Technology and Metallurgy, 8 Kl. Ohridski blvd., 1756 Sofia, Bulgaria

²Institute of Electrochemistry and Energy Systems, BAS, Acad. G. Bonchev bl.10, 1113 Sofia, Bulgaria

³Institute of Nanostructure Technologies and Analytics, University of Kassel, Heinrich-Plett-Str. 40, 34132 Kassel, Germany

Submitted on July 7, 2015; Revised on October 28, 2015

Abstract. Boron doped nanocrystalline diamond films (BDD) immobilized with photosensitive molecules have been studied as electrode material for reduction of nitrate in waste water. This process is one of the most important goals of the modern electrochemistry. The diamond thin films were deposited on silicon substrate by Hot Filament Chemical Vapour Deposition (HFCVD) technique. Manganese phthalocyanine has been used as photosensitive material for immobilization.

The BDD electrode has been electrochemically studied in three electrode cell. The electrochemical properties have been studied by Cyclic Voltammetry (CV) at different experimental conditions in dark and under illumination.

The results approve that the boron doped diamond electrode grafted with phthalocyanine serves as an efficient and stable electrode for nitrate reduction. The diamond electrode has wide potential range. The obtained results are promising for future electrochemical application.

Keywords: diamond electrode; electrochemistry; water treatment

1. INTRODUCTION

Diamond is a very hard crystalline form of carbon with unique mechanical, chemical and physical properties. Diamond as a wide bandgap semiconductor is an electrical insulator. The resistivity however can be controlled by doping mostly with boron or nitrogen [1, 2].

Today the electrochemical behaviors of boron-doped diamond films are subject of scientific and technological interest. Conducting diamond films exhibit inert surface, corrosion stability in aggressive media, wide potential window in aqueous and non-aqueous electrolytes, and low background current. Due to these properties the diamond is a very promising electrode material in various electrochemical devices [1, 3]. One of the most important advantages of the boron doped diamond as an electrode material is the high overpotential for oxygen and hydrogen evolution in aqueous electrolytes [4, 5].

The reduction of nitrates and nitrites is a very important process in the control of the wastewater. The process is kinetically unfavorable because of the highly negative redox potential of ammonia (-2.85 V vs SCE) [2, 6]. The strong cathode polarization under the conditions of ammonia production destabilizes most of the electrodes and they lose the electrocatalytic activity after several cycles. The ideal electrode material should be very stable in the

electrolyte, cheap, with high catalytic activity towards nitrate reduction and low activity towards secondary reactions [7]. Boron doped diamond meets these requirements due to its outstanding electrochemical behaviors which make it one of the candidates for application in wastewater treatment [6, 8].

The present work deals with the application of conductive boron doped diamond functionalized with phthalocyanine for the electrochemical reduction of nitrate. The phthalocyanines are organic compounds, which are thermally very stable and absorb light between 600 and 700 nm.

2. EXPERIMENTAL

2.1. Preparation of diamond films

Boron doped diamond thin films were synthesized on silicon substrate by hot-filament chemical vapor deposition (HFCVD) technique. The precursor gas was a mixture of methane and hydrogen. Typical CVD diamond synthesis includes activation of the gas mixture, gas phase reactions and a subsequent transfer of the diamond forming gas species onto the substrate surface. Scanning electron microscopy was used to reveal the homogeneous and typical morphology of the nanocrystalline diamond (NCD) films with crystallites of sub-micron size (Figure 1) [9, 10].

Boron doping was achieved by addition of trimethyl borate into the reactor chamber during the diamond growth. The NCD surfaces are chemically inert and have a hydrogen termination after the

*To whom all correspondence should be sent:

E-mail: silviq_pehlivanova@abv.bg

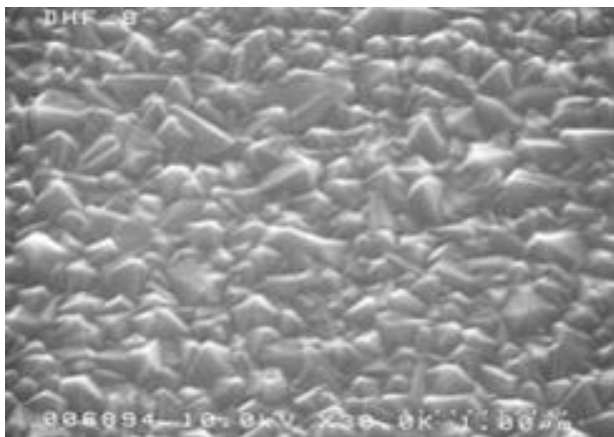


Figure 1. Top-view SEM image of NCD film.

deposition. The surface is modified by plasma- or photo-chemical processes to achieve a desired surface termination. In this work the samples were subjected to oxygen plasma modification (2.45 GHz) in oxygen asher (TePla 200-G) for 5 min at 200 W discharge power and 0.67 mbar working pressure [11]. Oxygen-terminated diamond surface shows hydrophilic character.

2.2. Preparation of the NCD films as electrodes

The diamond films after the modification with oxygen plasma were functionalized with a catalyst. As a catalyst in the present work manganese phthalocyanine (Mn-Pc) was used [10]. The grafting of the Pc on the NCD surface was completed as follows: the samples were immersed in Mn-Pc (1 μ M solution in CH_2Cl_2) for 12 hours, then cleaned in ultrasonic bath with CH_2Cl_2 and dried with N_2 flow.

The modified with O_2 plasma and functionalized with Mn-Pc films were arranged as electrodes for electrochemical measurements. The electrode was attached with silver paste to platinum wire and the assembly was tightly encapsulated in Teflon tape with a small hole. This opening was perforated before the encapsulation in order to provide a 0.5 cm^2 working area for the electrode.

2.3. Electrochemical study of the diamond electrodes

The electrochemical measurements were carried out in a three electrode cell. The boron doped diamond film was used as a working electrode with an active area of 0.5 cm^2 . The counter and reference electrodes were a platinum wire and a standard calomel electrode, respectively. The experimental investigations on the behavior of the conducting diamond electrode were done by cyclic voltammetry at different conditions. Experiments under illumination were carried out by

means of He-Ne laser (25-LHP-111-230) with $\lambda=688$ nm, wavelength in the absorption range of the

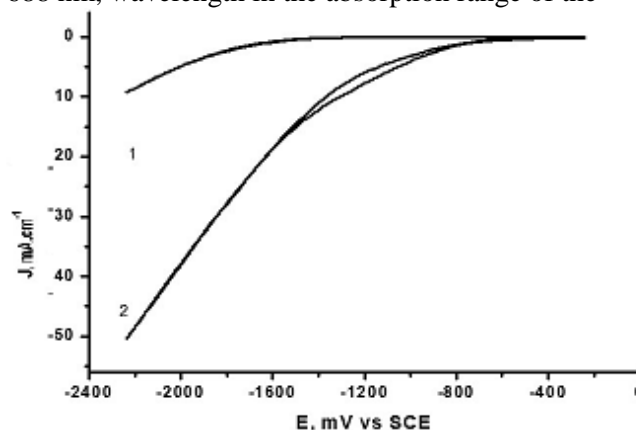
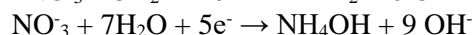
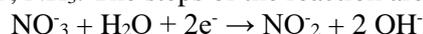


Figure 2. Cyclic voltammograms of a boron doped diamond in 0,1M KCl (curve 1) and 0,1M KNO_3 (curve 2) at a scan rate of 50 mV/sec.

Mn-phthalocyanine. The reduction of nitrate was continuously controlled. The cyclic voltammograms were recorded in two different electrolytes – 0.1 KCl and in 0.1 M KNO_3 . The reduction process was studied with Solartron with scan rates of 10 mV/sec, 20 mV/sec and 50 mV/sec. The concentration of the nitrate ions was determined titrimetrically using a modified Leithe's method [12]. The content of nitrite ions in the electrolyte was determined indirectly as a difference between titrated nitrate ions without and with added urea.

3. RESULTS AND DISCUSSION

One of the most suitable treatments of the nitrate containing water is the direct cathode reduction. The electrochemical reduction of the nitrate is a multistep reaction and the products expected out of these reactions are NO_2^- , N_2 , NH_4OH , NH_3 . The steps of the reaction are:



The cyclic voltammograms were achieved in 0.1 M KNO_3 and 0.1 KCl electrolytes, the latter used as a supporting electrolyte (Figure 2).

The curve recorded in KCl is completely flat while on the curve obtained in 0.1 M KNO_3 a slightly modified region in the potential range from -0.8 to -1.4 V is observed, most probably due to a weak reduction process. The curves approve the very large potential window of the diamond electrodes for hydrogen evolution at approximately -1.5 V in both electrolytes.

The difference in cyclic voltammograms of the boron doped diamond electrode and boron doped diamond electrode functionalized with

phthalocyanine are shown on Figure 3. The measurements are carried out in 0,1M KNO_3 solution from 0 to -0.8 V at a scan rate of 20 mV/sec.

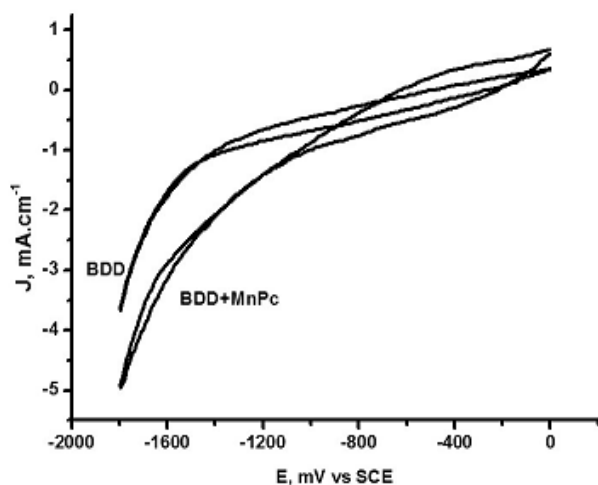


Figure 3. Cyclic voltammograms of a boron doped diamond and boron doped diamond functionalized with phthalocyanine in 0,1M KNO_3 at a scan rate of 20 mV/sec.

The curve recorded with the electrode with catalyst shows larger range of potentials where the reactions take place. The electrode functionalized with phthalocyanine possesses a cathode current of -5 J, mA.cm^{-1} at $-1,5 \text{ V}$, while that of the boron doped diamond reaches $-3,6 \text{ J, mA.cm}^{-1}$ at the same potential.

The reactions occurring at the electrode surface are more pronounced when a lower scan rate is applied. The curve for the electrode functionalized with phthalocyanine recorded at 10 mV/sec and under illumination is presented in Figure 4.

Two well visible peaks are observed at -0.4 V and at -0.8 V which are not present in the curves obtained at the higher scan rate. The first peak is most probably due to the reduction of nitrate to nitrite (reaction 1) and the second one can be attributed to the reduction of nitrite to ammonia (reaction 3) (Figure 4).

The experiment shows that the suitable potential for nitrate reduction as derived from the cyclic voltammetry measurements is between $-0,4$ and $-0,8 \text{ V}$ vs SCE. For this reason, one hour electrolysis was carried out at a constant potential of -0.8 V in 0.1 M KNO_3 electrolyte. Boron doped diamond and boron doped diamond functionalized with Mn phthalocyanine electrodes were additionally studied in dark and under illumination. The variation of the concentration of the nitrate ions measured periodically is shown in Figure 5. From the figure it can be seen that the concentration of nitrate ions is reduced in the first 15 min and

then remains constant. The most efficient reduction of nitrates is observed when the boron doped diamond functionalized with phthalocyanine was used as a working electrode under illumination. The results show that the concentration of the nitrates decreases almost two times: from 6.2 g/l NO_3 to 3.6

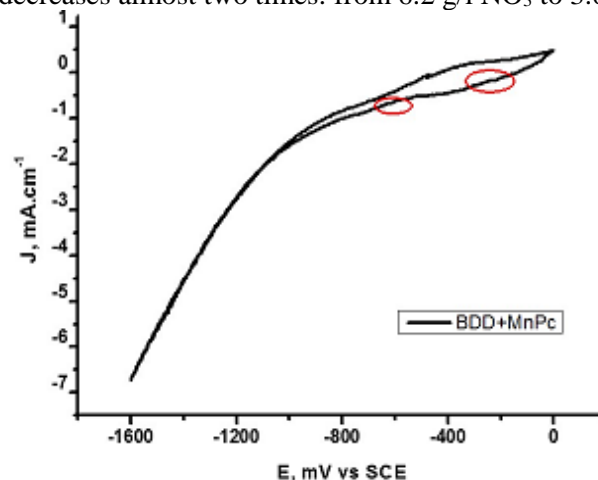


Figure 4. Cyclic voltammogram of boron doped diamond functionalized with phthalocyanine in 0,1M KNO_3 at a scan rate of 10 mV/sec under illumination.

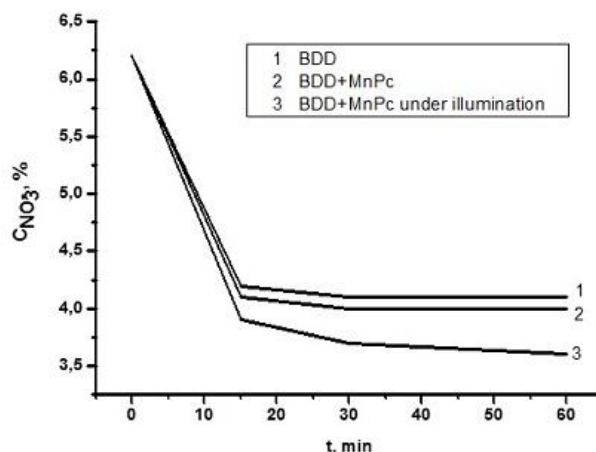


Figure 5. Variation of the concentration of nitrate during one hour electrolysis in 0,1M KNO_3

g/l NO_3 in the measurement under illumination. The nitrate concentration in the experiments with BDD and BDD+MnPc without light decreases from 6.2 g/l to 4.1 g/l and 4.0 g/l respectively (Figure 5).

The analytically measured content of the electrolyte reveals that initially, the nitrate favors the conversion to nitrite, but as the treatment proceeds and the nitrite level increases, the nitrite is further converted to either ammonium or nitrogen gas, finally disappearing by the end of the treatment.

4.CONCLUSIONS

The boron doped diamond electrode grafted with phthalocyanine serves as an efficient and stable electrode for nitrate reduction. Elimination of

nitrate ions was achieved by applying an external potential to the modified and functionalized with phthalocyanine diamond electrode. The studies performed in dark and under illumination reveal that the process under light is more efficient. After 15 minutes 37% nitrate purification of the solution in dark and 42% under illumination have been achieved.

REFERENCES

1. J. H. T. Luong, K. B. Maleb, J. D. Glennona, Analyst, Royal Society of Chemistry, 2009.
2. C. Reuben, E. Galun, H. Cohen, R. Tenne, R. Kalish, Muraki, K. Hashimoto, A. Fujishima, J.M. Butler, C. Levy-Cement, *J. Electroanal. Chem.*, 233 (1995).
3. F. Bouamrane, A. Tadjeddine, J.E. Butler, R. Tenne, C. Levy-Clement, *J. Electroanal. Chem.*, **405**, 95 (1996).
4. C. Levy-Cleement, N. A. Ndao, A. Katty, M. Bernar, A. Deneuve, C. Comninellis, A. Fujishima, *Diamond & Related Materials*, **12**, 606 (2003).
5. M. A. Q. Alfaro, S. Ferro, C. A. Martínez-Huitle, Y. M. Vong, *J. Braz. Chem. Soc.*, 227 (2006).
6. R. Tenne, K. Patel, K. Hashimoto, A. Fujishima, *J. Electroanal. Chem.*, **347**, 409 (1993).
7. M. Panizza, E. Brillas, Ch. Comninellis, *J. Environ. Eng. Manag.*, **18**, 139 (2008).
8. C. A. Martínez-Huitle, M. A. Quiroz Alfaro, *J. Environ. Eng. Manag.*, 155 (2008).
9. Ch. Petkov, U. Glebe, E. Petkov, A. Pasquarelli, C. Pietzka, M. Veres, L. Himics, R. Merz, W. Kulisch, U. Siemeling, J. P. Reithmaier, C. Popov, *Physica Status Solidi (a)*, 2048 (2013).
10. A. Kraft, M. Stadelmann, M. Blaschke, *J. Hazard. Mater.*, **B103**, 247 (2003).
11. S. Pehlivanova, Ch. Petkov, C. Popov, P. Petkov, V. Boev, T. Petkova, Nanoscience Advances in CBRN Agents Detection, Information and Energy Security, NATO Science for Peace and Security Series A: Chemistry and Biology, NATO ASI, Springer, Chapter 49, p. 479 (2015).
12. G.W. Latimer Jr, O.K. Chambers, *Talanta*, **12**, 417 (1965).

ДИАМАНТЕНИ ЕЛЕКТРОДИ ЗА ТРЕТИРАНЕ НА ОТПАДЪЧНИ ВОДИ

С. Пехливанова^{1,2,*}, Х. Петков³, А. Сурлева¹, П. Петков¹, К. Попов³, Т. Петкова²

¹Химикотехнологичен и металургичен университет, бул. "Климент Охридски" №8, 1756 София, България

²Институт по електрохимия и енергийни системи, БАН, ул. "Акад. Г. Бончев" Бл. 10, 1113 София, България

³Институт по наноструктурни технологии и аналитика, Университет Касел, 34132 Касел, Германия

Постъпила на 7 юли, 2015 г. коригирана на 28 октомври, 2015 г.

(Резюме)

Бор-дотирани диамантени филми (BDD) имобилизирани с фталоцианинови молекули са изследвани като материал за редукция на нитрати в отпадъчни води. Този процес е една от най-важните цели на съвременната електрохимия.

Тънките нанокристални диамантени слоеве са отложени върху силициеви подложки посредством химическо отлагане на пари (Chemical Vapor Deposition). Върху така синтезираните и опроводени слоеве за по-добра и ефективна работа, като катализатор е нанесен фталоцианин.

Получените електроди са изследвани в три електродна клетка по метода на циклична волтаперометрия. Изследванията са проведени при различни експериментални условия без и със светлина.

Получените резултати показват, че бор-дотираните диамантени електроди имобилизирани с фталоцианин могат да бъдат използвани като ефективен и стабилен електрод за редукция на нитрати. Освен това, те са обещаващ материал и за други електрохимични приложения.

Thermoelectric oxide materials based on cobalt perovskites

Sonya G. Harizanova^{1,*}, Ekaterina N. Zhecheva¹, Mitko G. Khristov¹, Vassil D. Valchev² and Radostina K. Stoyanova¹

¹*Institute of General and Inorganic Chemistry, Bulgarian Academy of Sciences, Acad. G. Bonchev Str., Bldg. 11, Sofia 1113, Bulgaria*

²*Faculty of Physics, University of Sofia, 1164 Sofia, Bulgaria*

Submitted on July 15, 2015; Revised on October 23, 2015

Abstract. Perovskites on the basis of LaCoO₃ are nowadays regarded as thermoelectric materials with a potential to replace conventional bismuth and tellurium-based semiconductors. In this contribution, we examine in details the effect of multiple metal substitutions on the thermoelectric properties of LaCoO₃-based perovskites. Two groups of compositions are studied: LaCo_{1-2x}Ni_xFe_xO₃ (x=0.1, 0.25) where both Ni and Fe substitute for Co, and La_{1-x}Sr_xCo_{0.8}Ni_{0.1}Fe_{0.1}O₃ (0≤x≤0.25) where Sr substitutes for La. This study demonstrates that by a rational choice of the content of strontium, iron and nickel additives it is possible to obtain eco-compatible LaCoO₃-based perovskites with desired thermoelectric efficiency.

Keywords: Thermoelectric oxides; cobalt-based perovskites

1. INTRODUCTION

The capability of thermoelectric materials to convert waste heat into electricity determines them as a key source of the “clean” energy of the future [1]. Thermoelectric oxides are nowadays considered as more stable and less toxic materials in comparison with the conventionally used metals and semiconductors, but their thermoelectric efficiency is still lower. The state-of-the-art research is mainly devoted to identify new oxide materials with higher thermoelectric efficiency [1, 2]. Among oxides, three groups of cobaltates can be outlined: Na_xCoO₂ with a layered structure; misfit Ca₃Co₄O₉, with similar CoO₂ layers and LaCoO₃ with a perovskite structure. LaCoO₃ is one of the most interesting as a material with potential application in thermoelectric devices due to its high Seebeck coefficient ($|S| > 500 \mu\text{V/K}$ at room temperature) [3-5]. The transport properties of LaCoO₃ are determined (to a great extent) by the ability of Co³⁺ ions to adopt low-, intermediate- and high-spin configurations in the perovskite structure, leading to an additional spin entropy effect [6,7]. However, the electrical resistivity is high (about 10 Ωcm at room temperature) [8], which lowers the thermoelectric activity ($ZT < 0.01$ at T=300 K) [4,7].

Recently we have reported that LaCoO₃ perovskite displays an improved thermoelectric efficiency when Co is replaced simultaneously by

nickel and iron ions: LaCo_{1-y}(Ni_{0.5}Fe_{0.5})_yO₃ [9]. The important feature of the transport properties of single-substituted cobaltates is that the nickel ions give rise to electron delocalization, which is opposite to the effect of the iron ions acting as electron trapping centers [9]. The improvement of the thermoelectric efficiency for double substituted perovskites is achieved by balancing the opposite effects of nickel and iron ions.

In this contribution, we extend our studies and provide new data on the improving the thermoelectric properties of LaCoO₃ by multiple substitutions at both La and Co-sites with strontium, nickel and iron ions. Two groups of compositions are studied: LaCo_{1-2x}Ni_xFe_xO₃ with x=0.1 where both Ni and Fe substitute for Co, and La_{1-x}Sr_xCo_{0.8}Ni_{0.1}Fe_{0.1}O₃, 0≤x≤0.25 where Sr substitute for La. All perovskites are obtained from freeze-dried citrate precursors at 900 °C. This method is shown to be effective for the preparation of substituted perovskites, where all metal additives are randomly distributed [10, 11]. Structural and morphological characterizations are carried out by powder XRD and SEM analysis. The thermoelectric efficiency of the perovskites is determined by the dimensionless figure of merit, calculated from the independently measured Seebeck coefficient (S), electrical resistivity (ρ) and thermal conductivity (λ).

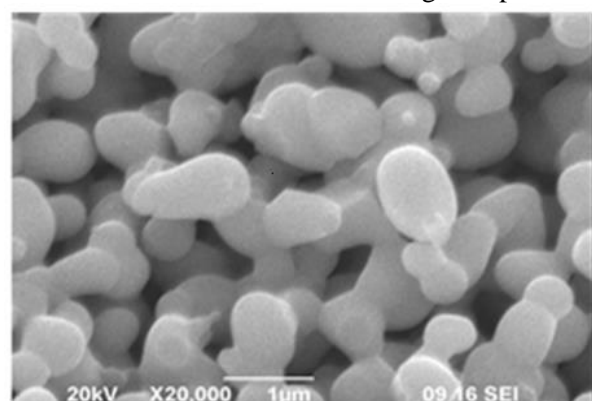
2. EXPERIMENTAL

A precursor-based method was used for the preparation of La_{1-x}Sr_xCo_{0.8}Ni_{0.1}Fe_{0.1}O₃, LaCo₁₋

*To whom all correspondence should be sent:

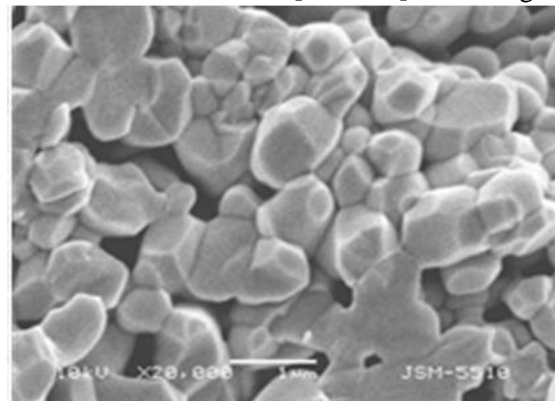
E-mail: sonya@svr.igic.bas.bg

$x\text{Ni}_x\text{O}_3$ and $\text{LaCo}_{1-x}\text{Fe}_x\text{O}_3$ following the procedure



(a)

described elsewhere [10, 11]. Homogeneous



(b)

Figure 1. SEM images of the cross section of the pellets consisting of LaCoO_3 (a) and $\text{LaCo}_{0.5}\text{Fe}_{0.4}\text{Ni}_{0.1}\text{O}_3$ (b) sintered at $900\text{ }^\circ\text{C}$ for 40h.

La-Co-Fe-Ni citrate precursors were obtained by freeze-drying of mixed citrate solutions of La-Co-Fe-Ni ions (1M La). The ratio between the components was $\text{La}:\text{Co}_{1-2x}\text{Fe}_x\text{Ni}_x:\text{Citric acid} = 1:1:10$. After stirring, a clear solution was obtained, which was diluted to 0.25M La. The solution was instantly frozen with liquid nitrogen and dried *in vacuum* at $-30\text{ }^\circ\text{C}$ in Alpha-Christ Freeze-Dryer, leading to the formation of freeze-dried precursors. The thermal decomposition of the citrate-precursors was achieved at $400\text{ }^\circ\text{C}$ for 3 h in air. The obtained solid residue was annealed at $900\text{ }^\circ\text{C}$ for 40 h in air, then cooled down to room temperature with a rate of $5^\circ/\text{min}$. The same procedure was used for the synthesis of the samples with following compositions:

$\text{La}_{1-x}\text{Sr}_x\text{Co}_{0.8}\text{Ni}_{0.1}\text{Fe}_{0.1}\text{O}_3$, $\text{LaCo}_{1-x}\text{Ni}_x\text{O}_3$ and $\text{LaCo}_{1-x}\text{Fe}_x\text{O}_3$.

X-ray structural analysis was performed on a Bruker Advance 8 diffractometer with $\text{Cu K}\alpha$ radiation. Step-scan recording for structure refinement by the Rietveld method were carried out using $0.02\text{ }^\circ 2\theta$ steps of 5s duration. XRD patterns are analyzed by a structural model comprising rhombohedrally distorted perovskite-type structure ($R\bar{3}c$ space group) where La occupies the $6a$ position $(0, 0, \frac{1}{4})$, Co/Fe/Ni are in the octahedral $6b$ position, and oxygen is in the $18e$ position. In accordance with our previous data [11], the replacement of Co by Ni and Fe led to lattice expansion of the perovskite structure. It is worth to mention that all metal additives (Ni, Fe and Sr) are randomly distributed over the $6a$ and $6b$ positions.

The transport properties were measured on pellets sintered at $900\text{ }^\circ\text{C}$ for 40 hours. Pellet density was determined by Archimedes' method. The property was evaluated by comparison with the theoretical density of LaCoO_3 (7.299, JCPDS No25-1060). For the pellets with different

perovskites compositions the porosity varied between 20 and 25 % despite the Ni, Fe and Ni, Fe content. SEM analysis was also undertaken to analyze the pellet porosity. SEM images of pellets coated with gold were obtained by Zeiss DSM 962 microscope and Philips XL30 scanning electron microscope. Figure 1 shows the porosity of the pellets for unsubstituted and double substituted perovskites. The SEM images demonstrate that well shaped particles fused one to another give rise to the pellet porosity. The close pellet porosities allow us to compare the thermoelectric properties of the perovskites with different level of substitution.

Electrical resistivity (ρ), density and mobility of charge carriers were determined by MMR's Variable temperatures Hall System (k2500-5SLP-SP) using Van der Pauw method over a temperature range from 90K to 600K. The benchtop permanent magnet (0.5T) is used. Thermal conductivity was determined at room temperatures on Thermal Conductivity Analyzer TCi (SETARAM). In order to compare the thermal conductivities of samples having different lappet porosity, the thermal conductivity is normalized to 95% of the theoretical density (λ_t) using the following density correction [2]: $\lambda_t = \lambda(0.95^{1.5})/(1-P)^{1.5}$, where λ is the measured thermal conductivity and P is the fractional porosity of the pellet.

3. RESULTS AND DISCUSSIONS

The multiple substitutions at La and Co sites proceed in the framework of the rhombohedrally distorted perovskite type structure. Lattice parameters for $\text{LaCo}_{1-2x}\text{Ni}_x\text{Fe}_x\text{O}_3$ and $\text{La}_{1-x}\text{Sr}_x\text{Co}_{0.8}\text{Ni}_{0.1}\text{Fe}_{0.1}\text{O}_3$ are summarized in Table 1. The multiple substitutions at La and Co sites lead to a lattice extensions irrespective of the origin of metal additives.

Table 1. Lattice parameters of $\text{LaCo}_{1-2x}\text{Ni}_x\text{Fe}_x\text{O}_3$ and $\text{La}_{1-x}\text{Sr}_x\text{Co}_{0.8}\text{Ni}_{0.1}\text{Fe}_{0.1}\text{O}_3$.

Samples	$a \pm 0.0001, \text{ \AA}$	$c \pm 0.0003, \text{ \AA}$	$V, \text{ \AA}^3$
LaCoO_3	5.4407	13.0914	335.61
$\text{LaCo}_{0.8}\text{Ni}_{0.1}\text{Fe}_{0.1}\text{O}_3$	5.4532	13.1191	337.86
$\text{LaCo}_{0.50}\text{Ni}_{0.25}\text{Fe}_{0.25}\text{O}_3$	5.4737	13.1676	341.67
$\text{La}_{0.95}\text{Sr}_{0.05}\text{Co}_{0.8}\text{Ni}_{0.1}\text{Fe}_{0.1}\text{O}_3$	5.4540	13.1397	338.49
$\text{La}_{0.90}\text{Sr}_{0.10}\text{Co}_{0.8}\text{Ni}_{0.1}\text{Fe}_{0.1}\text{O}_3$	5.4524	13.1536	338.65
$\text{La}_{0.75}\text{Sr}_{0.25}\text{Co}_{0.8}\text{Ni}_{0.1}\text{Fe}_{0.1}\text{O}_3$	5.4488	13.1880	339.09

Transport properties of single-substituted cobaltates have been already studied [2, 12], while the double substituted cobaltates are still not explored. The electrical resistivity (ρ) significantly decreases during the replacement of cobalt by nickel, while the substitution of iron for cobalt leads to an increase in ρ (Table 2). For double substituted oxides $\text{LaCo}_{1-2x}\text{Ni}_x\text{Fe}_x\text{O}_3$, the electrical resistivity decreases as compared to that of LaCoO_3 and it does not depend on the total Ni+Fe content: 0.0722 and 0.0939 $\Omega\cdot\text{cm}$ for $x=0.1$ and $x=0.25$, respectively. This means that when Ni and Fe ions are in equal amounts, their effects are balanced leading to the formation of $\text{LaCo}_{1-2x}\text{Ni}_x\text{Fe}_x\text{O}_3$ with a resistivity, which is concentration-insensitive despite of the replacement of 50% of Co ions. The reduction in the resistivity is a result from the increase in the carrier density induced by double substitution: from $2-3 \times 10^{18}\text{cm}^{-3}$ for LaCoO_3 to $7-9 \times 10^{18}\text{cm}^{-3}$ for $\text{LaCo}_{0.8}\text{Ni}_{0.1}\text{Fe}_{0.1}\text{O}_3$. The carrier mobility seems to be unchanged during the replacement of the cobalt ions: 1-3 $\text{cm}^2/\text{V}\cdot\text{s}$ for LaCoO_3 and 4-6 $\text{cm}^2/\text{V}\cdot\text{s}$ for $\text{LaCo}_{0.8}\text{Ni}_{0.1}\text{Fe}_{0.1}\text{O}_3$.

The electrical resistivity of LaCoO_3 decreases also when La^{3+} ions were replaced by aliovalent Sr^{2+} ions (Fig. 2). Because the transport properties of $\text{LaCo}_{1-x}\text{Ni}_x\text{O}_3$ and $\text{La}_{1-x}\text{Sr}_x\text{CoO}_3$ are usually interpreted in the same manner [13, 14], there is a need to compare the density of the charge carriers for both $\text{LaCo}_{0.8}\text{Ni}_{0.1}\text{Fe}_{0.1}\text{O}_3$ and $\text{La}_{1-x}\text{Sr}_x\text{Co}_{0.8}\text{Ni}_{0.1}\text{Fe}_{0.1}\text{O}_3$ compositions (Fig. 2). As one can be expected, the electrical resistivity decreases with the Sr content (Fig. 2). This decrease is valid in the whole temperature range of measurement: from 250 to 600 K. For $\text{La}_{1-x}\text{Sr}_x\text{Co}_{0.8}\text{Ni}_{0.1}\text{Fe}_{0.1}\text{O}_3$, the density of the charge carriers is higher in comparison with the unsubstituted LaCoO_3 and double substituted $\text{LaCo}_{0.8}\text{Ni}_{0.1}\text{Fe}_{0.1}\text{O}_3$ (Fig. 2). In addition, Sr^{2+} ions induce a strong increase in the carrier mobility: from 4-6 $\text{cm}^2/\text{V}\cdot\text{s}$ for $\text{LaCo}_{0.8}\text{Ni}_{0.1}\text{Fe}_{0.1}\text{O}_3$ to 20-35 $\text{cm}^2/\text{V}\cdot\text{s}$ and 70-80 $\text{cm}^2/\text{V}\cdot\text{s}$ for $x=0.1$ and $x=0.25$ (Fig. 2). In the temperature range of 250-600K, the charge density increases slightly. The carrier mobility for unsubstituted LaCoO_3 and double substituted $\text{LaCo}_{0.8}\text{Ni}_{0.1}\text{Fe}_{0.1}\text{O}_3$ increases with the registration

temperature, while all Sr-substitute perovskites display constant carrier mobility in the temperature range of 250 – 600 K. Therefore, the enhanced electrical conductivity for Sr-substituted

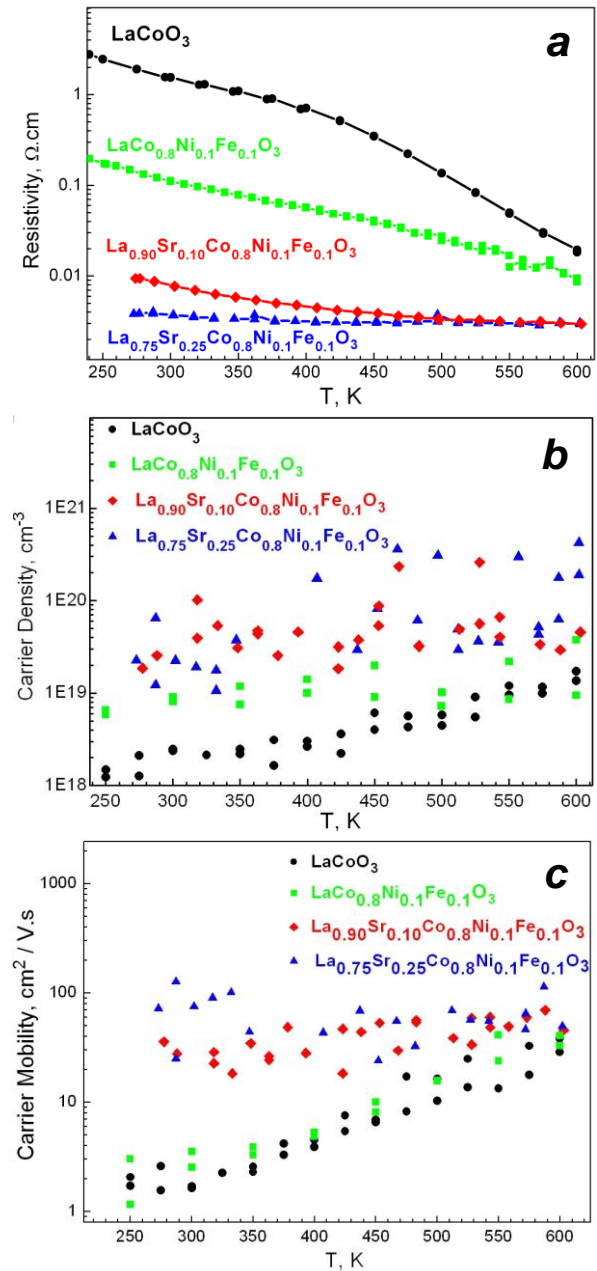


Figure 2 Temperature dependence of the electrical resistivity (a), carrier density (b) and carrier mobility (c) for LaCoO_3 , $\text{LaCo}_{0.8}\text{Ni}_{0.1}\text{Fe}_{0.1}\text{O}_3$ and Sr-substituted $\text{La}_{1-x}\text{Sr}_x\text{Co}_{0.8}\text{Ni}_{0.1}\text{Fe}_{0.1}\text{O}_3$.

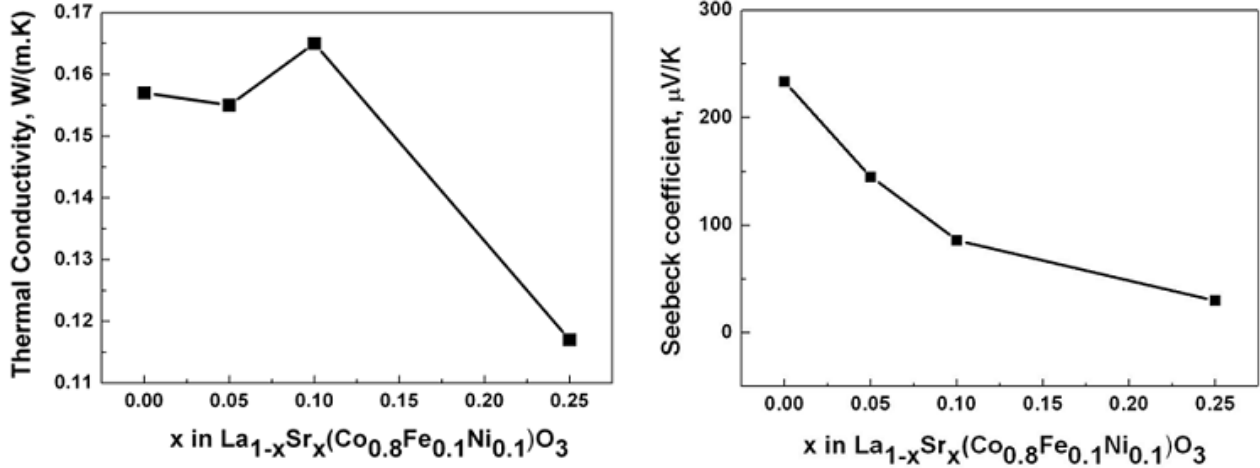


Figure 3. Concentration dependence of the thermal conductivity (left) and Seebeck coefficient (right) for $\text{La}_{1-x}\text{Sr}_x\text{Co}_{0.8}\text{Ni}_{0.1}\text{Fe}_{0.1}\text{O}_3$. (All parameters are measured at 300 K).

Table 2. Electrical resistivity (ρ), thermal conductivity (λ), Seebeck coefficient (S), Power factor ($\text{PF} = S^2/\rho$), Figure of merit ($\text{ZT} = S^2T/(\rho k_B)$) for single, double and multiple substituted perovskites. (For better comparison, all parameters are measured at 300 K).

Samples	ρ $\Omega\cdot\text{cm}$	λ W/m.K	S $\mu\text{V/K}$	PF $\mu\text{W/K}^2\cdot\text{cm}$	FM
LaCoO_3	1.555	0.434	600	0.231	0.015
$\text{LaCo}_{0.9}\text{Ni}_{0.1}\text{O}_3$	0.066	0.425	264	1.056	0.075
$\text{LaCo}_{0.9}\text{Fe}_{0.1}\text{O}_3$	2.549	0.257	599	0.141	0.016
$\text{LaCo}_{0.8}\text{Ni}_{0.1}\text{Fe}_{0.1}\text{O}_3$	0.0722	0.157	234	0.761	0.158
$\text{La}_{0.9}\text{Sr}_{0.1}\text{Co}_{0.8}\text{Ni}_{0.1}\text{Fe}_{0.1}\text{O}_3$	0.0446	0.123	86	0.165	0.040

perovskites can be regarded as a consequence from the increased carrier density and mobility, while the carrier density accounts mainly for the electrical conductivity of Ni, Fe-substituted cobaltates.

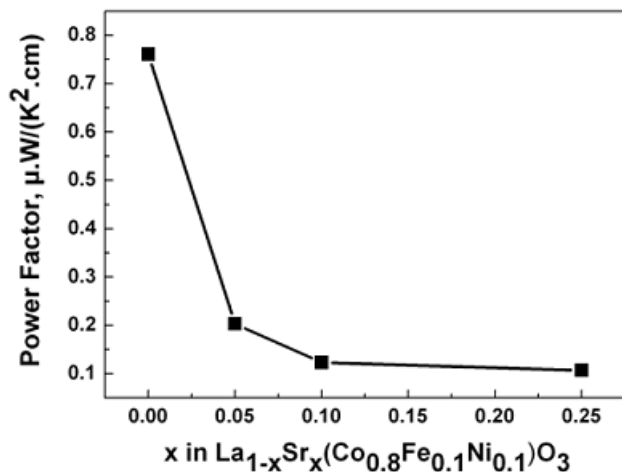
The thermal conductivities of the single and double-substituted perovskites are shown in Fig. 3. In general, the thermal conductivity decreases upon increasing the metal content (Ni, Fe and Ni, Fe, respectively). It is shown that the double substitution yields a more significant decrease in the thermal conductivity in comparison with the single substitution (Table 2). The thermal conductivity comprises two contributions that are due to conductive carriers (λ_e) and phonon scattering. If the electron conduction is due to one type of charge carriers only, then λ_e can be calculated by the Wiedemann–Franz law: $\lambda_e = LT/\rho$ (the Lorentz number, L , is $2.45 \times 10^{-8} \text{ V}^2 \text{ K}^{-2}$). It is obvious that the λ_e term increases for Ni-substituted perovskites ($3 \cdot 10^{-4}$ and 0.015 W/m.K for $\text{LaCo}_{1-2x}\text{Fe}_x\text{Ni}_x\text{O}_3$ with $x=0.1$ and 0.25 , respectively), but it remains lower than the total thermal conductivity (0.101 and 0.069 W/m.K , respectively). This means that even in this case the total thermal conductivity is governed by the lattice contribution. As a result, the thermal conductivities of the nickel- and iron-substituted perovskites are close. The dopant-

induced decrease in the thermal conductivity of the cobaltates can mainly be explained by the enhanced phonon scattering due to the disordering of Co-Ni or Co-Fe ions in the octahedral $6b$ position (with coordinates $0, 0, 0$) of the perovskite structure. This is a consequence of the ionic mismatch of the nickel, iron and cobalt ions. The appearance of Sr in the $6a$ position leads to a further decrease in the thermal conductivity (Fig. 3).

The Seebeck coefficient is strongly dependent on the amount of nickel, iron and strontium dopants (Fig. 3). All perovskite compositions display positive sign of the Seebeck coefficient (S), thus indicating that the predominant mobile charge carriers are holes. It is well known that Sr and Ni additives lead to a decrease in the S -value, while Fe additives have an opposite effect (Table 2). When Sr, Ni and Fe additives are included together into the perovskite structure, there is a smooth decrease in the S -value. It is noticeable that after 50% of Co substitution the sign of S remains positive reaching a value of $108 \mu\text{V/K}$ for $\text{LaCo}_{0.5}\text{Ni}_{0.25}\text{Fe}_{0.25}\text{O}_3$.

Based on the Seebeck coefficient and electrical resistivity data, the power factor is estimated: $\text{PF} = S^2/\rho$ (Fig. 4). The power factor displays a decrease during the increase in the Sr content. The highest PF is obtained for the single substituted

LaNi_{0.1}Co_{0.9}O₃ perovskite (Table 2). The addition of Fe into LaNi_{0.1}Co_{0.9}O₃ leads to a decrease in the PF, but it remains higher than that of unsubstituted LaCoO₃. This reveals that nickel additives have a positive effect as compared to iron and strontium ones (Table 2, Fig. 4). The observed power factor



for multiple substituted cobaltates is lower than the unusually high power factor established for SrTiO₃ (20 $\mu\text{W}/(\text{K}^2\cdot\text{cm})$) [15,16]. However, the extremely large thermal conductivity of SrTiO₃ (about 10 W/m.K) reduces its figure of merit [15, 16].

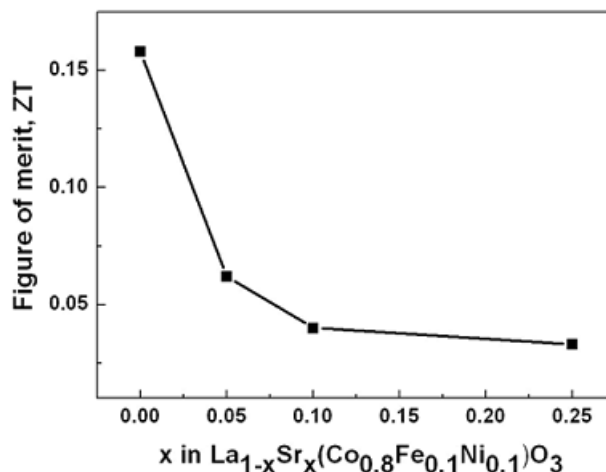


Figure 4. Concentration dependence of the power factor (left) and figure of merit (right) (left) for La_{1-x}Sr_xCo_{0.8}Ni_{0.1}Fe_{0.1}O₃. (All parameters are measured at 300 K).

The figures of merit for single- and multiple-substituted perovskites are summarized on Table 2 and Figure 4. The lower level of nickel substitution causes a strong increase in thermoefficiency due to the enhanced electrical conductivity, while iron additives do not have any effect. In comparison with single substituted perovskites, the thermoelectric efficiency strongly increases for double-substituted perovskites. This means that the thermoelectric activity is a result from the synergic effect of the simultaneous appearance of Fe and Ni in the cobalt perovskite structure. The perovskite containing Fe and Ni ions in equal amount exhibits the higher thermoelectric activity. The increased thermoelectric activity can mainly be related with the decreased thermal conductivity for double-substituted perovskites (Fig. 3). The figure of merit is not improved when Sr ions substitutes for La ions (Fig. 4). Comparing the transport properties of Sr, Ni and Fe substituted perovskites, it appears that the perovskite with LaCo_{0.8}Fe_{0.1}Ni_{0.1}O₃ composition exhibits best thermoelectric activity with $ZT=0.16$. This figure of merit is comparable with that reported for La_{0.92}CoO_{2.93} that contains vacancies in both lanthanum and oxygen sites (ZT -value (of about 0.18) [17]. The comparison shows that double-substituted cobaltates, LaCo_{1-x}(Ni_{0.5}Fe_{0.5})_xO₃, exhibit a relatively good figure of merit, that makes them interesting as materials with thermoelectric properties.

4. CONCLUSIONS

The thermoelectric activity of LaCoO₃-based perovskites is effectively controlled by multiple substitutions at the La- and Co-sites. The highest figure of merit is observed for double substituted perovskites with composition LaCo_{0.8}Ni_{0.1}Fe_{0.1}O₃. The improved thermoelectric efficiency is a consequence from the decreased thermal conductivity for double-substituted perovskites. The multiple substituted cobalt perovskites are also of interest as eco-compatible thermoelectric materials since iron and nickel ions are less toxic and cheaper in comparison with cobalt ions. In addition, the structural approach of selective ion substitution can be extended towards other groups of thermoelectric oxide materials.

Acknowledgments. Authors are grateful to the financial support from ESF (Grant BG051PO001-3.3.06-0050).

REFERENCES

1. J. R. Sootsman, D.Y. Chung, M.G. Kanatzidis, *Angew. Chem. Int. Ed.*, **48**, 8616 (2009).
2. A. Maignan, L. B. Wang, S. Hébert, D. Pelloquin, B. Raveau, *Chem. Mater.*, **14**, 1231 (2002).
3. M.A. Señarís Rodríguez, J. B Goodenough, *J. Solid State Chem.*, **116**, 224 (1995).
4. K. Berggold, M. Kriner, C. Zobel, A. Reichl, M. Reuther, R. Müller, A. Freimuth, T. Lorenz, *Phys. Rev. B*, **72**, 155116 (2005).
5. P. Herve, T. Ngamou, N. Bahlawane, *Chem. Matter.*, **22**, 4158 (2010).

6. P. M. Raccach, J. B. Goodenough, *Phys. Rev.*, **155**, 932 (1967).
7. K. Berggold, M. Kriener, P. Becker, M. Benomar, M. Reuther, C. Zobel, T. Lorenz, *Phys. Rev. B*, **78**, 134402 (2008).
8. Y. Tokra, Y. Okimoto, S. Yamaguchi, H. Taniguchi, *Phys. Rev. B*, **58**, R1699 (1998).
9. V. Vulchev, L. Vassilev, S. Harizanova, M. Khristov, E. Zhecheva, R. Stoyanova, *J. Phys. Chem. C*, **116**, 13507 (2012).
10. S. Ivanova, A. Senhyshin, E. Zhecheva, K. Tenchev, V. Nikolov, R. Stoyanova, H. Fuess, *J. Alloys Comp.*, **480**, 279 (2009).
11. S. Ivanova, A. Senhyshin, E. Zhecheva, K. Tenchev, R. Stoyanova, H. Fuess, *J. Solid State Chem.*, **183**, 940 (2010).
12. J. Dho, N. H. Hur, *Solid State Commun.*, **138**, 152 (2006).
13. T. Kyômen, R. Yamazaki, M. Itoh, *Phys. Rev. B*, **68**, 104416 (2003).
14. M. Viswanathan, P.S. Anil Kumar, *Phys. Rev B*, **80**, 012410 (2009).
15. R. Chen, R. D. Delgado, E. C. Garnett, A. I. Hochbaum, W. Liang, A. Majumdar, M. Najarian, P. Yang, *Nature*, **451**, 734 (2008).
16. D. Chateigner, K. Chong, R. Funahashi, E. Guilmeau, M. Mikami, *Appl. Phys. Lett.*, **85**, 1490 (2004).
17. M. Viswanathan, P. S. Anil Kumar, *Phys. Rev B*, **80**, 012410 (2009).

ТЕРМОЕЛЕКТРИЧНИ ОКСИДНИ МАТЕРИАЛИ НА ОСНОВА НА КОБАЛТ

С. Г. Харизанова^{1,*}, Е. Н. Жечева¹, М. Г. Христов¹, В. Д. Вълчев², Р. К. Стоянова¹

¹Институт по обща и неорганична химия, Българска академия на науките,
бул. Акад. Г. Бончев, бл. 11, София 1113, България

²Физически факултет, Софийски университет, 1164 София, България

Постъпила на 15 юли, 2015 г. коригирана на 23 октомври, 2015 г.

(Резюме)

Перовскитите на основа на LaCoO_3 се разглеждат като термоелектрични материали, които имат потенциал да заместят добре известните полупроводници на основата на бисмут и телур. В това съобщение са представени резултатите от наши детайлни изследвания за подобряване на термоелектричните свойства на LaCoO_3 чрез многокомпонентно заместване с Ni, Fe и Sr. Две групи съединения са изследвани: $\text{LaCo}_{1-2x}\text{Ni}_x\text{Fe}_x\text{O}_3$ с $x=0.1$, където Ni и Fe заместват Co, и $\text{La}_{1-x}\text{Sr}_x\text{Co}_{0.8}\text{Ni}_{0.1}\text{Fe}_{0.1}\text{O}_3$, $0 \leq x \leq 0.25$, където Sr замества La. Получените резултати показват, че чрез рационален подбор на количеството на заместителите от Sr, Ni и Fe могат да се получат оксидни материали на основата на LaCoO_3 с желаната термоелектрична ефективност и безвредност към околната среда.

Sodium deficient transition metal oxides $\text{Na}_{1/2}\text{Co}_{1/3}\text{Ni}_{1/3}\text{Mn}_{1/3}\text{O}_2$ as alternative electrode materials for lithium-ion batteries

Sv.G. Ivanova*, E.N. Zhecheva, R.K. Stoyanova

*Institute of General and Inorganic Chemistry, Bulgarian Academy of Sciences,
Acad. G. Bonchev Str., Bldg. 11, Sofia 1113, Bulgaria*

Submitted on July, 17, 2015; Revised on October 23, 2015

Abstract. Sodium-deficient transition metal oxides exhibit flexible layered structures which are able to adopt different layer stacking and symmetry. In this study, we provide new data on the structure and reversible lithium intercalation properties of oxides with composition $\text{Na}_{1/2}\text{Co}_{1/3}\text{Ni}_{1/3}\text{Mn}_{1/3}\text{O}_2$. Novel properties of oxides determine their potential for using as alternative electrode materials for lithium-ion batteries. Between 700 and 800 °C, new layered oxide $\text{Na}_{1/2}\text{Co}_{1/3}\text{Ni}_{1/3}\text{Mn}_{1/3}\text{O}_2$ with a *P3*-type of structure is obtained by a precursor-based method. A new structural feature of $\text{Na}_{1/2}\text{Co}_{1/3}\text{Ni}_{1/3}\text{Mn}_{1/3}\text{O}_2$ as compared to well-known sodium stoichiometric oxides $\text{NaCo}_{1/3}\text{Ni}_{1/3}\text{Mn}_{1/3}\text{O}_2$ with an *O3*-type of structure is the development of layer stacking ensuring prismatic site occupancy for Na^+ ions with shared face on one side and shared edges on the other side with surrounding Co/Ni/MnO_6 octahedra. The reversible lithium intercalation in $\text{Na}_{1/2}\text{Co}_{1/3}\text{Ni}_{1/3}\text{Mn}_{1/3}\text{O}_2$ is demonstrated and discussed.

Keywords: Sodium–transition metal–oxides; Layered oxides; Intercalation; Lithium-ion battery

1. INTRODUCTION

Linkage of the intercalation properties with the crystal structure of solids is a research topic that is a basis for recent progress in the design of cathode materials for lithium ion batteries [1]. Among several groups of compounds, layered lithium transition metal oxides are of both research and practical interests since they are able to intercalate lithium reversibly at high potentials [2,3]. Lithium-cobalt-nickel-manganese oxides, $\text{LiCo}_{1-2x}\text{Ni}_x\text{Mn}_x\text{O}_2$, with compositions $x=1/3$ have been considered as next generation electrode materials [4]. Contrary to the conventional LiCoO_2 -based electrodes, $\text{LiCo}_{1/3}\text{Ni}_{1/3}\text{Mn}_{1/3}\text{O}_2$ oxides display two electron electrochemical reactions during reversible lithium intercalation, a phenomenon that is generally considered to be rare for layered oxides [5].

Nowadays, lithium ion batteries are the most widely used electrochemical storage systems. However, they are still expensive and are in nonconformity with technical requirements for large scale storage applications [6]. Searching for cheaper energy storage systems, sodium ion batteries have been advanced as an alternative to the lithium ones [6]. Sodium is one of the most abundant elements in the Earth's crust and its redox potential is slightly lower than that for Li, i.e. $E^\circ(\text{Na}^+/\text{Na}) = -2.71$ V and $E^\circ(\text{Li}^+/\text{Li}) = -3.03$ V versus standard hydrogen electrode [6]. This means that lithium-ion batteries offer higher power, while

sodium ion batteries appear to be cheaper and safer.

Lithium and sodium ion batteries operate by the same mechanism comprising the reversible electrochemical intercalation of Li^+ and Na^+ . Recently stoichiometric sodium cobalt nickel manganese oxide $\text{NaCo}_{1/3}\text{Ni}_{1/3}\text{Mn}_{1/3}\text{O}_2$ has been proposed as a cathode material for sodium ion batteries [5]. Both $\text{NaCo}_{1/3}\text{Ni}_{1/3}\text{Mn}_{1/3}\text{O}_2$ and $\text{LiCo}_{1/3}\text{Ni}_{1/3}\text{Mn}_{1/3}\text{O}_2$ analogues have crystal structure composed of discrete $\text{Co}_{1/3}\text{Ni}_{1/3}\text{Mn}_{1/3}\text{O}_2$ -layers [4,5]. The sodium and lithium ions are sandwiched between the $\text{Co}_{1/3}\text{Ni}_{1/3}\text{Mn}_{1/3}\text{O}_2$ -layers so as to occupy octahedral sites. Based on the number of the $\text{Co}_{1/3}\text{Ni}_{1/3}\text{Mn}_{1/3}\text{O}_2$ -layers in the unit cell and the site occupied by Na or Li, the structure of both sodium and lithium analogues is classified as *O3*-type according to notation of Delmas et al. [7].

In order to combine the advantages of lithium and sodium ion batteries, a new concept has recently been proposed [2]. The concept aims at using directly sodium transition metal oxides as electrode materials instead of lithium analogues [3]. This concept is beneficial especially in case of vanadium and manganese-based layered oxides such as $\text{Na}_x\text{V}_3\text{O}_8$, $\text{Na}_{2/3}\text{Mn}_{1-x}\text{Fe}_x\text{O}_2$, $\alpha\text{-Na}_{0.66}\text{MnO}_{2.13}$ and $\text{Na}_x\text{Ni}_{1/2}\text{Mn}_{1/2}\text{O}_2$.

In this contribution we provide new data on the structure and intercalation properties of sodium deficient cobalt nickel manganese oxides with the aim to analyze their potential usage as cathode materials in lithium-ion batteries. The studies are focused on $\text{Na}_x\text{Co}_{1/3}\text{Ni}_{1/3}\text{Mn}_{1/3}\text{O}_2$ compositions with $x=1/2$. For the synthesis of these oxides, we used a

*To whom all correspondence should be sent:

E-mail: svetlana@svr.igic.bas.bg

simple precursor-based method comprising thermal decomposition of mixed acetate-oxalate precursors [8]. The structure and morphology of Na_{1/2}Co_{1/3}Ni_{1/3}Mn_{1/3}O₂ are determined by powder X-ray diffraction and SEM analysis. The lithium intercalation in Na_{1/2}Co_{1/3}Ni_{1/3}Mn_{1/3}O₂ is carried out in model two-electrode lithium cells of the type Li|LiPF₆(EC:DMC)| Na_{1/2}Co_{1/3}Ni_{1/3}Mn_{1/3}O₂. The morphology and composition changes during the lithium intercalation are followed by *ex-situ* SEM analysis and laser ablation inductively coupled plasma mass spectrometry (LA-ICPMS).

2. EXPERIMENTAL

Na_{1/2}Co_{1/3}Ni_{1/3}Mn_{1/3}O₂ oxides were obtained by oxalate-acetate precursor method. According to this method, sodium hydroxide and oxalic acid were mixed in a molar ratio of 1:1 and ground in an agate mortar until the mixture became sticky. Then solid manganese, nickel and cobalt acetates were added, the molar ratio being Na:Co:Ni:Mn=1/2:1/3:1/3:1/3. Solid residue is treated at 400 °C, followed by thermal annealing at 700 and 800 °C for 10 hours.

The X-ray structural analysis is made by a Bruker Advance 8 diffractometer with LynxEye detector using CuK α radiation. Step-scan recordings for structure refinement by the Rietveld method are carried out using 0.02° 2 θ steps of 4-s duration. The diffractometer point zero, the Lorentzian/ Gaussian fraction of the pseudo-Voigt peak function, the scale factor, the unit cell parameters, the thermal factors, and the line half-width parameters are determined. The computer FullProf Suite Program (1.00) was used in the calculations [9].

The morphology of the precursors and target products is observed by JEOL JSM 6390 scanning electron microscope equipped with an energy dispersive X-ray spectroscopy (EDS, Oxford INCA Energy 350) and ultrahigh resolution scanning system (ASID-3D) in a regime of secondary electron image (SEI). The accelerating voltage is 15 kV and I ~65 A. The pressure is of the order of 10–4 Pa. The electrochemical charge–discharge of Na_{1/2}Co_{1/3}Ni_{1/3}Mn_{1/3}O₂ was examined by using two-electrode cells of the type Li|LiPF₆(EC:DMC)| Na_{1/2}Co_{1/3}Ni_{1/3}Mn_{1/3}O₂. The positive electrode, supported onto an aluminum foil, was a mixture containing 80% of the active composition Na_{1/2}Co_{1/3}Ni_{1/3}Mn_{1/3}O₂, 7.5% CENERGY KS 6 L graphite (TIMCAL), 7.5% Super C65 and 5 % polyvinylidene fluoride (PVDF). The electrolyte was a 1 M LiPF₆ solution in ethylene carbonate and dimethyl carbonate (1:1 by volume) with less than

20 ppm of water. Lithium electrodes were consisted of a clean lithium metal disk with a diameter of 18 mm. The cells were mounted in a dry box under Ar atmosphere. The electrochemical reactions were carried out using an eight-channel Arbin BT2000 system in galvanostatic mode. The cell is cycled between 1.8 and 4.4 V at C/100, C/20 and C/10 rates. Before the cycling, all cells were relaxed at open circuit for 10 hours.

The compositions of electrodes after the electrochemical reaction were determined by LA-ICPMS. The equipment consists of PerkinElmer ELAN DRC-e ICP-MS and state of the art New Wave UP193FX laser ablation system. The laser beam can analyze spots from 10 microns to 150 μ m.

3. RESULTS AND DISCUSSIONS

Figure 1 shows the XRD patterns of Na_{1/2}Co_{1/3}Ni_{1/3}Mn_{1/3}O₂ annealed at 700 °C and 800 °C. All XRD patterns display diffraction peaks that can be assigned to a mixture of the target layered phase and an impurity of NiO-like phase. Therefore, the XRD patterns are calculated based on the structural model that comprises two phases: (i) layered phase with Na in two 3*a* sites (0, 0, z_{Na}) and (1/3, 2/3, z_{Na}), Ni/Mn in 3*a* sites (0, 0, 0) and oxygen in 3*a* sites (0, 0, z_{O1}) and (0, 0, z_{O2}) for a *R3m* space group, and (ii) NiO phase with Ni and O in 4*b* (0.5, 0.5, 0.5) and 4*a* (0, 0, 0) sites for a space group *Fm-3m*. The amount of NiO impurity is less than 1% and it is insensitive towards the annealing temperature. According to the nomenclature of layered oxides [7], Na_{1/2}Co_{1/3}Ni_{1/3}Mn_{1/3}O₂ can be denoted as *P3*-type of structure. The lattice parameters look like slightly dependent on the annealing temperature: a = 2.8299(1) Å and c = 16.7842(14) Å versus a = 2.8308(1) Å and c = 16.7767(14) Å for the oxide annealed at 700 °C and 800 °C, respectively. The lattice volume remains unchanged (116.43 and 116.41 Å³, respectively), thus indicating constancy in the Na content during annealing of the oxides at 700 and 800 °C.

Sodium deficient oxides adopt the *P3*-type of structure, while a well known *O3*-type of structure is stabilized for the sodium stoichiometric oxide NaCo_{1/3}Ni_{1/3}Mn_{1/3}O₂. The structural difference between *P3* and *O3*-modifications comes from the symmetry of the sodium position: In the *P3*-modification all Na⁺ ions occupy one prismatic site that shares face on the one side and edges on the other side with the surrounding Co/Ni/MnO₆-octahedra, while one octahedral position for Na⁺ ions is available for the *O3*-modification (Fig. 2). It should be mentioned that there is a close structural

relation between *P3* and *O3* type structures: by gliding of the $\text{Co}_{1/3}\text{Ni}_{1/3}\text{Mn}_{1/3}\text{O}_2$ -layers, the *P3* structure easily transforms to *O3*. The transformation of *O3* to *P3* type structure has been reported during the electrochemical extraction of sodium from $\text{NaCo}_{1/3}\text{Ni}_{1/3}\text{Mn}_{1/3}\text{O}_2$ [10]. In addition, the *O3*-modification has been obtained at

temperatures higher than 900 °C. This means that the low-temperature synthesis enables to form a new structural modification of sodium deficient oxides $\text{Na}_x\text{Co}_{1/3}\text{Ni}_{1/3}\text{Mn}_{1/3}\text{O}_2$ with a *P3*-type of structure.

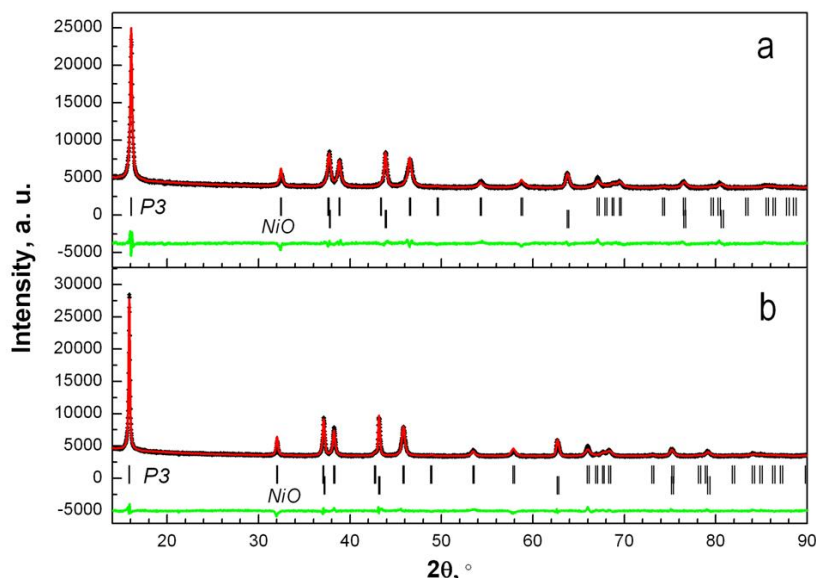


Figure 1. XRD patterns of $\text{Na}_{1/2}\text{Co}_{1/3}\text{Ni}_{1/3}\text{Mn}_{1/3}\text{O}_2$ annealed at 700 and 800 °C. The Bragg's reflections for *P3*-type of structure are given. The impurity phase (NiO) is also indicated. Dotted lines correspond to the simulated XRD patterns using Rietveld refinement method.

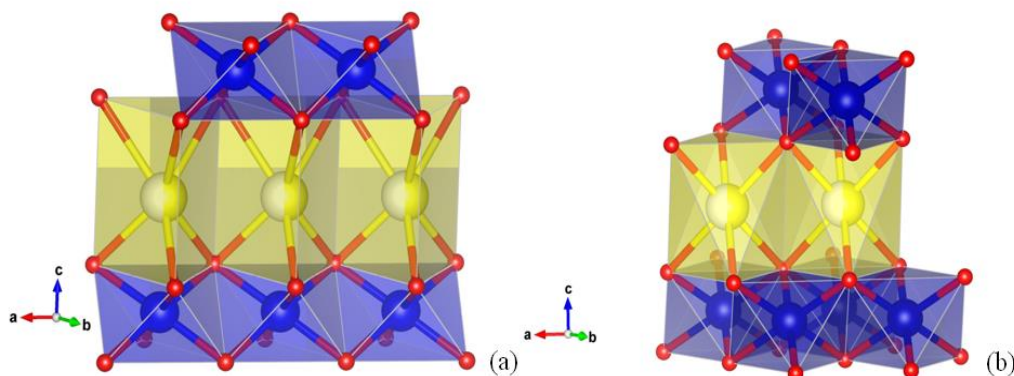


Figure 2. Schematic representation of the sodium position in the *P3*- $\text{Na}_{1/2}\text{Co}_{1/3}\text{Ni}_{1/3}\text{Mn}_{1/3}\text{O}_2$ and *O3*- $\text{NaCo}_{1/3}\text{Ni}_{1/3}\text{Mn}_{1/3}\text{O}_2$ (*a* and *b*, respectively). Blue and yellow colours correspond to Co/Ni/Mn and Na octahedra, respectively.

The morphology of $\text{Na}_{1/2}\text{Co}_{1/3}\text{Ni}_{1/3}\text{Mn}_{1/3}\text{O}_2$ annealed at 700 and 800 C is compared on Figure 3. SEM images show the formation of dense aggregates for $\text{Na}_{1/2}\text{Ni}_{1/2}\text{Mn}_{1/2}\text{O}_2$, which appears to be insensitive towards the annealing temperature (Fig. 3). EDS analysis demonstrates that all elements are homogeneously distributed over the aggregates. Based on SEM/EDS experiments, the composition of sodium-nickel-cobalt-manganese oxides annealed at 700 °C and 800 °C is shown on

Table 1. It is worth mentioning that the chemical composition determined from EDS coincides with that obtained from chemical analysis LA-ICPMS.

3.1. Reversible lithium intercalation in $\text{Na}_{1/2}\text{Co}_{1/3}\text{Ni}_{1/3}\text{Mn}_{1/3}\text{O}_2$

Comparing the electrochemical performance of oxides annealed at 700 and 800 °C, it appears that good cycling stability is achieved only for $\text{Na}_{1/2}\text{Co}_{1/3}\text{Ni}_{1/3}\text{Mn}_{1/3}\text{O}_2$ treated at the higher temperature. That is why, all electrochemical

characterization is focused on the oxide annealed at 800 °C.

Figure 4 gives the electrochemical curves for Li^+ intercalation in $\text{Na}_{1/2}\text{Co}_{1/3}\text{Ni}_{1/3}\text{Mn}_{1/3}\text{O}_2$ at the

potential range of 1.8-4.4 V with a charge/discharge rate of C/20 and C/100. When the cell starts with a discharge, a capacity of 157 mAh/g is obtained at a

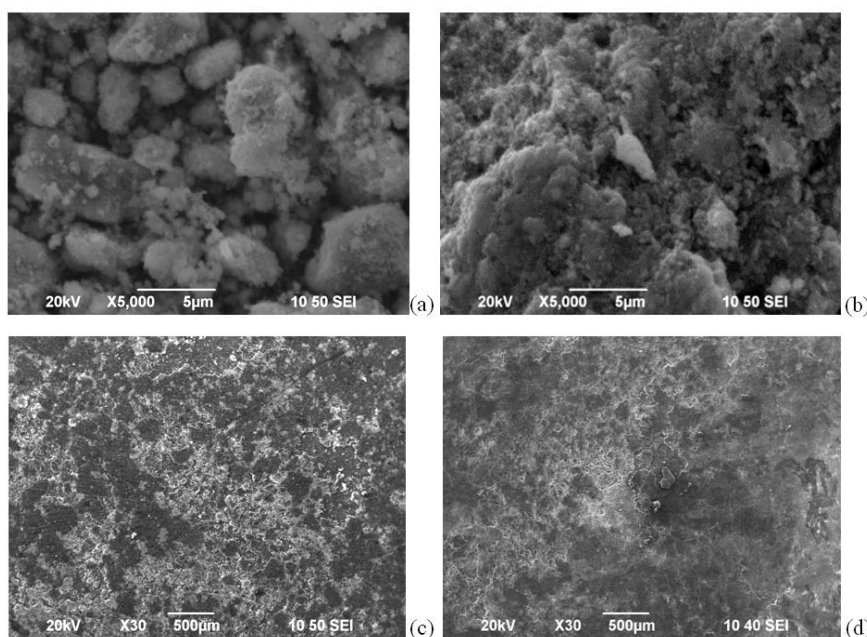


Figure 3. SEM micrographs of $\text{Na}_{1/2}\text{Co}_{1/3}\text{Ni}_{1/3}\text{Mn}_{1/3}\text{O}_2$ powders annealed at 700 (a) and 800 °C (b). Pristine electrode (c) and electrodes (d) after 10 cycles between 1.8 and 4.4 V at a rate of C/100 and stopped at 4.4V are also given. The electrode comprises a mixture of active oxide $\text{Na}_{1/2}\text{Co}_{1/3}\text{Ni}_{1/3}\text{Mn}_{1/3}\text{O}_2$ (85%) and 7.5 % graphite, 7.5 % active carbon and 5 % PVDF.

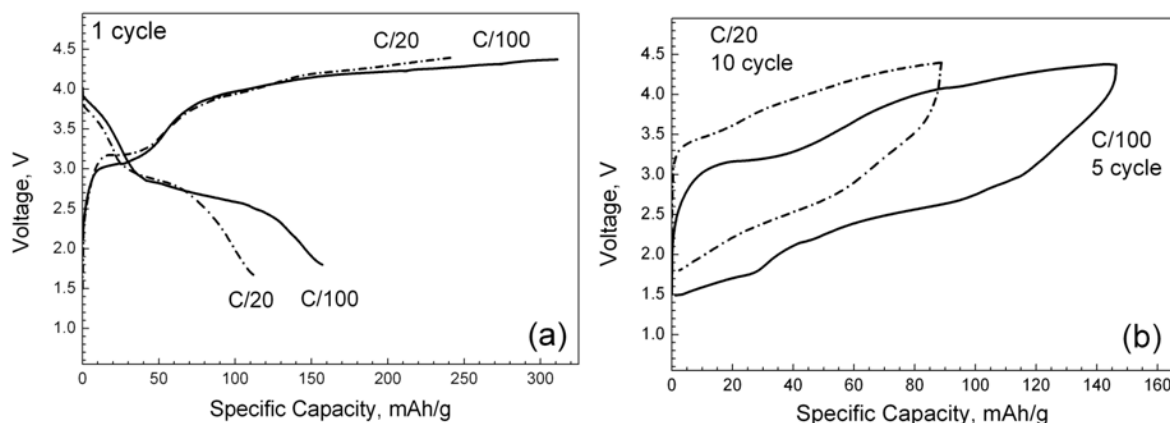


Figure 4. The first discharge and charge curves for $\text{Na}_{0.5}\text{Co}_{1/3}\text{Ni}_{1/3}\text{Mn}_{1/3}\text{O}_2$ annealed at 800 °C at rates of C/20 and C/100 (a). The cells start with a discharge mode. The charge-discharge curves after 5 cycles at a rate of C/100 and after 10 cycles at a rate of C/20 are also presented.

lower rate (i.e. C/100) (theoretical capacity 265.23 mAh/g). By increasing the discharge rate from C/100 to C/20, there is a decrease in the capacity from 157 to 113 mAh/g. It is noticeable that $\text{Na}_{1/2}\text{Co}_{1/3}\text{Ni}_{1/3}\text{Mn}_{1/3}\text{O}_2$ delivers the capacity in two potential plateaus of 3.7 and 2.7 V irrespective of the used discharge rate (Fig. 4). This indicates that lithium extraction proceeds with a structural transformation of $P3\text{-Na}_{1/2}\text{Co}_{1/3}\text{Ni}_{1/3}\text{Mn}_{1/3}\text{O}_2$. Supposing that the electrochemical reaction

includes only intercalation of Li^+ into the layered $\text{Na}_{1/2}\text{Co}_{1/3}\text{Ni}_{1/3}\text{Mn}_{1/3}\text{O}_2$ without proceeding of side-reactions between the electrode and the electrolyte, the amount of intercalated Li^+ can be calculated. Thus, the calculated values corresponding to the first discharge capacities at a rate of C/100 and C/20 are 0.62 and 0.44 mol Li per formula unit $\text{Na}_{1/2}\text{Co}_{1/3}\text{Ni}_{1/3}\text{Mn}_{1/3}\text{O}_2$. It appears that at higher rate (i.e. at C/20), the intercalated amount of Li^+ approaches the sodium deficiency content. It is

noticeable that the amount of Li^+ and Na^+ is slightly lower than 1 (i.e. $0.44+0.50=0.94$), which is in an agreement with the structural constrains for the site occupancy by alkali metals in the layered structure: the occupancy is restricted up to 1 mol of alkali ions. When the slow rate is used, the intercalated Li amount is higher than that corresponding to the sodium deficiency content. This means that the added amount of Li^+ and Na^+ ions per formula unit becomes higher than 1 (i.e. $0.62+0.50=1.12$). To explain the obvious inconsistency with the structural requirements, one could suppose a possible interaction of the oxide with the electrolyte leading to a preferential Na^+ extraction or partial Li^+/Na^+ exchange.

The analysis of the stability of $\text{Na}_{1/2}\text{Co}_{1/3}\text{Ni}_{1/3}\text{Mn}_{1/3}\text{O}_2$ in the electrolyte solution is performed by following the change in the voltage

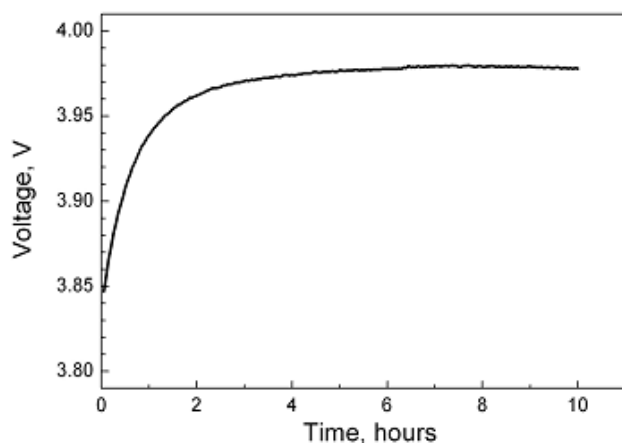


Figure 5. The voltage-time curves for $\text{Na}_{1/2}\text{Co}_{1/3}\text{Ni}_{1/3}\text{Mn}_{1/3}\text{O}_2$ at open circuit.

of the cell at open circuit (Fig. 5). As one can see, the voltage of the cell increases before the electrochemical reaction, indicating a corresponding rising of the oxidation state of the transition metal ions. The steady state potential is achieved after 3 hours of contact between the electrode and the electrolyte. For the sake of

comparison, the voltage of the cell using $\text{LiCo}_{1/3}\text{Ni}_{1/3}\text{Mn}_{1/3}\text{O}_2$ analogue as an electrode is stable (not shown). It is important to note that changes in composition of $\text{Na}_{1/2}\text{Co}_{1/3}\text{Ni}_{1/3}\text{Mn}_{1/3}\text{O}_2$ encompass only the sodium content. Table 1 shows the LA-ICPMS data on the chemical composition of $\text{Na}_{1/2}\text{Co}_{1/3}\text{Ni}_{1/3}\text{Mn}_{1/3}\text{O}_2$ electrodes after the first discharge down to 2.5 V and 1.8 V. It is clear that the ratio between transition metal ions remains constant during the electrochemical reaction, while the sodium content decreases reaching a value of 0.17. Therefore, the changes in the sodium content and related oxidation states of transition metal ions in $\text{Na}_{1/2}\text{Co}_{1/3}\text{Ni}_{1/3}\text{Mn}_{1/3}\text{O}_2$ in the electrolyte solution can be regarded as a result from the competition between Na^+ extraction and Na^+/Li^+ exchange reactions. All these reactions can be related with the thermal instability of LiPF_6 salt, which is found to decompose to LiF and PF_5 even at room temperature [8]. The reaction product PF_5 has acidic properties and can initiate a series of reactions of Na^+ extraction. For example, acidic PF_5 has been shown to play a crucial role in the formation of the solid electrolyte interphase layer that is composed of organic and inorganic decomposed compounds [8].

During the reverse process of charging, the two-stage intercalation reactions are still distinguished: the two reaction plateaus are shifted to 3.1 and 4.1 V, respectively (Fig. 4). An important issue is that the first charge capacity exceeds the corresponding discharge capacity: 312 and 240 mAh/g for C/100 and C/20, respectively. This means that lithium together with sodium is extracted from the oxide during the first charge process. In addition, a partial exchange of Na^+ with Li^+ cannot be excluded. To analyze the processes of Li^+/Na^+ deintercalation and exchange, Table 1 gives the chemical compositions of electrodes determined by LA-ICPMS.

Table 1. LA-ICPMS and EDS data for chemical composition of $\text{Na}_{1/2}\text{Co}_{1/3}\text{Ni}_{1/3}\text{Mn}_{1/3}\text{O}_2$ in the form of the powder annealed at 800 °C and in the form of working electrode.

Element	Powder		Pristine electrode	Electrode after the first discharge down to 2.5 V	Electrode after the first discharge down to 1.8 V	Electrode after 10 cycles between 1.8-4.4 V at a rate of C/100	Electrode after 10 cycles between 1.8-4.4 V at a rate of C/10
	LA-ICPMS	EDS	EDS	LA-ICPMS	LA-ICPMS	EDS	EDS
Na	0.52	0.49	0.55	0.25	0.17	0.19	0.12
Mn	0.32	0.34	0.30	0.31	0.31	0.28	0.31
Co	0.33	0.34	0.36	0.32	0.3	0.33	0.37
Ni	0.35	0.32	0.34	0.37	0.39	0.39	0.32

After the first discharge up to 2.5 V (i.e. after Li intercalation), there is a strong increase in the Li-to-Na ratio, which reveals a lowering of the sodium content in the electrodes in comparison with the pristine compositions (Table 1). The extraction of Li⁺ ions during the charge process up to 4.4 V is manifested by a consecutive decrease in the Li-to-Na ratio (Table 1). The observed changes in the Li-to-Na ratio imply that partial Li⁺/Na⁺ exchange reactions starts to develop at the beginning of the Li intercalation (Table 1). Contrary to lithium and sodium, the nickel and manganese content remains constant during the electrochemical reaction (Table 1).

Stable electrochemical performance is achieved after several cycles. Figure 4 gives the charge/discharge curves after 5 cycles at a rate of C/100, as well as after 10 cycles at a rate of C/20. It is obvious that charge/discharge curves become smoother during cycling with Coulombic efficiency exceeding 96%. The reversible capacity reaches a value of about 145 and 85 mAh/g for a rate of C/100 and C/20, respectively. This means that the electrochemical reaction takes place through reversible intercalation of about 0.55 and 0.35 mole of Li in the oxides charging and discharging with rates of C/100 and C/20, respectively. The changes in the shape of the charge/discharge curves suggest for structural transformations of P3-Na_{1/2}Co_{1/3}Ni_{1/3}Mn_{1/3}O₂ occurring during lithium intercalation. On the other hand, the complex form of the electrochemical curves implies that all Ni²⁺/Ni⁴⁺, Co³⁺/Co⁴⁺ and Mn³⁺/Mn⁴⁺ ionic couples participate in the electrochemical reaction.

Following the structural requirement for restricted site occupancy by alkaline ions, we can suggest that the reversible lithium intercalation is accomplished between two phases: Na_{x<0.5}Ni_{0.5}Mn_{0.5}O₂ and Li_{-0.5}Na_{x<0.5}Ni_{0.5}Mn_{0.5}O₂ phases, respectively. The possible formation of layered transition metal oxides containing Li⁺ and Na⁺ in the interlayer space (i.e. Li_{-0.5}Na_{x<0.5}Ni_{0.5}Mn_{0.5}O₂) is an interesting finding. In comparison with Na⁺ ions, Li⁺ ions prefer to reside in octahedral sites only, as a result of which the crystal chemistry for sodium and lithium transition metal oxides is different [12]. However, a good example for the formation of a mixed Li⁺/Na⁺-oxide are the cobaltates with a composition Li_{-0.42}Na_{-0.37}CoO₂ [13]. The structure of Li_{-0.42}Na_{-0.37}CoO₂ consists of two alternative AO₂ blocks: a P2-type sodium block and an O3-type lithium one [12, 13]. Contrary to Li_{-0.42}Na_{-0.37}CoO₂, the incorporation of Li into O3-NaNi_{0.5}Mn_{0.5}O₂ has recently been shown to proceed by the formation of a P2/O3 intergrowth at an atomic scale [14]. Based

on HRTEM analysis, we have demonstrated that lithium intercalation into Na_xNi_{1/2}Mn_{1/2}O₂ leads to a structural transformation from the P3- to the O3-type of structure, where small amount of Na⁺ remains in the layered structure and the Li-to-Na ratio is 0.7. In analogy, the structure of mixed Na⁺/Li⁺-nickel-manganese oxides could be described as composed of P3 and O3-type blocks.

4. CONCLUSION

New sodium-deficient cobalt–nickel–manganese Na_{1/2}Co_{1/3}Ni_{1/3}Mn_{1/3}O₂ oxides with a P3-type structure are obtained in the temperature range of 700 - 800 °C. The method of synthesis comprises thermal decomposition of mixed acetate-oxalate sodium–transition metal precursors followed by thermal annealing between 700 and 800 °C. Layered oxides Na_{1/2}Co_{1/3}Ni_{1/3}Mn_{1/3}O₂ display a reversible lithium intercalation between 1.8 and 4.4 V. During the first discharge of the electrochemical cell up to 1.8 V, Li⁺ ions are inserted in the empty sodium positions, leading to the formation of a mixed Li⁺/Na⁺ oxides Li_{1-x}Na_xCo_{1/3}Ni_{1/3}Mn_{1/3}O₂ with a structure that deviates from the pristine layered structure. The electrochemical reaction takes place via structural transformation due to the participation of Ni²⁺/Ni⁴⁺, Co³⁺/Co⁴⁺ and Mn³⁺/Mn⁴⁺ ionic couples. A partial exchange of Na⁺ with Li⁺ occurs during the first few cycles, followed by a steady-state performance. The capability of Na_{1/2}Co_{1/3}Ni_{1/3}Mn_{1/3}O₂ to intercalate reversibly lithium in high amounts determines their potential for applications in lithium or sodium rechargeable batteries. Although the voltage range and the electrolyte composition are not optimized, it seems that novel compositions Na_{1/2}Co_{1/3}Ni_{1/3}Mn_{1/3}O₂ display a satisfactory reversible capacity in a wide potential window, where the reversible capacity of LiCo_{1/3}Ni_{1/3}Mn_{1/3}O₂ analogues diminish quickly.

Acknowledgments. This work was supported by European Social Fund (Grant BG051PO001-3.3.06-0050).

REFERENCES

1. V. Palomares, P. Serras, I. Villaluenga, K.B. Hueso, J. Carretero-Gonzalez, T. Rojo, *Energy & Environ. Sci.*, **5**, 5884 (2012).
2. S. Bach, J. P. Pereira-Ramos and P. Willmann, *Electrochem. Acta*, **52**, 504 (2006).
3. M. Yoncheva, R. Stoyanova, E. Zhecheva, E. Kuzmanova, M. Sendova-Vassileva, D. Nihtianova, D. 4. Carlier, M. Guignard and C. Delmas, *J. Mater. Chem.*, **22**, 23418 (2012).

5. X. R. Ye, D.Z. Jia, J.Q. Yu, X.Q. Xin, Z. Xue, *Adv. Mater.*, **11**, 941 (1999).
6. M. Sathiya, K. Hemalatha, K. Ramesha, J.-M. Tarascon, A. S. Prakash, *Chem. Mater.*, **24**, 1846 (2012).
6. B. L. Ellis, L. F. Nazar, *Curr. Opin. Solid State Mater. Sci.*, **16**, 168 (2012).
7. C. Delmas, C. Fouassier, P. Hagenmuller, *Phys B+C*, **91**, 81 (1980).
8. Sv. Ivanova, E. Zhecheva, D. Nihtianova, R. Stoyanova, *J. Mater. Sci.*, **46**, 7098 (2011).
9. J. Rodriguez-Carvajal, in: Satellite Meeting on Powder Diffraction of the XV Congress of the IUCr, p. 127 (1990).
10. S. Komaba, N. Yabuuchi, T. Nakayama, A. Ogata, T. Ishikawa, I. Nakai, *Inorg Chem.*, **51**, 6211 (2012).
11. Sv. Ivanova, E. Zhecheva, R. Stoyanova, D. Nihtianova, S. Wegner, P. Tzvetkova, Sv. Simova, *J. Phys. Chem. C*, **115**, 25170 (2011).
12. R. Berthelot, M. Pollet, J. P. Doumerc, C. Delmas, *Inorg. Chem.*, **50**, 6649 (2011).
13. Z. Ren, J. Shen, S. Jiang, X. Chen, C. Feng, Z. A. Xu, G. H. Cao, *Journal of Physics: Condensed Matter*, **18**, L379 (2006).
14. E. Lee, J. Lu, X. Zhang, D. Miller, A. DeWahl, S. Hackney, B. Key, D. Kim, M.D. Slater and C.S. Johnson, *Advanced Energy Materials*, DOI: 10.1002/aenm.201400458.

НАТРИЕВО-ПРЕХОДНОМЕТАЛНИ ОКСИДИ С НЕДОСТИГ НА НАТРИЙ $\text{Na}_{1/2}\text{Co}_{1/3}\text{Ni}_{1/3}\text{Mn}_{1/3}\text{O}_2$ КАТО АЛТЕРНАТИВНИ ЕЛЕКТРОДНИ МАТЕРИАЛИ ЗА ЛИТИЕВО-ЙОННИ БАТЕРИИ

Св. Г. Иванова*, Е. Н. Жечева, Р. К. Стоянова

Институт по обща и неорганична химия, Българска академия на науките, бул. Акад. Г. Бончев, блок 11, София 1113

Постъпила на 17 юли, 2015 г. коригирана на 23 октомври, 2015 г.

(Резюме)

В тази статия представяме нови данни за структура и обратима интеркалация на литий в оксиди със състав $\text{Na}_{1/2}\text{Co}_{1/3}\text{Ni}_{1/3}\text{Mn}_{1/3}\text{O}_2$. Натриево-преходнометалните оксиди са синтезирани по оксало-ацетатен метод при 700 и 800 °С, с P3-тип структура. Обратима интеркалация на литий се осъществява в потенциалните граници 1.8-4.4 V. По време на първи разряд литиевите йони се интеркалират в незаетите натриеви позиции като се образуват оксиди със състав $\text{Li}_{1-x}\text{Na}_x\text{Co}_{1/3}\text{Ni}_{1/3}\text{Mn}_{1/3}\text{O}_2$, чиято структура е различна в сравнение със структурата на изходните съединения. Електрохимичната реакция се осъществява посредством редокси-двойките $\text{Ni}^{2+}/\text{Ni}^{4+}$, $\text{Co}^{3+}/\text{Co}^{4+}$ и $\text{Mn}^{3+}/\text{Mn}^{4+}$. По време на първите няколко цикъла се обменят литиеви и натриеви йони, след което клетката продължава да работи стабилно. Способността на $\text{Na}_{1/2}\text{Co}_{1/3}\text{Ni}_{1/3}\text{Mn}_{1/3}\text{O}_2$ да интеркалира обратимо литий в големи количества определя потенциалното прилежание на тези оксиди в презареждаеми литиеви и натриеви батерии.

Effect of the synthesis procedure on the electrochemical properties of $\text{Na}_{2/3}\text{Ni}_{1/2}\text{Mn}_{1/2}\text{O}_2$ used as an electrode material in lithium-ion batteries

M. Kalapsazova*, R. Stoyanova, E. Zhecheva

*Institute of General and Inorganic Chemistry, Bulgarian Academy of Sciences,
Acad. G. Bonchev Str., Bldg. 11, Sofia 1113, Bulgaria*

Submitted on July 20, 2015; Revised on October 23, 2015

Abstract. In this contribution, we study in details the effect of synthesis procedure on the electrochemical properties of $\text{Na}_x\text{Ni}_{1/2}\text{Mn}_{1/2}\text{O}_2$ with $x=2/3$ when it is used as an electrode in lithium cells. For the preparation of oxides $\text{Na}_{0.67}\text{Ni}_{0.5}\text{Mn}_{0.5}\text{O}_2$, the precursor-based method was chosen. The method of synthesis is based on the formation of homogeneous precursor phases, which are easily transformed to the target product by a sequence of low-temperature reactions. The precursors are obtained by freeze-drying of aqueous solutions of Li(I), Ni(II) and Mn(II) salts. Two types of soluble salts are selected: acetate and nitrates. Thermal treatment of freeze-dried acetate-nitrate precursors at temperatures above 400 °C yields layered $\text{Na}_{0.67}\text{Ni}_{0.5}\text{Mn}_{0.5}\text{O}_2$ with a *P3*-type of structure. Thermal properties of acetate-nitrate precursors are studied by DTA/TG analysis. The crystal structure and morphology of $\text{Na}_x\text{Ni}_{1/2}\text{Mn}_{1/2}\text{O}_2$ are analyzed by means of X-ray powder diffraction and SEM analysis. The electrochemical properties of $\text{Na}_{0.67}\text{Ni}_{0.5}\text{Mn}_{0.5}\text{O}_2$ are examined in model lithium cells. The oxide $\text{Na}_{0.67}\text{Ni}_{0.5}\text{Mn}_{0.5}\text{O}_2$ obtained from freeze-dried acetate precursors displays a better electrochemical performance in terms of reversible capacity and cycling stability.

Keywords: Sodium deficient transition metal oxides; Layered oxides; Intercalation; Lithium-ion battery

1. INTRODUCTION

Searching for high-power electrode materials for lithium ion batteries, lithium transition metal oxides with a layered structure have been identified as the most suitable compounds [1,2]. Because of the two-dimensional Li diffusion, the electrochemical performances of oxides critically depend on the method of synthesis [1,2]. Two main types of synthetic procedures are developed during the last years [3,4]. The first one aims to stabilize the layered structure of delithiated oxides by rational metal substitution for electrochemically active ions [3], the second type of procedure is directed to design the morphology of oxides in order to make the Li diffusion more easy [4].

Recently, we reported a new concept for design of electrode materials. The concept is aimed at using directly new structure modification of sodium deficient nickel-manganese oxides $\text{Na}_x\text{Ni}_{0.5}\text{Mn}_{0.5}\text{O}_2$ ($x=0.50$ and 0.67) as electrode materials instead of lithium analogues [5,6]. The advantage of using $\text{Na}_x\text{Ni}_{0.5}\text{Mn}_{0.5}\text{O}_2$ is based on their larger interlayer space, which is beneficial both for a rapid exchange of Na^+ with Li^+ and for an easier lithium diffusion. The electrochemical intercalation of Li^+ into layered $\text{Na}_x\text{Ni}_{0.5}\text{Mn}_{0.5}\text{O}_2$ takes place at 3.04 V and leads to a structural transformation from the *P3*- to the *O3*-type of structure [7]. The *in-situ* generated *O3*-phase containing simultaneously lithium and

sodium determines the further electrochemical response of $\text{Na}_x\text{Ni}_{0.5}\text{Mn}_{0.5}\text{O}_2$ in terms of voltage profile, cycling stability and rate capability. Our findings reveal the unique ability of the new structure modification of $\text{Na}_x\text{Ni}_{0.5}\text{Mn}_{0.5}\text{O}_2$ (i.e. *P3*-type of structure) for application as low-cost electrode materials in lithium ion batteries.

In this contribution, we extend our studies by exploring the effect of the synthesis procedure on the electrochemical properties of $\text{Na}_x\text{Ni}_{1/2}\text{Mn}_{1/2}\text{O}_2$ with $x=2/3$ when it is used as an electrode in lithium cells. For the preparation of oxides $\text{Na}_x\text{Ni}_{1/2}\text{Mn}_{1/2}\text{O}_2$, the precursor-based method was chosen. The method of synthesis is based on the formation of homogeneous precursor phases, which are easily transformed to the target product by a sequence of low-temperature reactions. The precursor-based procedure is a powerful tool for the formation of electrode materials with well defined structure and morphology [8,9]. In this study, the precursor phases are obtained by freeze-drying of aqueous solutions of Li(I), Ni(II) and Mn(II) salts. Two types of soluble salts are used: acetate and nitrates. The advantage of this method is related with the ability to control the extent of mixing of Li(I), Ni(II) and Mn(II) ions in the solid precursor phases. Thermal treatment of acetate-nitrate precursors at temperatures above 400 °C yields $\text{Na}_x\text{Ni}_{1/2}\text{Mn}_{1/2}\text{O}_2$ products. Thermal properties of acetate-nitrate precursors are studied by DTA/TG analysis. The crystal structure and morphology of

*To whom all correspondence should be sent:
E-mail: maria_l_k@svr.igic.bas.bg

$\text{Na}_x\text{Ni}_{1/2}\text{Mn}_{1/2}\text{O}_2$ is analyzed by means of X-ray powder diffraction and SEM analysis. The electrochemical properties of $\text{Na}_x\text{Ni}_{1/2}\text{Mn}_{1/2}\text{O}_2$ are examined in model lithium cells.

2. EXPERIMENTAL

Sodium-nickel-manganese oxides are prepared from freeze-dried acetate precursors. The procedure of the preparation is given elsewhere [5,6]. The homogeneous acetate precursors were prepared by freeze-drying of the corresponding Na, Ni and Mn acetate solutions (0.5 M). The nominal Na-to-(Mn+Ni) ratio was 0.67. The freeze-drying process was performed with an Alpha-Crist Freeze-Dryer at $-20\text{ }^\circ\text{C}$ in vacuum. The freeze-dried acetate precursors are decomposed at $400\text{ }^\circ\text{C}$ in O_2 atmosphere for 3 hours. After thermal decomposition of the precursors, the solid residue was homogenized, pelleted and annealed at $700\text{ }^\circ\text{C}$ in air for 24 hours, followed by cooling down to room temperature.

The same procedure is applied for the preparation of $\text{Na}_x\text{Ni}_{1/2}\text{Mn}_{1/2}\text{O}_2$ from mixed nitrate-acetate precursors, where nickel nitrate is used instead of nickel acetate. For the sake of convenience, $\text{Na}_{0.67}\text{Ni}_{0.5}\text{Mn}_{0.5}\text{O}_2$ obtained from acetate and mixed nitrate-acetate precursors will be denoted further by NNM-Ac and NNM-NAc.

The thermal analysis (simultaneously obtained DTA-, TG-, DTG-, and evolved gas curves) of the freeze-dried precursors was carried out by a combined LABSYSTM EVO DTA/TG system of the SETARAM Company, France, with a gas-analyser of the OmniStarTM type. The samples are investigated at a heating rate of $10\text{ }^\circ\text{C}/\text{min}$ in O_2 flow ($20\text{ ml}/\text{min}$).

The X-ray structural analysis was made by a Bruker Advance 8 diffractometer with LynxEye detector using $\text{CuK}\alpha$ radiation. Step-scan recordings for structure refinement by the Rietveld method are carried out using $0.02^\circ\ 2\theta$ steps of 4 s duration. The diffractometer zero point, the Lorentzian/Gaussian fraction of the pseudo-Voigt peak function, the scale factor, the unit cell parameters, the thermal factors and the line half-width parameters were determined. The computer FullProf Suite Program (1.00) was used in the calculations [10].

The morphology of the precursors and target products is observed by JEOL JSM 6390 scanning electron microscope equipped with an energy dispersive X-ray spectroscopy (EDS, Oxford INCA Energy 350) and ultrahigh resolution scanning system (ASID-3D) in a regime of secondary electron image (SEI). The accelerating voltage is 15

kV and $I \sim 65\text{ A}$. The pressure is of the order of 10^{-4} Pa.

The electrochemical charge-discharge behavior of $\text{Na}_x\text{Ni}_{0.5}\text{Mn}_{0.5}\text{O}_2$ was examined by using EL-CELL type two-electrode cells comprising $\text{Li} \mid \text{LiPF}_6$ (EC:DMC) $\mid \text{Na}_x\text{Ni}_{0.5}\text{Mn}_{0.5}\text{O}_2$. The positive electrode, supported onto an aluminium foil, represented a mixture, containing 80% of the active composition $\text{Na}_x\text{Ni}_{0.5}\text{Mn}_{0.5}\text{O}_2$, 7.5% C-ENERGY KS 6 L graphite (TIMCAL), 7.5% Super C65 (TIMCAL) and 5% polyvinylidene fluoride (PVDF). The electrolyte contains 1M LiPF_6 solution in ethylene carbonate and dimethyl carbonate (1:1 by volume) with less than 20 ppm of water. Lithium electrodes consisted of a clean lithium metal disk with diameter of 15 mm. The cells were mounted in a dry box under Ar atmosphere. The electrochemical reactions were carried out using an eight-channel Arbin BT2000 system in galvanostatic mode. The test cells were galvanostatically cycled between 2.5 V and 4.5 V. The charge and discharge rates can be expressed as C/h, being h the number of hours needed for the insertion of one lithium per formula unit at the applied current intensity. All cells are cycled at a rate of C/30.

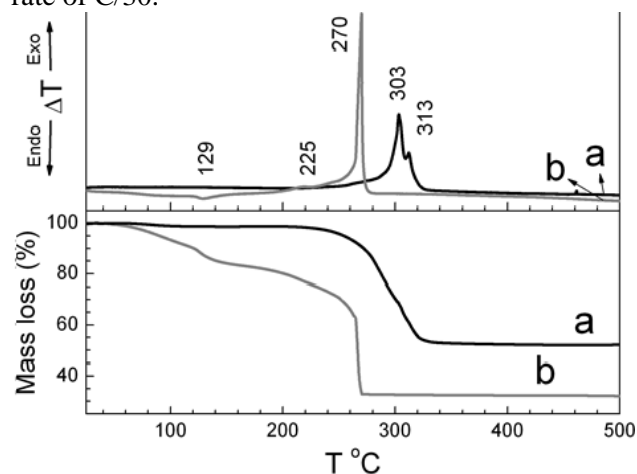


Figure 1. DTA and TGA curves for freeze-dried acetate (a) and nitrate-acetate (b) precursors.

3. RESULTS AND DISCUSSION

3.1. Structure and morphology of $\text{Na}_{0.67}\text{Ni}_{0.50}\text{Mn}_{0.50}\text{O}_2$

Freeze-drying of acetate and mixed nitrate-acetate solutions yields amorphous Na-Ni-Mn precursors. Figure 1 compares the DTA and TGA curves of two types of precursors. Acetate precursor displays one endothermic effect between 80 and $120\text{ }^\circ\text{C}$ accompanied with a weight loss of 1.8% due to H_2O release. This enables to estimate the composition of acetate precursor: $\text{Na}_{0.67}\text{Ni}_{0.50}\text{Mn}_{0.50}(\text{CH}_3\text{COO})_{2.67} \sim 0.2\text{H}_2\text{O}$. Above

220 °C, there is a broad and complex exothermic peak corresponding to the decomposition of the acetate. The decomposition process is completed at 335 °C, where the weight loss reaches about 45%. In comparison with the acetate precursor, the freeze drying process for nitrate-acetate precursor is less effective. Between 80 and 165 °C, the nitrate-acetate precursor displays one endothermic effect together with a weight loss of 17% due to the release of 2.5 mole H_2O . However, the thermal decomposition of nitrate-acetate precursor is more complex process: the decomposition starts above 200 °C followed by a strong exothermic peak in a close temperature range of 260-280 °C. The total weight loss is of 51%. It is noticeable that the decomposition of nitrate-acetate precursor is completed at lower temperature in comparison with that of the acetate precursor.

At 700 °C, thermal annealing of decomposed precursors yields layered sodium nickel-manganese oxides containing impurities of the NiO-like phase. Figure 2 presents the XRD patterns of NNM-Ac and NNM-NAc. Irrespective of the type of the organic component in precursors, the XRD patterns of NNM-Ac and NNM-NAc are satisfactory fitted by the Rietveld analysis on the basis of two-phase model: layered phase ($R\bar{3}m$ space group) and cubic

NiO phase ($Fm\bar{3}m$ space group). The crystal structure of $\text{Na}_{0.67}\text{Ni}_{0.5}\text{Mn}_{0.5}\text{O}_2$ is built from $\text{Ni}_{0.5}\text{Mn}_{0.5}\text{O}_2$ -layers of edge-sharing metal octahedra where the Na^+ ions are sandwiched between the layers. Based on the number of the $\text{Ni}_{0.5}\text{Mn}_{0.5}\text{O}_2$ -layers in the unit cell and the Na site symmetry (i.e. prismatic), the structure of $\text{Na}_{0.67}\text{Ni}_{0.5}\text{Mn}_{0.5}\text{O}_2$ can be classified as $P3$ -type. This is a general structure notation for both sodium and lithium transition metal oxides proposed by Delmas *et al.* [11]. The lattice parameters of acetate- and nitrate-derived oxides $\text{Na}_{0.67}\text{Ni}_{0.5}\text{Mn}_{0.5}\text{O}_2$ are summarized in Table 1. The comparison shows that lattice parameters are the same and they are insensitive towards the type of the organic component used in the precursors. This means that at 700 °C a stable $P3$ -modification of $\text{Na}_{0.67}\text{Ni}_{0.5}\text{Mn}_{0.5}\text{O}_2$ is formed.

In addition, the amount of the NiO-related phase is less than 1%. This is consistent with previous data on limited solubility of Ni in $P3$ - Na_xMnO_2 (up to 0.5 mol) [5,12,13]. It appears that the synthesis of $\text{Na}_{0.67}\text{Ni}_{0.5}\text{Mn}_{0.5}\text{O}_2$ takes place as in case of a formation of high-voltage $\text{LiNi}_{1/2}\text{Mn}_{3/2}\text{O}_4$ spinel, where the impurity NiO-like phase pursues always the target phase [14].

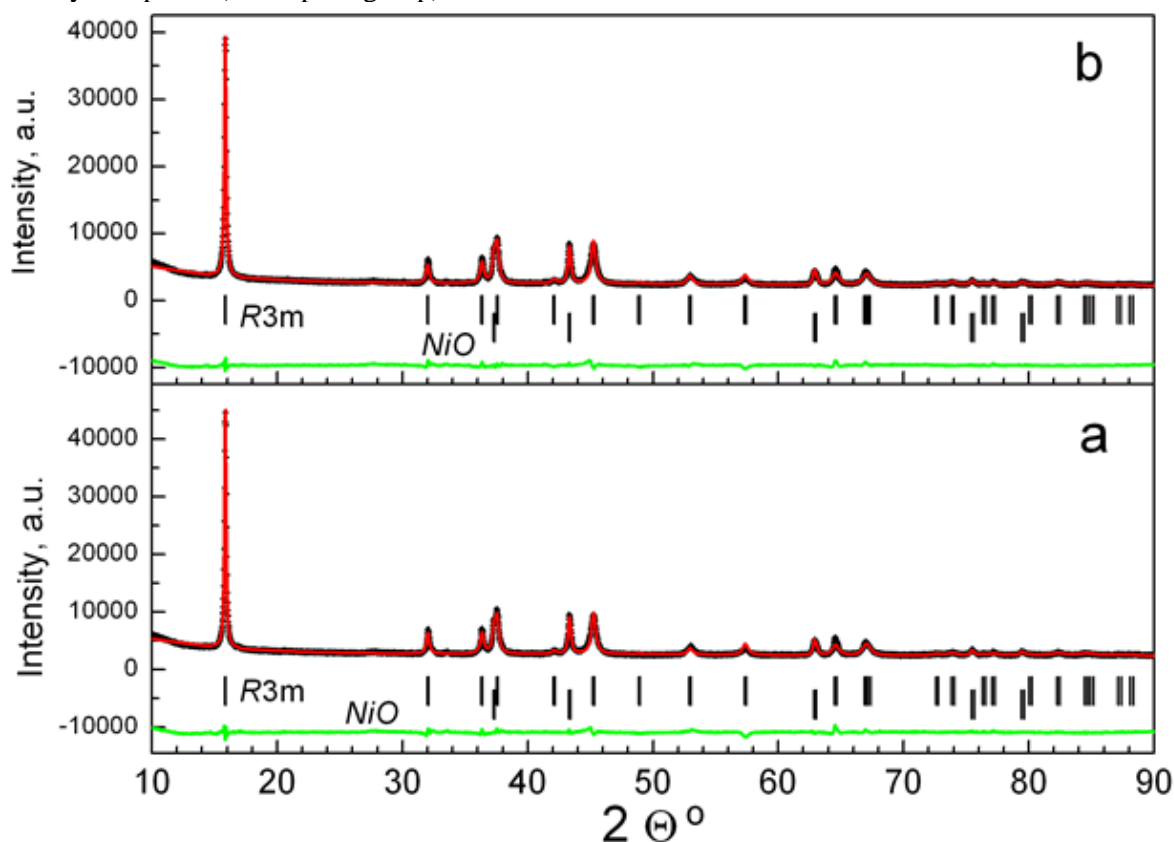


Figure 2. XRD patterns of $\text{Na}_{0.67}\text{Ni}_{0.5}\text{Mn}_{0.5}\text{O}_2$ obtained from the acetate (a) and the nitrate-acetate (b) precursors at 700 °C. The Bragg's reflections for $P3$ -type structure and NiO-like phase are given. Dotted and full lines correspond to the experimental and simulated XRD patterns using Rietveld refinement. The difference between experimental and simulated is shown below the spectra.

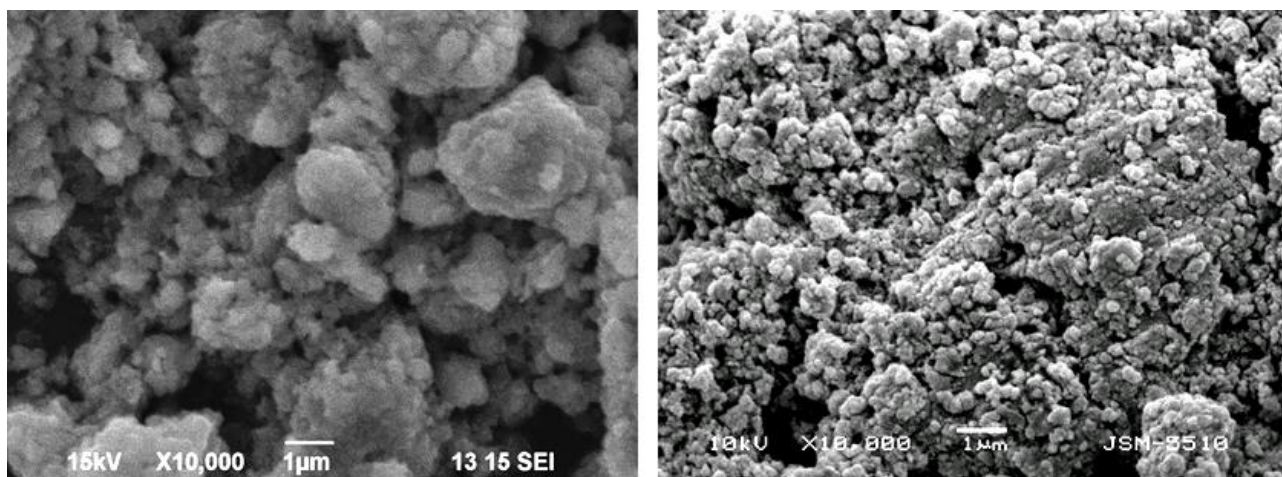


Figure 3 SEM images of $\text{Na}_{0.67}\text{Ni}_{0.5}\text{Mn}_{0.5}\text{O}_2$ obtained from the acetate (left) and the nitrate-acetate (right) precursors at $700\text{ }^\circ\text{C}$.

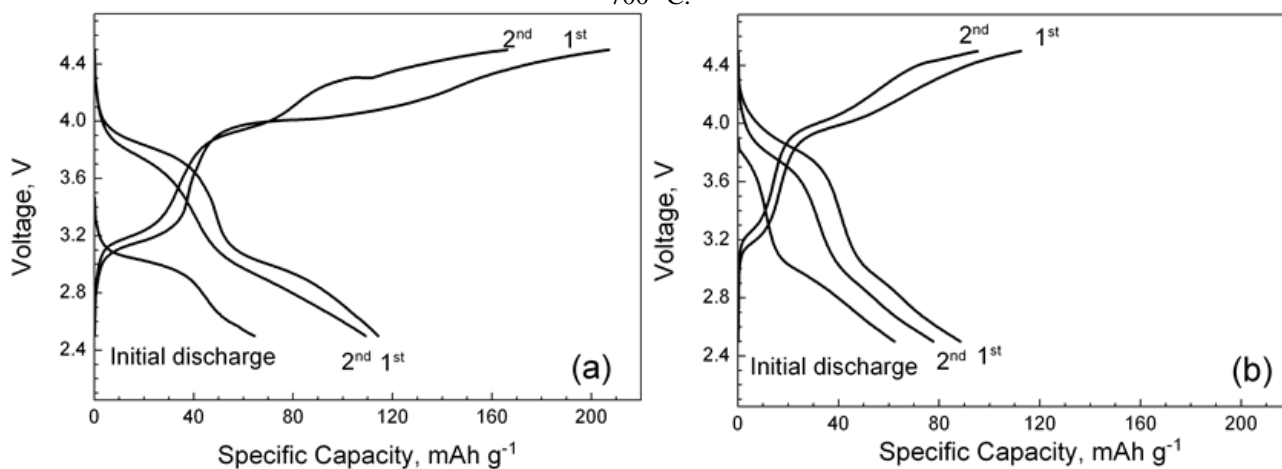


Figure 4. First and second charge/discharge curves of NNM-Ac (a) and NNM-NAc (b). All cells starts with a discharge mode, which is indicated as initial discharge.

The SEM images of acetate- and nitrate-derived oxides are compared on Figure 3. On the first glance, all oxides are composed from particles with sizes of about 100 nm that are bounded into aggregates (Fig. 3). However, close inspection of SEM images reveals a different density of aggregates. It appears that nanoparticles are loosely coupled between them when the acetate precursor is used. In the case of the nitrate-acetate precursor, all nanoparticles seem to be stick together into more dense aggregates. This can be related with the thermal properties of two types of precursors: the nitrate-acetate precursor mimics the combustion process between 240 and $280\text{ }^\circ\text{C}$ due to the simultaneous presence of the nitrate ions as an oxidizer and the acetate ions as a fuel (Fig. 1). In order to create an oxidation atmosphere during the thermal decomposition of acetate precursors, an oxygen flow is used.

3.2. Electrochemical properties of $\text{Na}_{0.67}\text{Ni}_{0.50}\text{Mn}_{0.50}\text{O}_2$

Recently, we have demonstrated that $P3\text{-Na}_{0.67}\text{Ni}_{0.5}\text{Mn}_{0.5}\text{O}_2$ can participate in a series of

reactions comprising lithium intercalation and exchange of Li^+ for Na^+ [5,6,7]. This fact, in its turn, determines the potential of $P3\text{-Na}_{0.67}\text{Ni}_{0.5}\text{Mn}_{0.5}\text{O}_2$ for direct use as a cathode in lithium ion batteries. In this study we are focused on the effect of the synthesis procedure on the electrochemical performance of $P3\text{-Na}_{0.67}\text{Ni}_{0.5}\text{Mn}_{0.5}\text{O}_2$.

Figure 4 shows the first and second charge/discharge curves for NNM-Ac and NNM-NAc. The cell starts with a discharge mode, which corresponds to a lithium intercalation in sodium deficient oxides. During the discharge, a capacity of about 65 mAh g^{-1} is obtained for both oxides (Fig. 4). This value corresponds to the intercalation of 0.3 mole Li^+ into $P3\text{-Na}_{0.67}\text{Ni}_{0.5}\text{Mn}_{0.5}\text{O}_2$. It is worth to mention that the content of intercalated Li^+ coincides with the amount of sodium deficiency in $P3\text{-Na}_{0.67}\text{Ni}_{0.5}\text{Mn}_{0.5}\text{O}_2$. The discharge profile shows a distinct plateau at 3.0 V, which is more pronounced for the acetate-derived oxide. This indicates that lithium intercalation into $P3\text{-Na}_{0.67}\text{Ni}_{0.5}\text{Mn}_{0.5}\text{O}_2$ is a two-phase reaction and its mechanism is not dependent on the method of

oxide synthesis. Based on HR-TEM and SAED, we have demonstrated a structure transformation from the *P3*- to the *O3*-type of structure during electrochemical intercalation of Li^+ into layered $\text{Na}_x\text{Ni}_{0.5}\text{Mn}_{0.5}\text{O}_2$ at 3.04 V [7].

During the reverse process of charge, both oxides are clearly distinguished: a higher charge capacity is achieved for the oxide obtained from the acetate precursors, i.e. 207 versus 113 mAh g^{-1} , respectively (Fig. 4). These values exceed significantly the discharge capacity, thus indicating a possible participation of Na^+ in addition to Li^+ in the charge process. However, it could be taken into account that additional side reactions (such as electrode-electrolyte interactions, electrolyte decomposition, etc.) take also place above 4.4 V.

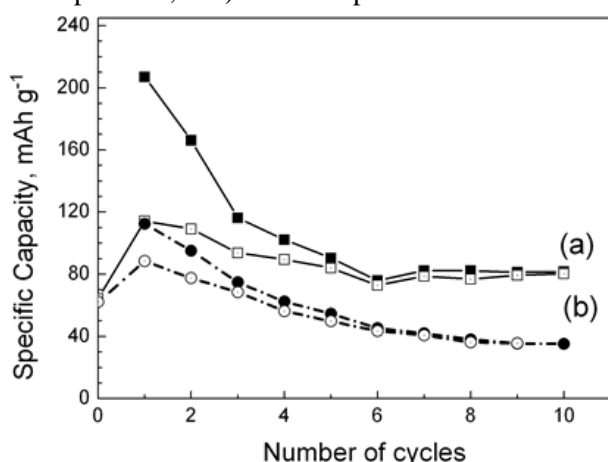


Figure 5 Cycling stability curves of of NNM-Ac (a) and NNM-NAc (b). The open and close symbols correspond to the discharge and charge capacity.

The difference in the electrochemical performances of both NNM-Ac and NNM-NAc oxides remains during the second discharge: NNM-Ac delivers a higher capacity in comparison with that for NNM-NAc, i.e. 115 versus 90 mAh/g , respectively. This means that about 0.45 and 0.35 mole of Li^+ is reinserted in NNM-Ac and NNM-NAc. The important issue is related with an irreversible capacity after the first charge and discharge. It appears that the acetate-derived oxide NNM-Ac has a higher irreversible capacity. The irreversible capacity diminishes during cycling. Figure 5 gives the cycling stability curves for NNM-Ac and NNM-NAc. After several charge/discharge cycles, a steady state performance is reached: for NNM-Ac the coulombic efficiency tending to 100% is reached after 5 cycles, while after 3 cycles NNM-NAc displays coulombic efficiency higher than 97%. During prolonged cycling, the reversible capacity delivered by NNM-Ac is significantly higher in comparison with that

for NNM-NAc: 85 mAh g^{-1} versus 45 mAh/g , respectively.

The comparison of cycling stability curves outlines clearly that after the first irreversible capacity the electrochemical performance of acetate-derived $\text{Na}_{0.67}\text{Ni}_{0.5}\text{Mn}_{0.5}\text{O}_2$ is much better than that of the nitrate-acetate derived oxide. The huge irreversible capacity is a specific feature for NNM-Ac and can be explained if we suggest a higher reactivity of NNM-Ac towards the electrolyte leading to the formation of surface electrochemical interface (SEI). The formation of possible SEI does not interrupt the reversible lithium intercalation into NNM-Ac. The same scenario has recently been established for lithium transition metal oxides $\text{Li}_{1+x}\text{M}_{1-x}\text{O}_2$ having lithium in excess [15]. The excess of lithium is accommodated in the transition metal layers by substituting for transition metal ions. Above 4.4 V, it has been found that oxides with lithium excess undergo a structural transformation by releasing of lithium from transition metal layers in the form of Li_2O , the layered structure being preserved. It is worth to note that after this structural transformation a high reversible capacity and a good cycling stability are achieved. Contrary to lithium-excess oxides, sodium and transition metals forms only sodium deficient and sodium stoichiometric transition metal oxides. Therefore, we can suppose that the formation of SEI on sodium deficient oxides obtained from acetate precursors is most plausible phenomenon. Based on XPS analysis, we have demonstrated that, in the course of the electrochemical reaction, the oxide surface is covered with sodium and lithium phospho-fluorine-based compounds, which remain stable during the cycling [6]. This is a consequence of the reactivity of sodium deficient oxides towards LiPF_6 salt in the electrolyte, the reaction being intensified at potentials higher than 4.4 V [6]. The important finding of the present study is the different reactivity of oxides obtained from the acetate and nitrate-acetate precursors towards LiPF_6 salt in the electrolyte. It appears that SEI formed on oxides contributes to their cycling stability. Further optimization of the electrochemical properties of sodium deficient oxides are closely related with the selection of appropriate electrolyte composition.

4. CONCLUSIONS

Sodium-deficient nickel-manganese oxides $\text{Na}_{0.67}\text{Ni}_{0.5}\text{Mn}_{0.5}\text{O}_2$ with a *P3*-type of structure are obtained at 700 °C from freeze-dried acetate and nitrate-acetate precursors. The morphology of both acetate and nitrate-acetate derived oxides consists

of aggregates with micrometric dimensions, which are building from particles with nanometric dimensions. The density of aggregates shows a dependence on the type of organic component used in precursors: nanoparticles are loosely coupled between them when the acetate precursor is used, while for the oxide derived from nitrate-acetate precursor, all nanoparticles seem to be stick together into more dense aggregates.

Both acetate and nitrate-acetate derived oxides display reversible lithium intercalation when used as electrodes in model lithium cells. The better electrochemical behavior (in terms a reversible capacity and cycling stability) is observed for $\text{Na}_{0.67}\text{Ni}_{0.5}\text{Mn}_{0.5}\text{O}_2$ obtained from the acetate precursor. The good electrochemical behavior is related with a higher reactivity of acetate-derived oxides towards the electrolyte leading to the formation of SEI during the first charge to 4.5 V. The electrochemically formed SEI has a main contribution to improved cycling stability.

Acknowledgments. This work was supported by European Social Fund (Grant BG051PO001-3.3.06-0050).

REFERENCES

1. R. Alcántara, P. Lavela, J. L. Tirado, E. Zhecheva, R. Stoyanova, *J. Solid State Electrochem.*, **3**, 121 (1999).
2. B.L. Ellis, K.T. Lee, L.F. Nazar, *Chem. Mater.*, **22**, 691 (2010).
3. N. Nitta, F. Wu, J.T. Lee, G. Yushin, *Mater. Today*, **18**, 252 (2015).
4. X. Xu, S. Lee, S. Jeong, Y. Kim, J. Cho *Mater. Today*, **16**, 487 (2013).
5. M. Kalapsazova, R. Stoyanova and E. Zhecheva, *J. Solid State Electrochem.*, **18**, 2343 (2014).
6. M. Kalapsazova, R. Stoyanova, E. Zhecheva, G. Tyuliev, D. Nihtianova, *J. Mater. Chem. A*, **2**, 19383 (2014).
7. M. Kalapsazova, G. F. Ortiz, J. L. Tirado, O. Dolotko, E. Zhecheva, D. Nihtianova, L. Mihaylov and R. Stoyanova, *ChemPlusChem* (in press).
8. M. K. Song, S. Park, F. M. Alamgir, J. Cho, M. Liu, *Mat. Sci. Eng.* **R72**, 203 (2011).
9. Z. Gong, Y. Yang, *Energy Environ. Sci.*, **4**, 3223 (2011).
10. J. Rodriguez-Carvajal, *Commission on Powder Diffraction Newsletter*, **26**, 12 (2001).
11. C. Delmas, C. Fouassier, P. Hagenmuller, *Phys B+C*, **91**, 81 (1980).
12. Z. Lu, R.A. Donaberger, J.R. Dahn, *Chem. Mater.*, **12**, 3583 (2000).
13. J.M. Paulsen, R. Donaberger, J.R. Dahn, *Chem. Mater.*, **12**, 2257 (2000).
14. Sv. Ivanova, E. Zhecheva, R. Stoyanova, D. Nihtianova, S. Wegner, P. Tzvetkova, Sv. Simova, *J. Phys. Chem. C*, **115**, 25170 (2011).
15. Y. Wu, C. Ma, J. Yang, Z. Li, C. Liang, L.F. Allard, M. Chi, *J. Mater. Chem. A*, **3**, 5385 (2015).

ВЛИЯНИЕ НА НАЧИНА НА СИНТЕЗ ВЪРХУ ЕЛЕКТРОХИМИЧНИТЕ СВОЙСТВА НА $\text{Na}_{2/3}\text{Ni}_{1/2}\text{Mn}_{1/2}\text{O}_2$, ИЗПОЛЗВАН КАТО ЕЛЕКТРОДЕН МАТЕРИАЛ В ЛИТИЕВО-ЙОННИ БАТЕРИИ

М. Калъпсзова*, Р. Стоянова, Е. Жечева

*Институт по обща и неорганична химия, Българска академия на науките,
Ул. Акад. Г. Бончев, бл. 11, София 1113, България*

Постъпила на 20 юли, 2015 г. коригирана на 23 октомври, 2015 г.

(Резюме)

В настоящата статия ние изследваме в детайли влиянието на начина на синтез върху електрохимичните свойства на $\text{Na}_x\text{Ni}_{1/2}\text{Mn}_{1/2}\text{O}_2$ с $x=2/3$ при използването му като електрод в литиеви клетки. За получаването на оксидите $\text{Na}_{0.67}\text{Ni}_{0.5}\text{Mn}_{0.5}\text{O}_2$ е избран метода на прекурсорите. Този метод се основава на образуване на хомогенни прекурсорни фази, които лесно се превръщат в целевия продукт чрез серия от нискотемпературни реакции. Прекурсорите са получени чрез лиофилизация на водни разтвори на соли на Li(I), Ni(II) и Mn(II). Избрани са два вида разтворими соли: ацетати и нитрати. При термична обработка на лиофилизираните ацетатни-нитратни прекурсори при температури над 400 °C се получава слоест $\text{Na}_{0.67}\text{Ni}_{0.5}\text{Mn}_{0.5}\text{O}_2$ с P3-тип структура. Термичните свойства на ацетатните-нитратните прекурсори са изследвани чрез DTA/TG анализ. Кристалната структура и морфологията на $\text{Na}_x\text{Ni}_{1/2}\text{Mn}_{1/2}\text{O}_2$ са изследвани посредством прахова рентгенова дифракция и СЕМ анализ. Електрохимичните свойства на $\text{Na}_{0.67}\text{Ni}_{0.5}\text{Mn}_{0.5}\text{O}_2$ са изучени в моделни литиеви клетки. Оксидът $\text{Na}_{0.67}\text{Ni}_{0.5}\text{Mn}_{0.5}\text{O}_2$ получен от лиофилизиран ацетатни прекурсори показва по-добри електрохимични характеристики по отношение на обратим капацитет и стабилност при циклиране.

Surface studies of fly ash zeolites via adsorption/desorption isotherms

S.V. Boycheva, D.M. Zgureva*

Technical University of Sofia, Department of Thermal and Nuclear Power Engineering, 8, Kl. Ohridsky Blvd., 1000 Sofia, Bulgaria

Submitted on July 14, 2015; Revised on November 3, 2015

Zeolites of types Na-A (Linde, LTA) and Na-X (Faujasite, FAU) are perspective adsorbents in environment protection systems due to their extremely developed surface area and pore size exceeding molecular diameter of variety gaseous pollutants. Recently, synthetic analogous of these zeolites being obtained of aluminosilicate residues for saving natural resources. In this study LTA and FAU zeolites were synthesized by alkaline conversion of coal fly ash by different techniques in order to be further applied for adsorption of carbon dioxide from flue gases. The main key factors predeterminating the adsorption ability of solids are their surface and porosity characteristics. For these considerations, selected samples were subjected to surface studies by the help of surface area and porosity analyzer Tristar II 3020, Micromeritics. Experimental adsorption/desorption isotherms were measured at 77 K using analytical gas nitrogen 5N. Specific surface areas (S_{BET} , m^2/g) of the investigated samples were evaluated applying the standart multi-point Brunauer-Emmett-Teller (BET) model to the adsorption data. The raw fly ash is characterized with a very low specific surface area of $10 \text{ m}^2/\text{g}$, while S_{BET} values for the fly ash zeolites (FAZ) of Na-X type were found in the range of $125\text{--}250 \text{ m}^2/\text{g}$ depending on the synthesis procedures applied. The highest specific BET surface area of $280 \text{ m}^2/\text{g}$ in the frame of this study was measured for FAU type coal fly ash zeolite, obtained by atmospheric self-crystallization for about of a year. However, FAZ possess three times lower S_{BET} values in comparison to a referent zeolite Na-X prepared from pure components. Mesopore distribution was studied by the Barrett-Joyner-Halenda (BJH) model applied to the experimental desorption isotherms. Micropore volume/area yield was computed from the adsorption data using t-plot model.

Key words: fly ash zeolites, surface area, porosity, adsorption isotherms

INTRODUCTION

Since tens of years, enormous amounts of ash residues including bottom ash, boiler slag and fly ash (FA) are generated all over the world by coal supplied Thermal Power Plants (TPP). Recently, different approaches for high-value added utilization of coal ash in practice have been developed instead of its disposal in landfills [1,2]. Thus, this solid by-product became a raw material for production of building materials, composites, agricultural amendments, geopolymers, low-cost adsorbents, as well as a source for separation of ferrous oxides (magnetite, hematite) or for extraction of titanium oxide, alumina, cenospheres, etc. Due to aluminosilicate macro composition of FA, its conversion into zeolites has been widely investigated [3,4]. Fly ash zeolites (FAZ) similarly to their natural and pure synthetic analogies are perspective materials for many advanced applications such as ion-exchangers, molecular sieves, and adsorbents [5,6]. Making efforts for finding a solution of global warming by reduction of the greenhouse gas emissions exhausted into the atmosphere, zeolites have been studying as potential

adsorbents for carbon dioxide uptake from flue gas streams. Physical adsorption of CO_2 on solids possesses a number of advantages in comparison to the broadly studied chemisorption by amine-based solutions consisting of technical feasibility, low-energy desorption, environmental harmless, process reversibility, absence of secondary liquids, adsorbent multiple usage without loses, and cost effectiveness [7]. Pressure (PSA) and vacuum swing adsorption (VSA) have been considered as the main potential techniques for capture of CO_2 from flue gas flows [8,9]. Many studies on carbon dioxide sequestration on commercial 5A (CaA) and 13X (NaX) zeolites have been done indicating their high capacity and preferential adsorption toward CO_2 [10,11]. FAZ have to meet a numbers of requirements mostly directed to their surface properties for being competitive in practice. The most recently, the research interest has been provoked by the FAZ suitability as adsorbents of carbon dioxide in post-combustion carbon capture systems striving to develop zero emission TPP [12]. However, the implementation of such innovative technology claims materials with extremely developed specific surface area and appropriate pore size distribution.

This study is focused on the evaluation of the main surface characteristics of fly ash zeolites of

*To whom all correspondence should be sent:
E-mail: dzgureva@gmail.com

Na-X (Faujasite, FAU) and Na-A (Linde, LTA) types by experimental adsorption and desorption isotherms in comparison to those of the raw fly ash and pure synthetic zeolite Na-X as a referent.

EXPERIMENTAL

FAZ were synthesized by alkaline conversion of lignite coal fly ash collected by the electrostatic precipitators of TPP "Maritza East 2" in Bulgaria. Chemical and phase composition, morphology and the main thermal properties of the raw FA were previously studied [13]. Zeolite phases were obtained by three manners of alkaline activation of FA, as follows: (1) double stage fusion-hydrothermal synthesis; (2) self-crystallization of FA/sodium hydroxide mixtures at room conditions; (3) hybrid fusion/self-crystallization method. The influence of the synthesis conditions on the morphology, phase composition and crystallinity of the obtained zeolites was investigated [14,15].

Nitrogen adsorption/desorption isotherms of selected FAZ samples, raw FA and a referent Na-X obtained from pure starting components were measured at 77 K using a volumetric adsorption analyzer Tristar II 3020, Micromeritics. Samples were preliminary degassed in a set-up FlowPrep 60, Micromeritics, at 260 °C for 2 h under helium flow. BET specific surface areas (S_{BET} , m^2/g) were evaluated applying the multi-point Brunauer–Emmett–Teller (BET) model for description of the experimental nitrogen adsorption data in the range of relative pressures p/p_0 corresponding to formation of monolayer. Mesopore distribution for the investigated FAZ, FA and the referent zeolite Na-X (FAU) was studied from the desorption branch of the isotherms by the Barrett-Joyner-Halenda (BJH) model. The theory of the models can be found in Ref. [16]. Micropore volume/area yield was evaluated using t-plot model for the adsorption data.

RESULTS AND DISCUSSION

Preliminary studies

The raw FA used for these studies is mostly aluminosilicate material consisting of SiO_2 and Al_2O_3 in a ratio of 2.25, as their total amount exceeds 76 wt. %. The amorphous vs. crystalline part was found to be 43/57. FA was used as a starting material for synthesis of zeolites by alkaline activation with sodium hydroxide (NaOH) applying three different methods for preparation, designated as follows: (1) atmospheric self-crystallization; (2) two stage fusion-hydrothermal synthesis and (3) two-stage fusion-atmospheric crystallization. Synthesis conditions of the investigated samples are summarized in Table 1, while more detailed description can be found in Refs. [15,17]. The obtained FAZ were studied by X-ray diffraction (XRD) and scanning electron microscopy (SEM) to identify their phase composition and morphology. The predominant zeolite phase obtained at different synthesis conditions is indicated in Table 1.

N_2 -adsorption/desorption isotherms

The experimental N_2 -adsorption/desorption isotherms of the investigated FAZ, starting FA and referent Na-X zeolite are plotted in Fig.1. The isotherms represent the function between the amount of the adsorbed gas (mmol) by unit mass of solid (g) and the relative pressure p/p_0 , which is the ratio between the equilibrium (p) and the saturation pressure (p_0) at $T=77$ K.

The types of the isotherms were described according to the IUPAC classification (1985). A thorough analysis of the shapes of different physisorption isotherms in view of material structure has been made in Ref. [18]. FA shows a N_2 -adsorption isotherm of type II that is usually typical for non-porous or macroporous materials with relatively small specific surface area (Fig. 1).

An adsorption-desorption hysteresis loop of H3 shape, which is normally attributed to materials

Table 1. Synthesis conditions of FAZ samples.

Sample	Method of FAZ synthesis	FA/NaOH ratio	NaOH M	Fusion at 90 °C for 1 hour	Synthesis temperature, °C	Time of synthesis	FAZ type
A-2	Atmospheric self-crystallization	1/0.6	1.5	NO	approx. 20	240 days	X
A-3	Atmospheric self-crystallization	1/0.6	1.5	NO	approx. 20	360 days	X
FH-5	Two stage fusion-hydrothermal	1/1.6	2	YES	90	4 hours	A
FH-7	Two stage fusion-hydrothermal	1/2.4	3	YES	90	4 hours	X
FA-1	Two stage fusion-atmospheric	1/1	2.5	YES	approx. 20	30 days	X

containing slit-shaped pores can be observed. Physical sorption isotherms of type II have also been reported for F-class FA in other investigations [19]. The referent Na-X sample exhibits adsorption isotherm of type I with a narrow desorption loop most similar to H4 shape. The adsorption of N₂ on the Na-X zeolite rises rapidly at low relative pressures $p/p_0 < 0.01$ filling almost the entire free volume available, and thereafter the adsorbed quantity increases slowly attaining a nearly horizontal plateau. This is indicative for size-distribution of micropores in a limited range and for a very small external surface area. Hysteresis loops of type H4 are also given by slit-shaped pores, but in this case the pore size distribution is mainly in a microscale range. Taking into account the narrow area of adsorption/desorption loop, it can be assumed

that the FAU used as a referent sample is a microporous material consisting predominantly of cylindrical pores with a defined pore width, and a small yield of slit-shaped pores. At $p/p_0 > 0.95$, the isotherm of Na-X begins to increase indicating the presence of some macropores [18]. FAZ FH-5 which is predominantly composed of zeolite A crystalline phase characterizes with an isotherm of type II that is very similar in shape to those of the raw FA. However, some differences can be observed between the two isotherms that can be summarized as follows: at FAZ FH-5 the hysteresis loop is narrower and the adsorption and desorption branches coincide at p/p_0 below 0.4, while at FA a very small deviation between the branches can be observed resulting in an opened isotherm.

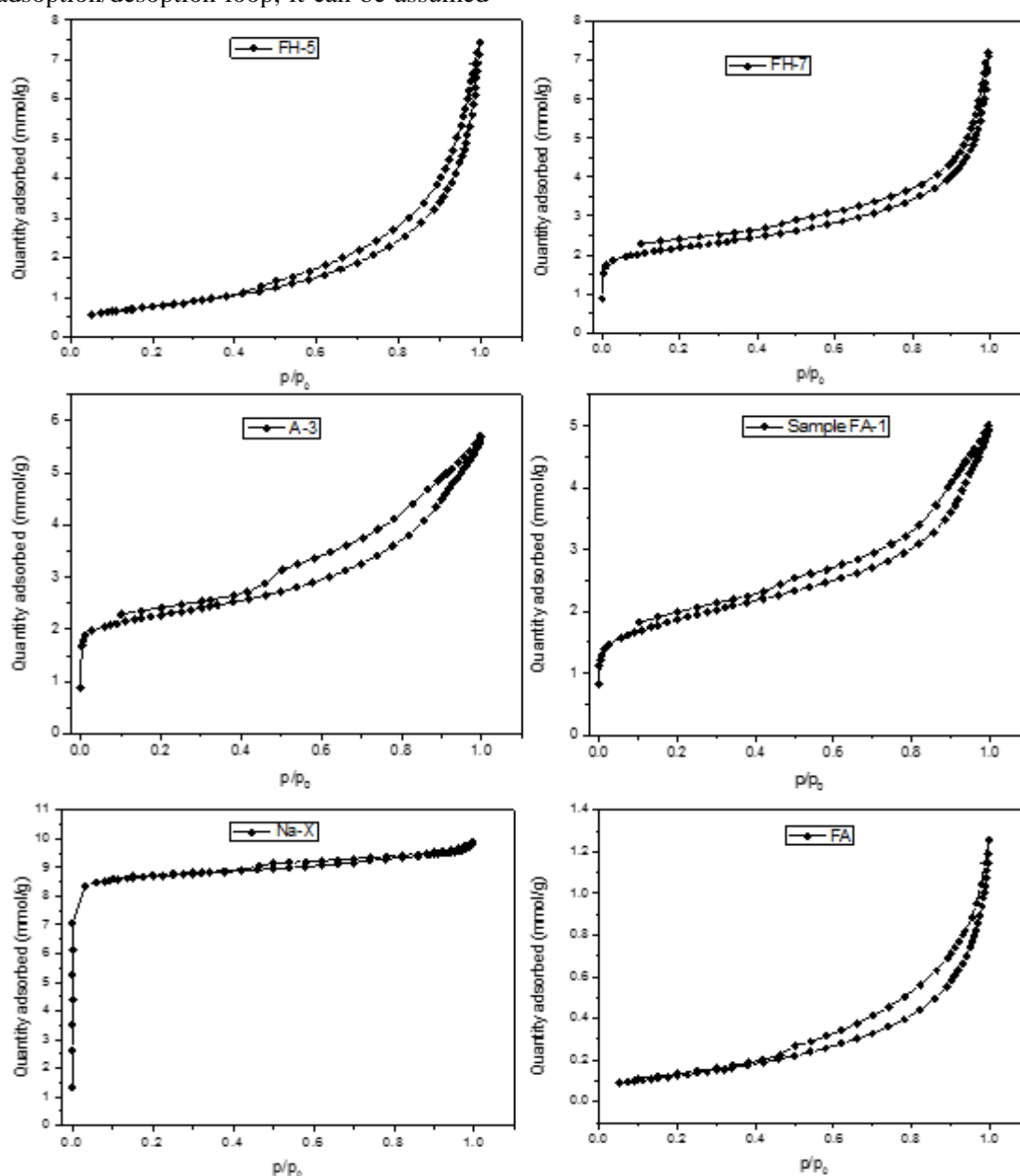


Fig. 1. Experimental N₂-adsorption/desorption isotherms of the raw fly ash, fly ash zeolites and referent Na-X.

FAZ FH-7, FAZ A-3 and FAZ FA-1 are mainly composed of Na-X phase obtained from one and the same raw material by different techniques. The all investigated Na-X fly ash zeolites exhibit isotherms very closed to type IV with hysteresis loops of H4 shape. Unlike to the pure FAU, adsorption of N₂ on Na-X FAZ takes part slightly in the monolayer region (less than 2 mmol/g) and much stronger at higher p/p₀ values. At middle p/p₀ range a progressive adsorption process takes part leading to capillary condensation in mesopores. Adsorption and desorption branches do not go over describing open isotherms with broad loops, which are indicative for wide pore size distribution and the presence of narrow slits. The broadest hysteresis region is observed for FAZ A-3. Sample FH-7 behaves very sharp adsorption at high pressures p/p₀ → 1, which can be obeyed by macropore filling. The adsorption capacity of the pure Na-X toward N₂ at studied conditions reaches about 10 mmol/g, while those of FAZ varies between 5.0 and 7.5 mmol/g at p/p₀=1, as the highest values are reached for ash zeolites obtained by a double stage fusion-hydrothermal synthesis. FA is characterized by a negligible N₂ adsorption capacity around 1.3 mmol/g.

BET specific surface area

The BET specific surface area (S_{BET}, m²/g) of the investigated samples was evaluated applying the multipoint Brunauer–Emmett–Teller (BET) method to the experimental nitrogen adsorption data. Taking into account the transform contributed by Rouquerol et al. [20] for adjusting range used for fitting BET parameters at microporous materials, it was found that for the investigated FAZ, the function 1/Q[(p₀/p)-1]=f(p/p₀), where Q is the adsorbed volume, is linear in the range p/p₀=0.01-

0.05, corresponding to the monolayer adsorption region, where the BET constant C takes positive values.

S_{BET} values correspond to the total area, that includes the external surface of the particles and the internal surface described by pores. Typical BET plots for Na-X FAZ and the referent Na-X are presented in Fig. 2.

It is clearly seen the linearity of the adsorption functions at p/p₀=0.01-0.05 and the positive Y-intercept (C>0), which is indicative for the reliability of the BET calculations. Into the insertion in Fig.2, the knee of monolayer adsorption is presented.

The obtained data for S_{BET} are summarized in Table 2. Fly ash has a very low BET surface area of 10 m²/g, whereas FAZ zeolites possess S_{BET} values from 6 to 28 times higher. FAZ of Na-X types are characterized with higher values of BET surface area than those composed of Na-A phase. The highest S_{BET} is measured for FAZ A-3 due to its strongest crystallinity in comparison to the other samples. Fly ash zeolites of Na-X type have three to five times lower specific surface area in comparison to the referent FAU sample. Despite of this and taking into account the benefits of ecological effect of FA conversion into zeolites, FAZ of Na-X type obtained by different techniques are characterized with sufficient surface characteristics, which make them suitable materials for gas-adsorption purposes for removal of different atmospheric pollutants.

Micro- and mesopore volume/area distribution

The internal surface area described by micropores (S_{micro}, m²/g) and the micropore volume (V_{micro}, m³/g) was calculated using t-plot model (Table 2). Macro- and mesopore size distribution

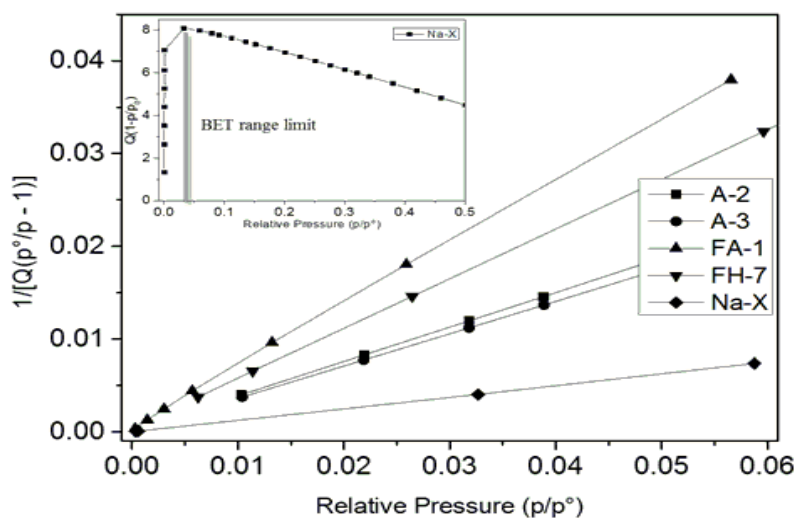
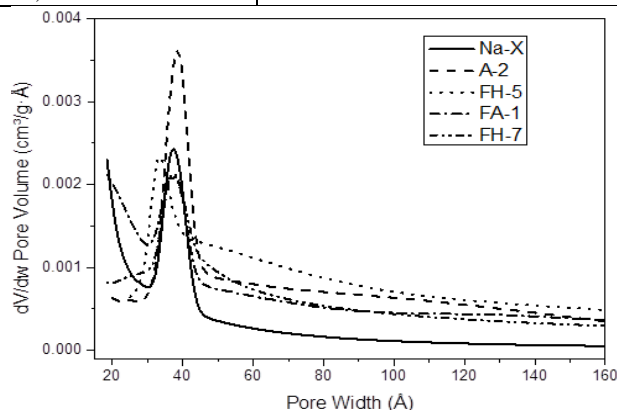


Fig. 2. BET plots for FAZ and referent Na-X.

Table 2. Surface characteristics and porosity of raw fly ash, fly ash zeolites and referent Na-X.

Characteristics	Samples						
	FA	A-3	A-2	FH-5	FH-7	FA-1	Na-X
S_{BET} , m ² /g	10.4	279.6	262.4	60.7	181.7	146.4	779.8
S_{micro} , m ² /g	-	119.4	173.8	-	109.5	45.5	718.6
V_{micro} , cm ³ /g	-	0.048	0.069	-	0.044	0.025	0.275
$S_{\text{meso/macro}}$, m ² /g	13.9	84.6	78.0	77.2	83.8	97.0	62.5
$V_{\text{meso/macro}}$, cm ³ /g	0.012	0.116	0.105	0.119	0.103	0.105	0.055
Average mesopore width, nm	5.8	5.6	5.7	6.2	5.3	4.8	3.5
Average micropore width, nm	-	1.36	1.29	-	1.33	1.38	1.35

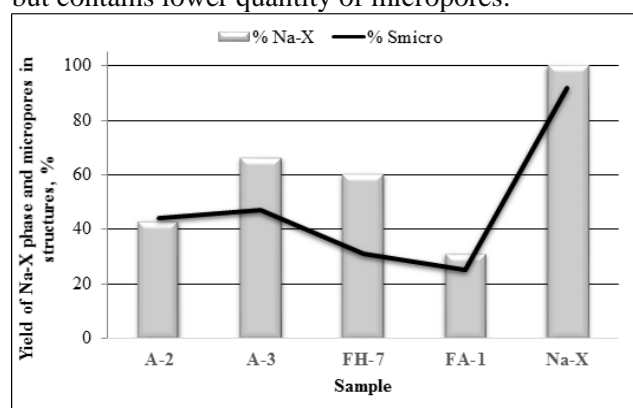
**Fig. 3.** Pore size distribution functions of investigated FAZ and the referent Na-X.

was studied by the Barrett-Joyner-Halenda (BJH) model applied to the desorption branch of the experimental isotherms. The obtained results for adsorption cumulative surface area ($S_{\text{meso/macro}}$, m²/g) and cumulative volume ($V_{\text{meso/macro}}$, cm³/g) of meso- and macropores with diameters between 1.7 and 300.0 nm, are listed in Table 2. The obtained values show that the referent zeolite Na-X is mostly microporous material with a small yield of meso- and macropores, while FAZ of Na-X type possess mixed micro-, meso-, and macroporous structure. Nevertheless, the samples consisting of high quantity of FAU phase obtained by atmospheric self-crystallization (A-2 and A-3) and two stage fusion-hydrothermal synthesis (FH-7) are predominantly microporous. Evidently, lack of micropores is observed at FA and FAZ of LTA type, which corresponds to their isotherms. The highest yield of meso- macroporosity is observed at the FAZ obtained by two stage fusion-atmospheric crystallization.

Pore width distribution functions in the mesoporous region of investigated FAZ and the referent Na-X are presented in Fig. 3. Average mesopore width calculated from desorption data by BJH method is given in Table 2. The mesoporosity of FAZ of FAU type and the referent zeolites is dominated by pores with sizes around 4 nm, while for FH-5 composed of LTA phase the maximum of

distribution function is shifted toward 3 nm but significant amount of pores with sizes between 4-8 nm can be also observed. That is why, the highest average mesopore width is obtained at FH-5. Average micropore width calculated by BET method varies slightly and is comparable to the value for the referent Na-X.

The dependence of micropore percentage and the yield of the Na-X phase is presented in Fig. 4. The microporosity exceeds as higher is the crystallinity of the samples obtained by atmospheric self-crystallization. Sample FH-7 prepared by two stage fusion-hydrothermal synthesis is characterized with high yield of FAU zeolite comparable to that at A-3 but contains lower quantity of micropores.

**Fig. 4.** Dependence between the yields of micropore surface area and Na-X phase.

CONCLUSIONS

Fly ash zeolites of Na-X (Faujasite, FAU) type synthesized from coal fly ash by different techniques were studied with respect to their surface characteristics by experimental adsorption and desorption isotherms. Coal fly ash zeolites of FAU type obtained by different ways possess similar adsorption behavior which describes by isotherms of type IV with hysteresis loops corresponding to a micro-mesoporous texture. Surface parameters such as BET surface area, internal micro- and mesopore surface and volume, as well as pore size distribution were evaluated applying standard multipoint BET, BJH and t-plot models to the experimental data. The

obtained results were compared with those for the raw fly ash and the referent FAU. The highest specific BET surface area of 280 m²/g was measured for coal fly ash zeolite of Na-X type, and despite that is roughly three times lower in comparison to the referent sample, it enlarges fly ash surface more than 28 times. The yield of micropores in FAU based on coal ash depends on their crystallinity and the synthesis technique, whereas the yield of mesopores is dominant at all fly ash zeolites. Average mesopore width for Na-X fly ash zeolites was found in a sort range between 4.8 and 5.7 nm, as the main part of the porosity is due to pores with width about 4 nm, which is indicative for structural definiteness. It could be expected that mesoporosity of fly ash zeolites will facilitate mass transport though the materials which will be of benefit for their application for adsorption of gas molecules. Mesopore size will worsen their selectivity in a case of application as molecular sieves. On the other hand, it could be expected stronger affinity toward polar CO₂ molecules that will decide the drawbacks of structural diversity.

Acknowledgements: The authors are thankful to the Technical University of Sofia for the financial support under contract No. 152PD0020-02; D. Zgureva thanks to Karoll Financial Group for the PhD Fellowship.

REFERENCES

1. M. Ahmaruzzaman, *Progress Energy Combustion Sci.*, **36**, 327 (2010).
2. S. V. Patil, S.C. Nawle, S. J. Kulkarni, *Int. J. Sci. Eng. Technol. Res.*, **2**, 1659 (2013).
3. X. Querol, N. Moreno, J.C. Umana, A. Alastuey, E. Hernandez, A. Lopez-Soler, F. Plana, *Int. J. Coal Geol.*, **50**, 413 (2002).
4. Inada, M., Eguchi, Y., Enomoto, N., Hojo, J., *Fuel*, **84**, 299 (2005).
5. M. Franus, M. Wdowin, L. Bandura, W. Franus, *Environ. Bull.*, **24**, 854 (2015).
6. A. Srinivasan, M. W. Grutzeck, *Environ. Sci. Technol.*, **33**, 1464 (1999).
7. W. Jan, *CHEMIK*, **67**, 889 (2013).
8. L. Hauchhum, P. Mahanta, *Int. J. Energy Environ. Eng.*, **5**, 349 (2014).
9. J. Ling, A. Ntiamoah, P. Xiao, D. Xu, P. A Webley, Y. Zhai, Overview of CO₂, *Austin J Chem Eng.*, **1**, 1009 (2014).
10. Q.H. Dirar, K.F. Loughin, *Adsorption*, **19**, 1149 (2013).
11. R.V. Siriwardane, M.-Sh. Shen, E.P. Fisher, *Energy Fuels*, **19**, 1153 (2005).
12. Ch.-H. Lee, S.-W. Park, S.-S. Kim, *Korean J. Chem. Eng.*, **31**, 179 (2014).
13. S. Boycheva, D. Zgureva, V. Vassilev, *Fuel*, **108**, 639 (2013).
14. S. Boycheva, D. Zgureva, A. Shoumkova, *Coal Combustion Gasification Prod.*, **7**, 1 (2015).
15. D. Zgureva, S. Boycheva, In: Nanoscience Advances in CBRN Agents Detection, Information and Energy Security, Eds. P. Petkov, D. Tsiulyanu, W. Kulisch, C. Popov, Springer 2015, p. 199.
16. D. Ruthven, Principles of Adsorption and Adsorption Processes, John Wiley & Sons, USA, 1984.
17. D. Zgureva, S. Boycheva, *Ecol. Eng. Environ. Protection*, **2**, 12 (2015).
18. F. Rouquerol, J. Rouquerol, K. Sing, Adsorption by Powders and Porous Solids: Principle, Methodology and Applications, Academic Press, UK, 1999.
19. M. Wdowin, M. Franus, R. Panek, L. Badura, W. Franus, *Clean Techn. Environ. Policy*, (2014).
20. J. Rouquerol, P. Llewellyn, and F. Rouquerol, In: Characterisation of porous solids, Studies in Surface Science and Catalysis, 2007, p. 49.

ИЗСЛЕДВАНИЯ НА ПОВЪРХНОСТНИТЕ ХАРАКТЕРИСТИКИ НА ЗЕОЛИТИ ОТ ЛЕЛЯЩА ПЕПЕЛ ЧРЕЗ ИЗОТЕРМИ НА АДСОРБЦИЯ И ДЕСОРБЦИЯ

С.В. Бойчева, Д.М. Згурева*

*Технически университет – София, Катедра „Топлоенергетика и ядрена енергетика“,
бул. „Климент Охридски“ 8, София 1000, България*

Постъпила на 14 юли, 2015 г. коригирана на 3 ноември, 2015 г.

(Резюме)

Зеолитите от типа Na-A (LTA) и Na-X (FAU) са перспективни адсорбенти в системи за опазване на околната среда, благодарение на изключително развитата им повърхност и размер на порите, надвишаващ молекулните диаметри на широка гама газообразни замърсители. Напоследък интензивно се синтезират аналози на тези зеолити от отпадъчни алумосиликати с цел опазване на природните ресурси. За целите на настоящето изследване са синтезирани LTA и FAU зеолити чрез алкална конверсия на летяща пепел от въглища с оглед последващото им прилагане за адсорбцията на въглероден диоксид от димни газове. Основните ключови фактори, предопределящи адсорбционната способност на твърдите вещества, са тяхната повърхност и порьозност. В тази връзка са изследвани повърхностните характеристики на избрани образци от синтезираните въглищни зеолити с помощта на порьозиметър Tristar II 3020, Micromeritics. Построени са експериментални изотерми на адсорбция и десорбция с аналитичен газ азот 5N при 77 К. Специфичната площ ($S_{\text{ВЕТ}}$, m^2/g) на изследваните образци е определена чрез прилагането на модела на Brunauer-Emmett-Teller (BET) към данните от адсорбционните изотерми. Изходната летяща пепел се характеризира с много ниска специфична повърхност от $10 \text{ m}^2/\text{g}$, докато стойностите на $S_{\text{ВЕТ}}$ за синтезираните пепелни Na-X зеолити са в диапазона $125\text{-}250 \text{ m}^2/\text{g}$ в зависимост от условията на синтез. В рамките на настоящето изследване, най-голяма повърхност по BET от $280 \text{ m}^2/\text{g}$ е измерена за пепелен зеолит от FAU тип, получен чрез самокристализация на сместа от летяща пепел, натриева основа и вода в продължение на около година. Тези стойности са до три пъти по-ниски в сравнение с $S_{\text{ВЕТ}}$ на референтен Na-X зеолит, синтезиран от чисти изходни компоненти. Разпределението на мезопорите на материалите по размер е изчислено от данните от експерименталните десорбционни изотерми чрез прилагането на модела на Barrett-Joyner-Halenda (BJH). Обемът, площта и делът на микропори са изчислени от адсорбционните изотерми с помощта на t-plot модела.

BULGARIAN CHEMICAL COMMUNICATIONS

Instructions about Preparation of Manuscripts

General remarks: Manuscripts are submitted in English by e-mail or by mail (in duplicate). The text must be typed double-spaced, on A4 format paper using Times New Roman font size 12, normal character spacing. The manuscript should not exceed 15 pages (about 3500 words), including photographs, tables, drawings, formulae, etc. Authors are requested to use margins of 3 cm on all sides. For mail submission hard copies, made by a clearly legible duplication process, are requested. Manuscripts should be subdivided into labelled sections, e.g. **Introduction, Experimental, Results and Discussion, etc.**

The title page comprises headline, author's names and affiliations, abstract and key words.

Attention is drawn to the following:

a) **The title** of the manuscript should reflect concisely the purpose and findings of the work. Abbreviations, symbols, chemical formulas, references and footnotes should be avoided. If indispensable, abbreviations and formulas should be given in parentheses immediately after the respective full form.

b) **The author's** first and middle name initials, and family name in full should be given, followed by the address (or addresses) of the contributing laboratory (laboratories). **The affiliation** of the author(s) should be listed in detail (no abbreviations!). The author to whom correspondence and/or inquiries should be sent should be indicated by asterisk (*).

The abstract should be self-explanatory and intelligible without any references to the text and containing not more than 250 words. It should be followed by key words (not more than six).

References should be numbered sequentially in the order, in which they are cited in the text. The numbers in the text should be enclosed in brackets [2], [5, 6], [9–12], etc., set on the text line. References, typed with double spacing, are to be listed in numerical order on a separate sheet. All references are to be given in Latin letters. The names of the authors are given without inversion. Titles of journals must be abbreviated according to Chemical Abstracts and given in italics, the volume is typed in bold, the initial page is given and the

year in parentheses. Attention is drawn to the following conventions:

a) The names of all authors of a certain publications should be given. The use of “*et al.*” in the list of references is not acceptable.

b) Only the initials of the first and middle names should be given.

In the manuscripts, the reference to author(s) of cited works should be made without giving initials, e.g. “Bush and Smith [7] pioneered...”. If the reference carries the names of three or more authors it should be quoted as “Bush *et al.* [7]”, if Bush is the first author, or as “Bush and co-workers [7]”, if Bush is the senior author.

Footnotes should be reduced to a minimum. Each footnote should be typed double-spaced at the bottom of the page, on which its subject is first mentioned.

Tables are numbered with Arabic numerals on the left-hand top. Each table should be referred to in the text. Column headings should be as short as possible but they must define units unambiguously. The units are to be separated from the preceding symbols by a comma or brackets.

Note: The following format should be used when figures, equations, *etc.* are referred to the text (followed by the respective numbers): Fig., Eqns., Table, Scheme.

Schemes and figures. Each manuscript (hard copy) should contain or be accompanied by the respective illustrative material as well as by the respective figure captions in a separate file (sheet). As far as presentation of units is concerned, SI units are to be used. However, some non-SI units are also acceptable, such as °C, ml, l, etc.

The author(s) name(s), the title of the manuscript, the number of drawings, photographs, diagrams, etc., should be written in black pencil on the back of the illustrative material (hard copies) in accordance with the list enclosed. Avoid using more than 6 (12 for reviews, respectively) figures in the manuscript. Since most of the illustrative materials are to be presented as 8-cm wide pictures, attention should be paid that all axis titles, numerals, legend(s) and texts are legible.

The authors are asked to submit **the final text** (after the manuscript has been accepted for

publication) in electronic form either by e-mail or mail on a 3.5" diskette (CD) using a PC Word-processor. The main text, list of references, tables and figure captions should be saved in separate files (as *.rtf or *.doc) with clearly identifiable file names. It is essential that the name and version of the word-processing program and the format of the text files is clearly indicated. It is recommended that the pictures are presented in *.tif, *.jpg, *.cdr or *.bmp format, the equations are written using "Equation Editor" and chemical reaction schemes

are written using ISIS Draw or ChemDraw programme.

The authors are required to submit the final text with a list of three individuals and their e-mail addresses that can be considered by the Editors as potential reviewers. Please, note that the reviewers should be outside the authors' own institution or organization. The Editorial Board of the journal is not obliged to accept these proposals.

EXAMPLES FOR PRESENTATION OF REFERENCES

REFERENCES

1. D. S. Newsome, *Catal. Rev.–Sci. Eng.*, **21**, 275 (1980).
2. C.-H. Lin, C.-Y. Hsu, *J. Chem. Soc. Chem. Commun.*, 1479 (1992).
3. R. G. Parr, W. Yang, *Density Functional Theory of Atoms and Molecules*, Oxford Univ. Press, New York, 1989.
4. V. Ponec, G. C. Bond, *Catalysis by Metals and Alloys* (Stud. Surf. Sci. Catal., vol. 95), Elsevier, Amsterdam, 1995.
5. G. Kadinov, S. Todorova, A. Palazov, in: *New Frontiers in Catalysis* (Proc. 10th Int. Congr. Catal., Budapest, 1992), L. Guzzi, F. Solymosi, P. Tetenyi (eds.), Akademiai Kiado, Budapest, 1993, Part C, p. 2817.
6. G. L. C. Maire, F. Garin, in: *Catalysis. Science and Technology*, J. R. Anderson, M. Boudart (eds), vol. 6, Springer-Verlag, Berlin, 1984, p. 161.
7. D. Pocknell, *GB Patent 2 207 355* (1949).
8. G. Angelov, PhD Thesis, UCTM, Sofia, 2001.
9. JCPDS International Center for Diffraction Data, Power Diffraction File, Swarthmore, PA, 1991.
10. *CA* **127**, 184 762q (1998).
11. P. Hou, H. Wise, *J. Catal.*, in press.
12. M. Sinev, private communication.
13. <http://www.chemweb.com/alchem/articles/1051611477211.html>.

CONTENTS

<i>Editors Preface</i>	5
<i>D.S. Ivanova, J.K. Angarska, E.D. Manev</i> , Kinetic and equilibrium properties of foam films stabilized by mixtures of n-dodecyl- β -D-maltoside with nonionic or ionic surfactants...	7
<i>I.K. Terziyski, R.K. Todorov, D.R. Exerowa</i> , Influence of corticosteroids on formation and stability of thin liquid films from pulmonary therapeutic preparations.....	13
<i>S.A. Alexandrov, R. K. Todorov, A. G. Jordanova, Z. I. Lalchev, D. R. Exerowa</i> , Foam films stabilized with lysophosphatidylglycerol in the presence of Na ⁺ and Ca ²⁺	18
<i>T.D. Andreeva, A.K. Danailova, P. Terziyska, S.B. Krumova, S.G. Taneva, R. Krastev</i> , Hofmeister anions effect on the thickness and morphology of polyelectrolyte multilayers for biofunctionalization of cardiovascular stents.....	23
<i>F.V. Hodzhaoglu, M. Conejero-Muriel, I. L. Dimitrov, J. A. Gavira</i> , Optimization of the classical method for nucleation and growth of rhombohedral insulin crystals by pH titration and screening.....	29
<i>E. Petkucheva, E. Lefterova, J. Heiss, U. Schnakenberg, E. Slavcheva</i> , Influence of the gold sub-layer on the catalytic properties of magnetron sputtered Pt and Ir thin films.....	38
<i>I.V. Slivkov, D.L. Lyutov, Z.Pl. Pancheva, L.G. Lyutov</i> , A new method for synthesis of a new class reducing agent with expected application in nanotechnology.....	44
<i>M.T. Peshova, V.D. Bachvarov, S.D. Vitkova, N.S. Boshkov</i> , Obtaining and protective properties of passive films on Zn and Zn-Fe-P ternary alloys.....	50
<i>N.D. Boshkova, P.D. Petrov, N.S. Boshkov</i> , Obtaining and comparative corrosion characterization of composite zinc and zinc alloy coatings with embedded stabilized polymeric micelles.....	57
<i>G.S. Chalakova, M.D. Datcheva, R.Z. Iankov, A.I. Baltov, D.S. Stoychev</i> , Comparative study via nanoindentation of the mechanical properties of conversion corrosion protective layers on aluminum formed in Cr ⁶⁺ -containing and Cr ⁶⁺ -free solutions.....	64
<i>V.I. Karabozhikova, V.Ts. Tsakova</i> , Silver electrocrystallization at PEDOT-coated electrodes – interpretation of current transients.....	71
<i>S. Pehlivanova, Ch. Petkov, A. Surleva, P. Petkov, C. Popov, T. Petkova</i> , Diamond electrodes for wastewater treatment.....	78
<i>S.G. Harizanova, E.N. Zhecheva, M.G. Khristov, V. D. Valchev, R.K. Stoyanova</i> , Thermoelectric oxide materials based on cobalt perovskites.....	82
<i>Sv.G. Ivanova, E.N. Zhecheva, R.K. Stoyanova</i> , Sodium deficient transition metal oxides Na _{1/2} Co _{1/3} Ni _{1/3} Mn _{1/3} O ₂ as alternative electrode materials for lithium-ion batteries.....	88
<i>M. Kalapsazova, R. Stoyanova, E. Zhecheva</i> , Effect of the synthesis procedure on the electrochemical properties of Na _{2/3} Ni _{1/2} Mn _{1/2} O ₂ used as an electrode material in lithium-ion batteries	95
<i>S.V. Boycheva, D.M. Zgureva</i> , Surface studies of fly ash zeolites via adsorption/desorption isotherms.....	101
<i>INSTRUCTIONS TO THE AUTHORS</i>	109

СЪДЪРЖАНИЕ

<i>Предисловие от редакторите</i>	5
<i>Д.Ст. Иванова, Ж.Кр. Ангарска, Е.Д. Манев</i> , Кинетични и равновесни свойства на пенни филми от смесени разтвори на α -D-малтозид с нейонни и йонни повърхностноактивни вещества.....	12
<i>И.К. Терзийски, Р.К. Тодоров, Д.Р. Ексерова</i> , Влияние на кортикостероиди върху формирането и стабилността на тънки течни филми от пулмонарни терапевтични препарати.....	17
<i>С.А. Александров, Р.К. Тодоров, А.Г. Йорданова, З.И. Лалчев, Д.Р. Ексерова</i> , Пенни филми от лизофосфатидилглицерол в присъствие на Na^+ и Ca^{2+}	22
<i>Т. Д. Андреева, А. К. Данаилова, П. Терзийска, С. Б. Крумова, С. Г. Танева, Р. Кръстев</i> , Ефект на Хофмайстерови аниони върху дебелината и морфологията на полиелектролитни мултислоеве за биофункционализиране на кардиоваскуларни стентове.....	28
<i>Ф.В. Ходжаоглу, М. Конехеро-Муриел, И.Л. Димитров, Х.А. Гавира</i> , Оптимизация на класическия подход за зараждане и растеж на ромбедрични кристали от инсулин чрез провеждане на pH титруване и кристализационен скрининг.....	37
<i>Е.Петкучева, Е. Лефтерова, Й. Хайс, У. Шнакенберг, Е. Славчева</i> , Влияние на подслоя от злато върху каталитичните свойства на тънки магнетронно разпрасени филми от Pt и Ir.....	43
<i>Ив.В. Сливков[†], Д.Л. Лютов, З.Пл. Панчева, Л.Г. Лютов</i> , Нов метод за синтеза на нов клас редуктори с очаквани приложения в нанотехнологиите.....	49
<i>М.Т. Пешова, В.Д. Бъчваров, С.Д. Виткова, Н.С. Божков</i> , Получаване и защитни свойства на пасивни филми върху цинк и тройни цинкови сплави Zn-Fe-P.....	56
<i>Н.Д. Божкова, П.Д. Петров, Н.С. Божков</i> , Получаване и сравнително корозионно характеризиране на композитни цинкови и сплавни цинкови покрития с вградени стабилизиращи полимерни мицели	63
<i>Г.С. Чалъкова, М.Д. Дачева, Р.З. Янков, А.И. Балтов, Д.С. Стойчев</i> , Сравнително изследване чрез наноиндентация на механичните свойства на конверсионни защитни слоеве върху алуминий, отложени от съдържащи и несъдържащи Cr^{6+} разтвори.....	70
<i>В.И. Карабожикова, В.Ц. Цакова</i> , Електрокристализация на сребро върху електроди, покрити с ПЕДОТ – интерпретация на токови транзиенти.....	77
<i>С. Пехливанова, Х. Петков, А. Сурлева, П. Петков, К. Попов, Т. Петкова</i> , Диамантени електроди за третиране на отпадъчни води.....	81
<i>С.Г. Харизанова, Е.Н. Жечева, М.Г. Христов, В.Д. Вълчев, Р.К. Стоянова</i> , Термоелектрични оксидни материали на основа на кобалт.....	87
<i>Св. Г. Иванова, Е. Н. Жечева, Р. К. Стоянова</i> , Натриево-преходнометални оксиди с недостиг на натрий $\text{Na}_{1/2}\text{Co}_{1/3}\text{Ni}_{1/3}\text{Mn}_{1/3}\text{O}_2$ като алтернативни електродни материали за литиево-йонни батерии.....	94
<i>М. Калъпсъзова, Р. Стоянова, Е. Жечева</i> , Влияние на начина на синтез върху електрохимичните свойства на $\text{Na}_{2/3}\text{Ni}_{1/2}\text{Mn}_{1/2}\text{O}_2$, използван като електроден материал в литиево-йонни батерии.....	100
<i>С.В. Бойчева, Д.М. Згурева</i> , Изследвания на повърхностните характеристики на зеолити от летяща пепел чрез изотерми на адсорбция и десорбция.....	107